IMPERIAL COLLEGE LONDON

New Physics with Cold Molecules: Precise Microwave Spectroscopy of CH and the Development of a Microwave Trap

by

Stefan Truppe

Thesis submitted in partial fulfillment of the requirements for the degree of Doctor of Philosophy in the

Department of Physics

November 2014

Declaration of Authorship

I declare that this thesis is my own work. Where I have used the work of others the sources are appropriately referenced and acknowledged.

Dass ich erkenne, was die Welt
Im Innersten zusammenhält.
Schau alle Wirkenskraft und Samen,
Und tu nicht mehr in Worten kramen.[1]

Goethe, *Faust*

There is much pleasure to be gained from useless knowledge.

Bertrand Russell

---

[1]That I may detect the inmost force / Which binds the world, and guides its course; / Its germs, productive powers explore, / And rummage in empty words no more.

Abstract

Cold polar molecules provide unique opportunities to test fundamental physics and chemistry. Their permanent electric dipole moments and rich internal structure arising from their vibrational and rotational motion, makes them sensitive probes for new physics. These features also make them ideal for studying ultracold chemistry, for simulating the behaviour of strongly-interacting many-body quantum systems, and for quantum information science.

This thesis describes a number of advances in cold molecule physics. The optimum method for producing an intense, pulsed, supersonic beam of cold CH molecules is investigated, resulting in a beam with 3.5×10^9 ground state CH molecules per steradian per shot. The beam has a translational temperature of $400\,\mathrm{mK}$ and a velocity that is tuneable between 400 and $1800\,\mathrm{m\,s^{-1}}$.

The lowest-lying Λ-doublet transitions of ground state CH, at $3.3\,\mathrm{GHz}$ and $0.7\,\mathrm{GHz}$, are exceptionally sensitive to variations in the fine-structure constant α and the electron-to-proton mass ratio μ. Many modern theories predict that these constants may depend on time, position, or local matter density. Using a novel spectroscopic method, the frequencies of these microwave transitions are measured with accuracy down to $3\,\mathrm{Hz}$. By comparing to radio-astronomical observations, the hypothesis that fundamental constants may differ between the high and low density environments of the Earth and the interstellar medium of the Milky Way is tested. These measurements find no variation and set upper limits of $|\Delta\alpha/\alpha| < 2.1 \times 10^{-7}$ and $|\Delta\mu/\mu| < 4.3 \times 10^{-7}$. The frequency of the lowest millimetre-wave transition of CH, near $533\,\mathrm{GHz}$, is also measured with an accuracy of $0.6\,\mathrm{kHz}$.

The development of a novel type of trap for ground-state polar molecules is presented. Trapping polar molecules is a necessary condition to cool them to ultracold temperatures of $1\,\mathrm{\mu K}$ and below. The trap uses a high intensity microwave field in a Fabry-Pérot resonator. Experimental and theoretical investigations are presented that explore the modes of the cavity, how to obtain the highest possible quality factor, and how to optimally couple the microwave power into the cavity.

Finally, a cold supersonic beam of BH molecules is developed. This molecule appears to be particularly well-suited to direct laser cooling due to its favourable rotational structure and Franck-Condon factors. The laser cooling concept is described, and a first spectroscopic investigation of the relevant molecular structure is presented.

Acknowledgements

Contents

List of Figures

List of Tables

Chapter 1

Introduction

If this nonsense of Bohr should in the end prove to be right, we will quit physics!

Otto Stern and Max von Laue

The study of matter at the level of fundamental particles has revolutionised our understanding of the building blocks of nature and their interactions. In particular, the development of the quantum atom in the early years of the last century has opened a completely new chapter in the history of physics. It has not only changed the way we describe matter at the most fundamental level, but also poses serious philosophical implications. Furthermore, quantum theory is important to understand the stability of atoms and it describes how atoms bond to form molecules. Modern technologies such as the laser, the transistor and magnetic resonance imaging are directly related to the development of quantum theory. Efforts are even under way to develop cryptography schemes based on quantum effects and computers that can perform certain tasks exponentially faster than current, classical computers.

Modern quantum theories, developed mainly between the 1930s and 1970s, are so successful that we can now describe three of the fundamental forces and nearly all the fundamental particles within one theoretical framework - the Standard Model of particle physics. The heart of the Standard Model are quantum field theories which are among the most stringently tested theories in physics and have reached accuracies the early pioneers of quantum physics might not even have dreamt of. However, even the Standard Model has its limits: it can not explain gravity, why the particles have the masses they have and why the coupling constants that govern their interactions have the values we measure. Another intriguing question the Standard Model can not answer is why there is so much more matter than antimatter in the universe. And finally, it has recently been discovered that most of the universe consists of some peculiar form of matter, dark matter and dark energy that the Standard Model in its current form, does not describe.

The precise study of atoms and molecules in the gas phase continues to provide insight into possible new physics, and one of the main tools for this study is the atomic/molecular beam. In

such a beam most unwanted effects such as collisions of atmospheric particles with the species under investigation can be prevented. This allows to reach unprecedented accuracies and to isolate and study quantum effects that are inaccessible otherwise. A specific branch of beam physics, the manipulation of atomic beams with laser light has reached such a high level of precision that it led to the redefinition of the SI second by using a beam of caesium atoms and later to the realisation of a new state of matter at extremely low temperatures - the Bose-Einstein condensate.

By the end of the 1990s new technologies emerged to control the motion of molecules. This stimulated interest in the possibility of controlling molecules to the same degree as already obtained for atoms, and then to harvest the new possibilities that arise from the complex internal structure of molecules. A quest to cool molecules to ever lower temperatures began.

1.1   Overview

This thesis describes several new developments in the field of cold molecules. I first describe the production of an intense and cold beam of CH molecules. I then describe how I use this beam to measure microwave and mm-wave transitions in the CH molecule with unprecedented accuracy. These transitions are sensitive to a possible variation in the fundamental constants, and I use my measurements to set limits on their possible variation. I go on to present a new kind of trap that uses a microwave field to confine molecules. Finally, I discuss the possibility of laser cooling a specific molecule - BH - and present the first steps in this direction.

Chapter 2 gives a brief theoretical description of the CH molecule which is necessary to understand the subsequent experiments. The characterisation and performance of each molecular beam source we built is presented in chapter 3. This chapter also presents a careful calibration of the detector, which allowed us to accurately determine the flux and density of the molecules we produced.

In chapter 4 and 5 I present the measurements of microwave and mm-wave transition frequencies in CH. By comparing the laboratory measurements with astrophysical measurements I set upper limits on the variation of the fine-structure constant, and the electron-to-proton mass ratio.

Chapter 6 presents the work done to build a suitable trap for ground-state molecules which will allow further cooling, either sympathetically or through forced evaporation. The first prototype of such a trap which is based on high-power microwave radiation is described and carefully characterised.

Some specific molecules have an internal structure that makes them amenable to laser cooling. The BH molecule appears to be a very promising candidate. Its simple structure facilitates the direct laser cooling considerably. A magneto-optical trap to cool the molecules to very low

temperatures and maybe even to quantum degeneracy straight from a molecular beam may be feasible using this molecule. The first experiments, i.e. the creation of a the molecular beam of BH molecules and initial spectroscopy experiments are presented in chapter 7.

Before the individual experiments are described, the motivation for our research on polar molecules will be described in more detail. The recent development in the field of ultracold matter science is intimately linked to the development of the atomic and molecular beam. A brief outline of this history is given followed by a more detailed discussion of the potential applications of cold and ultracold molecules.

1.2 The Atomic and Molecular Beam

This section gives a historical account of the development and applications of atomic and molecular beams. It is not essential for an understanding of the rest of the thesis, and so can be skipped if desired. However, the interested reader will find a comprehensive summary of the historical milestones that influenced the development of our modern physical world view, with particular emphasis on the role of the atomic theory and the nature of heat. In my view the understanding of the historical development of a field of research is as important as learning the relevant theoretical and experimental skills. It highlights the dynamics that led to a specific scientific breakthrough which helps to put modern developments into a wider context.

1.2.1 Motion is Heat

With thermodynamics, one can calculate almost everything crudely; with kinetic theory, one can calculate fewer things, but more accurately; and with statistical mechanics, one can calculate almost nothing exactly.

Eugene Paul Wigner

In 1738 the Swiss mathematician Daniel Bernoulli argues in *Hydrodynamica* that "elastic fluids", like air, consist of a large number of "very minute corpuscles, which are driven hither and thither with a very rapid motion" [1]. He further assumes that if such an elastic fluid is contained in a cylinder an increase in temperature by heating will result in a "more intense motion in the particles of air" [1].[1] He then uses Leibniz's concept of "vis viva", an early expression for energy, and Newton's second law to infer that a more intense motion of the particles results in

---

[1]The concept of elasticity of air goes back to Robert Boyle who stated in his woollen fleece theory of 1660, that air behaved like the wool in a fleece, whose rolled and springy hairs easily yielded to external pressure, and recovered when the pressure was released. In 1662 he used this concept in the appendix to the second edition of his "New Experiments Physico-Mechanical Touching the Spring of the Air [...]" to find his famous law relating pressure and volume. He also put forward the idea of Rene Descartes that "the Air is nothing but a Congeries or heap of small Particles".

an increase in pressure onto the container walls.[2] Thus, Bernoulli was able to derive Boyle's law by assuming that tiny particles move in a "rectilinear" way and can be interrupted by collisions with other particles and with the walls of a containing vessel [2].

Bernoulli's theory was almost entirely ignored. It was just one among many other theories of gases. The most significant one was introduced by Isaac Newton in Book II of the *Principia*. He explains the pressure of air by repulsive and attractive forces between particles and its expansion with temperature by vibrations of the particles. This theory explained everything that was required of it at that time, so there was simply no necessity for other theories. Antoine Lavoisier took Newton's idea further and proposed a fluid he called *caloric* as the substance of heat. He thought of this substance to be composed of Newton's particles that repel each other and are attracted to ordinary matter. In his perception the fluid flows from cold to hot and the quantity of this substance is constant throughout the universe.

Although we know now that this is conceptually wrong it provided many successful explanations. It was so successful in explaining physical and chemical phenomena that the early kinetic theory of Bernoulli slowly disappeared from the scientific stage. The early 18th century brought new hope through novel experiments conducted by talented scientists. In 1787 Jacques Charles and later in 1802 Joseph Louis Gay-Lussac found that the volume of a gas at constant pressure is proportional to its temperature. Joseph Louis Proust and John Dalton who independently studied the same phenomena reintroduce atoms to explain why elements always combine in ratios of small whole numbers.[3] Dalton is the first to assign a characteristic weight to what he called the "ultimate particles of several gases". So for him "an atom of water or steam [is] composed of one atom of [the element] oxygen and one atom [of the element] hydrogen, retained in physical contact by a strong affinity". In the same year Dalton published his first part of *A New System of Chemical Philosophy* [3].[4]

Gay-Lussac discovered that there are simple volumetric ratios for reactions between gases. For example, two volumes of Hydrogen combined with one volume of Oxygen yield 2 volumes of gaseous water [4]. Dalton rejected Gay-Lussac's results by criticising his measurement accuracy among other things. He was convinced of Newton's conception that the atoms were composed of a small centre which is surrounded by a large atmosphere of caloric. In his opinion a gas is composed of static, contiguous particles the size of which is related to their volume. This idea, however, was difficult to reconcile with Gay-Lussac's simple volume ratios.

In 1811, Amedeo Avogadro tried to solve this conflict by assuming that "the number of integral molecules[5] contained in a given volume is always the same for equal volumes" [5]. Thus, he abandons the idea that a gas consists of large, static particles in favour of a dynamic view

---

[2]Actually, Boyle proposed this idea already, but only mentions in a sentence that one could explain the increase in pressure that way. Bernoulli, however, describes it quantitatively.

[3]Robert Boyle was the first to show that there are more than the four classical elements, but it was Antoine Lavoisier who published an extensive list of fundamental elements that could not be broken down further.

[4]Various parts and ideas of this manuscript were published earlier already. In 1803 he gave a brief outline of his ideas regarding heat and chemical combinations in a course of lectures at the Royal Institution in London.

[5]He distinguished between molecules elementaires, atoms, and molecules integrantes, molecules.

in which the particles are not in contact and are quite small compared to the distance between them. Dalton and the majority of chemists and physicists, however, did not believe that either. If one volume of oxygen reacts with two volumes of hydrogen to produce two volumes of water, Avogadro's hypothesis would suggest that each water molecule possesses only half an oxygen atom. Widespread reluctance that two atoms of the same element could form diatomic molecules delayed a further development of Avogadro's hypothesis for over thirty years.

John Herapath is another unsung hero of the kinetic theory of gases. Over the course of the second decade of the 19th century he was "amusing [himself] with calculating some of the lunar equations from theory" [6]. While doing so he found a slight discrepancy between Newton's theory of gravity and astronomical observations. In order to resolve this problem he turned to explain the actual cause of gravity. Herapath concluded that the medium mediating gravity could be "of the same nature as our atmosphere and other gaseous bodies" [6]. Thus, he tried to explain gravity through density changes of the atmosphere between the very hot sun and the colder earth and started to investigate the actual cause of heat. Although he "wished to persuade [himself] that the discovery was altogether beyond the reach of human ability", he continued: "Thus between hope and despair, between unceasing attempts and mortifying failures, I continued until March 1814, at which time my ideas of heat underwent a complete revolution" [6]. He started with the widely accepted idea that heat is the effect of an elastic fluid, but through careful investigations he came to the conclusion that this was the wrong picture. A much more simple picture in his view was that gases were made up of particles, or atoms mutually, impinging on one another and the sides of the vessel containing the gas. This allows to explain heat by "rapid intestine motion". He submitted his paper to the Transactions of the Royal Society where it was rejected by Sir Humphry Davy. After nine months during which he experienced "[...] an unlooked-for, and I might almost venture to say, illiberal opposition" he was forced to publish in the *Annals of Philosophy* [6].

In contrast to Bernoulli, Herapath took *momentum* as the measure of temperature rather than the square of the velocity. Thus he was the first to account for Dalton's discovery that atoms of different gases have different weights, although in a wrong way. Herapath continued his work on the kinetic theory, but was ignored by most scientists.

John James Waterston has undergone an even worse fate than Herapath, as he invented the kinetic theory for the third time but this time the right way.[6] Waterston correctly identified that the gas pressure is a function of the number of molecules per unit volume, the molecular mass and their mean square velocity. He applied this idea to explain temperature and derived the ideal gas law. Like Herapath he sent his paper to the Royal Society. Since Waterston was not a Fellow of the Royal Society his paper could only be *read* in front of the society and it then became the property of the Society and would not be returned to the author even if it were not published. Baden Powell, Professor at Oxford, replied after reading it, that the principle

---

[6]It is unlikely that Waterston knew of Herapath's or Bernoulli's work when he developed his theory as Lord Rayleigh points out in the introduction to the publication of the paper in the *Philosophical Transactions*.

that the pressure of a gas is due to the impacts of the molecules onto its containing vessel, was "very difficult to admit, and by no means a satisfactory basis for a mathematical theory" [7]. The other referee, Sir John William Lubbock, first Vice Chancellor of the University of London at the time wrote: "the paper is nothing but nonsense, unfit even for reading before the Society" [7]. At this stage the president, Davy, usually informed the author that it would not be published, but only read in front of the Society. Waterston, however, was working for the East India Company in Bombay at that time and thus did not submit the paper personally. A friend of his, who submitted the paper agreed that it should be read in front of the Society, apparently not knowing the consequences. An abstract was published in the Proceedings of the Royal Society and the paper disappeared in the archives. It stayed there and remained unknown until 1892[7], when Lord Rayleigh discovered and published it in the *Philosophical Transactions* noting that it "marks an immense advance in the direction of the now generally received theory. The omission to publish it at the time was a misfortune, which probably retarded the development of the subject by ten or fifteen years" [7]. After Bernoulli, Herapath and Waterston, it was a German chemist, Karl Krönig, who invented the kinetic theory for the fourth time.[8] This time with more luck. James Joule, Julius Robert Mayer and Hermann von Helmholtz have established heat as a form of energy and introduced the concept of energy conservation.

Krönig's publication provided the occasion for Rudolf Clausius to publish his independently developed kinetic theory in 1857. This marks the beginning of the modern kinetic theory. Clausius formulated the second law of thermodynamics, introduced the term *entropy* and the concept of mean free path and postulates the virial theorem. He thus was the first to relate the macroscopic world of thermodynamics to properties of atoms.

Stimulated by Clausius' paper, James Clerk Maxwell embarked on an "exercise on mechanics" to "deduce the laws of motion of systems of particles acting on each other only by impact". In this exercise he found (independently of Ludwig Boltzmann) that the molecular velocities are distributed and thus laid the foundations for modern statistical mechanics [8]. He related the mean free path to gas properties such as viscosity and even conducted experiments to test his prediction that the viscosity of a gas is independent of its density.

It was Ludwig Boltzmann, however, who took the kinetic theory to a whole different level. He studied in Vienna with Josef Stefan and Joseph Loschmidt. Stefan investigated experimentally the thermal radiation of a blackbody and Loschmidt gave the first reliable estimate of the size of molecules using the theory developed by Clausius and Maxwell. This allowed him to calculate the number of gas molecules per volume for the first time. Boltzmann named this number Loschmidt's number which is approximately equal to what is now known as Avogadro's constant.

Boltzmann was able to generalise Maxwell's velocity distribution to arbitrary gases and gas

---

[7]Eleven years after Waterston mysteriously vanished during his morning outing and was declared dead.

[8]An abstract of Waterston's presentation at the British Association for the Advancement of Science in 1851 appeared in "Die Fortschritte der Physik". Krönig was the editor of that journal at that time. Krönig thus might have been influenced by Waterston.

mixtures which could even be under the influence of external forces. He further related the thermodynamic quantity entropy to the statistical distribution of molecular configurations and showed that the increase in entropy of an ideal gas is an irreversible process.

Loschmidt immediately pointed out that a theory which is based on Newtonian mechanics cannot predict irreversibility, since every single collision is reversible. This reversibility paradox and the fact that the theory predicts a wrong value for the specific heat of gases which are composed of diatomic molecules were treated as serious problems of the atomistic-mechanical viewpoint in general.

This triggered a fierce scientific debate about the reality of atoms. Ostwald wanted to replace atomic theories by "Energetics", a kind of generalized thermodynamics. For the positivist Mach, knowledge could only be gained from experience and logical analysis. Since one cannot observe small things such as atoms he insisted that atoms were not considered to have a real existence, although he recognized that it is a useful hypothesis for science. Boltzmann was a bit more pragmatic. In his opinion the atomic view yielded an analogy, a picture or model of reality which is useful to understand the behaviour of gases. Nothing more or less.

He further argued that the reversibility problem can be solved if entropy is conceived as a measure of the probability of a state. The most likely state, the state with the highest entropy, is thermal equilibrium. Hence, it is possible that entropy decreases, but it is extremely unlikely. However, it is these fluctuations of entropy which certainly occur if one waits long enough that led Ernst Zermelo, a student of Max Planck, and Henri Poincaré to refute the kinetic theory and any theory that is based on the assumption that matter is composed of particles moving with the laws of mechanics.

Boltzmann also showed great interest in Maxwell's electrodynamic theory. He derived the empirical law obtained by Josef Stefan, which accounted for the total intensity of the radiation emitted by a heated blackbody using a connection between radiation and the second law of thermodynamics.

Wilhelm Wien picked up on this idea and developed it further to describe the dependence of the energy distribution of heat radiation on temperature, now known as Wien's displacement law. Wien, however, could only restrict the distribution itself to a certain class that would transform correctly under his law and other thermodynamic assumptions. He developed this theory from statistical methods and thermodynamic arguments only and it agreed well with Friedrich Paschen's empirical law.

Max Planck tried to derive Wien's law without any of the assumptions Wien had to make. Up to that point Planck mainly worked on thermodynamics and its application to physical chemistry and was quite sceptical about the utility of the atomic-kinetic theory and Boltzmann's statistical approach. Opposing Boltzmann, he wanted to deduce the principle of irreversibility rather from electromagnetic theory than from molecular models in a kinetic theory of gases. He considered an idealized system of oscillators (resonators) which absorb and emit electromagnetic waves. He later revoked his scepticism and stressed that Boltzmann's statistical interpretation

of entropy is the key to the understanding of the quantum theory of radiation. Planck realised that Wien's law corresponds to a very simple formula for entropy and that it was perfectly consistent with the second law of thermodynamics. So he identified what he called electromagnetic entropy, with the thermodynamic entropy and derived from it Wien's law of blackbody radiation.

Planck analysed the relation between energy and entropy of a radiating blackbody to derive Wien's law in a more systematic way directly from the second law of thermodynamics. In the same session of a meeting of the German Physical Society in 1900, as Planck presented the new derivation of Wien's law, Lummer and Pringsheim showed that this very law breaks down at high temperatures and low frequencies. Rubens and Kurlbaum performed new experiments at very long wavelengths and informed Planck that the intensity of the radiation increases proportionally to the temperature, in agreement with Lord Rayleigh's formula. Planck took this as an occasion to study the theoretical implications of these experimental results using his entropy approach. He then proposed an empirical interpolation between his earlier results which would reduce to Lord Rayleigh's formula in the limit of long wavelengths. This formula, now known as Planck's law of radiation, successfully described the experimental data. The theoretical derivation of this empirical law, however, still remained unclear. Although Planck initially showed a very indifferent attitude towards the atomistic theory and probabilistic interpretation of entropy, developed by Boltzmann, he recognised the similarity between his concept of irreversibility through radiation and Boltzmann's molecular chaos. Hence he started to search for a physical interpretation of his radiation formula using Boltzmann's statistical theory of molecular gases. And indeed he discovered a similar expression for his equilibrium entropy of blackbody radiation in one of Boltzmann's early papers. In this paper Boltzmann calculates the combinatorial arrangements of atoms the energies of which are proportional to a basic quantum. Boltzmann would at the end of his calculation take the limit of an infinitesimally small quantum. Planck, however, realised that if he calculated the combinatorial arrangement of a certain number of oscillators among which the total amount of energy is distributed in integral multiples of a basic quantum, he arrives, after using Boltzmann's formula for entropy, exactly at the desired expression for the equilibrium entropy he discovered earlier by empirical interpolation. He thus could derive his radiation law by assuming that the given amount of energy is not infinitely divisible but is rather composed of a completely definite number of finite, equal parts, distributed among the resonators according to Boltzmann's formula. Planck presented these results at a meeting of the German Physical Society in Berlin on 14 December 1900 which, as Arnold Sommerfeld would later call it, marks the birthday of quantum theory.

Although the success of the kinetic theory and especially the statistical concepts introduced by Maxwell, Boltzmann and later also by Gibbs led to wide acceptance of the theory under scientists, direct evidence for the molecular structure of matter was still missing. Atoms and molecules were still widely considered as purely hypothetical constructs, although evidence was growing from a different field of research: cathode rays. In 1864 Heinrich Geissler used his newly

invented mercury displacement pump to evacuate glass tubes to unprecedented levels. After solving the problem of how to get an electrode into such a tube he could demonstrate the first glow discharge. William Crookes managed to evacuate tubes based on Geissler's design to even lower pressure using improved vacuum pumps. He noticed that as he lowered the pressure the glowing disappeared and the glass walls behind the anode started to fluoresce. In 1876 Eugen Goldstein proved that these were rays originating from the cathode, and thus called them cathode rays.

Heinrich Hertz discovered that thin metal leaves transmit cathode rays and showed it to his assistant Philipp von Lenard. Hertz suggested that this could be very useful to use as a window to separate two chambers of different pressures in order to study these rays in more detail and to decide if these rays were a "kind of undulatory motion in the ether" or consist of negatively charged particles ejected by the cathode. Lenard, however, was more interested to see what effect these rays had on air of normal density. He separated a discharge tube from a tube filled with air with thin aluminium foil and could indeed show that cathode rays would pass through air of normal density, however only up to a few centimeters. He argued that since light passes through air, the molecules that make up air must be much smaller than the wavelength. However, since the cathode rays are hindered by each of these air molecules, he concluded that these rays must be extremely fine. He further suggested that one could use cathode rays to find out more about atoms and molecules. He showed that the energy of rays produced by irradiating metals with ultraviolet light[9] depends on the wavelength of the light and not on its intensity.

Whereas Lenard was convinced that he discovered electricity itself, so electrical charge without charged bodies, or "unknown parts of the ether" [9], John J. Thomson believed that cathode rays were made up by tiny corpuscles with a "mass much smaller than any atom of any known element" [9]. Thomson measured the charge to mass ratio and found that it does not depend on the material of the electrode or the gas he used. Thus these particles must be of "very general occurrence" [10]. So evidence for the reality of atoms with a definite mass and size was piling up. Einstein became interested in the foundations of the kinetic theory in order to find "facts which would guarantee as much as possible the existence of atoms of finite size" [11]. Einstein, in complete ignorance of Gibbs' and most of Boltzmann's work, rediscovered all the essential features of statistical mechanics in 1902 in order to derive a law for blackbody radiation directly from kinetic theory [12]. He pointed out that Planck did not give a proper interpretation of his newly introduced universal constant and that his derivation was not consistent with Maxwell's electrodynamic theory.

Einstein assumed that "monochromatic radiation of low density [...] behaves, in a thermodynamic sense, as if it consisted of mutually independent radiation quanta [...]" [13]. Using this hypothesis he could elucidate three unexplained phenomena: fluorescence, the photoelectric effect and the ionization of gases by ultraviolet light. While working on his statistical mechanics

---

[9]An effect first described by Heinrich Hertz in 1887.

Einstein wanted to prove that, "according to atomistic theory, there would have to be a movement of suspended microscopic particles open to observation [...] [13]."

It is quite remarkable that he arrived at these results ignorant of anything done on the subject already. Just during the final stages of his theory that describes the motion of these microscopic particles he became aware that Brown had observed this motion nearly 80 years earlier and that there were numerous earlier attempts to describe it. Einstein embarked on this journey through statistical physics with the aim to find facts that would prove the reality of atoms and molecules. He was convinced that he found a suitable test that would decide this fundamental question.

Max Born would later write that Einstein's theory "did more than any other work to convince physicists of the reality of atoms and molecules, of the kinetic theory of heat and of the fundamental part of probability in the natural laws" [12]. Motivated by his earlier work on cathode rays and X-rays, Jean Baptiste Perrin, became interested in the kinetic theory of gases and thus stumbled across Einstein's explanation of Brownian motion. In 1908 he showed experimentally that small soap like particles, gamboge, suspended in water, obeyed the laws predicted by Einstein's theory which is based on the kinetic theory. He was able to calculate the size of a water molecule and thus Avogadro's number which was consistent with values obtained by completely different methods. In this way the discrete nature of matter was proved beyond doubt and he was awarded the Nobel prize in physics, although nearly twenty years later. This finally convinced most scientists of the physical reality of atoms and molecules.

The very fundamental assumption of the kinetic theory that atoms and molecules move in straight lines was demonstrated three years later by a student and assistant of Perrin, Louis Dunoyer. He used a glass tube and divided it into three sections by using small apertures. He filled sodium metal into the first part and evacuated the tube. He then heated the metal so that it evaporates and condensed the sodium vapour on the other end of the tube by cooling the wall with liquid air. He could show that the shape of the sodium deposit is consistent with the fact that atoms and molecules move in straight lines like rays of light. Therefore, he called such a beam a molecular ray or molecular beam. This can not only be seen as the birth of the molecular beam method but also of the thin film deposition technique. Subsequent experiments on fluorescence of a beam of sodium atoms helped to establish the new technique and stimulated the interest of other scientists.

1.2.2 Otto Stern - Of Spatial Quantisation and Bad Cigars

Otto Stern received his PhD in 1912 in physical chemistry for his work on the kinetic theory of osmotic pressure in concentrated solutions, e.g. soda water, and joined Albert Einstein as an assistant in Prague. He followed him to ETH in Zürich a year after where they started to

work on the problem of zero point energy. Under Einstein's influence Stern became interested in statistical physics, the nature of atoms and light quanta. He thus became acquainted with the early stages of quantum theory and Bohr's model of the atom. He met and became friends with Max von Laue who recently discovered that X-rays are diffracted from crystals. They were later quoted by Wolfgang Pauli saying that "if this nonsense of Bohr should prove to be right in the end, we will quit physics" [14]. Stern then followed his friend Max von Laue to Frankfurt in 1914 where he was appointed Privatdozent in theoretical physics. During the first world war he had been engaged in military research in Belgium, Poland and later in Berlin where he joined the experimentalists James Franck and Max Volmer in Walther Nernst's laboratory. After the war had ended Stern went back to Frankfurt. Inspired by the experience in Nernst's laboratory and the pioneering work of Dunoyer he considered to conduct his own experiments to measure properties of single atoms and molecules. As Max von Laue left Frankfurt for Berlin, Max Born was appointed professor in Frankfurt and became Stern's boss. As Born recalled later, they were both not "very good with [their] hands" [14], so they relied on Adolf Schmidt their mechanic to do the experimental work while they told him what to do. Stern's first attempt was motivated by the kinetic theory. In particular, he wanted to measure the velocity distribution of a beam of silver atoms. He did so by mounting his atomic beam machine on a rotating platform which he could spin up to 2400 rotations per minute. By detecting the centrifugal displacement of the beam he could deduce the mean velocity of the atoms and confirm the theoretical predictions of Maxwell and Boltzmann. Stern could not measure the whole distribution due to experimental difficulties and thus decided to try something else.

It was known from spectroscopic experiments that atoms behaved like small magnets. Depending on the orientation of these magnets in an external field the spectral lines of atoms would split into components. This was shown experimentally already in 1896 by Pieter Zeeman. Joseph Larmor found a classical, theoretical description a year later, assuming rotating electrons. How these electrons could be confined to circular orbits around a heavy nucleus without losing energy by radiation remained unsolved until Niels Bohr proposed his atomic model of discrete, stationary electron orbits. Owen Richardson and later Einstein and De-Haas could prove the existence of these "molecular currents" by measuring the mechanical rotation induced in a ferromagnetic material.

In 1916 Arnold Sommerfeld and Peter Debye independently tried to amend Bohr's atomic model in order to account for the Zeeman effect. They proposed that Bohr's electron orbits not only possess discrete sizes and shapes, but that the orbital planes could only have certain, discrete spatial directions with respect to an externally applied field. This idea amounted to postulating that the magnetic moment associated with the orbiting electrons could only take certain discrete orientations in an external field, contrary to the classical, continuous case.

In contrast to his contemporaries Otto Stern took this idea literally, in the sense that one could use it to prove that the whole concept of Bohr's model was flawed. So his plan was to design an experiment to decide if the classical or the quantum interpretation was correct. Max

Born and even Debye thought of this "spatial quantization" rather as a kind of symbolic expression for something they did not understand. Born even tried to persuade Stern that there was no sense to look for such an effect using his atomic beam machine. But Stern remained stubborn and conceived an experiment to subject an atomic beam of silver atoms to an inhomogeneous magnetic field. If the classical description was right then one should only observe a broadening of the beam, since the classical magnets would only precess but remain randomly oriented. If, on the other hand, the quantum description was right then the beam should split into two components, corresponding to the two directions of the magnetic moment allowed by the quantization condition. Stern immediately ran into experimental challenges, regarding his beam machine. Luckily, in 1920, a very talented young man joined the experimental institute in Frankfurt, Walther Gerlach. As Gerlach would recall later, Born was very happy about having him around: "Thank God, now we have someone who knows how to do experiments." Gerlach had already made first attempts on molecular beams as an assistant to Friedrich Paschen in Tübingen, where he had set up Dunoyer's sodium machine for spectroscopic purposes and magnetic studies of bismuth.

The experiment proved to be incredibly difficult. They used an oven in vacuum which they had to heat to $1000\,°C$ and collimated the beam using two slits only $30\,\mu m$ wide. Thus a misalignment of the two slits or the magnet by less than $10\,\mu m$ could spoil an experimental run which took hours of operation. Due to the small collimation slits the deposited silver film was very thin. First they could not see it, but as Dudley Herschbach and Norman Ramsey recalled later, Stern smoked bad cigars which contained a considerable amount of sulphur. While staring at the plate Stern's sulphurous breath turned the silver into silver sulphide, which is black and easily visible [14, 15]. Stern became Professor in Rostock in 1921 and thus Gerlach had to finish the experiment by himself. After further refinements he could unambiguously show a splitting of the beam into two parts in February 1922. He immediately sent a telegram to Stern, which read "Bohr is right after all!" [14]. This agreement with what is now known as the "old" quantum theory of Bohr and Sommerfeld was a lucky coincidence since it is actually not the quantised orbital angular momentum that causes the magnetic moment of the silver atoms but rather the magnetic moment of the electron itself, caused by its spin angular momentum. This internal angular momentum of the electron was not discovered until three years later when George Uhlenbeck and Samuel Goudsmit proposed the concept of spin in order to solve the decade long struggle to explain the anomalous Zeeman effect[10]. After Uhlenbeck and Goudsmit sent their paper to *Die Naturwissenschaften* they became aware of the fact that Pauli and Lorentz had thought about the same problem but rejected the idea because they were frightened of the incompatibility of a spinning electron with special relativity. Worried about the publication, their mentor Paul Ehrenfest consoled them with: "You are both young enough to afford a stupidity like that" [12]. As it turned out later, Lorentz and Pauli were wrong as Llewellyn Thomas

---

[10]It was found that for the majority of atoms under the influence of a magnetic field, the spectral lines would split into an even number, which could not be accounted for by the Bohr-Sommerfeld or classical model.

showed that a spinning electron actually does not violate special relativity. Ralph Kronig, an assistant of Landé, working at Columbia University had conceived the concept of spin a few months earlier, but Pauli had frightened him when he presented the idea in Tübingen and he subsequently refrained from publishing it.

Stern stayed in Rostock for two years only and moved to Hamburg in 1923 to become professor of physical chemistry and director of the newly founded Institute for Physical Chemistry at the University of Hamburg. He set up a world renowned research group which helped to establish the atomic/molecular beam method as an essential tool for atomic, molecular and nuclear physics. After this great initial success he immediately came up with a hugely ambitious research plan which contained eight major research goals. Among others he wanted to use the molecular beam method to measure nuclear magnetic moments, to determine the recoil of photons and confirm Louis de Broglie's wave-particle duality. Hence he immediately started to improve every single aspect of the molecular beam machine. He developed novel, more intense molecular sources, velocity selectors and more efficient detectors, based on hot tungsten wires. With these and other measures Stern wanted to improve the angular resolution of his experiments by a factor of 10^5 which should make it possible to detect scattering of molecular beams from gases and surfaces to measure van der Waals forces. Stern's reputation attracted many, very talented young research fellows from all over the world. Among them were Isidor Rabi and Emilio Segrè who would later become leading figures as well. But it was also the close relation to the theoretical institute which fostered an especially stimulating and creative atmosphere. Among the theorists working in Hamburg at that time were Wolfgang Pauli, Ernst Ising, Walter Gordon, Wilhelm Lenz, Pascual Jordan and Hans Jensen. Stern was the first to diffract helium and hydrogen molecules to confirm the "dual nature of rays of matter". Thus, in addition to the experiment of Davisson and Germer with electrons, he could show that de Broglie's hypothesis is also true for composite particles such as atoms and molecules. Subsequently, matter wave interferometry with electrons was picked up again in the 1950s, with neutrons in the 1960s, and with atoms in the late 1960s. With the advent of nanofabrication, the diffraction from material gratings became feasible in the late 1980s. In 1999 even the diffraction of heavy, complex molecules such as Fullerenes from a material grating could be demonstrated [16]. The interference of de Broglie waves has since become a rich branch of atomic physics with many applications in modern science. One can even envision many practical applications, such as the construction of highly sensitive, miniaturized gravitational detectors, frequency standards or accelerometers based on such matter waves [17].

Knauer, one of Stern's assistants, succeeded in measuring the differential cross sections for scattering of He, H_2, O_2, H_2O molecules from each other. This would later be picked up again in the 1960s and lead to the Nobel prizes for Dudley Herschbach, Yuan Lee and John Polanyi for their studies on molecular collisions and reaction dynamics which is still an active field of research today in physical chemistry.

Otto Frisch, another assistant, was able to detect the recoil of a sodium beam upon absorption of a resonant photon. This work was picked up again in the late 1960s and early 1970s when better light sources, especially lasers, became commonly available. This work would lead to the development of powerful methods for cooling, trapping and manipulating of neutral atoms with laser light. This led to dramatic achievements and to an explosion of the field of atomic physics.

Most importantly for the further development of the molecular beam method were Stern's attempts to measure the magnetic moment of the proton. Pauli and other theorists told him that there was no point in measuring it since it should just be inversely proportional to the masses of the particles times the magnetic moment of the electron. Nevertheless, Stern measured it the theorists were wrong, and Stern's measurement pointed to an internal structure of the proton. This work would be further pursued and developed by Isidior Rabi.

1.2.3 My Name is Rabi, I Have Come Here to Work

Isidor Rabi came to Europe after finishing his PhD at Columbia University because there were no jobs in the US at that time. Rabi remarked later that "in the United States, as far as theoretical physics was concerned, we were provincial. Definitely provincial" [18]. He was awarded a small fellowship and went to Zurich to work with Schrödinger, although without any arrangements. On his first day he sat in a colloquium and did not understand a word. In his desperation he looked around for fellow Americans ("they always wore white shirts with their collars attached"). Luckily he found one and it turned out to be Linus Pauling, who consoled him by saying,"don't worry, he was not talking German, he was talking Schwitzerdeutsch" [18]. Schrödinger left on the same day to Berlin and Rabi went to Munich to visit Sommerfeld. Again without any arrangements, he came to Sommerfeld's office and said, "My name is Rabi, I've come here to work." He was shown a room where Sommerfeld's students, Hans Bethe was among them, were working and joined them. In the autumn, Rabi went to London, but soon left to Copenhagen when he realised that he would see "financial disaster staring me in the face" if he stayed there. Copenhagen was the Mecca for theoretical physics at that time. "Everything good came out of Copenhagen in one way or another." In Copenhagen he went to the Institute for Theoretical Physics, rang the bell and said his usual sentence "My name is Rabi, I've come here to work." He was granted access. Bohr was busy and arranged, without asking Rabi, for him to go to work with Pauli in Hamburg. First disappointed he quickly realised that "Hamburg was actually the greatest institution in the world for physics at that moment". He became friends with Ronald Fraser and John Taylor, who worked in Stern's lab, "to talk some English". Rabi became interested in the molecular beam method and was allowed to conduct his first experiments in Stern's lab.

Rabi obtained a lectureship at Columbia and started to build his own molecular beam experiments by 1931. Over the next couple of years, together with his assistant, Sidney Millman, and his colleagues Polykarp Kusch and Jerrold Zacharias, Rabi refined the technique of manipulating atoms and molecules with a combination of inhomogeneous and homogeneous fields. After Cornelius Gorter suggested to use varying radio waves to manipulate the orientation of the magnetic moments, Rabi added this new feature to his beam machine. He could deflect molecules in a strong magnetic field by tuning the frequency of electromagnetic waves (or varying the magnetic field strength) and hence measure the transition from one energy state to the other. This also enabled him to measure magnetic moments with unprecedented accuracy for a variety of atoms and molecules.

Through the discovery by Ed Purcell and Felix Bloch that one could observe such nuclear resonances in solids and liquids as well, Rabi's technique led to nuclear magnetic resonance imaging in medicine and nuclear magnetic resonance spectroscopy of complex molecules, such as proteins. Purcell was also the first to detect radio emission from neutral galactic hydrogen (the famous 21 cm line). This observation launched the extremely fruitful field of radio astronomy. Radio frequency and microwave spectroscopy soon revealed new aspects concerning the structure of galaxies and a huge variety of molecules in interstellar clouds.

Further improvements in radio frequency and microwave technology during the second world war allowed Kusch, using Rabi's technique, to measure the magnetic moment of the electron to unprecedented accuracy and found a slight discrepancy with Dirac's relativistic quantum theory [19].

Willis Lamb started his career as a theorist at the University of California with Oppenheimer, working on electromagnetic properties of nuclear systems. In 1938, he went to Columbia and "came into close relation with Professor I. I. Rabi" [20]. He immediately became interested in Rabi's newly developed resonance technique. During the war he was working at the Columbia Radiation Laboratory to improve microwave radar for military applications. He would later use this experience to resolve a minute energy difference between the $^2S_{1/2}$ and $^2P_{1/2}$ levels of hydrogen. Dirac's theory could not account for such a difference either. Both experiments thus pointed towards something new, which would later become known as quantum electrodynamics.

In the 1950s Alfred Kastler together with his student Jean Brossel realised that one can selectively excite atoms to a single Zeeman sublevel with polarised light and use it to optically detect the magnetic resonance of excited states [21]. This technique would later be called the double-resonance method, because it combines a magnetic (radio frequency) resonance with an optical resonance. This improvement of Rabi's original method has proven to be extremely powerful and is still used today. Note that this also marks the birth of the manipulation of atoms with optical electromagnetic fields out of which the now extremely fruitful research area of ultracold matter would emerge.

Also in the 1950s Charles Townes and at the same time Nicolay Basov and Aleksandr Prokhorov could show coherent amplification of microwaves by a beam of ammonia molecules

[22–24]. This laid the foundation for the laser.

Norman Ramsey, a PhD student of Rabi, improved Rabi's resonance technique for measuring nuclear magnetic moments with unprecedented accuracy. He came up with the method of separated oscillatory fields. This method uses two short regions of oscillatory fields (rf or microwaves) instead of a single long region as in the case of Rabi's method. This has many advantages and increases the sensitivity: The resonance is narrower and the contrast is not reduced when there are non-uniform magnetic fields between the pulses.

The width of the resonance, and thus the accuracy, is proportional to the time between the pulses. Making the interaction time longer meant making the beam machine longer which was not very practical. So Ramsey soon realized that the two oscillatory fields do not have to be separated in space but can be separated in time. So he decided to use an atomic beam in which the atoms, after passing through the first oscillatory field would enter a storage box where they would bounce around for a period of time and then emerge to pass through the second oscillatory field. Initially he used caesium and teflon as a wall coating of his storage box. It worked, but the atoms lost their orientation after a few collisions with the wall. He could improve that by coating the walls with paraffin and obtained a resonance even after 190 collisions. He wanted to do even better and decided to use an atom with a lower mass and lower electric polarisability to reduce the wall interactions even further. Atomic hydrogen turned out to be ideal, however it was difficult to detect. Knowing of Townes' experiments on the ammonia maser, he designed and built the experiment to obtain maser oscillations at the atomic hydrogen hyperfine frequency. Ramsey was also the first to conceive the idea that one could use maser oscillation as a timing standard. Ramsey's work thus made it feasible to perform spectroscopy at a level many orders of magnitude more precise than with Rabi's technique. This stimulated extremely fruitful and extensive applications both in testing the foundations of physics with atomic and molecular beams and applications in technology. By the end of the 1950s and in the early 1960s the molecular beam method has become so widely used in physics, chemical physics and chemistry that it is impossible to list every major contribution. We thus conclude the historical overview by keeping in mind that everything began with the simple idea that heat can be expressed as motion of small particles. After Dunoyer's pioneering work on sodium it was the far reaching work of Otto Stern and his collaborators and students that truly helped the molecular beam method to take off and thus he can be seen as the founding father of experimental atomic physics.

With the improvement of laser technology and its potential for manipulating atoms and molecules, interest in the physics community to use atomic beams grew. Moreover, the success of cold and ultracold atomic physics, stimulated by the first Bose-Einstein condensation of an atomic vapour, boosted molecular beam research in the physics community. Efforts to reach ultracold temperatures for molecules as well got under way. As Dudley Herschbach put it, "much of the hot appeal of molecules [today lies] in the cold ($< 1\,\mathrm{K}$) and ultracold ($< 1\,\mathrm{mK}$)".

Molecules, however, are more complicated than atoms. Additional to electronic degrees of freedom molecules can rotate and vibrate. They can have an electric or magnetic moment, fine and hyperfine structure. Each of these properties can be seen as an additional tunable experimental parameter. And it is these parameters that give ultracold molecular gases unique properties that allow for the study of new physical phenomena. However, it is these additional degrees of freedom that prevent using the work horse of ultracold atomic physics - laser cooling. The problem is not so much the rotation of the molecule, since transitions between different rotational states are governed by strict selection rules. The main problem is the vibrational structure. In general, molecules end up distributed over a large number of vibrational states after a single or few spontaneous emission events which makes laser cooling challenging. The motivation to reach ultracold temperatures for molecules has led to the development of very general methods to manipulate molecular beams.

1.3   Why Cold Molecules?

As we can infer from the previous section, atomic and molecular beams and the manipulation of these revolutionised aspects of both physics and chemistry. The ability to control every degree of freedom of atomic and molecular ensembles has now reached a level the early pioneers may not even have dreamt of. This level of control, coupled with ground breaking developments of ultra stable lasers, have resulted in clocks that have an absolute uncertainty at the 17th decimal place. It paved the way for the observation of Bose-Einstein Condensation, "the most spectacular application of laser cooling and atom trapping" [25]. Interferometers exploiting the coherent manipulation of de Broglie matter waves, similar to that associated with atoms and their motion has led to precise measurements of gravity, gravity gradients, rotations and the photon recoil of an atom [17]. Furthermore, a whole optics toolbox for atoms has been developed, that includes beamsplitters, mirrors, lenses and more. This has led to numerous applications ranging from quantum physics to precision metrology already and will play a major role in addressing fundamental problems regarding gravity and quantum mechanics. The possibility of making artificial crystals for atoms with optical lattices is the first step towards realising Feynman's dream of building a quantum simulator [26, 27]. It has now become possible to use a controllable quantum system to simulate other systems that are currently not, or only poorly, understood. This high degree of control has been extended to the most fundamental level of single quantum systems, like single atoms and single photons [28, 29]. This allows to create elementary quantum communication, quantum computation and eventually maybe the quantum internet [30]. Complementary to manipulating the very small, the concepts of cold atom physics (quantum optics toolbox) have been extended to meso- and macroscopic objects. It is now possible to manipulate mechanical resonators that span the size from hundreds of nanometers in the case of nano-opto-mechanical or nano-electro-mechanical devices to tens of centimeters

in the case of gravitational wave detectors [31]. The coherent control of these large and heavy mechanical systems on the single-phonon level has now been achieved and first applications as novel measurement tools in technology and fundamental science have been demonstrated. Taking the step from ultracold atomic ensembles to molecules is expected to have a similar profound impact allowing us to address problems that are not accessible with atoms. Below, I review some of the applications of cold molecules.

1.3.1 High Resolution Spectroscopy and Precision Measurements

A general rule for spectroscopy experiments is that, in the absence of any systematic uncertainties and extraneous noise, the uncertainty in determining a transition frequency is proportional to $1/\left(T\sqrt{N}\right)$, where T is the time the particles spend in the observation region (coherence time) and N the total number of detection events. Consequently, if all other mechanisms that broaden an atomic or molecular transition are absent, it is the time the atom or molecule spends in the measuring device that determines its width and thus the accuracy with which the transition frequency can be determined. Ideally one wants to use a trapped sample of atoms or molecules. For example, the magnetic moment of the electron has been measured to 3 parts in 10^{13} using a single electron trapped for months [32]. Using a single trapped Aluminium ion in combination with sub-hertz linewidth lasers, a clock based on an optical transition with a fractional frequency inaccuracy of below 1 part in 10^{17} has been constructed [33]. However, trapping might not always be the most accurate way to do spectroscopy since the trapping fields might lead to perturbations of the measurement process. Another way to increase the interaction is by slowing the particles so that they spend more time in the interaction region, i.e. to increase the coherence time. A length of a typical atomic beam experiment is of the order of $1\,\mathrm{m}$. At room temperature a nitrogen molecule moves at about $500\,\mathrm{m\,s^{-1}}$ limiting the interaction time to a few milliseconds, which in turn limits the width of a spectral line to a few kilohertz. Decreasing the temperature to $1\,\mathrm{mK}$ leads to an average velocity of only $1\,\mathrm{m\,s^{-1}}$ and thus interrogation times of the order of seconds would become feasible. Furthermore, the cooling of the internal degrees of freedom, like rotation and vibration, dramatically enhances the number of molecules in a single quantum state and thus the number of detected particles.

1.3.2 Molecules and Time Reversal Symmetry

It is currently widely believed that the Standard Model of particle physics is invariant under the CPT-transformation. This means that we could not distinguish our universe from one where:

- Every particle is replaced by its antiparticle (charge conjugation transformation)

- The sign of the spatial coordinates fixing the particles position in space are flipped (parity transformation)

- The direction of time is reversed (time reversal transformation)

But why is this rather odd combination of C, P and T transformation needed to produce an identical copy of our universe? If a physical law does change under a given transformation it is said to break the symmetry of the underlying transformation. In 1956 Lee and Yang suggested some experiments that could be done to test whether or not the weak interaction violates the symmetries C and P [34]. Within a year Wu performed an experiment on β-decay and could show that the weak interaction indeed violates parity [35]. It was then thought that the weak interaction would preserve the combined symmetry, CP, meaning that particles could violate parity as long as their antiparticles did so in the opposite way. In 1964, however, James Watson Cronin, Val Logsdon Fitch and collaborators discovered that the decay of neutral K-mesons was not invariant under the combined CP transformation. Thus the conclusion was that physical laws must at least be invariant under the combined transformation of CP and T. Until now there is no experimental evidence for CPT violation. Gerhart Lüders, Wolfgang Pauli and implicitly Julian Schwinger independently showed that if any physical law is invariant under Lorentz transformations it also implies that it is invariant under CPT transformation [36]. Thus any violation of CPT symmetry would imply a violation of Lorentz invariance and thus of special and general relativity. Spin statistics and the fact that particles and antiparticles have identical properties, such as mass, lifetime and magnetic moment all arise from CPT invariance. Hence there is good reason, until proven wrong, to assume that physical laws do not change under CPT transformation. This implies that any process that violates CP symmetry must violate time reversal symmetry T as well. As Andrei Sakharov pointed out in 1967 CP-violation is one of three necessary conditions to explain why the universe mainly consists of ordinary matter and why all the antimatter has disappeared [37]. Thus studying CP or direct T violation provides a clue to the origin of the large-scale matter-antimatter imbalance of the universe. Until now CP violation has only been observed in mesons, unstable subatomic particles, and is essentially consistent with the predictions of Kobayashi and Maskawa in the framework of the Standard Model. The Standard Model, however, cannot explain the matter-antimatter asymmetry. Thus it is necessary to search for new sources of CP violation or direct T-violation.

In 1950 Ed Purcell and Norman Ramsey proposed testing P symmetry by using electric dipole moments (EDMs) of elementary particles [38]. In that time, parity was still thought to be a good symmetry and Purcell and Ramsey immediately designed an experiment to test it using neutrons. The dipole moment is a measure of the charge distribution of a particle. For example, a finite electric dipole moment of the electron suggests that there is an average displacement of the electron charge from the electron's centre of mass. The only way to specify an orientation of an elementary particle is to use the orientation of its angular momentum, the

spin in the case of an electron. The dipole moment has to lie either parallel or anti-parallel to the angular momentum. Since it is a displacement ($\propto r(x,y,z)$) it flips sign under the parity transformation. The angular momentum direction, however, does not change under P. Likewise, angular momentum changes direction under the T transformation, whereas the dipole moment does not. Thus, an electric dipole moment of a fundamental particle violates P and T individually. Hence if one believes that the CPT theorem is right it must also violate CP symmetry.

The Standard Model of particle physics predicts a small electric dipole moment for the electron, of approximately $10^{-40}\,e\,\mathrm{cm}$. This is too small to be detected by any currently conceived experiment.

Extensions of the Standard Model are usually accompanied by new particles. Supersymmetry, for example, introduces a bosonic partner for each fermion and a fermionic partner for each boson of the Standard Model. The contribution of these particles to EDMs depends on their masses and the resulting EDM can be significantly larger (up to $10^{-26}\,e\,\mathrm{cm}$ for the electron) than the Standard Model prediction. This should not really be a surprise, since one of the major flaws of the Standard Model is that it does not contain enough CP violation to explain the matter-antimatter asymmetry.

Therefore, measuring EDMs with high accuracy directly probes physics beyond the Standard Model and is capable of placing tight constraints to exotic particle physics. But what has all that to do with atomic and molecular beams? In order to measure an EDM one needs to apply a strong uniform electric field to the particle (align the dipole) and look for a response. Neutrons do not possess charge, so one can apply the electric field directly to a slow beam, or even to a trapped sample of neutrons. The current best limit on the EDM of the neutron was obtained in 2006 and is $d_n < 2.9 \times 10^{-26} e\,\mathrm{cm}$ (90 % confidence) [39]. The situation changes if one wants to measure the EDM of charged particles like the electron or proton. Since these particles possess charge they will be rapidly accelerated in the externally applied electric field.

A solution to this quite fundamental problem became apparent when Leonard Schiff studied the possibility to use atoms to measure the EDM of a nucleus [40]. Nuclear EDMs of an atom stem from neutrons, protons and P and T violating forces between the nucleons. If one applies an electric field to an atom the electrons rearrange and screen the nucleus from the external field. Consequently, the nucleus does not experience a net electric field at all and there is no interaction with the nuclear EDM. Schiff, however, when deriving the screening effect assumed that the particles are point particles and only interact via Coulomb forces. The nucleus, however, is an extended object and the distribution of charge and dipole moments of its constituents is quite different from a single point. Schiff could show that the finite volume of the nucleus leads to imperfect shielding and thus to a net interaction between the dipole moments and the external electric field. The attenuation scales with the square of the atomic number Z, thus favouring heavy atoms. The most stringent constraint on a nuclear EDM is $d_N < 2.1 \times 10^{-28}\,e\,\mathrm{cm}$ obtained from measurements in mercury vapour [41]. But even in such a heavy atom the external field is attenuated by about a factor of 1000.

Schiff also showed that atoms might be useful for measuring the EDM of the electron. Crucially one needs to use paramagnetic atoms, i.e. atoms with one unpaired electron. Schiff showed that relativistic and magnetic effects lead to imperfect shielding, especially if the electron moves close to the nucleus where the speed of the electron approaches the speed of light. However, the EDM interaction would average to zero in a purely spherical electron distribution. Thus an external electric field is needed to distort the electron distribution, i.e. to add a small portion of p orbital to the s state. A few years later Sandars pointed out that in heavy atoms, this effect does not only lead to imperfect shielding of the external electric field but can even enhance it. The amplification factor scales with the atomic number as Z^3 [42]. This means that the EDM interaction in a heavy atom is of the order of 100 times larger than that of a free electron in the same electric field!

An EDM experiment essentially looks for a minute change of the atom's response that depends on the orientation of an externally applied electric field. Spectroscopic measurements performed on an atomic beam of thallium atoms could put an upper limit to the EDM of the electron to $d_e < 1.6 \times 10^{-27}\,e\,\mathrm{cm}$ [43]. Because the thallium atom has a large Z the relativistic effects enhance the external field by a factor of -585. For a laboratory field of $1.23 \times 10^5\,\mathrm{V\,cm^{-1}}$ the electron effectively experiences a field of $7 \times 10^7\,\mathrm{V\,cm^{-1}}$. The magnitude of this electric field strength is only limited by the electric breakdown in a typical laboratory vacuum. Sandars pointed out that there is an alternative way to generate even higher electric fields by attaching a strong electro negative element, like F or O, to the heavy atom in order polarise it more efficiently. Such a polar molecule possesses a large internal field of the order of $10^{10}\,\mathrm{V\,cm^{-1}}$. This large internal electric field, averages to zero if no external electric field is applied to align the molecule in the lab frame. In order to do so one only needs an electric field strength of the order of $10\,\mathrm{kV\,cm^{-1}}$. For the particular case of the YbF molecule, which is used in our lab to measure the EDM of the electron, the effective internal field is as large as $26\,\mathrm{GV\,cm^{-1}}$ in a moderate laboratory field of $10\,\mathrm{kV\,cm^{-1}}$. This made it possible to set a new upper limit for an EDM of the electron of $1.05 \times 10^{-27}\,e\,\mathrm{cm}$ [44].

Measurements of EDMs using atoms or molecules in one way or another all involve using the magnetic resonance techniques developed by Rabi and Ramsey. In particular, one measures the precession frequency ω of the electron's spin in a uniform magnetic and electric field. The magnetic field provides a quantisation axis for the spin, around which it precesses with a certain frequency. The EDM changes this precession frequency depending on the orientation of the electric field, parallel or anti-parallel to the magnetic field. The fundamental statistical uncertainty of such a magnetic resonance experiment is proportional to $1/(T\sqrt{N})$, where N is the number of detection events and T is the spin precession time. Consequently, the only way to increase the statistical uncertainty is to increase the number of particles and/or increase their spin precession time. While the large internal electric field of polar molecules is a big advantage over atoms, it is much more difficult to make intense beams of molecules. The problem is compounded by the large number of states occupied in an ensemble of molecules at room temperature. This

means that N is typically much smaller for molecules than for atoms. Thus, efficient cooling of vibrational and rotational motion is necessary to enhance the number of molecules in the preferred state. To further improve molecular EDM experiments there is a need for brighter sources of molecules, an improved detection efficiency, and an increase in the observation time by cooling and slowing the molecules. Such improvements are of great advantage not only for EDM measurements but also for a large number of other experiments that would greatly benefit from an improved signal to noise ratio, lower velocity and lower temperature.

1.3.3   Do Enantiomers of Chiral Molecules have identical spectra?

Another fascinating question which can be addressed by high resolution spectroscopy of molecules is why nature shows a distinct preference for left-handed amino acids over their mirror images. The origin of this so called homochirality remains unknown, but some physicists have speculated that parity violation in the weak interaction might play a role. Calculations predict a minute energy difference between enantiomers (identical mirror images) of chiral molecules due to interactions of the weak force between the electrons and the nucleus in the molecule. The fractional frequency shift of a rovibrational transition due to weak interactions is expected to be of the order of $10^{-15} - 10^{-16}$ [45]. The most sensitive measurement so far has been performed in cells filled with CHFClBr molecules and was limited by impurities and systematic effects related to the high pressure in the spectroscopy cell [45]. The resolution of these experiments can be significantly enhanced by slowing the molecules in order to increase the coherence time. Furthermore, it is helpful to cool the internal degrees of freedom to enhance the population of molecules in the ground state.

1.3.4   Variation of Fundamental Constants

A total number of 22 free parameters must be included in the Standard Model of particle physics [46], the values of which can not be predicted by the theory. These free parameters are often referred to as fundamental constants and are determined by measurement. There lies hope that a future theory will predict the values of these constants, or at least reduce their number.

The first to think about possible variations of these dimensionless constants was Paul Dirac in 1937 who suggested that the value of the constants could be coupled to the evolution of the universe [47].[11] Dirac assumed that Newton's gravitational constant G would vary with time with a rate of about 10^{-10} per year. Dirac arrived at this conclusion by proposing his famous large number hypothesis: He noticed that the ratio between the electric and gravitational forces

---

[11]Dirac wrote this article while on honeymoon with Eugene Wigner's sister Margit. On a short note to George Gamov he remarked:"That happens if people get married."

between a proton and an electron is similar to the age of the universe in atomic units and further assumed that this could be true for all times. This would suggest that the value of fundamental constants are coupled to the evolution of the universe.

Dirac generated much interest with this idea and an important outcome of his reasoning is that the constancy of fundamental constants should be checked experimentally. Over ten years later Edward Teller argued that a decreasing G would contradict paleontological evidence[12] and thus initiated the search for experimental evidence for time-varying constants [48].

Modern theories of high energy physics offer new possibilities for varying constants. Kaluza and Klein introduced an extra space dimension in the late twenties of the last century to attempt a unification of gravity with electromagnetism. This approach has been revived in modern string and M-theories which attempt to unify gravity with the electric, weak and strong interaction. In general, string theories describe the coupling strengths not by dimensionless constants but rather as scalar particles that live in a $4 + D$ dimensional space. However, we do not experience these extra dimensions so it is assumed that they are compact, i.e. wrapped up on themselves. The string coupling constants depend on the size of this compact D dimensional space and any cosmological evolution of these extra spatial dimensions would lead to a temporal and/or spatial variation in the usual constants we measure in the lab. This represents a first step towards determining the values of fundamental constants in a self consistent way from theory and introduces a quite natural framework for a change of these constants with cosmological evolution.

Over the second half of the 20$^{\text{th}}$ century astronomical evidence grew that most of the matter in the universe is dark and of unknown character. This somewhat concerning fact was topped by the discovery that the expansion of the universe is accelerating, driven by an unknown force dubbed dark energy. This has led to a wide range of speculations and to a whole forest of new cosmological theories. A popular theory invokes a homogeneous, dynamical scalar field that is slowly rolling down a very shallow self-interaction potential [49]. This rolling behaviour is necessary to explain the cosmic coincidence problem, i.e. why the acceleration of the expansion of the universe started about six billion years ago. According to the theory, this happened when the kinetic energy of the scalar field became smaller than its potential energy. This model has become so popular that it even received a fancy name, quintessence, referring to its role as the fifth fundamental force that drives the expansion of the universe. There is, however, one problem. The coupling of this nearly massless, long range field to ordinary matter should lead to observable long-range forces. Such long range forces have not been observed in any experiments searching for fifth forces and would violate the equivalence principle and hence are severely constrained by Eötvös-type experiments. The standard solution to this problem is to introduce an unknown symmetry which suppresses such couplings [50].

---

[12]Teller reasoned that if G was 10% larger 300 million years ago the temperature of the sun must have been so high that the increase in temperature on earth would have prohibited life and thus contradict fossil evidence of trilobites that existed at that time.

An alternative attempt to reconcile a strongly interacting quintessence field with local gravity experiments appeared in 2004 [51]. In this model the mass of the scalar field, and thus its range, becomes dependent on its environment. In regions of high density, such as on Earth, the mass of the field is large and thus satisfies the constraints put in place by gravity experiments. On cosmological scales, however, where the matter density is about 10^{30} times smaller[13], the mass of the field is much smaller and thus allows for a cosmological evolution of the field. This means that scalar fields such as quintessence have not been detected by fifth force experiments because the dense environment we live in shields them. Since the characteristics of this field depends sensitively on its environment it was dubbed the chameleon field.

Furthermore, assuming the absence of an unknown symmetry that suppresses the coupling, the scalar field is expected to have a non-zero coupling strength to other fundamental forces. This could lead to a possible observable change of fundamental constants over the evolution of the universe. Hence measuring the values of fundamental constants through the history of the universe can provide strong constraints on the possibilities of cosmologies and new physics that deviates from the Standard Model [52]. Furthermore, if there are chameleon fields the value of fundamental constants will depend on the environment. Therefore detecting a change in fundamental constants can be seen as a rare example that allows to test and constrain predictions of string theories and new kinds of cosmologies.

Atoms and molecules, and their energy spectra in particular, provide us with a very sensitive tool to probe for any changes in such fundamental constants. One way to do so is by comparing emission and absorption spectra of atoms and molecules from distant gas clouds, i.e. gas clouds at high red shift, with laboratory data taken during present times. If at any other point in space-time the fundamental constants had different values this would show up as a shift in these transition frequencies. The direction and amount of this shift depends on the specific atomic or molecular species. High resolution laboratory spectra for a wide range of atoms and molecules are thus needed. There is a particular need for better laboratory data for molecules, because the current data is often less precise than the astronomical measurements.

Atomic and molecular beams have proven to be ideal means for measuring such transition frequencies to unprecedented accuracies in a laboratory environment. The control over atomic beams has led to the realisation of atomic fountains which are ideal for building very stable and accurate clocks. The transition frequencies of these atomic clocks depend on fundamental constants such as the fine structure constant α or the electron-to-proton mass ratio μ. Thus by comparing two very accurate clocks whose frequencies depends differently on fundamental constants, over a period of a few years one can put extremely tight constraints on the variation of the constants during present times [53, 54].

A molecular fountain for precision tests of fundamental physics theories is currently also under construction which will allow to measure potential drifts in the electron-to-proton mass

---

[13]The mass density of visible matter in the Universe is estimated to be $10^{-28}\,\mathrm{kg\,m^{-3}}$ which is 10^{-31} times the density of liquid water

ratio with unprecedented accuracy [55].

1.3.5   Cold Chemistry

Since temperature is directly related to the velocity one can increase the de Broglie wavelength of atoms and molecules by cooling them to low temperatures. If the wavelength associated with an atom or molecule becomes larger than the particle, or even the mean distance between particles in a cold gas cloud, interference and quantum phenomena emerge. A room-temperature nitrogen molecule is moving at about $500\,\mathrm{m\,s^{-1}}$ which corresponds to a de Broglie wavelength of about $30\,\mathrm{pm}$. This is far too small for quantum effects to influence chemical interactions, collisions or reaction dynamics. By cooling the molecular motion to mK temperatures the de Broglie waves extend to lengths that exceed intermolecular forces and quantum interference effects become important. External fields can then be used to control reaction dynamics, reaction rates and maybe even the outcome of a chemical reaction by shifting the interaction potentials [56]. The study of reaction dynamics at low temperatures ($1\,\mathrm{K}$) using molecular beams helps to understand the formation of complex molecules in interstellar gas clouds and planetary atmospheres. By gaining control over the translational motion of molecules to cool them even further one gets full access to the quantum nature of ultracold collisions which provides a detailed probe for fundamental chemical reactions. Calculations show that collision cross sections between molecules, or between atoms and molecules, show sharp resonances at low collision energies [57]. These sharp resonances can have a dramatic effect on the rate at which a chemical reaction takes place. The detection of these scattering resonances allows accurate determination of the interaction potentials that govern the collision dynamics.

1.3.6   Dipole Interactions and Quantum Gases of Polar Molecules

If one cools a dilute cloud of atoms to very low temperatures, something very peculiar happens. If the atoms are bosons, more and more atoms condense into the lowest energy state possible. At a critical temperature and density all the atoms become indistinguishable and occupy exactly the same space in the trap. This transition into a new state of matter was first observed in 1995 using Rubidium atoms [58] and has sparked immense interest in the atomic physics community and beyond. If the atoms are fermions, only one atom is allowed to occupy a single energy level and the atoms fill up the levels to a certain energy which is called the Fermi energy. The first observation of a Fermi degenerate gas was in 1999 [59].

Atoms in such a cold gas typically interact through short range van der Waals interactions. New, intriguing effects are expected to emerge in such cold clouds if one could introduce long

range interactions so that each particle is sensitive to every other particle in the cloud. One could think of using atoms with large magnetic moments. Chromium atoms, for example, have a magnetic moment of $\mu = 6\mu_B$, where $\mu_B = e\hbar/2m_e \sim 9.3 \times 10^{-24}\,\mathrm{J\,T^{-1}}$ is the Bohr magneton. Two atoms with a large magnetic moment exhibit long-range magnetic dipole-dipole interactions that scale as $\mu_0\mu^2/(4\pi r^3)$, where μ_0 is the vacuum permeability and r is the distance between the atoms. The interaction is also anisotropic depending on the relative orientation of the dipoles. Pioneering experiments with chromium atoms have shown that such long-range interactions can have significant influence on the dynamics of such a gas [60]. Recently the Bose-Einstein condensation of the highly magnetic species erbium ($7\mu_B$) [61] and dysprosium ($10\mu_B$) [62] have been demonstrated as well.

Dipolar interactions start to become important in the cold gas once the dipole-dipole interaction energy between two particles exceeds the centrifugal barrier that tends to keep them apart. For small angular momenta this centrifugal energy is $\hbar^2/(mr^2)$, where m is the mass of the atoms. This yields a characteristic dipole-dipole interaction length for magnetic atoms of $l_{DD} = \mu_0\mu^2 m/(4\pi\hbar^2)$. For dysprosium atoms, this is $414a_0$, with a_0 the Bohr radius, which is not much larger than typical s-wave scattering lengths. This means that the dipole-dipole interactions still do not dominate the physics of the gas cloud although their influence is observable.

Polar molecules, i.e. heteronuclear molecules with a net positive charge at one end and a net negative charge on the other end, possess an electric dipole moment μ_e. The interaction energy between two such dipoles scales with $\mu_e^2/(4\pi\epsilon_0 r^3)$, where ϵ_0 is the vacuum permittivity and r is the distance between the molecules. The interaction of two electric dipoles with an electric dipole moment of 1 D is equivalent to an interaction energy of two magnetic dipoles with $100\mu_B$. The corresponding dipole length for electric dipole-dipole interaction is $l_{EDD} = m\mu_e^2/(4\pi\epsilon_0\hbar^2) \approx 4 \times 10^6 a_0$ for the most polar molecule KBr (10.5 D).

Such strong, long-range interactions will have dramatic effects on a cold cloud of polar molecules, their reactions and collision properties. If the density increases and the temperature decreases the molecules will start to influence each other and begin to form a crystal like structure similar to ions in an ion trap. These would lead to fundamentally new condensed-matter phases and new complex quantum dynamics. A Bose-Einstein condensate of polar molecules would represent a quantum fluid of strongly and anisotropically interacting particles [63].

1.3.7 Quantum Simulation

As Richard Feynman put it in his presentation: "There's plenty of Room at the Bottom", at an American Physical Society meeting at Caltech in 1959 [64]: "Atoms on a small scale behave like nothing on a large scale, for they satisfy the laws of quantum mechanics. As we go down and fiddle around with the atoms down there we are working with different laws, and we can

expect to do different things". This seminal presentation is widely recognized as one of the main inspirations for the development of nanotechnology. In another visionary lecture from 1981 [65]: "Simulating physics with computers", Feynman proposed to overcome the severe limitations of classical computers in describing quantum systems by using quantum simulators which operate according to the laws of quantum mechanics. Hence one can simulate complex systems by using a set of controllable particles with engineered interactions and predict the value of physical quantities by simply performing the appropriate measurements. He predicted the advent of "a quantum machine that could imitate any quantum system, including the physical world". He summarised this challenge in the now famous sentence: "Nature isnt classical, dammit, and if you want to make a simulation of nature, youd better make it quantummechanical, and by golly its a wonderful problem, because it doesnt look so easy." He was certainly right that this challenge is not so easy. But great progress has been made since 1981. First prototypes of such quantum simulators, based on quantum gases, trapped ions, photonic or superconducting systems have become reality already over the last decade.

Cirac and Zoller identified five key criteria a quantum simulator should have [66]:

- It should be made up of a quantum system (bosons or fermions).

- One should be able to prepare a known quantum state.

- It should be possible to engineer a set of interactions with external fields between the different particles.

- Individual or collective addressing of the particles to perform measurements on the system.

- The simulation should be verifiable. There should be a way of increasing the confidence or to check the result (running it backwards).

Pioneering experiments use ultracold atoms confined in an optical lattice, i.e. a periodic potential created by the interference of opposing pairs of laser beams. The optical dipole force thus generates a periodic potential which resembles the periodic lattice electrons experience due to the array of atomic cores in condensed-matter system. The atoms can be filled into this optical lattice which then allows one to study the rich physics of a condensed matter system with a unique degree of control over the parameters. Using such a lattice system it became possible to realise and study the Bose-Hubbard model, which serves as one of the most prominent models for a solid in condensed-matter physics [67, 68]. Recent progress makes it now possible to address single lattice sites and prepare the spin of a single atom at a predetermined lattice site which allows to simulate the quantum Ising model [69].

The atoms in such a simulator only interact via short-range interactions. By using polar molecules in such an optical lattice one can get access to a whole new regime where long range dipole-dipole interactions govern the dynamics. This can be used to reproduce known, but

unsolvable, condensed-matter Hamiltonians [63]. In fact it is possible to simulate any arbitrary Hamiltonian for interacting spins on a lattice using molecules [70]. Molecules could thus serve as extremely versatile tools to realise and study exotic phases of matter and as an efficient modelling device for currently unsolvable condensed-matter Hamiltonians.

1.3.8   Quantum Information

Polar molecules possess a rich internal structure which allows to efficiently encode and store quantum information in long-lived states. The long range and strength of the dipole-dipole interactions can be a very fast and efficient way to entangle qubits and to engineer quantum gates. Many different proposals for the technical realisation have been suggested [63]. The large dipole moment makes it possible to tune the interactions with electric fields and inhomogeneous electric fields can be used to Stark shift the molecules in an optical lattice which will allow single site addressing.

1.4   How to Cool Molecules?

The possibility to cool atomic vapours to ultralow temperatures by using laser light has launched a rich and extremely fruitful research area over the last few decades. Therefore, the most straightforward approach would be to cool polar molecules in a similar way. However, the same reason that gives rise to the wide range of applications of polar molecules prevents using the standard techniques used to cool atoms - laser cooling which relies on the photon recoil due to $10^4 - 10^5$ excitation and spontaneous emission cycles. Such closed excitation and emission cycles are, in general, not accessible in molecules. Due to the large number of internal states the molecule ends up in a state inaccessible to the excitation laser after a few excitation and emission events.

However, in 2004 Di Rosa identified a specific class of molecules that can be used for laser cooling [71]. The direct free-space laser cooling of the highly polar SrF molecule was demonstrated by 2010 in the group of DeMille at Yale [72]. Naturally, this scheme, is limited to a few molecular species only. A more general laser cooling scheme based on coherent off-resonant scattering in a high finesse optical cavity has been proposed, but has not been realised yet [73–75].

The physical chemistry community have developed a set of very general techniques to produce beams of a large variety of molecular species using the supersonic expansion technique. The molecules produced in such a way typically move at a velocity of a few hundred metres per second. However, in their moving frame the molecules are translationally, and internally cold (1 K). Since the molecules are directly produced in a source such techniques are known as the *direct* approach to cold molecules. Since the mid 1990s new methods have been developed

to decelerate those fast moving molecules. Influences from the cold neutron community motivated the use of a cold, cryogenic buffer gas to cool and slow the molecules, which are typically produced at very high temperatures [76]. Slowing polar molecules using their interaction with electric fields (Stark decelerator) [77], with magnetic (Zeeman decelerator) [78, 79] or optical fields [80] has been demonstrated and are by now well established techniques. An excellent recent review which summarises the manipulation of molecules with electromagnetic fields is given in reference [81]. The filtering of the low velocity tail of a cryogenic, effusive beam has proven to be a very viable technique to get slow moving cold molecules [82]. Billiard-like collisions between molecular beams has also produced samples of cold molecules at rest [83]. A rotating nozzle whose fast backward-motion counter-acts the forward velocity of a molecular beam is another technique to provide slow and cold molecules [84]. Very recently cold molecules at rest have been produced by photo-dissociating a precursor molecule. The momentum recoil from the dissociation removes the kinetic energy and stops one of the dissociation fragments [85].

Most of these techniques provide sufficiently cold and slow molecules so that they can be confined in electro-static [86], ac electric [87] and magnetic traps [76]. Molecules in such traps have temperatures on the order of $10\,\mathrm{mK}$. Cooling them further turns out to be quite challenging. However, recently opto-electrical Sisyphus-type cooling of CF_3H molecules in an electric trap [88, 89] and evaporative cooling of OH in a magnetic trap [90] show that ultracold temperatures for molecules cooled from a molecular beam are reachable. The sympathetic cooling of molecules via elastic collisions with ultra cold atoms has been studied theoretically [91] and experimentally [92], but has not been successfully demonstrated yet.

The control of molecular beams with electric, magnetic and optical fields makes it possible to trap the molecules, measure the lifetimes of excited states, study and control the collision and reaction dynamics in crossed-beam experiments, and probe the time dependence of chemical reactions (e.g. see [81, 93] and references therein). The density of such molecular beams is, however, still too low and the temperature too high to observe any dipole-dipole interactions. However, the recent development of direct free-space laser cooling and the first demonstration of evaporative cooling show that it will become possible to cool molecules from a molecular beam to $1\,\mathrm{\mu K}$ and below where the dipole interaction and quantum effects govern the dynamics.

If the actual chemistry or type of molecule is unimportant and one purely wants to study polar molecules at low temperatures an alternative route exists. This is known as the *indirect* approach to producing cold molecules, which takes ultracold laser-cooled atoms and converts them pairwise into deeply bound molecules. The challenge is to efficiently bring the atoms together without heating the gas due to the release of the binding energy (a few thousand degrees). The first to accomplish this difficult task was the group of DeMille at Yale who used photoassociation to convert 10^8 laser-cooled Rb and Cs atoms to about 10 RbCs molecules in their absolute ground state, with a translational temperature of $100\,\mathrm{\mu K}$ [94]. This technique uses laser light to transfer a scattering state of two atoms to an electronically excited state of the molecule. The electronically excited molecule then decays to the electronic ground state via

spontaneous emission. However, the molecules are, in general, distributed over a large number of rovibrational states in the ground electronic state. The breakthrough for the indirect approach came by using a highly dense ensemble of atoms (quantum degenerate gas) in combination with an adiabatic, coherent transfer of the atoms into the ground state of the molecules. After evaporation, the atoms are confined in an optical dipole trap at 100 nK. A so-called Fano-Feshbach resonance occurs in the scattering cross-section of two atoms when the kinetic energy is equal to the bound state of a molecule. One can tune this energy separation with an external magnetic field and thus convert atoms into weakly bound molecules (molecules with a large internuclear separation). In a second step these weakly bound molecules are converted into ground-state molecules using a two-photon coherent process known as stimulated Raman adiabatic passage (STIRAP). This was first demonstrated for homonuclear molecules [95, 96] and then for the polar, fermionic species KRb [97]. Only chemical reactions at low temperature and high density prevented the demonstration of the first Bose-Einstein condensate (or degenerate Fermi gas for the case of the fermionic KRb) of polar molecules [98, 99]. Since then first experiments revealed the dipolar nature of the collisions between polar molecules [100] the possibility to control chemical reactions with external fields [98, 99], and recently the realisation of a lattice spin model using polar KRb molecules [101].

A measure for quantum degeneracy is a phase-space density of the gas $n\Lambda^3$ of the order of one, where n is the peak density of the gas and $\Lambda = h/\sqrt{2\pi m k_B T}$ is the thermal de Broglie wavelength of a particle with mass m and temperature T. A phase-space density of the order of one corresponds approximately to a molecular density of $7 \times 10^9 (m[\text{amu}])^{3/2}$ per cubic centimeter at a temperature of 100 nK. The major advantage of the indirect approach is that it can produce a phase-space density which is more than 10 orders of magnitude higher than the direct approach can currently produce. However, the indirect approach can only produce molecules the constituents of which can be laser-cooled (mainly alkali and alkaline earth metals). Furthermore, the dipole moment of these molecules is often quite small, e.g. 0.5 D for KRb. This limits the dipole-dipole interaction length to scales which is much shorter than the spacing between two sites in an optical lattice (≈ 530 nm). Therefore, molecules with much larger dipole moments such as LiCs (a predicted dipole moment of 5.5 D) are currently under investigation [102].

1.5   Summary & Conclusion

This chapter should convince the reader that despite the long tradition of molecular beam research there is still plenty of new developments to come. The recent developments of highly intense cryogenic sources, Stark and Zeeman decelerators, and direct laser cooling have opened up a completely new chapter in molecular beam research - the quest for reaching the ultra cold

and ultra precise. The molecular beam research after Ramsey and Rabi saw a shift from the physics to the chemistry community while the time since the mid 1990s can be described as the reviving period of molecular beams in the physics community. The boundaries between physics, physical chemistry and chemistry have started to blur, and this has created a very exciting and diverse field of research. Many of the new technologies needed to reach the ultracold for molecules have now been developed and the first great scientific breakthroughs are happening right now.

One approach towards using molecules to investigate some of the above mentioned exciting physics is described in this thesis and of course the start of every molecular beam experiment is the choice of a specific molecule one wants to study. We chose to study the CH molecule. It is light, has an electric dipole moment, and so is straightforward to manipulate with electric fields. It is important in combustion processes, fundamental chemical reactions, is highly sensitive to changes in fundamental constants and is an abundant species in interstellar gas clouds. It thus opens up many different potential applications. In addition, a number of molecular beam sources have been investigated over the past century and we were confident that we could produce it in large numbers, which is the precondition for any experiment that is to come. The possibility to reach a high density, the straightforward approach to decelerate and trap it, and the many potential applications of a beam CH molecules motivated us to investigate molecular beam sources. But before the various molecular beam sources are presented a brief introduction to molecular physics and the specific energy level structure of the CH molecule is presented in the following chapter.

Chapter 2

Molecular Physics - A Theoretical Description of the CH Molecule

[...] it is more important to have beauty in one's equations than to have them fit experiment.

Paul Dirac

2.1 Introduction

In this chapter a brief introduction to molecular physics is given, with the aim of describing the energy level structure of the CH molecule. First the essential steps of the Born-Oppenheimer approximation are presented. This allows us to plot the distribution of electronic, vibrational and rotational energies of CH. The orbital motion, electronic spin, and nuclear spin couple to the rotation of the molecule and lead to fine and hyperfine structure. The coupling scheme relevant to describe the exact rotational, fine and hyperfine structure of CH is presented. The knowledge of the electronic, vibrational and rotational structure then allows us to study transitions between the ground and excited electronic states and to introduce the notation specific to molecular spectroscopy. The chapter is concluded by a brief description of the interaction of CH with static electric (Stark effect) and static magnetic (Zeeman effect) fields. This will be used at a later stage to predict the sensitivity of particular transitions in CH to external electric and magnetic fields.

2.2 The Born-Oppenheimer Approximation

Two atoms form a covalent bond if the atomic orbitals of the electrons involved in the binding have similar energies and their wave functions possess the proper symmetry to interfere constructively. The bonding results in a molecular orbital with increased electron density between the two nuclei, and is of lower energy than the two separate atomic orbitals. The strength of the bond depends on the degree of orbital overlap. The wavefunction of a diatomic molecule, $\Psi(\mathbf{R}, \mathbf{r}_i)$, satisfies the Schrödinger equation:

$$\hat{H}\Psi(\mathbf{R}, \mathbf{r}_i) = E\Psi(\mathbf{R}, \mathbf{r}_i) \,, \tag{2.1}$$

where $\hat{H}$ is the Hamiltonian describing the molecule, $\mathbf{R} = \mathbf{R}_A\text{-}\mathbf{R}_B$, with $\mathbf{R}_A$ and $\mathbf{R}_B$ the positions of the two nuclei A and B with masses M_A and M_B respectively, and $\mathbf{r}_i$ is the position vector of the ith electron. The Hamiltonian $\hat{H}$ can be broken down into three components: the kinetic energy of the nuclei $\hat{T}_N$, the kinetic energy of the electrons $\hat{T}_e$ and the Coulomb potential between the electrons and the nuclei $\hat{V}$:

$$\hat{H} = \hat{T}_N + \hat{T}_e + \hat{V}. \tag{2.2}$$

The nuclear kinetic energy is given by:

$$\hat{T}_N = -\frac{\hbar^2}{2M_A}\nabla_A^2 - \frac{\hbar^2}{2M_B}\nabla_B^2 = -\frac{\hbar^2}{2\mu}\nabla_R^2 - \frac{\hbar^2}{2M}\nabla_{Rcm}^2 \,, \tag{2.3}$$

with $\mu = M_A M_B/(M_A + M_B)$ the reduced mass of the molecule, $M = M_A + M_B$ the total mass, ∇_R^2, the Laplace operator for the relative motion and ∇_{Rcm}^2, the Laplace operator for the centre of mass coordinate. We are not concerned about the centre-of-mass motion and so can drop this term in the Hamiltonian. The kinetic energy of the electrons is:

$$\hat{T}_e = -\sum_{i=1}^{N}\frac{\hbar^2}{2m_i}\nabla_i^2, \tag{2.4}$$

with N the number of electrons, and m_i the mass of a single electron. The potential energy between the electrons and the nuclei is:

$$V = \frac{Z_A Z_B e^2}{4\pi\epsilon_0 R} - \frac{e^2}{4\pi\epsilon_0}\sum_{i=1}^{N}\left(\frac{Z_A}{r_{i,A}} + \frac{Z_B}{r_{i,B}}\right) + \frac{e^2}{4\pi\epsilon_0}\sum_{i<j=1}^{N}\frac{1}{r_{ij}}. \tag{2.5}$$

The first term describes the Coulomb repulsion of the nuclei of charge Z_A and Z_B which are separated by $R = |\mathbf{R}_A - \mathbf{R}_B|$, the second term describes the attraction between the nuclei and the electrons with $r_{i,A} = |\mathbf{r}_i - \mathbf{R}_A|$ and $r_{i,B} = |\mathbf{r}_i - \mathbf{R}_B|$. The third term describes the mutual repulsion between the electrons with $r_{ij} = |\mathbf{r}_i - \mathbf{r}_j|$. Even for the simplest case of the

H_2^+ molecular ion the Schrödinger equation 2.1 cannot be solved exactly. We therefore need to introduce approximations that lead to a simpler Schrödinger equation.

The first useful approximation is known as the adiabatic approximation (sometimes referred to as the first step of the Born-Oppenheimer approximation). This approximation assumes that the electrons move much faster than the nuclei, i.e. the electron cloud adjusts instantaneously when the nuclear framework changes. This approximation is good as long as the kinetic energy of the nuclei is small compared to the electronic energy. We remove $\hat{T}_N$ from the total Hamiltonian 2.2 and solve the remaining electronic Schrödinger equation with the electronic Hamiltonian $\hat{H}_e = \hat{T}_e + \hat{V}$:

$$\hat{H}_e \psi_q(\mathbf{R}, \mathbf{r}_i) = E_q(\mathbf{R}) \psi_q(\mathbf{R}, \mathbf{r}_i). \tag{2.6}$$

The square of the wavefunction $\psi_q(\mathbf{R}, \mathbf{r}_i)$ yields the charge distribution of the electrons in an electronic state q for a fixed internuclear separation $\mathbf{R}$ which corresponds to an energy $E_q(\mathbf{R})$. By solving equation 2.6 for different parameters $\mathbf{R}$ we obtain the electronic energy eigenvalue $E_q(\mathbf{R})$ as a function of the internuclear separation. We can choose the electronic wave functions such that they form a complete orthonormal set of functions. This allows us to expand the wavefunctions $\Psi(\mathbf{R}, \mathbf{r_i})$ of the complete Schrödinger equation 2.1 in the basis of the electronic wavefunctions:

$$\Psi(\mathbf{R}, \mathbf{r}_i) = \sum_q \chi_q(\mathbf{R}) \psi_q(\mathbf{R}, \mathbf{r}_i). \tag{2.7}$$

We can substitute this into the complete Schrödinger equation, integrate over the electronic coordinates $\mathbf{r}_i$ and make use of the orthogonality $\int \psi_p \psi_q \, \mathrm{d}\mathbf{r}_i = \delta_{pq}$. This results in the coupled equations:

$$\hat{H}_e \psi_q(\mathbf{R}, \mathbf{r}_i) = E_q(\mathbf{R}) \psi_q \mathbf{R}, \mathbf{r}_i) \tag{2.8}$$

$$\hat{T}_N \chi_n(\mathbf{R}) + \sum_{q \neq n} c_{nq} \chi_q(\mathbf{R}) = (E - E_n(\mathbf{R})) \chi_n(\mathbf{R}), \tag{2.9}$$

where the coefficients $c_{nq} = c_{nq}(\psi_q)$ depend on the electronic wavefunctions ψ_q. In the second step of the Born-Oppenheimer approximation we neglect this coupling of the nuclear and electronic motion by setting $c_{nq} = 0$. Equation 2.9 then reduces to

$$\left[\hat{T}_N + E_n(\mathbf{R}) \right] \chi_n(\mathbf{R}) = E \chi_n(\mathbf{R}). \tag{2.10}$$

We can see that $E_n(\mathbf{R})$ takes the role of the effective potential for the motion of the nuclei. It contains the total potential and the kinetic energy of the electrons, averaged over the motion of the electrons. The Born-Oppenheimer approximation thus separates the complete Schrödinger equation into two uncoupled equations. The first describes the electronic part with fixed nuclei. We solve this equation for each electronic state and for many different internuclear distances $\mathbf{R}$ and obtain $E(\mathbf{R})$ which takes the role of the potential in the second equation. This second

equation describes the motion of the nuclei. To solve this equation it is easier to work in spherical polar coordinates and use an ansatz for the wavefunctions describing the nuclear motion $\chi(R, \Theta, \Phi) = \frac{1}{R}f(R)g(\Theta, \Phi)$. The solution to the angular part gives the spherical harmonics $g(\Theta, \Phi) = Y_{JM}(\Theta, \Phi)$ which leaves us with an equation for the radial part:

$$\left(-\frac{\hbar^2}{2\mu}\frac{d^2}{dR^2} + \frac{J(J+1)}{2\mu R^2} + E_n(R) - E \right) f(R) = 0. \tag{2.11}$$

To get an analytical solution we can expand the potential $E(R)$ in a Taylor series around the equilibrium distance R_e:

$$E_n(R) = E_n(R_e) + \left(\frac{dE_n}{dR} \right)_{R_e} (R - R_e) + \frac{1}{2} \left(\frac{d^2 E_n}{dR^2} \right)_{R_e} (R - R_e)^2 + \dots, \tag{2.12}$$

and choose the energy scale such that $E_n(R)$ reaches a minimum at $R = R_e$ which makes the second term zero. So to a first approximation the potential for the nuclear motion is harmonic and the Schrödinger equation describing this motion is that of the harmonic oscillator:

$$\left(-\frac{\hbar^2}{2\mu}\frac{d^2}{dR^2} - \frac{1}{2}k(R - R_e)^2 - E_v \right) f(R) = 0, \tag{2.13}$$

where we have used the shorthand $k = \left[d^2 E_n/(dR^2) \right]_{R=R_e}$ and gathered all the constants into $E_v = E - E_n(R_e) - E_r$, with $E_r = J(J+1)/(2\mu R_e^2)$. The solution to this equation give the well known harmonic oscillator wavefunctions and the energy eigenvalues $E_v = (v + 1/2)\hbar\omega_0$, with $v = 0, 1, 2, \dots$, an integer and $\omega_0 = \sqrt{k/\mu}$. We identify the harmonic motion of the nuclei around an equilibrium position with the vibrational degree of freedom with the corresponding quantised vibrational energy E_v.

The angular part of the Hamiltonian contributes $E_r = BJ(J+1)$ to the total energy, with $B = \hbar^2/(2I)$ which is known as the rotational constant and $I = \mu R_e^2$ the moment of inertia. Therefore, the angular part of the Schrödinger equation describes the rotational degree of freedom of the molecule. The Born-Oppenheimer approximation thus allows us to separate the total energy into three parts: an electronic part $E_n(R_e)$, a vibrational part E_v and a rotational part E_r.

This model is a good approximation for small vibration amplitudes. The restoring force $F = -k(R - R_e)$, however, keeps increasing with increasing distance from the equilibrium position. This can not be an accurate description of a real molecule because it does not include the limiting case of the molecule dissociating into its constituents, i.e. the binding energy should go asymptotically to zero when the internuclear spacing approaches infinity. Morse realised that a simple analytical form for the potential allows for a more accurate theoretical description which reproduces the empirically found expression for the energies:

$$E_n(R) = D_e \left[1 - \exp^{-a(R - R_e)} \right]^2, \tag{2.14}$$

where D_e is the dissociation energy (depth of the potential well), and $a = \omega_0/(\sqrt{2D_0/\mu})$, with $D_0 = D_e - (\hbar/2)\omega_0$. For small diatomic molecules the potential energy curves $E_n(R)$ can be computed to a reasonable accuracy using ab initio methods. Higher accuracy can be achieved by constructing the potentials from experimental data. To determine the exact shape of the potential for the different electronic states of a molecule is thus one of the main objectives for performing spectroscopy on molecules. The potential determines reaction rates for collisions and whether a reaction is endo- or exothermal. The most popular method to construct the potential energy curve is based on methods developed by Ragnar Rydberg [103], Otto Klein [104] and Albert Rees [105]. The so-called RKR method uses the measured energy levels to calculate the classical turning points where the total energy is equal to the potential energy $E = E_n(R)$. This gives the potential energy curves for each electronic state.

In the united atom picture, combinations of atomic orbitals are used to generate a molecular orbital. Molecular orbitals constructed from atomic $1s$ orbitals are denoted by 1σ. Similar to an atomic s orbital the molecular σ orbitals do not possess any nodes and are symmetric about the internuclear axis. The CH molecule in its ground state has a $1\sigma^2 2\sigma^2 3\sigma^2 1\pi^1$ electron configuration. Electronically excited states of molecules can be attributed to energetically higher electron configurations. If, for example one of the electrons from the 3σ orbital is promoted into the 1π orbital, there are four possible ways to arrange the electrons, each of which is attributed to a different electronically excited state. The potential curves for the ground state and three different electronic states of CH are shown in figure 2.1.

2.3   The Rotational Structure of CH

Let's concentrate on the ground electronic and vibrational state for the moment. Depending on the molecule rotational energies are between 10 and 1000 times smaller than vibrational energies. The rotational angular momentum ($\mathbf{R}$)[1] couples to the orbital ($\mathbf{L}$) and spin ($\mathbf{S}$) angular momentum of the electrons, and the interactions associated with the couplings contributes to the total energy. These angular momenta couple to form the total angular momentum ($\mathbf{J}$).

To describe the spectra of diatomic molecules German physicist, Friedrich Hund, devised a scheme for ordering the various possible couplings according to their strength into four extreme cases (a)-(d).[2] Each case corresponds to a specific set of "good" (well defined) quantum numbers and facilitates the choice of basis functions to describe the molecule's rotational structure. If a molecule can be described by case (a) strong electrostatic forces cause the orbital angular momentum $\mathbf{L}$ to precess rapidly about the internuclear axis. The spin $\mathbf{S}$ is strongly coupled

---

[1]Not to be confused with the internuclear separation $\mathbf{R}$.

[2]Hund originally only devised four cases but later on a fifth case (e) has been added. The most important ones for diatomic molecules are the cases (a)-(c). For our considerations of the CH molecule cases (a) and (b) suffice.
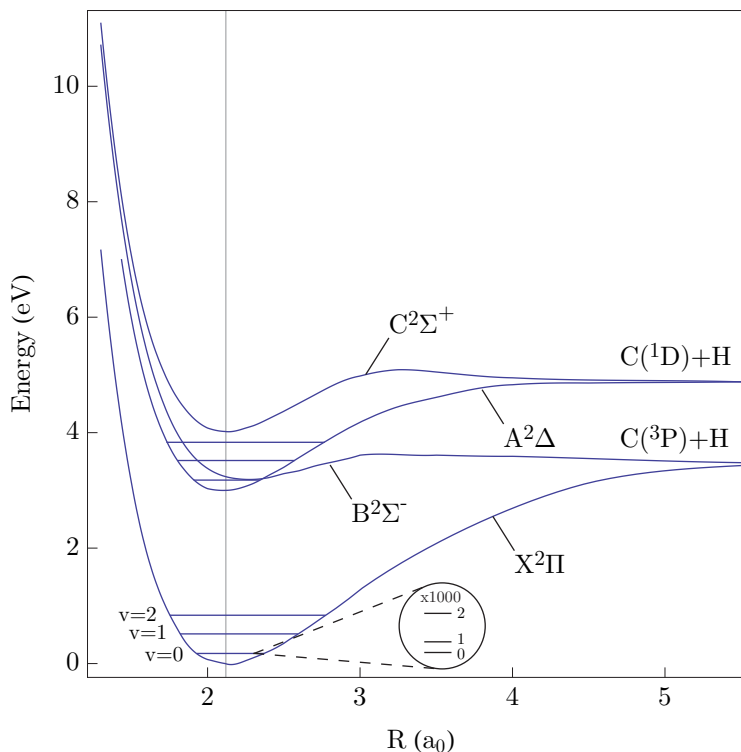
FIGURE 2.1: Potential energy curves $E_n(R)$ for the CH molecule [106]. The ground state is denoted by X. Electronically excited states are labelled according to their energy $E(R_e)$ with A, B, C,.... The superscript number gives the spin multiplicity $2S+1$. The Greek letter gives the projection of the electronic orbital angular momentum onto the internuclear axis $\Lambda = \Sigma, \Pi, \Delta$ which corresponds to $\Lambda = 0, 1, 2$. The CH molecule in its ground state has one unpaired electron in a $1\pi^1$ orbital which leads to $S = 1/2$ and $\Lambda = 1$ and thus to a $^2\Pi$ ground state. The $\pm$ of the Σ states denotes the symmetry of the wavefunction when reflected on a plane containing both nuclei. For the X and A state the vibrational energies are shown as horizontal lines. The vertical line indicates the equilibrium internuclear distance R_e of the ground state. The inset shows that for each vibrational state we get a number of rotational states.

to **L** due to a strong spin-orbit interaction and so also precesses about the internuclear axis. The orbital angular momentum **L** is thus not well defined, i.e. it is not a good quantum number to label energy levels. However, its projection onto the internuclear axis Λ is well defined. The total spin **S**, its projection, Σ[3], on the internuclear axis and the sum $\Omega = \Lambda + \Sigma$ are also well defined. Note that the precessions of **L** and **S** around the internuclear axis can have two equal, but opposite senses $\pm\Lambda$ (electrons orbiting clockwise or anti-clockwise about the internuclear axis) and $\pm\Sigma$. In the absence of any other angular momentum the two orientations of Λ lead to two degenerate energy levels. However, the coupling to the rotation of the molecule can lift this degeneracy, resulting in a Λ- or Ω-doublet. The total angular momentum is $\mathbf{J} = \mathbf{R} + \mathbf{L} + \mathbf{S}$. The corresponding Hamiltonian for the rotational energy is

$$H = B\mathbf{R}^2 = B(\mathbf{J} - \mathbf{L} - \mathbf{S})^2. \tag{2.15}$$

---

[3]The capital Greek letter Σ is used for both the case of $\Lambda = 0$ in the molecular term symbol and for the projection of the spin **S** onto the internuclear axis.

The total set of all good quantum numbers in case (a) is $(\eta, J, S, \Omega, \Lambda, \Sigma)$, where η contains all the other quantum numbers of the electronic and vibrational state. The basis functions are $|\eta, J, S, \Omega, \Lambda, \Sigma\rangle$. The requirement for case (a) to be applicable to a molecule is that the spin-orbit energy is much larger than the rotational energy $A\Lambda \gg BJ$, where A is the spin-orbit coupling constant. The spin orbit interaction leads to $2S + 1$ fine-structure states, with corresponding values of Ω. Each Ω state has its own rotational ladder with energies $BJ(J+1)$.

A molecule is described by case (b) if the spin-orbit coupling is small (or does not exist e.g. $\Lambda = 0$) compared to the rotation of the molecule ($A\Lambda \ll BJ$). As in case (a) the orbital angular momentum $\mathbf{L}$ is coupled to the internuclear axis and has a well defined projection Λ onto the internuclear axis. The spin-orbit interaction, however, is not strong enough to couple the spin $\mathbf{S}$ to the internuclear axis. Consequently Ω is not well defined. However, we can couple $\mathbf{L}$ and the rotation $\mathbf{R}$ and form $\mathbf{N} = \mathbf{L} + \mathbf{R}$. The total angular momentum $\mathbf{J} = \mathbf{N} + \mathbf{S}$ is formed by coupling $\mathbf{N}$ to the spin $\mathbf{S}$. The good quantum numbers are (η, Λ, N, S, J) and the basis functions are $|\eta, \Lambda, N, S, J\rangle$. The Hamiltonian describing the rotational kinetic energy is then

$$H = B\mathbf{R}^2 = B(\mathbf{N} - \mathbf{L})^2 = B\left(\mathbf{R}^2 + \mathbf{L}^2 - 2\mathbf{N} \cdot \mathbf{L}\right) \tag{2.16}$$

The rotational levels have the energies $N(N+1)$ with the lowest N level having a value $N = \Lambda$. The second term in equation 2.16 is a constant and can be added to the electronic energy, the third term is small and will be discussed later. For an electronic state with $\Lambda = 1$ and $S = 1/2$ (a $^2\Pi$ state, as in the case of ground state CH) each N-level is split by the spin-orbit interaction [4]. We therefore get two rotational ladders which we denote with F_1 for $J = N + 1/2$ and F_2 for $J = N - 1/2$. Note that the spin-orbit splitting $(F_1(N) - F_2(N))$ tends to zero for large N [107].

These two Hund's cases are the most important ones for diatomic molecules. Note however, that they are limiting cases and most molecules are described by an intermediate situation.

This allows us now to draw a level diagram of the CH molecule in its ground electronic and vibrational state. This is shown in figure 2.2 where Hund's case (b) labelling is used. CH is light (small moment of inertia) and thus has a large rotational constant $B = 14.457\,\mathrm{cm}^{-1}$. The spin-orbit constant is $A = 28.1\,\mathrm{cm}^{-1}$. As can be seen in figure 2.2 each J-level is split into a so-called Λ-doublet. To understand the origin of this splitting we need to look more closely at equation 2.16. The third term in the last expression is the so-called rotational electronic Coriolis interaction. The spin-orbit and the Coriolis interaction couple two different electronic states with $\Delta\Lambda = \pm 1$. In the case of a Π ground state these interactions lead to a small (second order) admixture of a distant Σ state. This small perturbation lifts the degeneracy between the states with $\Lambda = +1$ and $\Lambda = -1$ (electrons moving clockwise or counter-clockwise around the internuclear axis). Therefore, each J state is split into two closely spaced opposite parity states, which are shown in figure 2.2. The size of the splitting depends on the value of J.

---

[4]Note that the spin-orbit constant A is nearly the same as the $2B$. In the ground state ($N = 1$) there is no rotation ($R = 0$) and it is the spin-orbit interaction that leads to a splitting of the each N level.
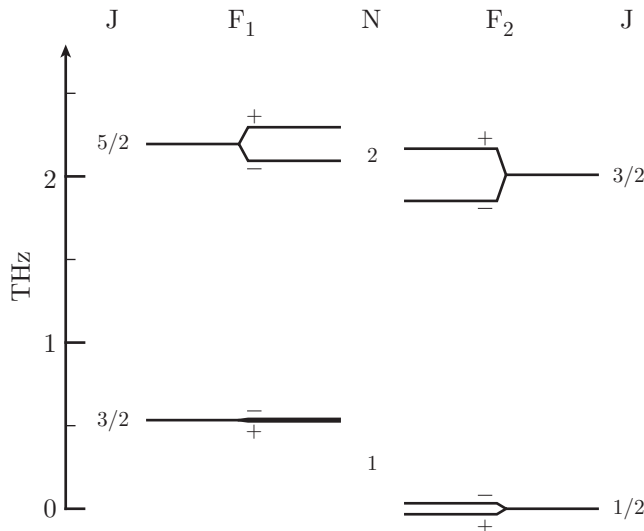
FIGURE 2.2: Rotational levels of CH in the $v = 0$ level of the $X^2\Pi$ ground state in Hund's case (b) notation. Each N level is split by the coupling of spin $(S = 1/2)$ and rotation into two manifolds which are labelled by F_1 and F_2 corresponding to $N + 1/2$ and $N - 1/2$ respectively. Note that for a molecule with $\Lambda = 1$ the lowest N quantum number is one. Each J level is split into a Λ-doublet. The size of the Λ-splitting depends on the value of J. The Λ-doublet is exaggerated by a factor of 20.

We have also neglected the angular momentum associated with the nuclear spins so far, i.e. the hyperfine structure. The interaction of the nuclear spin $\mathbf{I}$ with the other angular momenta of the molecule is very weak, i.e. it leads to a very small splitting. We couple the nuclear spin and electronic angular momenta to make the total angular momentum $\mathbf{F} = \mathbf{J} + \mathbf{I}$. Since $I = 1/2$, each Λ-doublet component splits into two levels with total angular momentum quantum numbers $F = J \pm 1/2$.

2.4 Transitions Between the Ground and Excited States

The energy difference between two electronic states of diatomic molecules corresponds to a frequency in the optical domain $(E/h \approx 500\,\text{THz})$ of the electromagnetic spectrum. The Born-Oppenheimer approximation allows us to separate the exact frequency at which the transition occurs into three parts (neglecting small splittings such as fine or hyperfine structure for the moment): an electronic, a vibrational and a rotational part.

An external electromagnetic field $\mathcal{E}$ induces a dipole moment $\mathbf{d}$ in the molecule. The Hamiltonian describing the interaction between the field and the dipole moment is $H_I = -\mathbf{d} \cdot \mathcal{E}$. The intensity of the dipole radiation scales with the square of the matrix element of the interaction

Hamiltonian between the initial and final states

$$d = \langle 1 \, | \mathbf{d} \cdot \mathcal{E} | \, 2 \rangle = \int_V \Psi_1^* \mathbf{d} \cdot \mathcal{E} \Psi_2 \, \mathrm{d}V \, . \tag{2.17}$$

The Born-Oppenheimer approximation allows us to separate the total wave function into its electronic, vibrational and rotational parts $\Psi = \psi_n f_v Y_{JM}$. The rotational, or angular part of d yields a constant factor of the form $M_{\mathrm{rot}} = \int Y_{J'M'} Y_{1M} Y_{J''M''} \, \mathrm{d}\Theta \, \mathrm{d}\Phi$. The single prime indicates that the rotational state belongs to the excited electronic state and the double prime that it belongs to the ground state. Hence the rotational factor is an integral over a product of three spherical harmonics which gives rise to a Wigner 3-J symbol. This 3-J symbol is zero unless $\Delta J = J' - J'' = 0, \pm 1$ and $\Delta M = M' - M'' = 0, \pm 1$. Note that for linearly polarised light $\Delta M = 0$ and for left/right circularly polarised light $\Delta M = -1/+1$. If we sum over all M' and M'' and square the angular factor we get the so-called Hönl-London factor $s_{J',J''}$ which is a measure for the relative strength of rotational lines, i.e. it indicates the intensity of a specific rotational line of a vibronic transition.

Evaluating the vibrational part of d yields a vibrational overlap integral $\int f_{v'}^*(R) f_{v''}(R) \, \mathrm{d}R$. The square modulus of this overlap integral is known as the Franck-Condon factor $q_{v',v''}$.

This leaves us with the electronic part of the transition matrix element, which we call $d_{n',n''} = \int \psi_{n'}^* \mathbf{d}_{el} \psi_{n''} \, \mathrm{d}\mathbf{r}_i$, with $\mathbf{d}_{el} = -e \sum_i \mathbf{r_i}$ is a sum over the position vectors of the electrons which contribute to the dipole moment. It depends on the internuclear separation R because the electronic wave functions $\psi = \psi(\mathbf{r}_i, \mathbf{R})$ depend on R. However, to a good approximation its dependence on R is small and we can thus replace it by its average value $d_{n',n''}(R_e)$. The square modulus of the electronic part of the transition dipole moment gives the electronic transition probability. The exact function of the electronic transition dipole moment as a function of internuclear distance can be calculated using ab initio techniques.

The transition probability for a molecule to undergo a transition between two electronic states is thus proportional to $|d_{n',n''}(R_e)|^2 q_{v',v''} s_{J',J''}$, i.e. it depends on the transition dipole moment, the overlap between the vibrational wavefunctions in the ground and excited state, and the Hönl-London factor. The angular part restricts the number of possible transitions and determines the intensity of particular rotational line of a vibronic transition. For light, linearly polarised along the laboratory z-axis, the transition must obey the selection rules $\Delta J = 0, \pm 1$ and $\Delta M = 0$. We can include the hyperfine structure as well and define the analogous selection rule $\Delta F = 0, \pm 1$ with the restriction that a $F'' = 0 \to F' = 0$ transition is forbidden. Because the dipole operator is an odd function of coordinates, the parity must change during an electric dipole transition.

With this information we can draw a level diagram that shows the possible transitions between the ground and excited electronic states of CH. The level diagram for the $B^2\Sigma^-(v' = 1) \leftarrow X^2\Pi(v'' = 0)$ transition is shown in figure 2.3 and the level diagram for the $A^2\Delta(v' = 0) \leftarrow X^2\Pi(v'' = 0)$ transition is shown in figure 2.4.
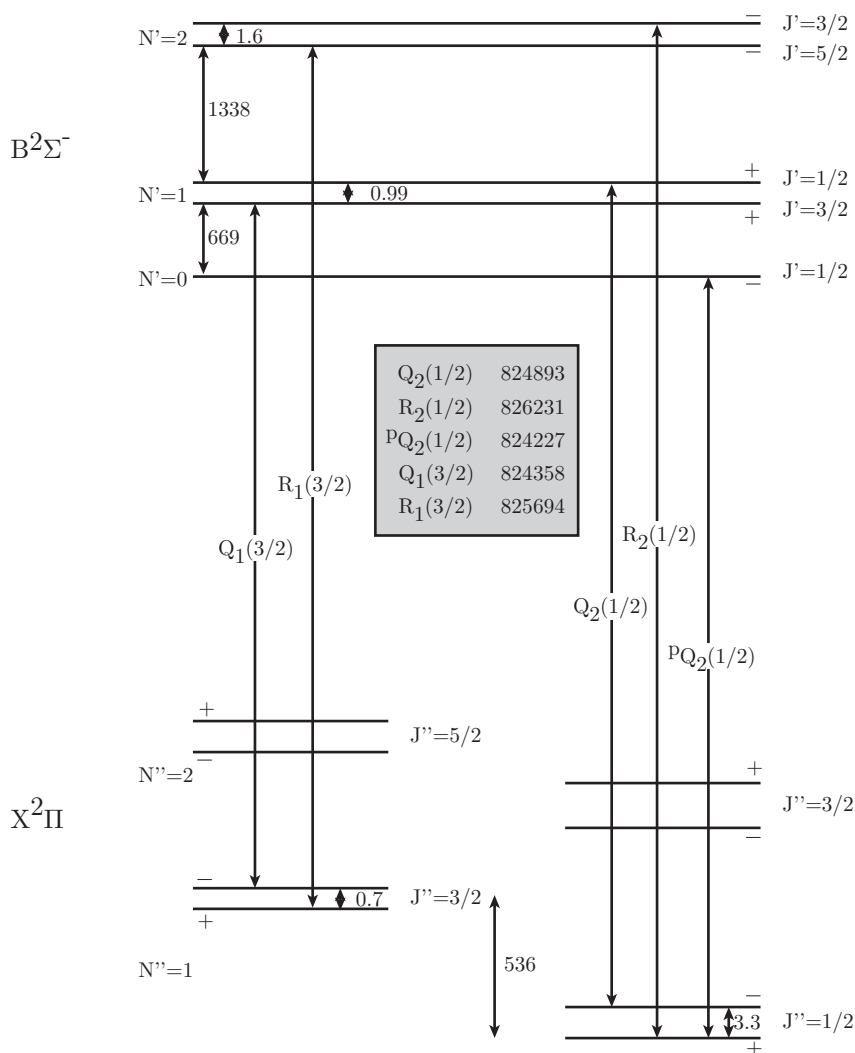
FIGURE 2.3: A few of the possible rotational lines for the $B^2\Sigma^-(v' = 1) \leftarrow X^2\Pi(v'' = 0)$ vibronic transition relevant to our experiment. The transitions are labelled according to $\Delta J_{F_{1,2}}(J'')$, where $\Delta J = 0$ corresponds to a Q line, $\Delta J = +1$ to an R line and $\Delta J = -1$ to a P line. The superscript p for the ^pQ line indicates that N is lowered by one. Note that each level is split into two hyperfine components which have been omitted. All the frequencies are given in GHz.

By choosing the frequency of the electromagnetic radiation we can excite the molecule on a specific transition. Once the molecule is excited it will in general dispose of its excitation energy by emitting radiation after an average time τ which is known as the lifetime of the excited state. The finite lifetime of the excited state leads to finite spectral width of the rovibronic transition. It follows from the uncertainty principle ($\Delta E \Delta \tau > \hbar$) that the full-width at half maximum (FWHM) of a transition $\Delta f = 1/(2\pi\tau) = \Gamma/(2\pi)$ with Γ the spontaneous decay rate. When the molecule disposes its excitation by emitting electromagnetic radiation it can end up in different rovibrational levels in the ground electronic state the lifetime of which are typically much longer than for an electronic transition. The probability to which vibrational level is governed by the
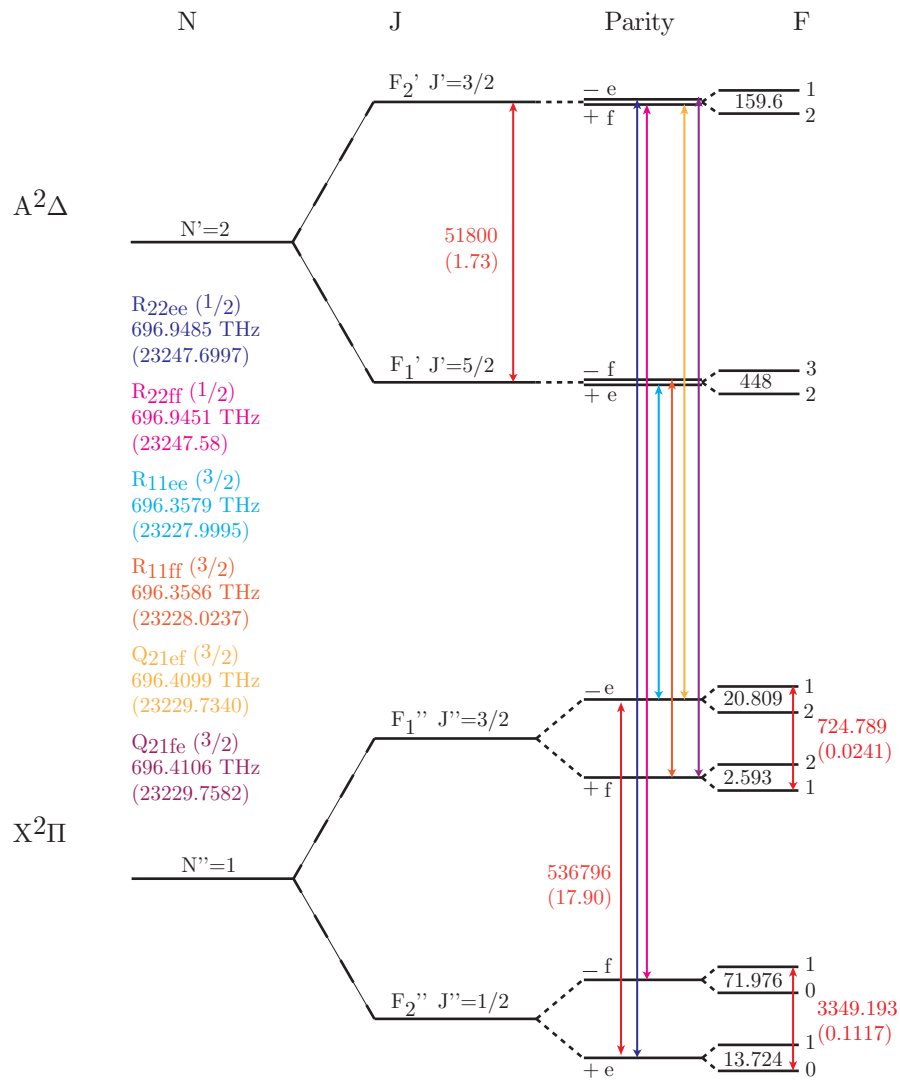
FIGURE 2.4: A selection of the possible rotational lines for the $A^2\Delta(v' = 0) \leftarrow X^2\Pi(v'' = 0)$ vibronic transition relevant to our experiment. The transitions are labelled according to $\Delta J_{F'_{1,2}, F''_{1,2}}(J'')$, where $\Delta J = 0$ corresponds to a Q line, $\Delta J = +1$ to an R line and $\Delta J = -1$ to a P line. Here the hyperfine structure is included. If not explicitly mentioned all frequencies are given in MHz. The values in brackets are in cm^{-1}

Franck-Condon factor. Note that the spontaneous decay rate and thus the spectral width of a transition is related to the dipole matrix element:

$$\Gamma_j = \frac{\omega^3}{3\pi\epsilon_0\hbar c^3} \sum_i d_{ij}^2 \,, \tag{2.18}$$

where d_{ij} are the dipole matrix elements for all possible decay channels from the excited state j to the ground state i. Hence we can measure the dipole matrix element by measuring the lifetime of the excited state.

2.5 Stark Effect

The interaction of a dipole μ with a homogeneous electric field $\mathcal{E}$ is expressed by the Stark Hamiltonian $H_s = -\mu \cdot \mathcal{E}$. The dipole moment μ has a well defined orientation in the rotating body-fixed frame of the molecule $(\mathbf{x}, \mathbf{y}, \mathbf{z})$. The electric field on the other hand has a well defined orientation in the laboratory frame $(\mathbf{X}, \mathbf{Y}, \mathbf{Z})$. It is convenient to express both quantities as irreducible spherical tensor operators of rank 1, $H_s = -\mu \cdot \mathcal{E} = -T^{(1)}(\mu) \cdot T^1(\mathcal{E})$ [108]. We can choose the Z-axis to be along $\mathcal{E}$ which reduces the Hamiltonian to $H_s = -T_0^{(1)}(\mu)\mathcal{E}$, where $T_0^{(1)}(\mu)$ is the projection of the dipole moment onto the space-fixed $\mathbf{Z}$ axis. A transformation from the space-fixed frame to the rotating molecular frame can be made by using the Wigner rotation matrices $\mathcal{D}$:

$$T_0^{(1)}(\mu) = \sum_{q=-1}^{1} (\mathcal{D}_{0q}^{(1)}(\theta, \phi, \chi))^* T_0^{(k)}, \tag{2.19}$$

with θ, ϕ and χ the Euler angles which define the orientation of the $(\mathbf{X}, \mathbf{Y}, \mathbf{Z})$ frame with respect to $(\mathbf{x}, \mathbf{y}, \mathbf{z})$. In a Hund's case (a) basis we have the eigenstates $|\eta, J, \Omega, M\rangle$ and we can evaluate the matrix elements as follows:

$$\left\langle \eta, J, \Omega, M \left| T_0^{(1)}(\mu)\mathcal{E} \right| \eta', J', \Omega', M' \right\rangle = \mathcal{E} \sum_q \left\langle J, \Omega, M \left| \mathcal{D}_{0q}^{(1)} \right| J', \Omega', M' \right\rangle \left\langle \eta \left| T_0^{(1)}(\mu) \right| \eta' \right\rangle. \tag{2.20}$$

Here, we have used the Born-Oppenheimer approximation to separate the vibronic and rotational parts. The last factor describes the matrix elements of the dipole moment operator between electronic states. Because of the large energy separation between electronic and vibrational states, matrix elements where $\eta \neq \eta'$ contribute very little to the Stark shift. Focussing then on the matrix elements where $\eta = \eta'$, only the term where $q = 0$ is non-zero because the dipole moment lies along Z. So we have

$$\left\langle \eta, J, \Omega, M \left| T_0^{(1)}(\mu)\mathcal{E} \right| \eta, J', \Omega', M' \right\rangle = \mu_e \mathcal{E} \left\langle J, \Omega, M \left| \mathcal{D}_{00}^{(1)} \right| J', \Omega', M' \right\rangle \tag{2.21}$$

with $\mu_e = \left\langle \eta \left| T_0^{(1)}(\mu) \right| \eta \right\rangle$ the permanent electric dipole moment of the ground state. To evaluate the remaining matrix element we can consult chapter 5.5.5 in Brown and Carrington's book [107] and get the final result for the matrix elements of the Stark interaction:

$$\left\langle J, \Omega, M \left| H_S \right| J', \Omega', M' \right\rangle = \mu \mathcal{E} (-1)^{M-\Omega} \sqrt{(2J+1)(2J'+1)} \begin{pmatrix} J & 1 & J' \\ -\Omega & 0 & \Omega' \end{pmatrix} \begin{pmatrix} J & 1 & J' \\ -M & 0 & M' \end{pmatrix}. \tag{2.22}$$

All we now need to do is to construct the matrix which contains the rotational energy as the diagonal elements and the interaction terms (Stark terms) as the off-diagonal terms. We can diagonalise it and the eigenvalues give the Stark shift of the energy levels.

For CH the situation is more complicated because of the spin-orbit splitting, the Λ-doubling

and the hyperfine structure. The Λ-doubling splits each J state into two closely spaced opposite parity levels. Therefore, the electric field can mix these levels which leads to a large Stark shift.[5] In fact the mixing of the Λ-doublet states is the dominant contribution to the Stark interaction in CH. In a Hund's case (a) basis set we get two spin components $^2\Pi_{|\Omega|=1/2}$ and $^2\Pi_{|\Omega|=3/2}$. Due to the fact that the spin-orbit interaction energy and the rotational interaction energy are comparable in size the energy eigenstates of the molecular Hamiltonian are not pure Hund's case (a) wavefunctions $|J, \Omega = 1/2, M\rangle$ or $|J, \Omega = 3/2, M\rangle$, but are rather a superposition of both:

$$|F_1, \pm, J, M\rangle = -C_1(J)|J, \Omega = 1/2, \pm, M\rangle + C_2(J)|J, \Omega = 3/2, \pm, M\rangle$$

$$|F_2, \pm, J, M\rangle = C_2(J)|J, \Omega = 1/2, \pm, M\rangle + C_1(J)|J, \Omega = 3/2, \pm, M\rangle \,, \qquad (2.23)$$

with

$$C_1(J) = \sqrt{(X + Y - 2)/(2X)} \qquad\qquad C_2(J) = \sqrt{(X - Y + 2)/(2X)} \qquad (2.24)$$

$$X = \sqrt{4(J + 1/2)^2 + Y(Y - 4)} \qquad\qquad Y = A/B \qquad (2.25)$$

The coefficients C_1 and C_2 are the components of the eigenvector of the Hamiltonian matrix, given in equation 9.74 in Brown and Carrington's book [107], which for the case of CH ($A \approx 2B$) give $C_1 = C_2 = 1/\sqrt{2}$. So for CH the energy eigenstates are nearly equal superpositions between the pure case (a) basis functions that correspond to $\Omega = 1/2$ and $\Omega = 3/2$. In equation 2.23 we have also added a parity quantum number $\pm$ to identify the Λ-doublet states.

The $J = 1/2$ state, however, is special: there is no $^2\Pi_{3/2}$ spin component for $J = 1/2$ level and it is thus a pure $^2\Pi_{1/2}$ state. The equations 2.23 define the so-called parity symmetrised basis. By using this basis set and assuming that the Λ-doubling is small compared to the rotational structure, i.e set $J = J'$ we can now determine the Stark shift of the Λ-doublet levels:

$$\langle F_1, \pm, J, M | H_s | F_1, \mp, J, M\rangle = -(\frac{1}{2}C_1^2 + \frac{3}{2}C_2^2)\mu_e\mathcal{E}(-1)^{2M-2J}\frac{M}{J(J+1)} \qquad (2.26)$$

$$\langle F_2, \pm, J, M | H_s | F_2, \mp, J, M\rangle = -(\frac{1}{2}C_2^2 + \frac{3}{2}C_1^2)\mu_e\mathcal{E}(-1)^{2M-2J}\frac{M}{J(J+1)}, \qquad (2.27)$$

Note that for the $J = 1/2$ state only the $\Omega = 1/2$ component contributes so that the matrix elements become:

$$\langle F_2, \pm, 1/2, M | H_s | F_2, \mp, 1/2, M\rangle = -\frac{1}{2}\mu_e\mathcal{E}(-1)^{2M-2J}\frac{M}{J(J+1)} \,. \qquad (2.28)$$

This allows us now to construct the Hamiltonian matrix, which contains the Λ-doubling energies as diagonal elements and the Stark interaction as off-diagonal elements. The Stark shift of both

---

[5]For small electric fields we can invoke perturbation theory: The Stark shift $\Delta E_s = \langle \psi_i | H_s | \psi_i\rangle + \sum_{j\neq i} \frac{|\langle \psi_i | H_s | \psi_j\rangle|^2}{E_i - E_j} + \dots$. The first term is zero because H_s is odd and the second term is large for small energy splittings $E_i - E_j$. Thus, the smaller the energy splitting between the states H_s can mix the larger the shift of the energy levels.

Λ-doublet components of the $J = 1/2$ ground sate is given by diagonalising the 2×2 matrix:

$$\begin{pmatrix} -E_\Lambda/2 & Q \\ Q & E_\Lambda/2 \end{pmatrix} \tag{2.29}$$

where E_Λ is the zero-field Λ-doublet splitting. The off-diagonal elements Q are given by equation 2.28. The Stark shift is:

$$E_\pm = \sqrt{\frac{E_\Lambda^2}{4} \pm \left(\frac{1}{2} \frac{M}{J(J+1)} \mu_e \mathcal{E} \right)^2}. \tag{2.30}$$

Note that for some experiments the low field behaviour is important and then the hyperfine structure must be included in the calculation. This calculation can be found in Brown and Carrington's book (equation 5.148). To account for the hyperfine structure in the Stark interaction we need to multiply the matrix elements 2.22 by the factor

$$f = (-1)^{F+F'+2J+I-M_F+1} \sqrt{(2F+1)(2F'+1)} \begin{Bmatrix} J' & F' & I \\ F & J & 1 \end{Bmatrix} \frac{\begin{pmatrix} F & 1 & F' \\ -M_F & 0 & M_F \end{pmatrix}}{(-1)^M \begin{pmatrix} J & 1 & J' \\ -M & 0 & M' \end{pmatrix}} \tag{2.31}$$

where, the curly brackets denote the Wigner 6J-symbol.

2.6   Zeeman Effect

The interaction of a molecule with an external magnetic field $\mathbf{B}$ is given by the Zeeman Hamiltonian [107] (in spherical tensor notation):

$$H_z = g_L \mu_B T^{(1)}(\mathbf{B}) \cdot T^{(1)}(\mathbf{L}) + g_S \mu_B T^{(1)}(\mathbf{B}) \cdot T^{(1)}(\mathbf{S}) - g_N \mu_B T^{(1)}(\mathbf{B}) \cdot T^{(1)}(\mathbf{I}) -$$
$$- g_r \mu_B T^{(1)}(\mathbf{B}) \cdot \left[T^{(1)}(\mathbf{J}) - T^{(1)}(\mathbf{L}) - T^{(1)}(\mathbf{S}) \right] \tag{2.32}$$

where g is the Landé g-factor associated with the particular angular momentum in question. The evaluation of the matrix elements is very similar to the one presented above for the Stark effect and will thus not be presented again. The matrix elements for all the terms are given in equation 9.71 in Brown and Carrington's book [107]. Ignoring the hyperfine and rotational contribution for the moment and using the parity symmetrised basis, we get two total molecular

	F_1			F_2	
J	F	g	J	F	g
3/2	1	1.081	3/2	1	-0.08
3/2	2	0.648	3/2	2	-0.048
5/2	2	0.578	5/2	2	-0.178
5/2	3	0.413	5/2	3	-0.127

TABLE 2.1: The molecular g-factors for the $J = 3/2$ and $J = 5/2$ states of the two F_1 and F_2 manifolds, including hyperfine structure.

g-factors for the two sets of states F_1 and F_2. These are

$$g_1 = \frac{1}{J(J+1)} \left[\frac{1}{2} \left(g_L - \frac{g_s}{2} \right) \right] C_2^2 + \frac{3}{2} \left[g_L + \frac{g_s}{2} \right] C_1^2 + \sqrt{(2J+3)(2J-1)\frac{g_s}{2} C_1 C_2} \qquad (2.33)$$

$$g_2 = \frac{1}{J(J+1)} \left[\frac{1}{2} \left(g_L - \frac{g_s}{2} \right) \right] C_1^2 + \frac{3}{2} \left[g_L + \frac{g_s}{2} \right] C_2^2 - \sqrt{(2J+3)(2J-1)\frac{g_s}{2} C_1 C_2}. \qquad (2.34)$$

Similar to the previous section we can account for the hyperfine structure by multiplying g_1 and g_2 with f from equation 2.31 which for small magnetic fields (neglecting matrix-elements off-diagonal in J and F) reduces to:

$$f = \frac{1}{8F(F+1)} \left[(2F-1)(2F+3) + 4J(J+1) \right]. \qquad (2.35)$$

The Zeeman shift of a particular energy level from the sets F_1 or F_2 is

$$\Delta E_{z,i} = g_i \mu_B B_z M_F \qquad (2.36)$$

where $i = 1, 2$. The molecular *g*-factors, including hyperfine structure, for the $J = 3/2$ and $J = 5/2$ of the (F_1, J, F, M_F) and (F_2, J, F, M_F) ladders are listed in table 2.1.

The $J = 1/2$ ground state is special since it is a pure case (a) $^2\Pi_{1/2}$ state. For this state the magnetic moments due to the orbital and spin angular momentum are very nearly equal and opposite. In a case (a) molecule both the orbital angular momentum and the spin angular momentum are strongly coupled to the internuclear axis. The magnetic moments associated with each angular momentum therefore lie along the internuclear axis with values of $\mu_B g_L \Lambda$ and $\mu_B g_S \Sigma$. Because $\Omega = \Lambda + \Sigma$ the magnetic moment along Ω is $\mu_\Omega = \mu_B (g_L \Lambda + g_S \Sigma)$. We are interested in the magnetic moment along the total angular momentum J. Since Ω is the projection of J onto the internuclear axis the magnitude of Ω along J is $\Omega/\sqrt{(J(J+1))}$ and thus the magnitude of the magnetic moment along J is $\mu_J = \mu_\Omega \Omega/\sqrt{(J(J+1))}$. If the magnetic field direction is along z the projection of J onto z is labelled by M_F and the magnetic moment along z is then $\mu_z = \mu_J M_F/\sqrt{J(J+1)}$. We can now put everything together and get the Zeeman shift $\Delta E = \mu_z B_z$:

$$\Delta E = \mu_B B_z \frac{\Lambda + 2\Sigma}{J(J+1)} \Omega M_F \qquad (2.37)$$

where we have used $g_L = 1$ and $g_S = 2$. For a $(^2\Pi, J = 1/2)$ state $\Lambda = 1$ and $\Sigma = -1/2$. This means that the contributions of the electron's orbital and spin angular momentum to the molecular g-factor cancel and that there is no Zeeman shift to first order. If we use a more accurate value for $g_S = 2.0023$ we get a molecular g-factor of $g = 7.7 \times 10^{-4}$. Relativistic corrections to g_L are negligible. This means the $J = 1/2$ state is extremely insensitive to magnetic fields.

Note that we have neglected the contributions of the nuclear spin g_I and the rotation g_r. The matrix elements for the total Zeeman Hamiltonian 2.32 are given in equation 9.71 of Brown and Carrington's book [107]. The g-factors are slightly different for the two parity components of the Λ-doublet. Using the molecular constants given in [109] we find $g_+ = -1.9 \times 10^{-3}$ and $g_- = 0.71 \times 10^{-3}$, for the two parity components of the $J = 1/2$ state.

2.7 Summary

The Born-Oppenheimer approximation is the fundamental concept that allows us to describe diatomic molecules and their spectra. It allows us to separate the total energy of diatomic molecule into three major parts: electronic, vibrational and rotational energy. The Born-Oppenheimer approximation can also be used to describe transitions between the electronic ground and excited states. Such transitions are governed by the electronic transition probability (electronic dipole moment), the Franck-Condon principle (overlap between vibrational wavefunctions) and angular momentum selection rules.

The rotational structure of the CH molecule in its ground vibronic state is complicated by the fact that the spin-orbit interaction is of similar size than the rotational energy ($A \approx 2B$). The coupling of the spin of one unpaired electron to the rotation of the molecule splits each rotational level, labelled by the Hund's case (b) quantum number N, into two fine-structure manifolds, labelled by F_1 and F_2. Each total angular momentum state J is again split into two Λ-doublet components due to a Coriolis interaction that couples higher lying electronic states to the ground state. Each Λ-doublet state is again split into two hyperfine components due to the coupling of the hydrogen nuclear spin with the other angular momenta. This description of the ground state is essential to understand and predict the high resolution spectroscopy experiments which will be presented in chapters 4 and 5. We have outlined the Stark effect in CH which will allow us to predict the sensitivity of certain transitions in CH due to external electric fields. The description of the Zeeman effect in CH reveals that the $(F_2, J = 1/2)$ state possess only a minute magnetic moment of the order of $10^{-3}\mu_B$. The $(F_1, J = 3/2)$ state, on the other hand, is highly sensitive to external magnetic fields with a magnetic moment of the order of $1\mu_B$. The accurate description of the Zeeman effect is necessary to predict the sensitivity of CH

transitions to external magnetic fields.

Chapter 3

Experimental Setup and Molecular Sources

An expert is a person who has found out by his own painful experience all the mistakes that one can make in a very narrow field.

Niels Bohr

3.1 Introduction

Most diatomic molecules that posses intriguing features like a permanent electric dipole moment have to be produced in a well controlled, isolated environment. This is because most of these species are highly reactive or not stable under ambient conditions. Naturally occurring polar, diatomic molecules such as CO, NO, HF, HCl have either a small dipole moment in their ground state (CO, NO) or are notoriously hard to detect (HF, HCl,...) in a state selective way, i.e. they only possess optical transitions in the deep ultra violet where no laser systems are available for resonant detection schemes. Salts or salt-like inorganic compounds like LiH, MgF or KBr can possess large dipole moments (up to 11 debye for KBr) but suffer from the problem that they have high boiling points and tend to react violently in the gas phase and to form clusters. Polar diatomic molecules that do not occur naturally have to be produced. These production techniques usually involve a precursor of some kind that undergoes a violent treatment through electron bombardment, high intensity laser ablation or ultra violet photolysis to name a few. The chemical processes happening during this step are very complex and not very well understood which makes this production process a highly empirical art that involves a certain degree of *black magic*. With few exceptions these production techniques are extremely inefficient which severely limits the number of molecules one has available for further experiments.

Another promising route to high density samples of polar molecules is the use of polyatomic

molecules such as NH_3 or CH_3F which can readily be supplied in gas bottles that can simply be plugged in to the experiment. Although these molecules are still hard to detect it is nowhere near as difficult as producing a comparable number of molecules through the above mentioned production techniques. With new cooling and manipulation techniques such as direct laser cooling of diatomic molecules or Sisyphus cooling of polyatomic molecules emerging it can only be a question of time until the first high density samples of ultracold molecules become reality. Recent results in Jun Ye's group at JILA even show evaporative cooling of OH molecules [90]. Although these results are still controversial it shows that efforts to reach this goal become extremely ambitious. The main limitation is and has always been the inefficiency of the molecular sources.

In this chapter the backbone of our molecular beam experiments is presented. In particular the vacuum apparatus, the laser system, the detector and the source are presented. A thorough characterisation of the detection efficiency provides a reliable measure of both the molecular flux and the density of polar molecules in the detection region. A brief overview and discussion of the wide range of molecular production techniques gives the background to the process of finding the optimum source. This is followed by a presentation of the tour de force of producing the CH molecule. We tried, tested and carefully characterised in total four different production techniques. Each technique is comprehensively analysed, characterised, compared to other molecular sources and to the ideal theoretical model. The characteristics and important parameters for each type of source are identified and presented. This will, hopefully, convince the reader that a persistent systematic approach to the art of molecular sources can be rewarding and allows to lift the curtain of black magic - at least a tiny bit.

3.2   The Vacuum System

In order to do experiments with diatomic polar molecules in a controlled and reproducible way it is of great importance to isolate them from any disturbing environmental influences. As we have learnt from the introduction, one of the best ways to do so is the use of a vacuum chamber and a free-jet molecular beam. So the starting point of a molecular beam experiment is the construction of an appropriate vacuum system. The outline and basic ingredients for such a vacuum system have more or less remained the same since the times of Rabi and Ramsey [110]. It consists of a source, a science, and a detector chamber. A sketch of the setup is shown in figure 3.1. The source chamber is used to create or introduce the species of interest. The science chamber is where the actual experiment takes place and the detector chamber, as the name suggests, houses an appropriate detector for the molecules of interest. The basis for the source and the detection chamber is a commercial DN200CF 6-way cross. The science chamber consists of a custom built cylinder that connects the two crosses. The whole system is evacuated by two turbomolecular pumps (Leybold MAG W 1300, Leybold Turbovac 1000) attached to the
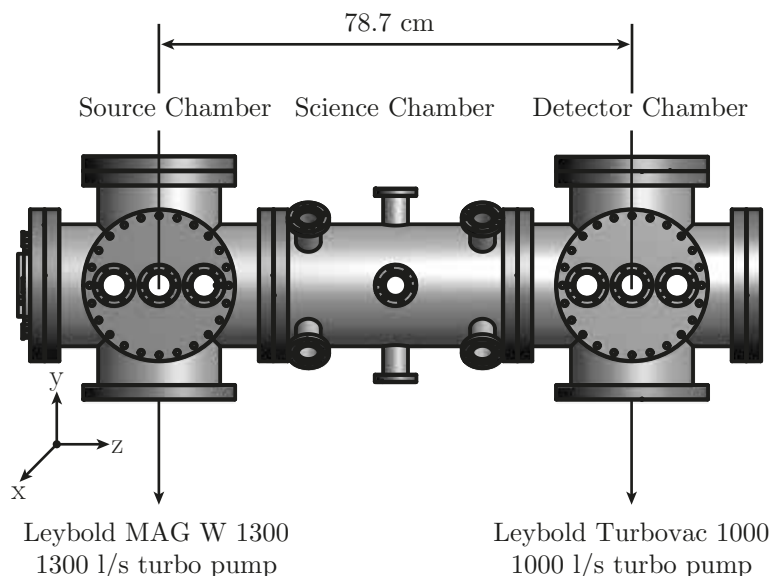
FIGURE 3.1: The vacuum setup

source and detector chamber respectively. The pump for the source chamber is equipped with oil-free magnetic bearings and has a pumping speed of $1300\,\mathrm{l s}^{-1}$. This allows to cope with large volumes of corrosive gases which are commonly used in molecular radical production techniques. The only conduction between the source and the other two chambers happens through the $2\,\mathrm{mm}$ diameter opening of a conical skimmer. Skimmers are used as collimating apertures that extract the centre of a molecular beam in order to limit its angular spread. Additionally, the small aperture limits the gas conduction between the chambers and thus allows for a large pressure differential between the source and other two chambers. Skimmers are specially designed apertures which minimize any interference with the molecular beam. Beam molecules can be scattered by molecules reflected from exterior surfaces and also by collisions with the gas that builds up inside the skimmer. To minimise these effects the skimmers are usually thin-walled, with very sharp edges, and are curved to maximize the interior angle.

The pumps are able to decrease the pressure inside the vacuum chambers to approximately $10^{-8}\,\mathrm{mbar}$. When the source is operated it introduces gas in short pulses of approximately $250\,\mathrm{\mu s}$ at a repetition rate of $10\,\mathrm{Hz}$. This leads to a pressure increase in the source chamber to $5 \times 10^{-5}\,\mathrm{mbar}$. However, because there is only a small aperture connecting the source and the other two chambers the pressure in the latter remains below $5 \times 10^{-7}\,\mathrm{mbar}$ when the source is operating. The entire vacuum chamber is mounted onto a rigid Bosch frame. A single rotary vane pump (Leybold CF4-25) sits beneath the setup and provides a rough vacuum of $10^{-3}\,\mathrm{mbar}$ for the turbomolecular pumps.

Now we have a basic vacuum chamber, but before we can start producing molecules we need to add a detector so we can detect and characterise the molecular source.
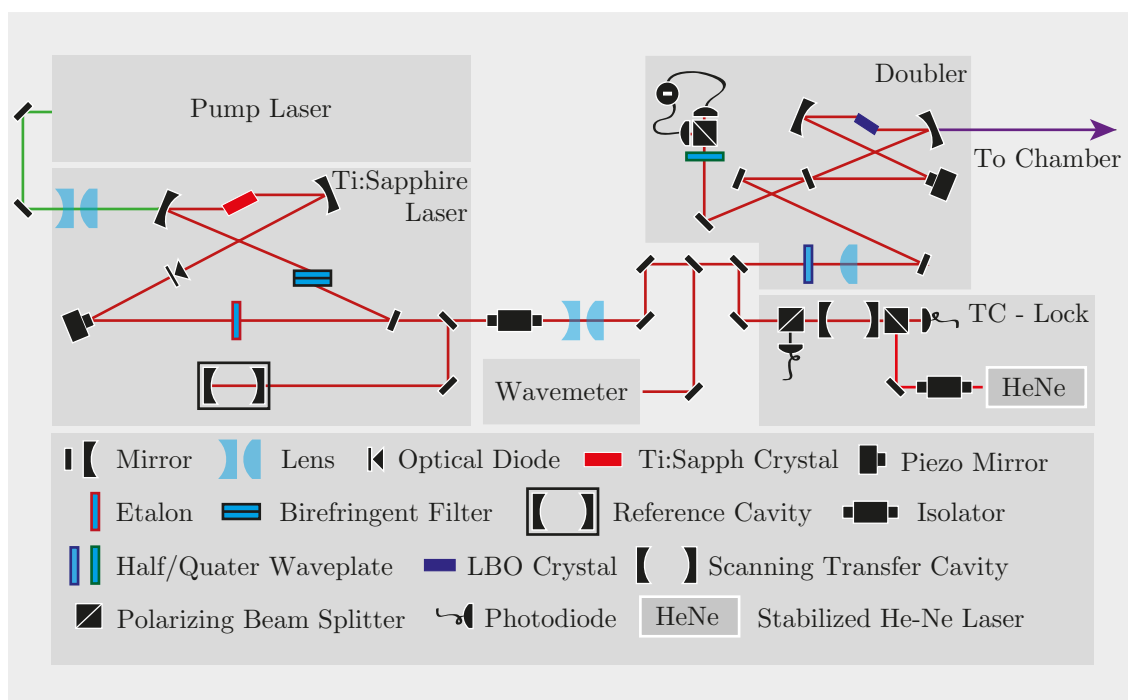
FIGURE 3.2: The laser system for detecting molecules. The Ti:Sapphire laser (MBR-110) is pumped by 8 W of green laser light. The emission of the crystal is very broad band and thus a single frequency is selected by birefringent elements inside the cavity. The red Ti:Sapphire light is then frequency-doubled by a non-linear crystal which sits in a build up cavity. The blue light is then directed through the detector chamber. The frequency of the Ti:Sapphire is stabilised with respect to a temperature stabilised helium neon laser via a transfer cavity (TC-Lock) which will be explained in the next section.

3.3 Detection Hardware and Laser System

Ideally the detector should enable us to count the molecules we have produced with high efficiency. It should be state selective, tell us the temperature of the molecules in their moving frame and their speed. All these properties are vital ingredients which allow us to analyse and characterise various molecular beam sources. Different techniques for detecting molecules have been developed over the last century. A particular useful one for our purpose was first demonstrated in 1968 by Ezekiel and Weiss from MIT [111]. They used the light of an argon ion laser to induce an electronic transition in iodine molecules. The molecules decay back into the ground electronic state by the emitting fluorescence light which is detected by a sensitive photon detector. This technique is since known as laser-induced fluorescence detection. We use the very same principle, however, with a different laser system. The laser we use for detecting molecules is a commercial single-mode, continuous wave Ti:Sapphire laser (Coherent MBR-110), the frequency of which is doubled in a non-linear crystal which sits in a build up cavity (Coherent MBD-200). A schematic of the setup is shown in figure 3.2.

The active laser medium of an MBR-110 consists of a sapphire crystal (Al_2O_3) which is doped with titanium ions, typically at a concentration of 0.1 % by weight. Sapphire is used

as a host crystal because of its high transparency, high thermal conductivity, good chemical inertness, high mechanical rigidity and hardness. The Ti:Sapphire crystal needs to be optically pumped to create the initial population inversion necessary for lasing to occur.

Due to the presence of titanium ions the crystal shows a broad absorption feature ranging from 380 to 620 nm which peaks at approximately 490 nm. The absorption of such a blue-green pump photon excites the titanium ion electronically and causes it to shift slightly with respect to its sapphire host lattice. Such phonon excitations of the host lattice are accompanied by relaxation processes which shift the emission wavelengths towards the red (Stokes shifted). The many possible vibrational excitations of the ion-crystal system lead to a very broad emission spectrum, the width of which exceeds 300 nm and is centred about 790 nm.

We use a frequency doubled Nd:YVO$_4$ laser (Coherent Verdi V8) which provides 8 W in a 2 mm diameter beam at 532 nm to pump the Ti:Sapphire crystal. The crystal itself sits in a bow-tie resonator which provides the feedback needed to sustain lasing.

A convenient way to choose the frequency at which lasing should occur is the use of bire-fringent elements inside the optical resonator. A birefringent plate (birefringent filter, BRF) is cut with its optical axis at a tilt angle to the surface of the plate. The plate itself is tilted such that the angle of incidence is at Brewster's angle. The transmission through the plate then depends on the phase difference between the two waves propagating as ordinary and extraordinary waves. For light of the right wavelength the filter acts effectively as a full waveplate. For all other wavelengths it introduces large losses at the Brewster surfaces. By rotating the birefringent filter about an axis perpendicular to its surface one effectively changes the angles of the refracted rays and thus one can shift the maximum transmission to a different wavelength. This is a very coarse wavelength control and so a thin Fabry-Pérot etalon inside the laser resonator is used to select a single cavity-mode. Hence rotating the birefringent filter does not change the frequency smoothly but rather in steps of 225 GHz which corresponds to the free spectral range (FSR$= c/2d$) of the etalon, where d is the thickness of the etalon. Fine tuning of the frequency can then be achieved by changing the angle of the etalon which effectively changes its thickness and thus the transmitted wavelength.

In order to stabilise the laser frequency a fraction of the laser light is directed into a temperature controlled reference cavity. The laser cavity is stabilised with respect to this reference cavity which results in a single frequency laser linewidth of below 100 kHz. It is possible to scan the laser frequency by up to 30 GHz with two pieces of polished fused silica plates which are mounted inside the laser cavity on galvanometers at Brewster's angle. A small change in angle of these plates changes the laser cavity length and thus the laser frequency slightly. A fraction of the output light is directed into a temperature controlled reference cavity. The laser is locked to one of the cavity fringes. In order to assure that the laser stays locked while scanning the frequency the length of the reference cavity can be scanned. Strain gauges attached to the reference cavity in combination with a servo-loop feed back to the galvanometer-mounted plates and thus ensures a highly linear frequency scan without unlocking the laser. Additionally, the

reflection from the etalon is monitored on a photodiode. This is used to stabilise the etalon position to prevent unwanted mode hops.

With 8 W of pump light, the Ti:Sapphire cavity well optimized and with all the elements thoroughly cleaned we have achieved output powers of up to 1.1 W at a wavelength of 860 nm. This optimum condition, however, does not last for very long, so on an everyday basis 850 mW is a more typical figure of merit. In order to produce the detection light for CH molecules the 860 nm light from the Ti:Sapphire laser is frequency doubled to produce light at 430 nm.

Frequency doubling was first achieved in 1961 shortly after the invention of the laser. Peter Franken and co-workers focused the intense light of a pulsed ruby laser into a crystalline quartz sample and analysed the emerging light with a spectrometer [112]. They clearly saw a spot on the photographic plate of their spectrometer at exactly half the wavelength. Note that only one part in 10^8 of the incident wave was converted into the second harmonic. In fact, the actual data point on the photograph of the spectrometer plate was so dim that the editor of the journal where the results were published removed it, mistaking it for a speck of dirt.

If a laser beam travels through a dielectric medium the electric field polarises the material, i.e. it displaces the electrons in the material from their equilibrium positions. This polarisation P may be expressed as a Taylor series in the electric field E in the following way,

$$P = \epsilon_0 \left(\chi^{(1)} \cdot E + \chi^{(2)} \cdot E^2 + \chi^{(3)} \cdot E^3 + \dots \right), \tag{3.1}$$

where $\chi^{(n)}$ are the n-th order susceptibilities of the material. The linear susceptibility $\chi^{(1)}$ is much greater than the other, higher order terms. However, for large electric fields (10^8 V m^{-1}) the higher order terms contribute a significant amount if the corresponding susceptibilities are non-zero. If we now assume a monochromatic plane wave of the form $E = E_0 e^{-i\omega t} + E_0^* e^{+i\omega t}$, oscillating at an angular frequency ω, enters the medium the polarisation becomes

$$P = \epsilon_0 \chi^{(1)} E + \epsilon_0 \chi^{(2)} \left(E_0^* E_0 + E_0 E_0^* + E_0^2 e^{-2i\omega t} + E_0^2 e^{+2i\omega t} \right) + \dots \tag{3.2}$$

This can be rewritten as

$$P = \epsilon_0 \chi^{(1)} E + 2\epsilon_0 \chi^{(2)} E_0^* E_0 + 2\epsilon_0 \chi^{(2)} E_0^2 \cos(2\omega t) + \dots \tag{3.3}$$

The term proportional to $\chi^{(1)}$ in equation 3.3 corresponds to the light that is re-radiated by the medium in response to the incident light. This is the usual refracted wave that propagates through the medium. The terms proportional to $\chi^{(2)}$ contain very interesting components. The first is a constant polarisation of the material proportional to $E_0^* E_0$ which establishes a constant voltage across the material which is proportional to the light intensity. The second term is at exactly twice the original frequency and is the reason for second harmonic generation in materials with a non-zero $\chi^{(2)}$. The polarisation varies at twice the fundamental frequency and thus the re-radiated light oscillates at twice the fundamental frequency. In isotropic media the

polarisation, or the displacement of the electrons in the material, is symmetric about inversion. This means that $P(-E) = -P(E)$. Hence in isotropic media such as glass or water the even orders of equation 3.3 are zero which means that no second harmonic generation is observed in such materials. However, in crystals that lack inversion symmetry the polarisation reacts non-linearly to the electric field which makes second harmonic generation possible. To double the red light from a Ti:Sapphire laser we use a lithium triborate (LiB_3O_5, or LBO) crystal. It has a very broad transmission range that spans from the UV to the mid-infrared, a very high damage threshold and a relatively large non linear susceptibility $\chi^{(2)}$. In such a crystal the doubling efficiency is still very small. To increase this efficiency it is useful to put the crystal into an enhancement cavity which is resonant with the pump light. The pump light passes many times through the crystal greatly increasing the intensity and hence the doubling efficiency.

The MBD-200 system is a bow-tie cavity system with a 2 cm long LBO crystal sitting in it. The faces of the crystal are cut at Brewster's angle for the fundamental wavelength. The cavity amplifies the incident fundamental light which results in an overall doubling efficiency as high as 16% per Watt of input power.

To achieve stable second harmonic generation in the MBD-200 system the length of the cavity must be stabilised. This is done by using a technique that was developed by Hänsch and Couillaud in 1980 [113]. It is based on monitoring the polarisation of the light that is reflected from the doubling cavity. In particular, it makes use of an intra-cavity polariser, which in our case is the crystal, the faces of which are cut at Brewster's angle. The polarisation of the incoming pump light possesses both vertical and horizontal polarisation components, the size of which can be adjusted by rotating a $\lambda/2$ plate before the beam enters the cavity. The wrong polarisation component (the one which experiences large losses at the Brewster surfaces of the crystal) is reflected from the cavity. This beam serves as a reference. The part of the beam with the right polarisation sees a cavity of low loss and experiences a frequency dependent phase shift. Part of it leaves the cavity and overlaps with the reference beam. Any relative phase change between the two beams due to a change in length of the cavity will make the combined beam elliptically polarised which is equivalent to a superposition of two counter-rotating circularly polarized components of different amplitudes. A $\lambda/4$ retarder then transforms the circular components into orthogonal linear polarisations which are separated by a polarising beam splitter. Each beam is then detected by a photodiode. The two photodiodes are connected through a differential amplifier which provides a dispersion-shaped error signal with a zero-crossing at the resonance frequency of the cavity. All one then needs to do is to feed the error signal into a servo-loop and stabilize the cavity length through a piezo-mounted mirror. This locking technique allows the doubler unit to follow scans of the fundamental frequency up to 30 GHz without decreasing the doubling efficiency. If everything is optimally aligned we have achieved up to 130 mW of output power with about 900 mW of fundamental light going into the doubler unit.
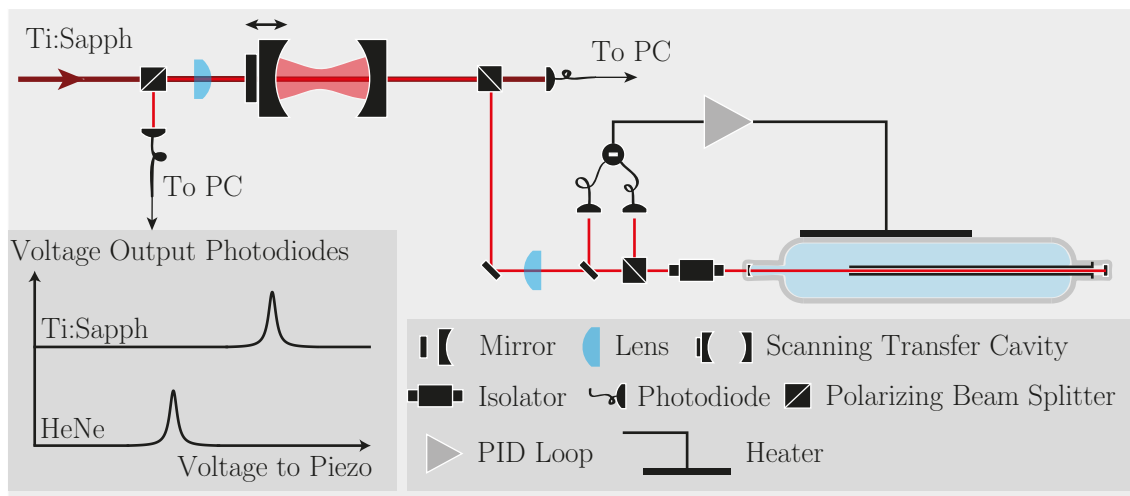
FIGURE 3.3: A sketch of the transfer cavity lock. The light of a helium-neon laser is frequency stabilised, sent through a scanning transfer-cavity and detected on a photodiode. The light from the Ti:Sapphire laser is sent through the same cavity and detected on a second photodiode. We see two transmission peaks and modulate the Ti:Sapphire laser frequency to keep its distance to the He-Ne peak constant.

3.3.1 The Transfer Cavity Lock

The reference cavity of the Ti:Sapphire laser is not sufficiently stable for our purpose. The frequency of the laser drifts by about 10 MHz per minute. This is not good enough if we want to stay on resonance with the CH transition for long periods of time. In order to stabilise the Ti:Sapphire laser against such temperature fluctuations we compare its frequency to the frequency of a stabilised He-Ne laser via a transfer cavity. A schematic of this setup is shown in figure 3.3. As a first step towards stabilising the Ti:Sapphire laser against frequency drift we need to stabilise the reference He-Ne laser. The length of the He-Ne tube determines the distance between two longitudinal (axial) cavity modes (free spectral range) to be $c/2L$, where c is the speed of light and L the length of the tube. For a length of 21 cm we expect about 20 modes to fit within the 1.5 GHz bandwidth of the neon gain medium. Due to mode competition it is energetically favourable for two adjacent axial modes to have orthogonal polarisation. We separate two orthogonal modes with a polarising beam splitter and detect them using two separate photodiodes. If the voltage difference is zero the two modes are symmetrical about the centre of the Doppler broadened neon emission profile (see figure 3.4). The relative intensity of the two modes changes with the resonator length. Hence in order to stabilise the cavity we need to keep the voltage difference between the photodiodes constant [114]. Whenever the photodiodes register an imbalance between the two intensities the error signal is sent to a thin film heater attached to the tube. This results in a significant local temperature rise and hence thermal expansion of the tube which changes the length of the cavity and balances the two components [115]. It is useful to bias the tube to a temperature well above ambient room temperature to minimize an asymmetry between heating and cooling periods. Furthermore, any
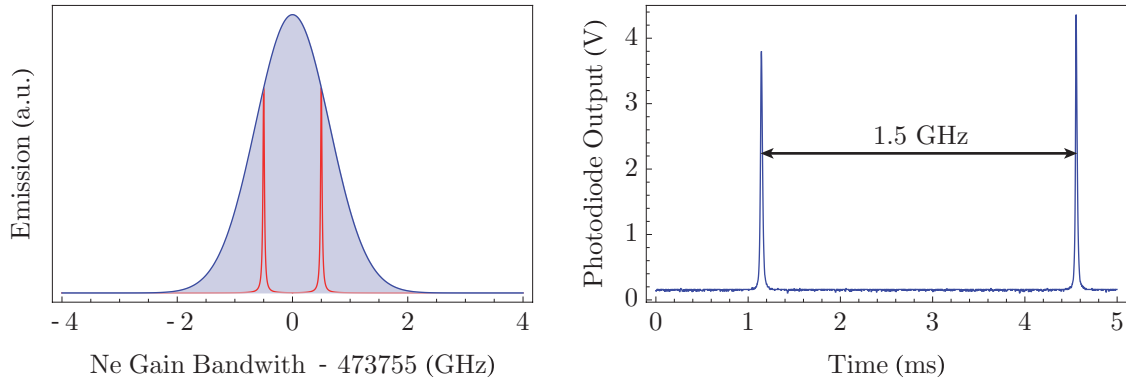
FIGURE 3.4: Left: Two axial cavity modes (red lines) under the gain bandwidth of neon. Right: Oscilloscope trace of the transmission of the Ti:Sapphire laser through the transfer cavity. The scope is triggered by the start of the voltage ramp. By fitting a Lorentzian function we determine the width of the peaks to be $\delta\nu = 8.5\,\text{MHz}$ which corresponds to a finesse $\mathcal{F} = \text{FSR}/\delta\nu = 190$.

turbulent air or draft leads directly to increased frequency noise of the output. A sealed box around the He-Ne tube is therefore obligatory. The stabilised laser beam then passes through an optical isolator and is reflected by another beamsplitter into a confocal cavity (Thorlabs SA200-5B) with a free spectral range of FSR $= 1.5\,\text{GHz}$. We call this the transfer cavity. The length of the transfer cavity is scanned by applying a voltage sawtooth (0-10 V, with a variable offset) to a piezoelectric transducer which is attached to one mirror. This voltage ramp is supplied by a ramp generator (TTI-TG210) at a rate of 100 Hz. When the cavity is on resonance with the He-Ne laser the light is transmitted through the cavity. It is then reflected by a second beamsplitter and focused onto a photodiode (see figure 3.3).

A small fraction of the Ti:Sapphire laser beam is redirected by a glass plate oriented near Brewster's angle and sent through the same transfer cavity onto a second photodiode. The ramp and the amplified output voltages from the two photodiodes are then read into the computer via a data acquisition card (NI PCI 6024E). A piece of software, mainly developed by Sean Tokunaga, then plots the signal from each photodiode against the ramp voltage. When the cavity is on resonance ($L = n\lambda/2$ with n an integer and λ the wavelength) either with the stabilised He-Ne laser or the Ti:Sapphire laser we register a transmission peak. An oscilloscope trace of the Ti:Sapphire transmission is shown in figure 3.4. The software fits a Lorentzian function to each photodiode signal and finds the centre of the transmission peaks. It then calculates the difference between the two ramp voltages at which the He-Ne and Ti:Sapphire transmissions peak. This difference is kept constant by feeding back to the Ti:Sapphire frequency.

Using this technique we can lock the Ti:Sapphire frequency to the CH transition frequency for a whole day. The software further allows to accurately scan the laser with respect to the stabilized He-Ne and to apply very precise detunings.

Small temperature fluctuations can cause drifts of the transfer cavity length. This changes the voltage corresponding to a He-Ne peak. Since the Ti:Sapphire has a different wavelength to the He-Ne the voltage change due to the temperature fluctuations is slightly different for

the two lasers by a factor of $\lambda_1^2/(2\epsilon) - \lambda_2^2/(2\epsilon)$, where λ_1 and λ_2 are the wavelengths of the He-Ne and Ti:Sapphire laser respectively and ϵ is the small length change due to temperature fluctuations. This makes it necessary to lock the transfer cavity first to the He-Ne laser before the Ti:Sapphire laser can be locked to the He-Ne laser via the transfer cavity. This can be achieved by adding a variable offset to the ramp voltage. This offset is adjusted such that the voltage at which the He-Ne peak appears is always constant.

3.3.2 The Detector

Next, we need a detector that is able to efficiently count the number of emitted photons from the molecules. Photomultiplier tubes (PMTs) are commonly used as such photo detectors. The high gain, low noise and fast response time make them to ideal detectors for our purposes. We use the R928P model from Hamamatsu which uses a multialkali photocathode which is made from a mix of sodium, potassium, antimony and caesium. This gives it a very large spectral response between 185 nm and 900 nm which peaks at approximately 400 nm. When a photon hits the photocathode it releases an electron with an efficiency of 20 %. This photo-electron is accelerated into a dynode which is held at a large positive voltage. The single electron with its large kinetic energy gets multiplied by secondary electron emission from the dynode. After eight more multiplying stages the initial single electron has been multiplied to 10^7 electrons. Finally the bunch of electrons reaches the anode where the sudden accumulation of charge results in a sharp current pulse indicating the arrival of a photon at the photocathode. For a typical anode rise time of 2 ns the current pulses can be as high as 0.7 mA. The small active area of $8 \times 20\, \text{mm}^2$ makes it necessary to construct an imaging system that covers a large solid angle. A sketch of the detection chamber with the containing collecting optics is shown in figure 3.5. We use a spherical mirror (Melles Griot 01MCG023) of diameter 90 mm and focal length of 30 mm, and two aspheric condenser lenses (Comar 55AF73) of diameter 73 mm and focal length of 55 mm. The mirror and one of the lenses are rigidly attached to the DN200CF top flange of the detector chamber. The second lens is mounted inside the PMT assembly outside the vacuum chamber. The optical elements are arranged such that a 1:1 image of the fluorescing gas pulse is formed at the position of the photocathode. The detector covers a total solid angle of 1.27 steradians.

The PMT output can be connected to a fast amplifier in combination with a fixed-threshold discriminator. The use of a discriminator ensures that only current pulses of a certain amplitude are counted as photons and thus gets rid of most of the background noise. It also converts each current pulse into a TTL pulse which is fed into a computer via a data acquisition card (NI PCI-6251). This is known as photon counting mode and is useful for detection at low count rates below 1 MHz. If the photon rate is too high the individual pulses cannot be distinguished any more and the output appears as a constant current. The photon counting mode saturates
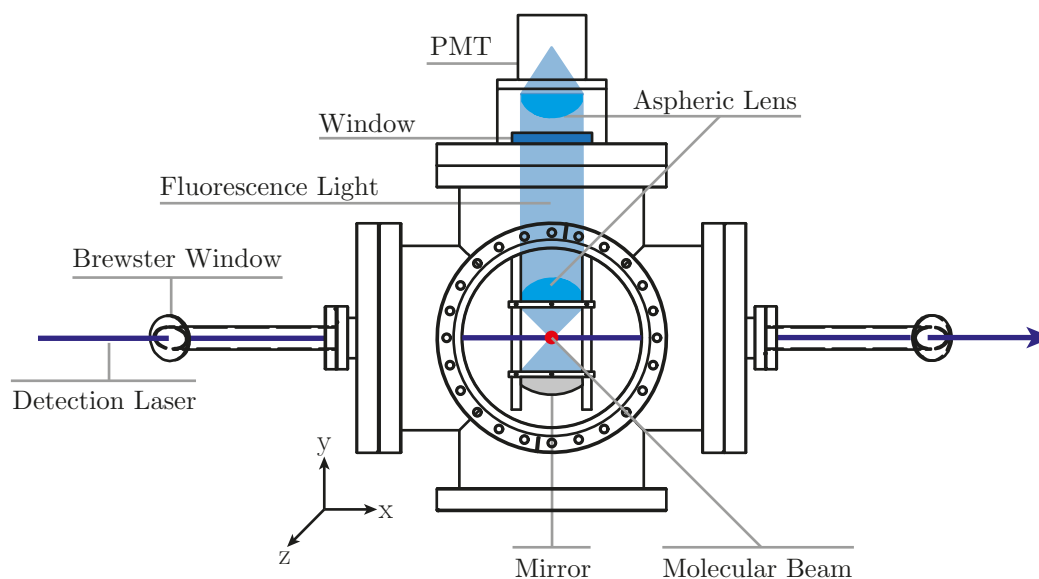
FIGURE 3.5: A sketch of the detection chamber and light gathering optics.
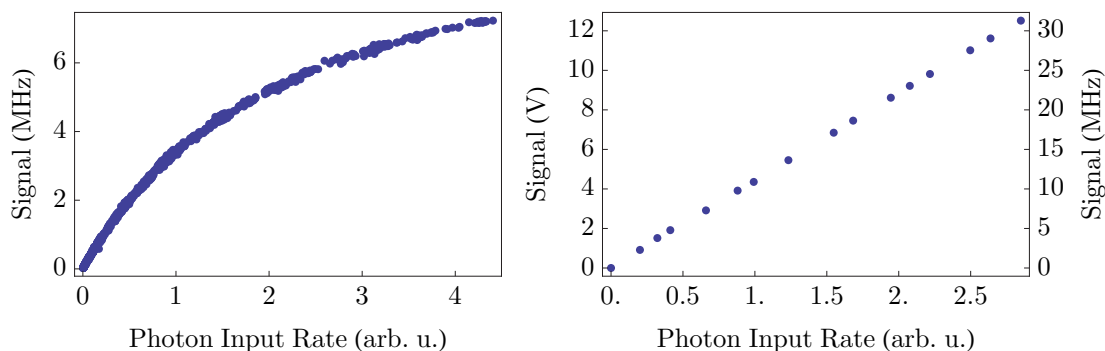
FIGURE 3.6: Left: Measured count rate versus photon input rate, showing that the photon counting mode saturates at high count rates. Right: Measured output current (converted to a voltage and amplified) versus photon input rate showing that in current mode the output of the PMT remains linear even for high count rates.

as shown in figure 3.6. This continuous current is still proportional to the incoming photon flux and can be converted into a voltage, amplified and read by the computer via the data acquisition card. This is what is known as operating the PMT in current mode. In figure 3.6, on the right, the output of the PMT in current mode is shown. In contrast to the photon counting mode it starts to saturate only for very high count rates, that exceed 100 MHz. There exists a large enough overlap between the two operating modes which allows us to calibrate the current mode against the photon count mode. Once the exact detection efficiency is determined we can relate the number of photons detected to the number of molecules in the detection volume.

3.3.3 Detection Efficiency

We can now estimate the total efficiency of our detector hardware. We measured the transmission through the lenses and the window at the detection wavelength to be $T_l = 0.96$ and $T_w = 0.95$ respectively. The reflectivity of the mirror is given by $R \gtrsim 0.87$ and the quantum efficiency of the PMT is $Q(430\,\mathrm{nm}) = 0.2$. Because the photo cathode can degrade over time we measured the quantum efficiency with a calibrated light source and detector to verify the number. All these factors with the solid angle covered by the first lens $\Omega = 1.3\,\mathrm{sr}$ can be put together into an overall wavelength dependent detector sensitivity

$$\epsilon = \frac{\Omega}{4\pi}(1 + R)T_l^2 T_w Q(\lambda) = 0.03\,. \tag{3.4}$$

We have also checked the alignment of the imaging system by imaging a light source (LED) fixed at the position where the detection laser crosses the molecular beam. Although all of the factors in equation 3.4 are slightly wavelength dependent, the main wavelength dependence is in the quantum efficiency of the PMT. In certain circumstances it is useful to use a filter in front of the PMT, which has to be accounted for in equation 3.4.

In addition to the detector efficiency, we also need to know how many photons are scattered by each molecule after excitation with the detection laser. In general, the number of photons emitted by a molecule after excitation depends strongly on molecular properties such as the electronic transition probability, the Franck-Condon factors, the rotational line strength and the intensity of the probe laser. All these factors have to be accounted for which involves a rather long and elaborate description. Such a detailed description can be found in [116, 117] and thus only a brief outline is given here.

We will consider a three level system where level 1 is the ground state of the molecule, level 2 is the electronically excited state, and level 3 represents all other relevant states of the molecule interacting with laser light. First, however we start with the description of a 2 level system. This is described by the usual optical Bloch equations (consult Foot's book, for example [118]):

$$\frac{d\tilde{\rho}_{22}}{dt} = -\frac{d\tilde{\rho}_{11}}{dt} = -\frac{1}{2}i\Omega\left(\tilde{\rho}_{12} - \tilde{\rho}_{21}\right) - \Gamma\tilde{\rho}_{22}\,, \tag{3.5}$$

$$\frac{d\tilde{\rho}_{12}}{dt} = -\frac{d\tilde{\rho}_{21}^*}{dt} = -\frac{1}{2}i\Omega\left(\tilde{\rho}_{11} - \tilde{\rho}_{22}\right) - \left(\frac{\Gamma}{2} - i\delta\right)\tilde{\rho}_{12}\,, \tag{3.6}$$

where $\tilde{\rho}_{11}$, $\tilde{\rho}_{22}$ are the populations of levels 1 and 2, $\tilde{\rho}_{11}$, $\tilde{\rho}_{22}$ are the coherences, Ω is the Rabi frequency and Γ is the damping rate. These equations are a set of coupled differential equations that tell us the exact temporal evolution of the population in each state of the system under the influence of an external oscillating light field. We can simplify the equations further by assuming that the coherences reach a steady state on the time scale of the excited state lifetime, which is short compared to the interaction time of the molecules with the laser. Setting $d\tilde{\rho}_{12}/dt = 0$,

the equations reduce to

$$\frac{d\tilde{\rho}_{22}}{dt} = \frac{\Gamma\Omega^2}{\Gamma^2 + 4\delta^2}\left(\tilde{\rho}_{11} - \tilde{\rho}_{22}\right) - \Gamma\tilde{\rho}_{22}\,. \tag{3.7}$$

We can now identify a laser excitation rate $R = \frac{\Gamma\Omega^2}{\Gamma^2+4\delta^2}$ and rename the state populations N_1 as the population in the ground state and N_2 the population in the excited state. The rate equation for the excited state then becomes

$$\frac{dN_2}{dt} = R\left(N_1 - N_2\right) - \Gamma N_2\,. \tag{3.8}$$

Another useful definition is the on-resonance saturation parameter

$$s_0 = \frac{I}{I_s} = \frac{2\Omega^2}{\Gamma^2} \tag{3.9}$$

where I is the intensity of the laser and $I_s = \epsilon_0 c\hbar^2\left(\Gamma/2\right)^2/d^2$ is the saturation intensity. Here $d = \left\langle 1\left|\hat{\mathbf{d}}\cdot\mathcal{E}\right|2\right\rangle$ is the matrix element of the electric dipole operator in the direction of the polarisation of the light. It is at the saturation intensity that the laser excitation rate starts to exceed the spontaneous decay rate Γ or where the Rabi frequency Ω becomes comparable to Γ.

A molecule, however is slightly different from a two-level system. The cycle is usually not closed because of leakage to other vibrational or rotational states in the electronic ground state. We call these levels collectively state 3 which is a dark state, because the laser does not address this level. We further assume that the decay to the ground state from level 3 is much longer than the time scale of the laser-molecule interaction. If the laser excites the molecule from level 1 to level 2, there are now two ways it can decay: either back to level 1 at a rate $r\Gamma$, with r the branching ratio, or to level 3 at a rate $(1-r)\Gamma$. Including this second decay channel the rate equation model becomes

$$\begin{aligned}
\frac{dN_1}{dt} &= -RN_1 + r\Gamma N_2 + RN_2 \\
\frac{dN_2}{dt} &= R\left(N_1 - N_2\right) - r\Gamma N_2 - \left(1-r\right)\Gamma N_2 \\
\frac{dN_3}{dt} &= \left(1-r\right)\Gamma N_2\,.
\end{aligned} \tag{3.10}$$

To get the number of fluorescence photons per molecule, n_p, we solve the coupled equations 3.10 for N_2 and integrate ΓN_2 over the laser interaction time τ [117]. The result is

$$n_p = \frac{R\Gamma}{R_+ - R_-}\left(\frac{e^{-R_+\tau}-1}{R_+} - \frac{e^{-R_-\tau}-1}{R_-}\right)\,, \tag{3.11}$$

where

$$R_\pm = R + \Gamma/2 \pm \sqrt{R^2 + rR\Gamma + \Gamma^2/4}\,. \tag{3.12}$$

Finally we account for the transverse velocity distribution of the molecular. This velocity distribution leads to Doppler broadening of the resonance linewidth $\Delta f_D = f\alpha v/c$, where f is the centre transition frequency, α is the full divergence angle of the molecular beam, and c is the speed of light. The divergence angle of the beam is mainly set by the distance of source to the skimmer, the size of the skimmer aperture the detector size and the spatial extent of the source. For typical parameters of our beam apparatus this amounts to a full divergence angle α of 20 mrad which corresponds to a Doppler broadening of the resonance width (FWHM) of 50 MHz. We verify this by scanning the laser frequency across the resonance. In order to account for this Doppler broadening we average the number of photons per molecule n_p over a Gaussian distribution with a FWHM of $\Delta f_D = 50$ MHz,

$$\bar{n}_p = \frac{\int_0^\infty n_p \exp\left[-\frac{(8\ln 2)\delta^2}{8\pi^2 \Delta f_D^2}\right] \mathrm{d}\delta}{\int_0^\infty \exp\left[-\frac{(8\ln 2)\delta^2}{8\pi^2 \Delta f_D^2}\right] \mathrm{d}\delta} \ . \tag{3.13}$$

We can now use this model to predict the number of photons the molecules scatter when they pass through the detection laser. Initially, we detected CH by exciting the $Q_2(1/2)$ line of the $B^2\Sigma^-(v'=1) \leftarrow X^2\Pi(v=0)$ transition near 366 nm and detected the Stokes shifted fluorescence of the ($v'=1 \rightarrow v''=1$) band near 403.5 nm. This allowed us to use a filter in front of the PMT that blocks any scattered light from the detection laser. Note that the filter used has a transmission of 0.5 at 403.5 nm which has to be accounted for in equation 3.4. We switched later to the $A^2\Delta(v=0) \leftarrow X^2\Pi(v=0)$ near 431 nm where our laser system is more efficient and we thus get more laser power which we needed for subsequent experiments[1]. Due to the large Franck-Condon factor of this transition the majority of the population decays back into the vibrational ground state which prevents the use of interference filters. For the B-X transition $\Gamma = 2.4$ MHz, the electronic part (see previous chapter) of the transition dipole moment $d_e = 0.271\,e\,a_0$, where e is the charge of the electron and $a_0 = 0.529 \times 10^{-10}$ m is the Bohr radius. In order to calculate the full transition dipole moment we need to include the vibrational and rotational part as well (see previous chapter). The Franck-Condon factor accounts for the vibrational part and is 0.1 for this transition. For the rotational or angular part we need to evaluate the 3J-symbol for the specific transition and sum over the different M sub-levels in the final J-state. This amounts to a factor of 0.45 in the branching ratio r. Hence the total transition dipole moment, including the vibrational and angular part becomes $\sqrt{0.1 \times 0.45 \times d_e^2} = 0.05\,e\,a_0 = 4.9 \times 10^{-31}$ C m $= 0.13$ D. This yields a saturation intensity $I_s = 177$ W m^{-2} which corresponds to 3.2 mW of laser power for a beam size of 6×3 mm^2. If we put these numbers into our model we expect on average 0.1 photon per molecule if the laser intensity is set to the saturation intensity I_s and the molecules are travelling at a speed[2] of 820 m s^{-1}, which corresponds to an interaction time of $\tau = 3.7\,\mu$s. Figure 3.7 on the left shows

---

[1]We also wanted to rule out a potential pre-dissociation in the B state which would decrease the CH signal.

[2]This is the velocity we measured for a particular molecular source. How we measure this and why the molecules are moving with that particular velocity will be explained in the next section
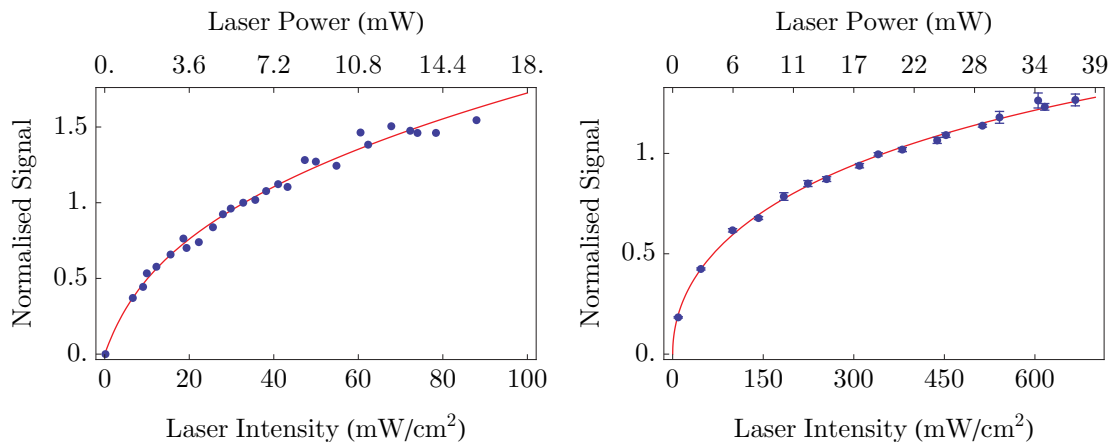
FIGURE 3.7: Left: CH signal plotted as a function of the probe laser intensity for the X-B transition (blue dots). The solid red line is a plot of equation 3.13 using the experimental data mentioned in the text. The model is normalised such that $\bar{n}_p = 1$ at $33\,\mathrm{mW\,cm^{-2}}$. Right: The same data as on the left but for the A-X transition. The model is normalised to $\bar{n}_p = 1$ at $350\,\mathrm{mW\,cm^{-2}}$.

a plot of the CH signal as a function of the probe laser intensity. Note that there are no fitting parameters used. The model is normalised to 1 for a laser intensity of $33\,\mathrm{mW\,cm^{-2}}$. The model shows striking agreement with the data and thus can accurately predict the number of photons we expect on average per molecule.

Knowing the number of photons we expect per molecule for a given transition, the transmission and solid angle subtended by the light-gathering lens, the reflectivity of the mirror and the quantum efficiency of the photomultiplier tube we can estimate our total detection efficiency for the $B^2\Sigma^-(v = 1) \leftarrow X^2\Pi(v = 0)$ transition to be $\bar{n}_p \cdot \epsilon = 0.15\%$ for a laser intensity of $177\,\mathrm{W\,m^{-2}}$ and an interaction time of $3.7\,\mathrm{\mu s}$.

The A state has a slightly longer lifetime of $540\pm5\,\mathrm{ns}$ as compared to the B state. So the natural linewidth Γ is $1.85\,\mathrm{MHz}$ and the electronic transition dipole moment is $0.294\,e\,a_0$. The Franck-Condon factor for this transition is 0.9913 and the rotational factor is 0.3. This gives a total transition dipole moment, including the vibrational and angular part of $D = 0.17\,e\,a_0 = 1.4 \times 10^{-30}\,\mathrm{C\,m} = 0.43$ D. The saturation intensity $I_s = 12.3\,\mathrm{W\,m^{-2}}$. Using these numbers we expect on average 0.2 photons per molecule for molecules travelling at a speed[3] of $570\,\mathrm{m\,s^{-1}}$ with a laser intensity of $71\,\mathrm{mW\,cm^{-2}}$ ($5\,\mathrm{mW}$ in a $0.4{\times}0.15\,\mathrm{cm^2}$ beam). For this transition we did not use any filter because the majority of the fluorescence stems from light of the same wavelength as the laser excitation. The comparison of the experimental data and the model is shown on the right of figure 3.7. This yields a total detection efficiency for the X-A transition of $\bar{n}_p\epsilon = 0.6\%$.

---

[3]The X-A data was taken with a different source and thus a different velocity.

3.4 The Ultimate Guide to Sources for the CH Molecule

By the 1950s molecular beams were still produced in the very same way as Dunoyer invented the technique in 1911 (see introduction). The apparatus consisted of a gas supply chamber, or source chamber, which was separated from the rest of the beam machine by a slit. The gas molecules in the source chamber have a Maxwellian velocity distribution and simply effuse through a slit into the science chamber. In 1950 Arthur Kantrowitz and Jerry Grey proposed that if one places the slit in the flow by a miniature supersonic nozzle similar to the ones used in steam turbines or rocket engines one can produce molecular beams of very high intensity [119]. An isentropic expansion through the nozzle converts most of the random translational and internal energy of the source chamber gas into directed motion. They realised that such a beam has a narrow velocity distribution and high average velocity.

In thermodynamics an isentropic expansion is both an adiabatic and reversible process with no change in the total entropy of the system. Hence there is no loss due to friction or dissipative processes but both the temperature and the pressure of the gas change due to the expansion of the gas. This leads to very efficient cooling of the gas molecules and thus reduces population in excited rotational and vibrational states. Kistiakowsky and Slichter implemented the Kantrowitz-Grey technique experimentally [120]. However, due to the limited pumping capacity available at that time they achieved only a partial success. Becker and Bier were the first to report experimental evidence that the Kantrowitz-Grey technique indeed works [121]. Otto Hagena showed in 1963 that the use of commercially available electromagnetic valves, in particular injection valves of combustion motors to modulate the molecular beam results in improved beam characteristics compared to the continuous type [122]. Pulsed supersonic beams produce higher densities, colder internal state distributions and a narrower velocity distribution. Furthermore, the use of such pulsed beams reduces the total gas load and thus the high pumping speeds required for nozzle beams. A wide variety of pulsed valves have been developed since. We tested three different valve types which will be described later in more detail. Modern valves can generate intense gas pulses with a peak particle number of 10^{16} in pulses as short as $7\,\mu s$. This corresponds to a beam brightness of $10^{22}\,\mathrm{sr}^{-1}\,\mathrm{s}^{-1}$ [123]. Such short pulses make it possible to design a very compact molecular beam apparatus with high quality supersonic beams.

3.4.1 How to Produce a Supersonic Beam of Diatomic Radicals

Interest grew over the decades to produce molecular beams of ever more species. Until the end of the 1970s only gases with a high enough vapour pressure allowed for a high enough pressure behind the valve to produce a supersonic beam. Abauf et al. [124] conceived the idea of seeding small concentrations of the molecular species of interest into an inert carrier gas to create intense beams of a large variety of complex and heavy molecules. It turns out that even for

fractions as low as 1% the supersonic beam still outperforms the traditional effusive source in terms of number density, velocity spread and temperature. In 1969 Miller and Patch combined the seeding technique with a high frequency gas discharge to create an intense supersonic beam of oxygen atoms by using a mixture of 5% O_2 in helium [125]. The first to combine a DC glow discharge with a nozzle type source was Searcy in 1974 [126]. He produced an intense beam of excited helium atoms this way. In the same year Larsen et al. succeeded to produce supersonic beams of alkali atoms [127] based on the seeding technique of Abauf et al. In 1976 Valentini and co-workers combined a high temperature oven with a graphite nozzle to thermally dissociate halogen molecules and create atomic beams of chlorine, bromine and iodine [128]. Such a heated nozzle is a very versatile technique to produce atoms and radicals. The hot nozzle, however, also leads to a very hot beam with a wide velocity distribution.

High frequency discharges only work for very low gas pressures and thus cannot make use of the full supersonic expansion cooling. Moreover, the DC glow discharge developed by Searcy is generally prone to arc discharges in a high pressure gas environment which has severe effects on the radical production efficiency. In 1983 Droege and Engelking developed a simple corona discharge source in order to circumvent the problems of these earlier discharge sources [129, 130]. A corona discharge is the low current version of an arc discharge where a high voltage is applied to a wire of small diameter which is inserted into a gas flow tube and ends just behind the nozzle aperture. When gas is present at the nozzle a small corona discharge forms. Droege and Engelking produced the OH radical using this method by dissociating a mix of 20 mbar of water in 4 bar of helium and the NH radical by dissociating NH_3. They observed the remarkable effect that the rotational temperature of the molecules decreased to only 11 K but that the vibrational temperature only to 3400 K. This indicates that the various degrees of freedom do not reach thermal equilibrium.

In parallel to the development of these early discharge sources for supersonic beams people realised that one could use intense light pulses to dissociate precursor molecules via a process called photolysis. This foundation of using light to induce and study photochemical reactions can be traced all the way back to 1949 to the work of Manfred Eigen, Ronald Norrish and George Porter who invented the technique of flash photolysis in that year [131]. They were awarded the Nobel Prize in Chemistry in 1967 for "their studies of extremely fast chemical reactions, effected by disturbing the equilibrium by means of very short pulses of energy". Back in the 1940s they used simple gas-discharge flash-lamps that were developed for photographic purposes to induce these photochemical reactions. By using a 1 m long tube with large tungsten electrodes they could produce 10^4 J in a 4 ms flash. The flash lamps were later replaced by pulsed gas lasers such as the nitrogen laser and finally excimer lasers which became commercially available by 1977. Excimer is a portmanteau of "excited dimer" and refers to the role of the active medium in such a laser. It typically uses a combination of a noble gas (Ar, Kr or Xe) with a reactive halogen gas (F, Cl). An electrical discharge excites and ionises the Ar atoms and dissociates the F_2 molecules into excited or ionised F atoms. The excited or ionised Ar

and F atoms form an excited dimer ArF which has a lifetime of approximately 10^{-8} ns. In the ground state the molecule dissociates very quickly into its constituents which guarantees a large population inversion. Depending on the gas mix that is used different output wavelengths can be generated. Early work concentrated on the photolysis studies in low pressure spectroscopy cells until Monts and co-workers applied the technique to create supersonic beams of the highly reactive methylene radical (CH_2) [132]. They focused the 337 nm light of a pulsed N_2 laser beam onto a pulsed supersonically expanding mix of 1% ketene (CH_2CO) in 3 bar of helium in order to produce CH_2. This marked a big breakthrough because it was the first time that unstable molecules or free radicals had been produced in a cold supersonic free jet expansion. In 1981 Heaven and his colleagues used for the first time the output of an ArF excimer laser to create a supersonic beam of SH and CN radicals by photolysis of hydrogen sulfide (H_2S) and BrCN respectively. They detected the products via laser induced fluorescence and could clearly show the versatility of this method and how useful cold spectra of radicals can be, i.e. the improved signal-to-noise ratio and resolution compared to spectra recorded at ambient temperatures in a spectroscopy cell.

All these sources still rely on a stable precursor that has a reasonable vapour pressure at a manageable temperature. Interest grew, especially in the analytical chemistry community, to analyse nonvolatile organic molecules. Various groups came up with ideas on how to bring the molecules into the gas phase. The most successful one has been suggested by Posthumus and associates in 1978 [133]. They coated the molecules onto a stainless steel probe which was placed under vacuum into a mass spectrometer. They then focused a pulsed laser onto the target and the resulting ablation plume was analysed in a mass spectrometer. To most people's surprise the fragile organic molecules survived the violent ablation process and thus could be analysed. It took not very long that this idea of ablating a solid precursor as a means to produce a supersonic jet would be picked up in the physical chemistry community.

This was mainly motivated by the fact that people wanted to study complex metal clusters and designed ever more sophisticated ovens combined with supersonic nozzles to produce continuous cluster beams of nearly any metal. These ovens were very challenging to operate and suffered from many disadvantages. By the early 1980s Vladimir Bondybey and Richard Smalley independently conceived the idea of laser ablation of the metal into a supersonically expanding helium carrier gas [134]. Smalley mounted a reaction channel onto the pulsed valve which increased the carrier gas density around the laser ablation plume in order to cool the atoms back to room temperature where the condensation into clusters begins. By varying the length of this nozzle channel he could even control the extent of cluster formation. At the end of this channel the mixture supersonically expands into the vacuum chamber and leads to a cold, collision-free and well-collimated beam of metal clusters. Later in 1985 Smalley and his group, while at Rice University in Houston, Texas, used the very same technique with graphite as a target in order to study carbon clusters. By analysing the mass distribution of their cluster beam they found a very pronounced peak at a mass of 60 carbon atoms and another smaller one at a mass of

70 carbon atoms. They had discovered a very intriguing new form of carbon the Buckminster-fullerenes, for which Kroto, Curl and Smalley received the Nobel Prize in Chemistry 1996.

Simard et al. showed that the technique of laser vaporisation in combination with supersonic cooling can also be used to produce very intense molecular beams and achieve very low temperatures and thus very high resolution spectra for molecules such as ZrO [135]. Before the invention of the laser desorption technique people relied on high source temperatures for molecular radicals such as ZrO. Arcs, ovens, exploding wires, flames or discharges were used to produce these radicals at very high temperatures which led to extremely complex spectra and suffered from very low concentrations of the species of interest. These hot sources resulted in broad spectra which prevented the investigation of small effects such as hyperfine interactions and interactions with external fields.

Simard et al. produced these high temperatures by focusing the beam of a XeCl excimer laser onto a rotating Zr rod. A mixture of 0.2% of molecular oxygen in 3.6 bar of helium expands through a pulsed valve into the ablation plasma. The vaporised Zr atoms then react with the oxygen molecules to form the diatomic species ZrO. The supersonic expansion efficiently cools the products from more than 10^4 K to very low temperatures of only a few K. Other groups immediately realised the importance and underlined the versatility of such a laser evaporation source which allowed them to study a wide range of small molecular radicals with great accuracy [136, 137]. Using this technique Ebben and colleagues produced and detected many different molecules: CuH, CH, SiH, CuO to FeO to name a few. These radicals are of great interest to chemists and physical chemists in order to understand fundamental chemical processes. Hence detailed knowledge about their electronic structure and therefore their electronic spectra was needed and were now accessible through the invention of this technique. Many other molecules followed soon after.

By the mid 1990s the group of John Doyle at Harvard University took this idea a step further: They surrounded the target by a copper box ($V \approx 1\,\text{cm}^3$) which was connected to a cold plate (4 K) of a helium cryostat. The box is filled with helium gas which thermalises with the cold walls of the copper box. This has two major advantages: First the temperature of the carrier gas is reduced to cryogenic temperatures which results in a slower molecular beam as compared to the traditional supersonic beam. This will be discussed in more detail in the next section. Second by using hydrodynamic effects one can extract a large fraction of the ablation plume into a molecular beam through an aperture in the box. This can boost the overall flux by up to two orders of magnitude as compared to the supersonic source. This simply stems from the fact that the interaction volume between the carrier gas and the ablation plume is much larger. However, the typical temporal width of such an extracted pulse of molecules is 10 - 100 times wider. This is mainly because the width is now not limited by the duration of the pulsed valve but rather by the time it takes to sweep the molecules out of the cell. This technique works well for solid targets that can be attached to the inside of the copper box. If one wants to introduce gaseous precursors or even liquids it becomes more challenging because of ice that forms at the

extraction hole and on the cell walls.

We tried nearly all of the techniques described above to produce an intense beam of CH molecules, but before I describe the various sources in more detail a brief description of the supersonic expansion is presented.

3.4.2 Supersonic Expansion

Early experiments showed that the simple model of adiabatic isentropic expansion introduced by Kantrowitz and Grey is sufficient to describe a supersonic beam very accurately [119]. This means that effects like the viscosity of the gas and heat transfer can be safely neglected.

Such a source consists of a high pressure region which is typically filled with an inert gas to a pressure p_0 at a temperature T_0. A small aperture connects this high pressure region with the source chamber which is evacuated by vacuum pumps to a very low pressure p_1. The pressure difference leads to a steady flow of the gas from the high pressure reservoir into the low pressure chamber at a flow velocity v. The flow is driven by a pressure gradient, so the correct thermodynamic potential to describe the system is enthalpy H which is defined as the total internal energy (rotation, vibration, kinetic energy of the gas particles) U plus the energy required to make room for the system pV where p is the pressure of the system and V its volume:

$$H = U + pV \, . \tag{3.14}$$

In differential form this can be written as

$$\Delta H = \Delta U + p\Delta V + V\Delta p \, . \tag{3.15}$$

The first law of thermodynamics tells us that a change in the internal energy of the system is equal to the heat added to the system Q minus the work done by the system W:

$$\Delta U = Q - W \, . \tag{3.16}$$

We do not add any heat to our system so $Q = 0$ and the work done by the system is $W = p_1 V_1 - p_0 V_0$. The work done by the system also creates the mass flow between the chambers which results in a kinetic energy of the gas of $\frac{1}{2}mv^2$, where m is the total mass of the gas flowing through the nozzle with a velocity v. The total change in internal energy is thus

$$\Delta U = -(p_1 V_1 - p_0 V_0) - \frac{1}{2}mv^2 \tag{3.17}$$

At this point it is useful to introduce the internal energy $u = U/m$ and enthalpy $h = H/m$ per unit mass. Using $\Delta u = u_1 - u_0$ and equation 3.15 the change in enthalpy is

$$\Delta h = -\frac{1}{2}v^2 \,. \tag{3.18}$$

In our sources we are mainly using monatomic inert gases such as He, Ne, Ar and Kr. Thus we can approximate the gas as an ideal gas with $pV = NRT$, where N is the amount of gas in moles and R is the universal gas constant. Both the enthalpy $h = c_p T$ and the internal energy $U = c_v T$ are then only a function of the temperature T. The rates at which these quantities change with temperature are called the specific heat capacity at constant volume $c_v = du/dT$ and the specific heat capacity at constant pressure $c_p = dh/dT$. This allows us now to relate the change in internal energy Δu due to the isentropic expansion to a change in temperature.

$$\Delta u = \int_{T_1}^{T_0} c_v \, dT \tag{3.19}$$

$$\Delta h = \int_{T_1}^{T_0} c_p \, dT \tag{3.20}$$

Furthermore, we can express the velocity of the gas pulse as a result of the pressure gradient between the two chambers as a function of the temperature by using equations 3.18 and 3.20 to

$$v = \sqrt{2c_p(T_0 - T_1)} \,. \tag{3.21}$$

Instead of using the specific heat at constant pressure it is more common to use the adiabatic ratio $\gamma = \frac{h}{u} = c_p/c_v$ because it is directly related to the degrees of freedom of the atoms/molecules f of an ideal gas $\gamma = 1 + \frac{2}{f}$. The specific heat c_p then becomes

$$c_p = \frac{\gamma}{\gamma - 1}\frac{R}{m_{mol}} \tag{3.22}$$

Where m_{mol} is the molar mass of the gas. We can now express the maximum velocity of the gas after expanding into vacuum as a function of the adiabatic ratio:

$$v = \sqrt{\frac{2R}{m_{mol}}\frac{\gamma}{\gamma - 1}(T_0 - T_1)} \,. \tag{3.23}$$

The most important result here is that the final velocity of the supersonically expanding gas scales with the square root of the temperature of the gas behind the nozzle. This is also the reason why it helps to use a buffer gas cell which is connected to a $4\,\mathrm{K}$ helium cryostat. This lowers the initial temperature and thus results in a beam with a terminal velocity that is about 9 times lower as compared to the room temperature helium beam. Furthermore, we see that the velocity of the gas pulse scales inversely with the mass of gas particles. Thus using heavier gases also results in a slower beam. Characteristic velocities for typical carrier gases used in

room temperature molecular sources such as He, Ne, Kr, Ar and Xe are 1744, 777, 552, 381, $305\,\mathrm{m\,s^{-1}}$ respectively.

Let us now turn to the question what temperatures T_1 we expect the gas to reach after the expansion. There is an alternative way to describe the supersonic expansion which is very useful. This description makes use of the Mach number M, which is the ratio of the average flow velocity of the expanding gas to the local speed of sound. This is also the more traditional way which was introduced by Kantrowitz and Grey and is a very general and elegant way to express all the thermodynamic variables with only two parameters, γ and M. A detailed derivation of this formalism can be found in [138]. The expression for the temperature then becomes:

$$\frac{T}{T_0} = \left(1 + \frac{\gamma - 1}{2}M^2\right)^{-1} . \tag{3.24}$$

Since we are dealing with an expanding gas through a nozzle both the temperature and the Mach number are position dependent. Considering the continuum properties of the expansion and assuming isentropic, compressible flow of an ideal gas with a constant specific heat ratio and by solving the fluid mechanics equations of conservation of mass, momentum and energy an expression for $M(x)$ can be found:

$$M(x) = A\left(\frac{x - x_0}{d}\right)^{\gamma - 1} - \frac{1}{2}\frac{(\gamma + 1)/(\gamma - 1)}{A[(x - x_0)/d]^{\gamma - 1}} , \tag{3.25}$$

where d is the nozzle diameter, which in our case is $0.8\,\mathrm{mm}$, $x_0/d = 0.075$ and $A = 3.26$ are constants of monatomic gases. Using this model we expect that the gas pulse cools to $1.5\,\mathrm{K}$ within $20\,\mathrm{mm}$ and to $0.24\,\mathrm{K}$ within $80\,\mathrm{mm}$ downstream from the nozzle from an initial temperature of $T_0 = 293\,\mathrm{K}$. So we can clearly see how effective the cooling due to a rapid expansion can be. This is why the technique has become the standard technique to generate molecular beams.

It is useful to introduce the ideal free-jet centerline intensity per steradian per second in terms of the nozzle flow rate. This makes it possible to compare our sources to the ideal case and lets us quickly estimate what molecular fluxes we can expect from the different production techniques. It further allows us to find an approximate production efficiency with respect to the ideal supersonic expansion. Beijernick and Verster found an analytical form to describe the mass flow rate out of a nozzle source and found good agreement with experimental results [138, 139]:

$$I_0 = \frac{\kappa \dot{N}}{\pi} , \tag{3.26}$$

with

$$\dot{N} = F(\gamma)n_0\sqrt{\frac{2k_B T_0}{m}}\frac{\pi d^2}{4} \quad \text{and} \quad F(\gamma) = \left(\frac{\gamma}{\gamma + 1}\right)^{1/2}\left(\frac{2}{\gamma + 1}\right)^{1/(\gamma - 1)} , \tag{3.27}$$

where I_0 is the centre-line beam intensity in molecules per steradian per second, $\kappa = 1.98$ is the peaking factor (this factor is 1 for an effusive source), $n_0 = p_0/(k_B T_0)$ is the initial gas density behind the nozzle, k_B the Boltzmann constant, T_0 the temperature of the gas behind the nozzle, m the mass of the gas particles, d the nozzle diameter and $\gamma = 5/3$ for a monatomic gas. For typical parameters in supersonic sources ($p_0 = 4$ bar of argon, $d = 0.8$ mm, $T_0 = 293$ K) this yields an ideal beam intensity of $I_0 = 6.4 \times 10^{21}\,\mathrm{sr}^{-1}\,\mathrm{s}^{-1}$, which translates to $6.4 \times 10^{17}\,\mathrm{sr}^{-1}$ per pulse for a typical pulse duration of 100 µs. Now we know how to describe the expansion and we know what velocity and final temperature we expect after the expansion. In a typical experiment the molecules, however, do not only possess a single velocity but there exists a distribution of speeds in the molecular beam about the central velocity calculated earlier. In our laser induced fluorescence detector this appears as a time-dependent fluorescence signal, which is called the time-of-flight profile. In order to find an expression for this velocity distribution, let's assume a box full of gas which has a temperature T. The distribution of velocities v of the molecules in an interval of v and $v + dv$ can be described by the function found by Maxwell and Boltzmann

$$f(v)\,\mathrm{d}v = Av^2 e^{-\frac{mv^2}{2k_B T}}\,\mathrm{d}v \tag{3.28}$$

where m is the mass of the particle, k_B is the Boltzmann constant, and A is a normalization constant. If we now drill a hole in this box the number of molecules leaving the hole with a velocity in the interval between v and $v + dv$ have a distribution of $F(v) \propto v f(v)\,\mathrm{d}v$. The extra v simply stems from the fact that we want to know the velocity distribution of a flux of molecules out of an aperture. Furthermore, in a beam the velocities are distributed about a centre velocity v_0 which is equivalent to the stream velocity of the gas pulse we calculated earlier. Putting everything together the velocity distribution of the flux of molecules in a molecular beam with a velocity between v and $v + \mathrm{d}v$ is

$$F(v)\,\mathrm{d}v = Bv^3 e^{-\frac{m(v-v_0)^2}{2k_B T}}\,\mathrm{d}v \,. \tag{3.29}$$

Our detector is not detecting velocities directly but rather counts the number of molecules as a function of time, hence the name time-of-flight profile. We should therefore transform 3.29 into a distribution of arrival times [140]

$$h(t)\,\mathrm{d}t = B\frac{L^4}{t_0^5} \exp\left[-\frac{mL^2}{2k_B T t_0^4}\left(t - t_0\right)^2 \right]\,\mathrm{d}t \,, \tag{3.30}$$

with $v = L/t$ and $\mathrm{d}v = -(L/t^2)\mathrm{d}t$, where L is the distance of the detector from the source, $t_0 = L/v_0$ and it is assumed that the spread of arrival times is small compared to the time-of-flight $t \approx t_0$. For many pulsed molecular source types we can safely assume that the source emits an infinitely narrow pulse with no spatial spread [140]. We can see that the spread in the arrival times of the molecules is mainly due to the finite temperature T of the gas pulse.

By fitting to the time-of-flight profile we can extract the full width at half maximum (FWHM) $w = 2\sigma\sqrt{2\ln 2}$ of the pulse, where σ is the standard deviation of the Gaussian distribution in equation 3.30, which is a direct measure of the translational temperature T of the gas pulse

$$T = \frac{\sigma^2 m L^2}{2k_B t_0^4} = \frac{w^2}{8\ln 2}\frac{mL^2}{k_B t_0^4}.$$ (3.31)

By using two well separated detectors one can test if the assumptions in 3.30 that the source produces molecules with zero temporal and spatial spread is justified. For a typical laser evaporation source the error in T by using only one detector has been determined to be of the order of 1% [140]. However, for discharge sources these assumption might not hold any more due to the relatively large volume involved in the discharge process. Hence using one detector sets only an upper limit to the temperature. For an ideal supersonic beam of argon the atoms travel at $552\,\mathrm{m\,s^{-1}}$ and have a translational temperature of $0.25\,\mathrm{K}$ (at the position of the skimmer) which corresponds to a velocity spread of $\Delta v/v_0 = 4\%$. This small velocity spread in combination with the small angular divergence of the beam and the reduced occupation of excited states makes the supersonic source so superior to a conventional, effusive oven source.

A very important figure to estimate the efficiency of the source is the flux of molecules per steradian per second (or per pulse) or the density of the molecules at the detector. The detector registers a photon count rate in MHz within a certain temporal width of the gas pulse. For a supersonic beam of CH molecules in argon we measure photon count rates typically of the order of $\Gamma_p = 10\,\mathrm{MHz}$ in a pulse the FWHM of which is $w = 90\,\mathrm{\mu s}$. So the total number of photons we register per shot is $n_c = \Gamma_p \times \tau = 900$. For the A-X transition we know from the detector calibration that the efficiency is $\bar{n}_p \times \epsilon = 0.6\%$. Hence we detect $N = n_c/(\bar{n}_p\epsilon) = 1.5 \times 10^5$ molecules per shot. This allows us to calculate the flux through the detection area.

The detection area is determined by the height of the laser beam along y and the length of the effective detection area along x. This can either be the size of the PMT along x or the finite spatial acceptance of the imaging system due to vignetting effects. By placing an aperture in front of the PMT one can carefully map the signal as a function of the effective detection area along x. We found that decreasing the PMT aperture along x from 20 to $10\,\mathrm{mm}$ changed the signal only by a few per cent. The background scatter from the detection laser, however, decreased by nearly a factor of 2. We estimate a detection area of $A = 0.5\times 1\,\mathrm{cm}^2$ which corresponds to a solid angle of the detection area of $\Omega_d = A/L^2 = 0.8 \times 10^{-4}\,\mathrm{sr}$, with L being the distance between the nozzle and the detector. The flux per steradian per pulse becomes $\phi = N/\Omega_d = 2.25 \times 10^9\,\mathrm{sr^{-1}}$ per pulse or $\Phi = \phi/w = 2.5 \times 10^{13}\,\mathrm{sr^{-1}\,s^{-1}}$ for a pulse width of $w = 90\,\mathrm{\mu s}$.

What density of molecules in the detection volume does that correspond to? If we assume that 1.5×10^5 molecules pass through the detection area $A = 0.5\,\mathrm{cm}^2$ in a time $t = 90\,\mathrm{\mu s}$ with a velocity $v = 570\,\mathrm{m\,s^{-1}}$ the density is given by $\rho = N/(Avt) = \Phi/(vL^2) = 5.1 \times 10^4\,\mathrm{cm^{-3}}$.

3.4.3 Beams of CH molecules

Studies of the CH molecule as well as the production techniques have a long history and go back as far as the 1920s when early spectroscopic investigations were performed in hydrocarbon flames of a Bunsen burner or discharge lamps. Such lamps consist of a vacuum glass tube that contains two electrodes. The tube is filled with benzene gas and when a high voltage is applied to the electrodes an electric discharge creates bright arcs which can be analysed with spectrometers [141–143]. The analysis of these emission spectra played an important role in the development of our understanding of spectra of diatomic molecules. Later on, more refined techniques evolved to deliberately produce CH for the sole purpose of measuring the spectra more accurately and even measure the lifetimes of its excited states. These systematic approaches to CH production involved electron bombardment of methane, photolysis of diazomethane and methane by means of the intense light of a Xe flash lamp and controlled discharges in Geissler-type tubes.

Herzberg and his colleagues used all these techniques to produce a wide range of diatomic radicals and generated a large amount of spectra this way. Especially the flash-photolysis technique developed in his lab turned out to be extremely fruitful. It consists of two quartz tubes next to each other, about 1 m long and 1 cm in diameter. One tube contains the gas which should be photo-dissociated and analysed and the other tube is used to create an intense flash of light. The flash tube is filled with Xe and dissipated 4800 J (600 μF at 4 kV) in a flash duration of 1.5 ms [144]. After the flash has done its job a second small white-light flash is ignited the light of which is directed through the gas tube containing the photolysis products. The beam which passed through the specimen tube is then analysed with a grating spectrometer. Still, today we rely on the immense amount of spectra taken by Herzberg over 50 years ago using this very method. He was awarded the Nobel Prize in Chemistry 1971 "for his contributions to the knowledge of electronic structure and geometry of molecules, particularly free radicals".

By the end of the 1970s, nearly fifty years after the first spectrum of CH had been recorded there was still interest in the spectroscopy of this molecule. The flash tubes were replaced by excimer lasers. In particular, the photolysis of $CHBr_3$ turned out to be a very efficient way to produce CH in a spectroscopy cell. With the advent of tunable pulsed dye lasers, laser induced fluorescence entered the stage of CH spectroscopy as well [145]. The first pulsed supersonic beam of CH was produced by Shinohara and Nishi in 1982 [146]. They did not intend to produce CH in the first place but rather studied the photo-fragments of acrolein (C_3H_4O). They focused the 193 nm radiation of an ArF excimer laser into the supersonic expansion of pure acrolein and found strong emission of A-X radiation from excited CH molecules.

The first to deliberately create a supersonic beam of CH molecules were Ubachs and colleagues in 1986 using a very different technique [147]. A microwave discharge (100 W, 2.45 GHz) through a mixture of H_2O and O_2 produces hydrogen and oxygen atoms which are flowing into a reaction zone where acetylene (C_2H_2) is added. The authors did not specify the actual reaction that leads to CH formation but do mention that the acetylene has to be added near the

supersonic expansion because the unstable CH molecules would immediately react with other discharge by-products. It is also very interesting that they could not observe any CH production when they used H_2 or O_2 only without adding any H_2O which indicates a quite complicated reaction path.

In 1998 Lindner and colleagues [148] reported the first supersonic beam of CH produced by photolysis of bromoform using $193\,nm$ and $248\,nm$ excimer light. We investigated and characterised this source and it will thus be described in more detail later. In the same year Weibel et al. showed the production of CH via a supersonic corona discharge of 3% CH_4 in argon [149]. The source Weibel and his colleagues used is based on the design by Engelking [130]. We developed a source based on a glow discharge across CH_4 as well which will be described in the following section.

Interest grew to study the fundamental reactions of CH with other molecules, particularly due to the dominant role of CH radicals as an intermediate step to create air pollutants such as nitrogen and carbon oxides via the combustion of hydrocarbon fuels. The production methods described so far, however, always led to other radicals of precursor material as well which had substantial influence on the measured reaction rates. This need to produce pure molecular beams free of any other by-products led to the invention of sophisticated sources in combination with manipulation techniques using electric and magnetic fields. An attempt to build such a clean, high intensity source of CH was reported recently by the group of Kasai and Ohoyama from the University of Kyoto [150]. They developed a very unique type of source which is based on a well known chemical reaction. We have built and characterized this source as well and it will thus be described in more detail. But let me first introduce the general source hardware which most of the sources we built share.

3.4.4 Source Hardware

The heart of the source is a pulsed valve. It is a General Valve Series 99 with a $0.8\,mm$ diameter orifice. It is actuated by passing a current pulse through a solenoid which exerts a magnetic force onto a ferromagnetic armature. A spring inside the armature pushes it back after actuation and seals the orifice with a PTFE poppet attached to it. A homebuilt voltage supply is triggered by the computer control and sends a voltage pulse of typically $230\,V$ with a duration of $150\,\mu s$ to the valve's solenoid. The valve then opens and releases a gas pulse with a typical FWHM of $250\,\mu s$.

The valve is rigidly attached to a translational valve assembly which allows to position it within the source chamber with high accuracy. The special design of this valve assembly allows further to optimize the valve position in x and y while the source is running under vacuum. In order to change the z-direction, i.e. the distance between the skimmer and the valve the chamber must be vented and the distance adjusted.
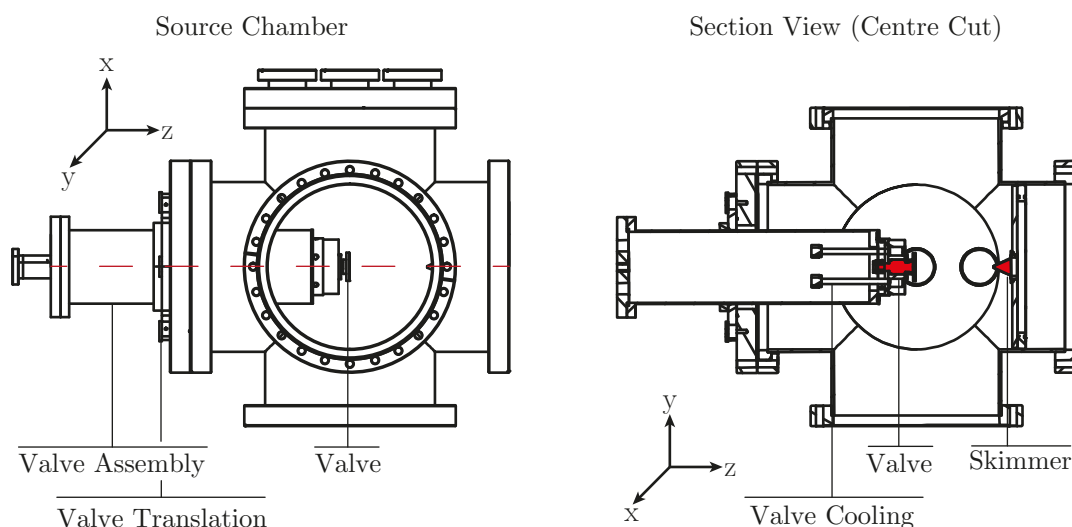
FIGURE 3.8: Left: A detailed view of the source chamber. Right: A section view through the centre which reveals the skimmer assembly.

At a later stage of the experiment this valve assembly was replaced by an ultra high vacuum compatible XYZ-stage (VG Scienta Miniax XYZ) which allows for even more accurate valve positioning and very precise measurements of the CH flux as function of the valve-to-skimmer distance.

3.4.5   A Glow Discharge Source for Producing CH Molecules

Until high intensity pulsed lasers became available one of the most widely used tools for generating radicals for spectroscopic purposes was based on electrical discharges. Engelking and co-workers pioneered the technique of combining an electrical discharge with a supersonic expansion. This allowed to greatly simplify the spectra of molecular radicals decreasing the congestion by hot vibrational bands and thermal excitation of rotational levels. Davis et al. then took this idea further and applied it to the pulsed supersonic jet [151]. Furthermore, they replaced the corona discharge by an intense glow discharge. The corona discharge typically extended into the expansion region of the gas pulse which caused additional heating and chemical degradation of the species of interest. The glow discharge on the other hand is ignited in a very short discharge channel (1 mm) in a high gas density. The radical precursors thus only spend a few µs in the discharge environment which is too short for gas kinetic radical-radical reactions. After the production all the reactions freeze out in the supersonic expansion and Davis and colleagues could measure densities of OH molecules as high as $8 \times 10^{12} \, \text{cm}^{-3}$ 1 cm downstream from the nozzle and could put an upper limit to the rotational temperature of $T_{rot} < 25\text{K}$. They used a mix of 0.1% H_2O in neon at a total pressure of 400 Torr. They could further show that the OH production scales linearly with the discharge current which indicates that the production efficiency was limited by the electron flux to about $1 - 2\%$ and not by subsequent radical-radical
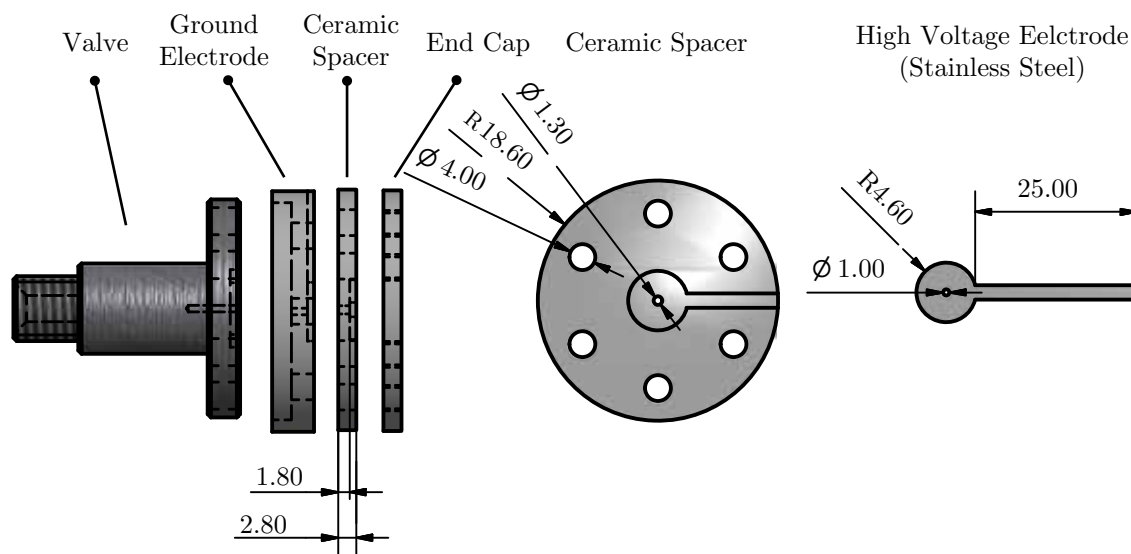
FIGURE 3.9: A sketch of the discharge assembly. A high voltage steel electrode is separated from ground by a ceramic spacer. The whole assembly is directly attached to the solenoid valve.

reactions.

We attempted to produce CH molecules using a pulsed discharge similar to the one used by Lewandowski and co-workers [152]. We attached a discharge assembly to the valve and supplied a negative voltage of up to $3.5\,\mathrm{kV}$ through a high voltage MOSFET switch to the front electrode. A sketch of this discharge assembly is shown in figure 3.9. The switch is controlled by the computer via a TTL input which makes it possible to adjust the duration and start of the high voltage pulse with an accuracy of $1\,\mathrm{\mu s}$. A variable resistor in series with the voltage supply and the discharge limits the discharge current. This is important to stabilise the discharge and prevents arcing. As the voltage is increased in the presence of the gas a small current flows between the electrodes that stems mainly from ionising radiation. At a certain voltage, the ignition voltage, the emitted electrons start to ionise the gas atoms. An avalanche process starts and becomes sustainable if enough current can be drawn from the power supply. If the power supply can deliver more current the gas will break down and will start to glow. This is known as the glow discharge regime and is accompanied by a sudden drop in discharge voltage. In this regime the discharge voltage is nearly independent over many orders of magnitude of discharge current. We monitor the voltage dropped between the discharge electrodes and the flow of current.

We found our first CH signal by discharging across a mix of 2% CH_4 in $3\,\mathrm{bar}$ of helium with a discharge voltage of $-1.5\,\mathrm{kV}$ applied to the cathode. We applied the discharge voltage for $1\,\mathrm{ms}$ which is basically DC for gas pulses that have a duration of $250\,\mathrm{\mu s}$ and probed for CH on the B-X transition. We detected a signal of 10 photons per gas pulse (shot) which corresponds to 7000 molecules in the detection region, or $8.75 \times 10^7\,\mathrm{sr}^{-1}$ per pulse. We optimised the position of the valve with respect to the skimmer and the probe laser beam. Then we shortened the

discharge pulse until we noticed a decrease in the CH flux. After that we shifted the start time of the discharge to optimise for maximum CH flux. Once we found the optimum position for the source we changed the discharge voltage and current until we observed a uniform glow discharge without arcing inside the chamber. This was confirmed by a smooth discharge voltage at about $600\,\mathrm{V}$ ($1.5\,\mathrm{kV}$ applied) and a stable discharge current of $100\,\mathrm{mA}$. After optimisation we saw an increase of the CH flux by a factor of 7. This flux would still make any deceleration, trapping or high resolution spectroscopy experiments very challenging so more source optimisation was needed. We thus started to investigate the influence of the insulating material between the electrodes and the geometry of the discharge assembly on the production efficiency. We found that polishing the stainless steel electrodes improved the discharge stability and thus the shot-to-shot stability of the discharge but had no influence on the peak flux. We then replaced the polymer thermoplastic (PEEK) electrode spacers with spacers made of macor, a machinable glass ceramic which possesses very good heat and chemical resistance and a large dielectric strength ($60\,\mathrm{kV\,mm^{-1}}$)[4]. Again this had no effect on the peak flux, but decreased the amount of large current spikes that appeared from time to time due to arcing.

In order to investigate the influence of the geometry of the discharge channel we kept the aperture in the grounded electrode constant at $1\,\mathrm{mm}$ and increased the hole in the spacer and high voltage electrode from 2 to $4\,\mathrm{mm}$. The discharge voltage and current had to be optimised but even for optimum discharge conditions we detected a decrease in the CH flux by a factor of 2. We concluded that a smaller discharge channel is favourable and returned to the previous version.

We then started to change the fraction of precursor to carrier gas by mixing pure methane with argon in a mixing bottle. We varied the amount of methane from $0.5 - 10\%$ in argon and found that the signal slightly increased between 0.5 and 2% and stayed constant thereafter.

We then added a hot filament close to the discharge region. The thermally emitted positive ions are accelerated towards the outer electrode which should, in principle, help to initiate a stable discharge at lower electrode voltage and shorter duration. We, however, did not observe any of these effects.

So with nothing else to change we decided to try a new precursor molecule. Our attention was drawn to $CHBr_3$ (96% $CHBr_3$ with 3% ethanol as stabilizer, Sigma Aldrich) which was used by a group in Paris to generate a supersonic beam of CH by means of discharge [153]. They measured the CH density they produced via cavity ring-down spectroscopy to $(5 \pm 1)\ 10^9\,\mathrm{cm^{-3}}$ $2.5\,\mathrm{cm}$ downstream from the nozzle. Note, however, that they only give the total number of CH molecules which includes all the molecules in higher rotational states in the vibrational ground state. By fitting to the rotational spectrum they deduce an occupation of the J=1/2 ground state of 0.14 of the total number of molecules produced in the source. Furthermore, they were using a pulsed detection laser, the bandwidth of which is larger than the Λ-doubling of the J= 1/2

---

[4]Note that HBC grade hot-pressed boron nitride is an even better choice due to its large thermal conductivity of $29\,\mathrm{W\,m^{-1}\,K^{-1}}$ (10% that of copper), even greater heat resistance and dielectric strength $>100\,\mathrm{kV\,mm^{-1}}$.
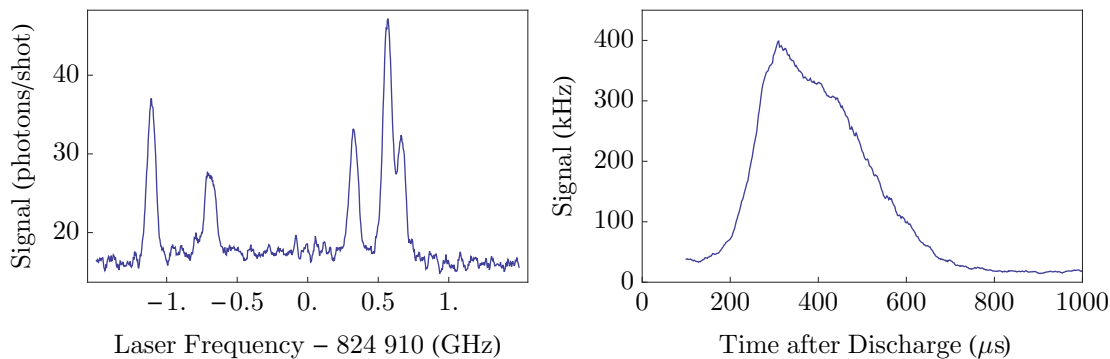
FIGURE 3.10: Left: A spectrum obtained when scanning across the $Q_2(1/2)$ line of the $B^2\Sigma^-(v'=1) \leftarrow X^2\Pi(v=0)$ transition reveals the fine and hyperfine structure of CH. The laser frequency is scanned over a range of $3\,\text{GHz}$ in steps of $15\,\text{MHz}$. We record the photon count rate for each frequency step and use a single molecular beam pulse for each frequency step. Right: A time-of-flight profile of the molecular pulse. We lock the laser to the peak frequency of the spectrum and average over 200 shots. The wide temporal width ($230\,\mu\text{s}$) and central arrival time of $375\,\mu\text{s}$ ($2000\,\text{m s}^{-1}$) show that the pulses are heated to considerable temperatures during the discharge process.

state. Hence, assuming an equal distribution in the two Λ-doublet states, the number of CH molecules in a single quantum state, ignoring hyperfine, becomes $\rho = 0.14 \times 0.5 \times 5 \times 10^9\,\text{cm}^{-3}$, which corresponds to a flux $\Phi = \rho v L^2 = 3.7 \times 10^{14}\,\text{sr}^{-1}\,\text{s}^{-1}$, where $v = 1700\,\text{m s}^{-1}$ is the typical velocity for a helium beam, and $L = 2.5\,\text{cm}$ the distance from the nozzle to the detector.

Bromoform ($CHBr_3$) is a liquid which has a vapour pressure of $6.7\,\text{mbar}$ at room temperature. The conventional way to mix it with the inert carrier gas is to bubble the carrier gas through the liquid. A stainless steel container is filled with bromoform. The gas inlet tube ends just above the bottom of the steel container. The outlet sample tube is well above the surface of the liquid and is connected to the valve. Through this tube it is also possible to evacuate the gas lines before the inert gas is bubbled through. In order to prevent pumping air through the liquid one can cool the container to below the freezing temperature and pump on both the inlet and outlet tube. However, we find that this makes no difference to the CH production efficiency. After the tubes have been evacuated the carrier gas is bubbled through the liquid which results in a mixture of $< 1\%$ of bromoform in the carrier gas. After optimising the discharge parameters we, surprisingly, measured exactly the same CH flux as for the case of 2% methane in argon. A scan across the $Q_2(1/2)$ line of the $B^2\Sigma^-(v'=1) \leftarrow X^2\Pi(v=0)$ transition is shown in figure 3.10, on the left. We can also record the fluorescence as the molecules fly through the laser beam. This gives information about the velocity distribution and thus the temperature of the molecules. Such a profile is called time-of-flight profile. Comparing the maximum flux of $6.1 \times 10^8\,\text{sr}^{-1}$ per pulse we measured to the one measured by Romanzin of $3.72 \times 10^{10}\,\text{sr}^{-1}$ per pulse we conclude that our flux is a factor of 60 lower. As we found out later during the operation of the source presented in the next section it is extremely important that the discharge voltage is as low as possible. Hence the drop to $600\,\text{V}$ in the presence of the gas might not have been large enough. By controlling the gas density in the discharge region

more carefully it might have been possible to tune the discharge conditions to a lower voltage.

Using other carrier gases than helium resulted in an even worse signal-to-noise ratio. In addition to that we detected a considerable increase in luminescent discharge by-products (also known as glowing crap). This has also been observed by Romanzin. In general the source operation was prone to large shot-to-shot fluctuations, the electrodes had to be cleaned after about two weeks of operation and the sealing poppet of the valve degrades quickly due to the discharge. Finally we tried methanol and acetone as precursors as well which gave even less CH as compared to bromoform or methane. The low production efficiency, the high temperature, and worse signal-to-noise ratio for carrier gases of larger mass left us with no other option but to try something completely different.

3.4.6 A Discharge-Reaction Source for Producing CH Molecules

Over a course of 10 years starting from 1995 Hiroshi Ohoyama and his colleagues from the Department of Chemistry at Osaka University developed a new kind of CH source which is based on the well known exothermic chemical reaction

$$C\left(^1D\right) + H_2 \rightarrow CH(X^2\Pi) + H \left(+25\,kJ\,mol^{-1}\right). \tag{3.32}$$
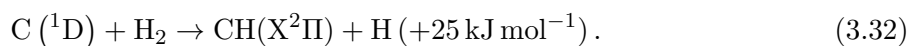
The first to investigate this reaction in great detail were Jursich and Wiesenfeld at Cornell University in 1984 with the aim to study its importance in combustion processes [154]. By that time chemists have already performed extremely fruitful experiments with oxygen in its metastable excited state, $O(^1D)$ and thus expected to get new insights into a rich carbon chemistry from reactions involving the excited (^1D) state of carbon. The first experiments of such kind date back to the end of the 1960s. Until 1984, however, no one has succeeded in building a convenient and clean source of excited carbon atoms which hindered detailed investigations of the reaction dynamics. Jursich and Wiesenfeld were flowing a mixture of carbon suboxide (C_3O_2) and molecular hydrogen (H_2) through a reaction chamber. In the middle of the chamber they dissociated the carbon suboxide with a fluorine F_2 excimer laser operating at $157\,nm$ which yields about 3% of $C(^1D)$ and 97% of $C(^3P)$ [155]. They then probed for CH molecules with a pulsed dye laser on the X-A transition via laser induced fluorescence. A nice feature of this reaction is that only the production of CH in its electronic and vibrational ground state is energetically possible (exothermic by $25\,kJ\,mol^{-1}$) which they could confirm by the absence of any spectral lines originating from excited vibrational states. The rotational distribution was consistent with a Boltzmann distribution characteristic of $300\,K$. It is quite remarkable that they could not even detect any additional rotational heating due to the release of the binding energy. This means most of the energy is converted into translational energy of the reaction products CH and H. This could be confirmed by an extensive study of the reaction by Mikulecky and Gericke in 1993 [156].

Ohoyama, however, chose an alternative way to produce the excited carbon atoms: a DC glow discharge across helium promotes the carbon atom into the metastable (2^3S) state. The metastable helium is then injected into a reaction channel further downstream which is filled with a mixture of 50% CO and 50% H_2 molecules. The nearly $20\,\text{eV}$ of internal energy of metastable helium is enough to break the CO triple bond ($11.19\,\text{eV}$) and excite the carbon atom to its metastable C(^{1}D) state ($1.26\,\text{eV}$). The metastable carbon then reacts with a hydrogen molecule according to the path described in equation 3.32. The complete reaction pathway is (one asterisk denotes an excited state and two asterisks a metastable state):

$$\text{He} + \text{e}^- \quad \rightarrow \quad \text{He}^{**}(2^3S) \tag{3.33}$$

$$\text{He}^{**}(2^3S) + \text{CO}(X^1\Sigma^+) \quad \rightarrow \quad \text{C}^{**}(2^1D) + \text{O} + \text{He} \tag{3.34}$$

$$\rightarrow \quad (\text{CO}^+)^* + \text{He} + \text{e}^- \tag{3.35}$$

$$\text{C}^{**}(2^1D) + \text{H}_2 \quad \rightarrow \quad \text{CH}(X^2\Pi, v = 0) + \text{H} \tag{3.36}$$
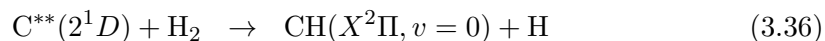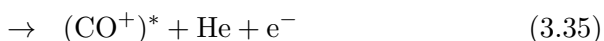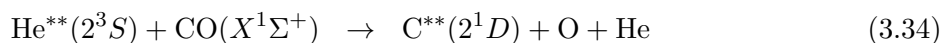
It is worth pointing out that the primary reaction channel is the Penning ionisation process (3.35) that produces excited carbon monoxide ions. Furthermore, it is possible that after the dissociation of CO the oxygen atom is excited into a metastable state instead of the carbon atom. Hurt measured the relative reaction rates to be 96% Penning ionisation and 4% to dissociation of the carbon monoxide molecule [157]. To be more precise, the most probable production of metastable carbon involves an intermediate electronically excited state. This means that after the dissociation the carbon atom is either in the 3^1P, 3^3P or 3^3D state. The only allowed radiative decay channel to the 2^1D level thus stems from population in the 3^1P state which has a radiative lifetime of about $10\,\text{ns}$. This means that the overall efficiency of creating metastable carbon atoms via the reaction path 3.34 is of the order of 1%.

Ohoyama produced the metastable helium by a simple pulsed DC discharge geometry very similar to the one used by us for the discharge across methane and bromoform. Figure 3.11 provides an overview of our source hardware. A teflon reaction channel ($20\,\text{mm}$ long and $13\,\text{mm}$ in diameter) is directly attached to the discharge source. The CO/H_2 mix is injected directly into the mixing channel through a second pulsed valve. The reaction then takes place in the mixing channel and produces CH molecules which then supersonically expand through a $3\,\text{mm}$ diameter hole in the end cap of the assembly. Great care must be taken to achieve full control over the individual parameters:

- The stagnation pressure behind the helium valve.

- The voltage supplied to the helium valve and the duration it opens for.

- The discharge voltage, current, length and time after opening the valve.

- The stagnation pressure behind the CO/H_2 valve.
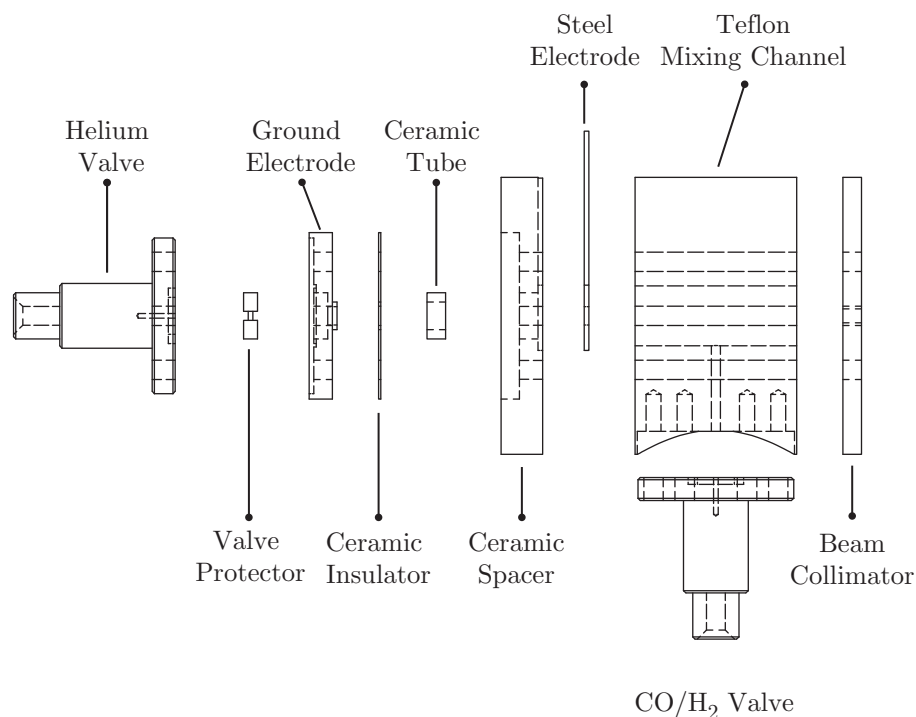
FIGURE 3.11: An exploded view of the apparatus used to test the discharge-reaction source.

- The voltage supplied to the CO/H_2 valve and the duration it opens for.

- The time the CO/H_2 mix is injected with respect to the helium.

So there are in total eleven parameters we can independently vary. First we characterized each valve carefully using a fast ionisation gauge. A fast ionisation gauge can be put into the molecular beam and responds directly to the molecular density on the microsecond time scale. This allowed us to pin down the exact voltage needed to open the valve for a given duration and stagnation pressure. Additionally, these measurements allowed us to identify the exact time it takes the valve to open after the drive pulse is supplied to valve. The peak of the helium gas pulse for example arrives 720 µs after the rising edge of the voltage that is supplied to the valve. This depends on the stagnation pressure and the gas species. Knowing the exact time it takes for the helium to emerge we knew when to apply the discharge. Similar to our earlier discharge source we put a variable current limiting resistor in series between the high voltage switch and the high voltage electrode. First we applied the discharge voltage for a very long time of up to 1.5 ms. As soon as the gas arrives the voltage drops and a constant discharge current appears. This is another very useful technique to identify when the gas actually appears. We then shortened the duration the discharge voltage is applied to approximately 450 µs. The discharge typically drew a current of 120 mA at an ignition voltage of −1.7 kV. In the presence of the gas this voltage dropped to about 400 V. Figure 3.12 shows an oscilloscope trace of the discharge current and voltage. As we found out later the ideal conditions are such that a bright
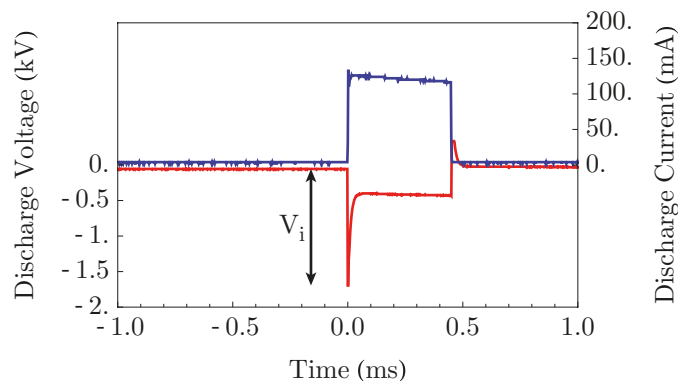
FIGURE 3.12: An oscilloscope trace of the discharge current (blue) and voltage (red). To start the discharge a high ignition voltage V_i is necessary which drops to a stable discharge voltage of -400 V as the gas arrives. Both the voltage and current have to be stable and smooth without any current spikes. Furthermore, the discharge voltage must not vary when changing the discharge current. This indicates that we operate in the smooth glow regime.

white glow can be seen in the source chamber in contrast to a dim blue/UV glow. On the discharge voltage monitor only the white glow showed a large drop in voltage to about 400 V which seems to be crucial for efficient CH production. With this setup we could only produce a small amount of CH, similar to the earlier discharge sources. Ohoyama used two general valves (series 99) with a slightly smaller nozzle diameter of 0.5 mm and applied 200-250 V for about 250 μs. When he was operating the source the chamber pressure increased to 4×10^{-5} mbar which was very similar to our operation conditions. It was not until we built the next version of Ohoyama's source [158] that we would realise the key to success. This source is described now in more detail.

During the testing of the source we realised that Ohoyama and his colleagues published another version of the source which solved one of the major drawbacks of the previous version - it could only be operated with helium, so the molecules travelled with a speed of over $1700 \, \mathrm{m \, s^{-1}}$. It turned out that other carrier gases only yielded extremely poor dissociation efficiencies for CO. Although metastable Ne (16.6 eV) and Ar (11.5 eV) possess enough energy to dissociate CO there is not enough energy to excite ground state carbon into the 3^1P state which radiatively decays into the metastable 2^1D state. Hence Ohoyama and his colleagues replaced the dissociation of carbon monoxide to produce $C(2^1D)$ with the collision of highly excited species with solid carbon. The heat of sublimation of solid carbon is 7.4 eV and the excitation energy to the 2^1D and 3^1P states are 1.3 eV and 7.7 eV respectively. The reaction paths are:

$$\mathrm{Rg} + \mathrm{e}^- \quad \rightarrow \quad \mathrm{Rg}^{**} \tag{3.37}$$

$$\mathrm{Rg}^{**} + \mathrm{C}^{**}(\mathrm{solid}) \quad \rightarrow \quad \mathrm{C}(^1D) + \mathrm{Rg} \tag{3.38}$$

$$\mathrm{C}^{**}(^1D) + \mathrm{H}_2 \quad \rightarrow \quad \mathrm{CH}(X^2\Pi, v = 0) \tag{3.39}$$
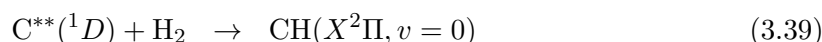
where Rg is the rare gas used which is either helium, neon or argon. The source hardware itself is only marginally different from the earlier one. Two carbon electrodes are sandwiched between the stainless steel electrode and the reaction channel and a graphite tube (10 mm long with a 6 mm central aperture) is inserted into the reaction channel. Pure H_2 is now injected into the reaction channel instead of a mixture of H_2/CO. It was in this source configuration that we got the source finally working. We found that the crucial parameter was the duration for which the voltage is supplied to the valves. By changing this time with an accuracy of 1 µs, which is only a minute change in gas density, we could stabilise the "good" white light discharge condition and as soon as we got the time right for the H_2 injection we could detect a healthy amount of CH. The timing of the H_2 injection is rather peculiar. The source only works if the hydrogen is pre-injected into the mixing channel. In addition, we produced the most CH using the CO/H_2 mix in combination with the carbon version. In particular the following parameters are crucial to get right:

- The pressure conditions in the discharge region and the reaction channel are important.

- The time of the H_2/CO injection with respect to the He injection.

- The timing of the discharge with respect to the He and H_2/CO injection.

- The time for which the discharge voltage is applied (unnecessary excessive discharge extensively decreases the CH beam intensity).

- A uniform, soft glow discharge with bright visible light instead of UV/blue light yields more CH.

The top left plot of Figure 3.13 shows a time-of-flight profile for this source using He carrier gas, where zero is the rising edge of the trigger sent to the high voltage switch of the discharge source. The arrival time of 570 µs ($1366 \, \text{m s}^{-1}$) indicates that the rising edge of the discharge does not define the actual time when the molecules are created. Ohoyama measured the velocity using the focusing curve of their hexapole field to be $1900 \, \text{m s}^{-1}$ which is much more reasonable for a hot helium beam. Furthermore, the large mixing volume has an impact on the beam quality. From the FWHM of $w = 211 \, \text{µs}$ we infer a temperature of 44 K, which again must be treated with care since the initial spatial and temporal width is unknown.

The top right hand side plot of figure 3.13 shows a parameter scan. We lock the laser to the resonance frequency and scan the time when the voltage is supplied to the CO/H_2 valve with respect to the helium valve. We can clearly see that it is crucial to pre-inject the gas mix into the mixing channel by 840 µs before the helium which is a very peculiar feature of this source.

The bottom left plot shows the dependence of the CH signal as a function of the pressure behind the CO/H_2 valve. We noticed that the discharge conditions change for different CO/H_2
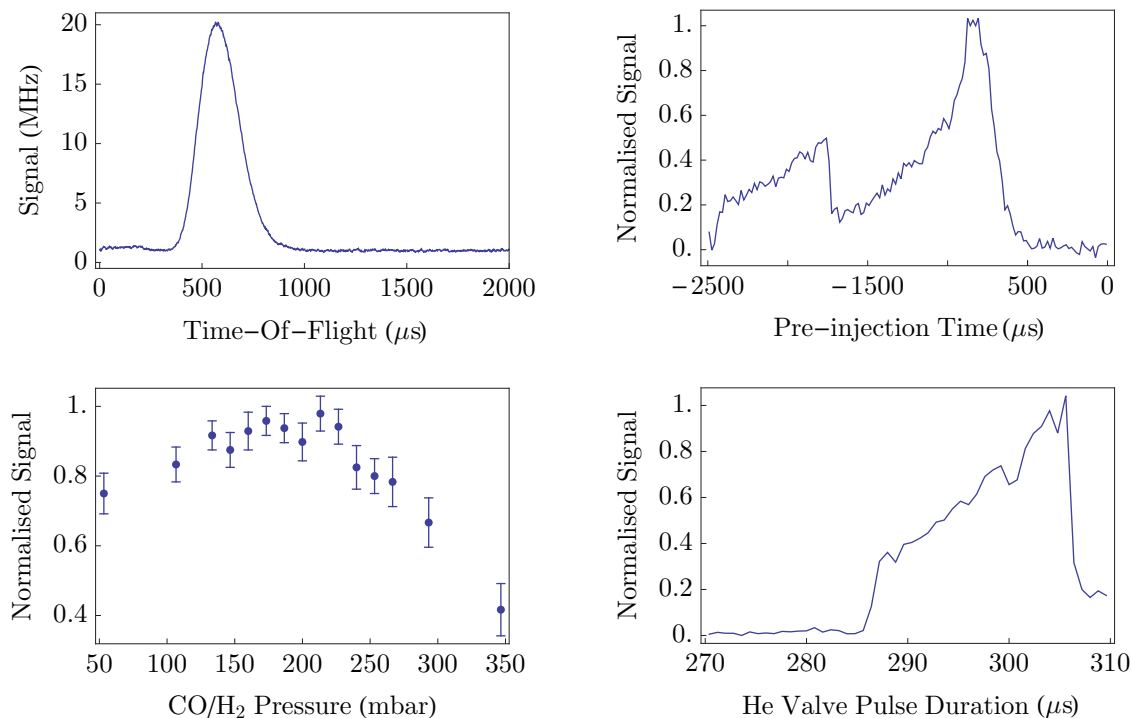
FIGURE 3.13: Top left: A time-of-flight profile of CH molecules produced by the discharge-reaction source. Top right: A parameter scan. We lock the laser to the transition frequency and scan the time when the CO/H_2 valve fires with respect to the helium valve. Zero in this plot is the rising edge of the helium valve trigger. Bottom left: The optimised CH signal as a function of the CO/H_2 stagnation pressure. Bottom right: The optimised CH signal as a function of the opening time of the helium valve.

pressures which indicates that due to the pre-injection the part of the gas mix enters the discharge region. We scanned the time when the discharge was applied for the different stagnation pressures and took the maximum value of that scan for each pressure value. With the optimum discharge conditions fixed for each pressure we then optimized the duration of the voltage pulse that is sent to the CO/H_2 valve.

The bottom right figure shows the dependence of the CH signal as a function of the voltage pulse duration that is sent to the helium valve. When we started investigating the source we left this value constant at $315\,\mu s$ which was an unfortunate choice since the signal is then very small. Once we started to scan this parameter the signal increased dramatically. The tuning of this parameter also allows to tune the discharge condition between the dim blue glow regime with a high residual discharge voltage of $800\,V$ and the bright white glow regime with residual discharge voltages as low as $300\,V$. The lower the discharge voltage the bigger the signal.

3.4.6.1 Determining the Flux

The maximum photon count rate we measured for detecting CH in the J= $1/2^-$ state on the R_{22} line of the A-X transition with a laser intensity of $670\,W\,m^{-2}$ ($1\,mW$ in a beam of

$5 \times 1.5\,\mathrm{mm}^2$) was $\Gamma_p = 20.5\,\mathrm{MHz}$ in a pulse of FWHM $w = 211\,\mu\mathrm{s}$. For such a laser intensity and speed of the molecules ($1900\,\mathrm{m\,s}^{-1}$) the detection efficiency is $\bar{n}_p\epsilon = 0.35\%$. The total number of molecules registered by the detector $0.79\,\mathrm{m}$ downstream from the nozzle is then $N = \Gamma_p w/(n_p\epsilon) = 1.2 \times 10^6$. This corresponds to a beam flux of $\phi = N/\Omega_d = 1.55 \times 10^{10}\,\mathrm{sr}^{-1}$ per pulse ($\Phi = \phi/w = 7.3 \times 10^{13}\,\mathrm{sr}^{-1}\,\mathrm{s}^{-1}$). Ohoyama and his colleagues report a flux of $\Phi = 1.3 \times 10^{16}\,\mathrm{sr}^{-1}\,\mathrm{s}^{-1}$ in the J= 1/2 state. They use a pulsed detection laser which cannot resolve the Λ-doubling. Accounting for that we were missing approximately a factor of 100 in flux. Let us put that into context with the ideal supersonic source.

The ideal supersonic source with 1 bar of helium behind the nozzle produces a beam flux of $\Phi = 2 \times 10^{21}\,\mathrm{sr}^{-1}\,\mathrm{s}^{-1}$ through an aperture of $0.5\,\mathrm{mm}$ diameter. The production efficiency for a highly optimised continuous metastable helium source is of the order of 10^{-5} [159]. Assuming that all the metastable helium atoms are converted into CH molecules via the reaction mentioned in 3.39 we expect a flux of $\Phi = 2 \times 10^{16}\,\mathrm{sr}^{-1}\,\mathrm{s}^{-1}$. Ohoyama and colleagues measure a similar flux which is quite surprising since it is well known that the production efficiency of metastable helium decreases rapidly in a supersonic source due to the fast quenching of the metastable state in the high pressure environment of the expansion. Halfmann and colleagues for example report an efficiency of only 10^{-7} for such a source [160]. Furthermore, we have not accounted for the fact that only about 1% of the initial number of metastable carbon atoms is converted into CH.

Although this source produced a CH beam with a brightness about ten times greater than other supersonic molecular beams in our lab, the molecules were translationally hot ($50\,\mathrm{K}$) and moving at $1900\,\mathrm{m\,s}^{-1}$. This significantly degrades its practicality to applications such as Stark deceleration, cooling or high resolution spectroscopy experiments. The high temperature leads to a large velocity spread and the high, central velocity to very long decelerators and short interaction times. All our efforts to produce a slower beam using argon as a carrier gas failed. Furthermore, the source was very complex and the discharge behaviour very erratic which resulted in large shot-to-shot fluctuations. Because of the high temperature, high speed, complexity and erratic discharge behaviour, in combination with the fact that we could not operate it using krypton or xenon carrier gas (even in principle) we decided to abandon the use of this source.

3.4.7   Laser Ablation

To cut a long story short, laser ablation does not work at all. We tried ablating a solid graphite target into an expansion of 2% H_2 in argon. This is not really surprising because ablating carbon from a graphite rod is the main method of producing large carbon clusters such as fullerenes. We also tried ablation in a buffer gas cell: We mounted a graphite rod inside a small copper box which was connected to a 4 K cold plate of a closed cycle cryocooler. We sprayed hydrogen

into the cell and ablated the carbon rod under steady flow of cold helium buffer gas. We could, however, not detect any CH molecules via laser absorption in the cell nor through laser induced fluorescence outside the cell.

3.4.8   Photodissociation of Bromoform

When a molecule absorbs a photon it gets electronically excited. If this excited state is repulsive, i.e no bound states exist the molecule dissociates into its constituents. That is because the radiative decay back into the ground state is very slow (ns) compared to dissociation which usually occurs within one vibrational period (10^{-13} s). The dissociation cross-section is continuous with photon energy and the shape is only governed by the Franck-Condon principle, i.e it peaks close to a vertical excitation. Consequently the energy used to dissociate a molecule can be much larger than what is commonly defined as the dissociation energy (the depth of the molecular potential). This process is called direct photodissociation.

Predissociation happens if the initial absorption occurs into a bound excited state which is perturbed by a nearby repulsive electronic state. The dissociation rates then typically depend on the strength of the coupling and the specific levels that are involved. The photodissociation cross section then consists of a series of discrete peaks.

A third way for a molecule to dissociate is if the excited state is not predissociated but radiatively decays into the continuum of a lower lying repulsive state. The dissociation cross section consists now of a series of peaks narrower than in the predissociation case.

We are dealing mainly with polyatomic precursor molecules which possess many excited electronic states. Detailed information about the electronic states of the molecules is usually not available and hence a full description is, in general, not possible. We can thus expect that a mixture of all of the above mentioned dissociation processes will happen in such molecules. The photodissociation typically cleaves the weakest bond. The rupture of two bonds followed by the formation of a new bond, however appears to be more common in polyatomic molecules [161].

As the molecules get larger the density of vibrational states increases which decreases the probability that the molecule "finds its way" along a specific dissociative path. In addition, the extremely high intensities available from pulsed lasers leads to non-linear effects in the light-matter interaction. This can lead to the effect that a single molecule absorbs more than one photon. When this happens sequentially, via a real intermediate excited state, it is referred to as resonant-multiphoton excitation: the first photon transfers the molecule into an excited electronic state and before the molecule can decay back into the ground state it absorbs a second photon which can transfer it into a dissociative state. A second mechanism is non-resonant multi-photon excitation where there is no resonant intermediate state involved and several photons are absorbed simultaneously: Through such higher order processes molecules whose dissociation energy is less than twice the single photon energy can be dissociated. The

higher the order of the process the more laser intensity is necessary for efficient dissociation.

A good precursor has a large absorption cross section in the UV. It also has a high quantum yield for the species of interest. The quantum yield of a photo dissociation product is simply defined as the ratio of the number of desired product molecules formed by the overall process to the number of quanta absorbed by the precursor molecule. Hence the more dissociation channels are energetically allowed the lower the quantum yield will be. Note that the quantum yield can, in principle, be larger than one if a single photon is enough to produce more than one product. One photon for example can be enough to dissociate H_2O_2 into two OH molecules. The production of the OH radical using photodissociation is especially efficient. Usually only a single bond must be cleaved since most acids and all alcohols possess a loosely bound OH group attached to a hydrocarbon chain which makes it very likely to be the weakest bond. In particular, the C-O bond energy is lower than the O-H bond energy by 1.1 eV. An extremely efficient precursor for OH is nitric acid (HNO_3) whose UV absorption cross section reaches a maximum of $\sigma = 2 \times 10^{-17}\,\mathrm{m}^{-2}$ at 185 nm [162]. Furthermore, the quantum yield for producing OH from nitric acid has been measured to be 0.3 for 193 nm and is close to unity for 248 nm [163].

For CH it is quite challenging to find an ideal precursor. Due to the four unpaired electrons of the carbon atom, CH cannot be found as a loose attachment to another molecule. At first sight acetylene (C_2H_2) might appear as the ideal candidate since it is made up of two CH molecules. However, the covalent triple bond, between the carbon atoms is so strong (8.7 eV compared to the 4.3 eV for the C-H bond) that the CH bond breaks instead of the triple bond. Furthermore, the UV absorption cross section is three orders of magnitude smaller as compared to nitric acid. Consequently, hardly any CH is produced by photolysis even through higher order processes.

The most promising route is to look for molecules with a single carbon atom where the carbon-hydrogen bond is the strongest. The attention is then immediately drawn to the halomethanes. These molecules are derivatives from methane (CH_4) with one or more hydrogen atoms replaced with halogen atoms (F, Cl, Br, I). The heavier the halogen atom the weaker its bond to the carbon atom. Iodoform would be preferable because iodine forms the weakest bond under the common halogens to carbon. At room temperature it is a solid so it must be heated to high temperatures to produce an appreciable vapour pressure. We therefore decided to use bromoform which is a liquid and has a high enough vapour pressure to be a useful precursor.

It is believed that CH production from bromoform occurs via a sequential dissociation process [153, 164]. Figure 3.14 shows some of the possible dissociation channels. A single-photon dissociation leads mainly to prompt C-Br bond fission,

$$\mathrm{CHBr_3} + h\nu \rightarrow \mathrm{CHBr_2} + \mathrm{Br}\,. \tag{3.40}$$
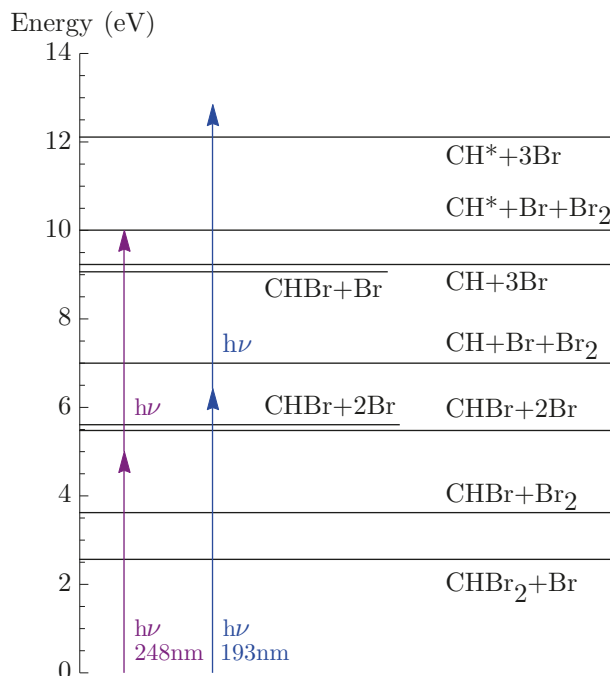
FIGURE 3.14: Various photodissociation channels are possible after the irradiation of bromoform with the 193 or 248 nm light of an excimer laser.

There are then three competing fragmentation channels of $CHBr_2$ through secondary photodissociation,

$$CHBr_2 + h\nu \rightarrow CHBr + Br\,, \qquad (3.41)$$

$$CHBr_2 + h\nu \rightarrow CH + Br_2\,, \qquad (3.42)$$

$$CHBr_2 + h\nu \rightarrow CBr + Br_2\,. \qquad (3.43)$$
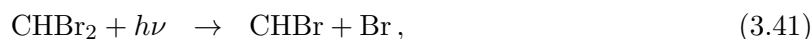
We can see that the CH production is bound to be a quite inefficient process due to the many possible dissociation channels. Romanzin and colleagues measured the quantum efficiency of CH from photodissociation of bromoform in a vacuum flow cell using cavity ring-down spectroscopy to be $(5 \pm 2.5) \times 10^{-4}$ [153]. The efficiency in a supersonic expansion is expected to be even less. It is well known that heavy molecules tend to cluster when they expand supersonically into vacuum and the fact that bromoform is liquid already at room temperature enhances this effect even further. In addition, the CH radical is known to be very reactive which could lead to rapid loss by reactions with the more abundant parent molecule $CHBr_3$ and other dissociation products in the high density region just after the nozzle. All this needs to be considered when trying to find the best precursor molecule and thus an extensive trial and error phase is obligatory.

To get started we used a GAM EX5 excimer laser which delivers up to 12 mJ in an 8 ns pulse at a wavelength of 193 nm with a maximum repetition rate of 1 kHz. We focused the output of the excimer laser with a 500 mm focal length lens (fused silica) right in front of the nozzle
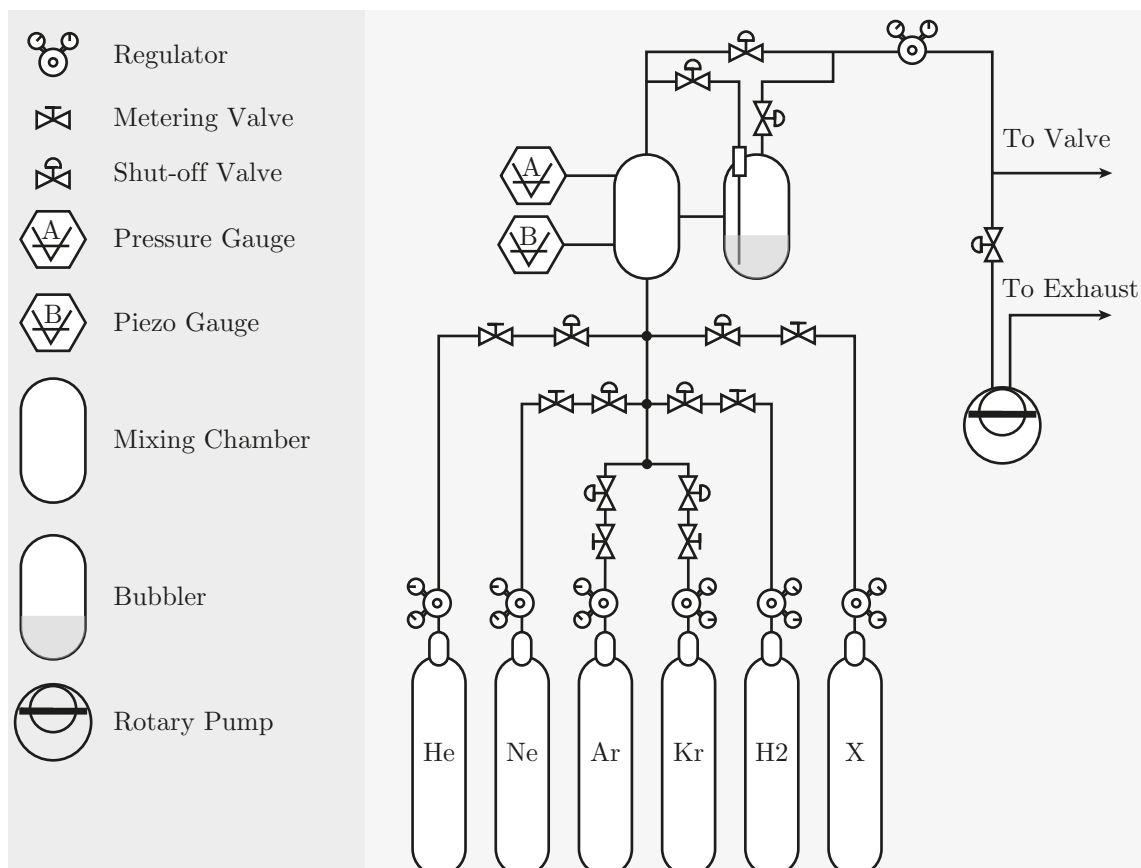
FIGURE 3.15: A sketch of the gas handling system built for the experiment. This allows us to mix the precursor with the carrier in arbitrary ratios. The bottle labelled with X is a symbol for all other gases that have been used.

of the solenoid valve to an area of $5 \times 2\,\text{mm}^2$. The excimer laser beam was orthogonal to the molecular beam with the long axis along the molecular beam. Note that a pulse of argon gas with a FWHM of $w = 200\,\mu\text{s}$ has a spatial extent of $\Delta x = vw \approx 10\,\text{cm}$. The excimer pulse duration is only 8 ns long so that only the molecules that spatially overlap with the laser beam length of 5 mm are dissociated. Hence the ideal scenario would be to co-propagate the excimer laser beam with the gas pulse. Direct focusing of the excimer beam into the nozzle, however, damages the sealing poppet and the valve starts to leak. One could think of a valve protector in front of the nozzle to prevent damage to the poppet, but a more serious issue forced us to abandon this idea. We found that focusing the laser under a steep angle onto the valve leads to a large amount of ablation from the valve face plate which has detrimental effects on the CH production. Hence we remained with the orthogonal configuration.

Before we can start we must prepare the gas mix. We found that care must be taken regarding the cleanliness of the gas/precursor handling system. Thus we only used high grade stainless steel tubing. A sketch of the gas handling system is shown in figure 3.15. We built a mixing chamber to investigate the CH yield for various precursor fractions. We prepared a mix of 0.2% bromoform in 4 bar argon. From the measurements with the fast ionisation gauge
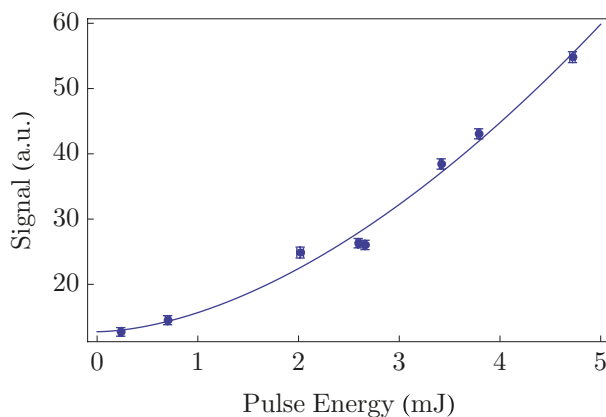
FIGURE 3.16: The CH signal as a function of the excimer laser intensity reveals a quadratic dependence which is characteristic for a two-photon dissociation process.

we knew approximately when the gas appeared in front of the nozzle for a given valve voltage and duration of the voltage pulse. We noticed a dim blue glow which mainly stems from the A-X fluorescence of excited CH when the timing of the excimer beam and alignment is correct. CH production following the photodissociation of ketene (CH_3COCH_3), acetone (($CH_3)_2CO$), methyl iodide (CH_3I), dibromomethane (CH_2Br_2), chlorodibromomethane ($CHClBr_2$) and chloroform ($CHCl_3$) have also been reported. We tried the dissociation of bromoform ($CHBr_3$), chloroform ($CHCl_3$), methyl iodide (CH_3I), methane (CH_4), methanol (CH_3OH) and acetone (($CH_3)_2CO$). In the end, after trying all these precursors at various mixing ratios it turned out that simply bubbling the inert carrier gas through bromoform yields the most stable source with the highest CH flux.

An important parameter when characterising the source is the dependence of the CH signal as a function of the dissociation laser intensity. This immediately gives access to the number of photons that are involved in the dissociation process. If the dependence is linear it is a single photon process and if it scales quadratically with the laser intensity it is a two photon process. The important question then is: can we deliver enough intensity to saturate the CH production? The first experiment with the GAM EX5 revealed a quadratic dependence which is shown in figure 3.16. The solid blue line in figure 3.16 is a fit to a power law, $S = kI^n$, where S is the signal, I the laser intensity, and k, n fitting parameters. This fit gives $n = 1.7 \pm 0.3$ which is consistent with a two-photon process and confirms earlier findings of Lindner [148]. We did not see any signs of saturation at the maximum pulse energy of the EX5 laser. Lindner et al. found that a pulse energy of 30 mJ, in a beam size similar to ours, saturated the CH production. Note that we could not focus the excimer beam any further than $4 \times 2 \, mm^2$ in order to explore saturation at higher intensities. First the laser beam mode is not particularly Gaussian, i.e it does not focus very well, and second we were restricted by the vacuum chamber to lenses with focal lengths longer than 300 mm. Furthermore, reducing the excimer beam size would reduce the spatial overlap of the excimer beam with the gas pulse even further. Hence in the ideal case we would like to saturate the production for a very gentle focus which means we needed more
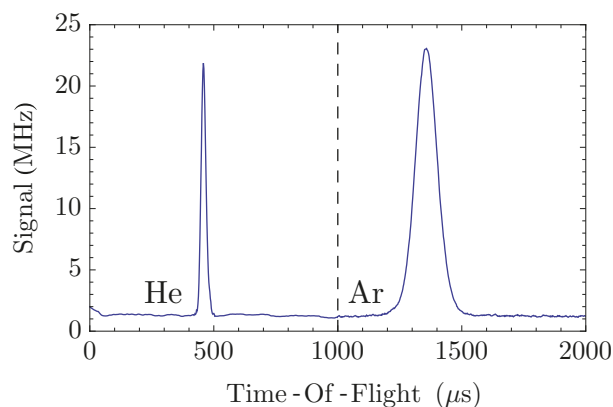
FIGURE 3.17: Two time-of-flight profiles of CH using either helium or argon as carrier gas. The velocity and temperatures are very close to the ideal supersonic expansion which indicates very little additional heating of the dissociation products. The profiles are averaged over 200 shots.

energy per pulse. This also means buying a bigger laser. So we upgraded to the SEMENTO ASX-750 that can provide up to 230 mJ in 20 ns at 193 nm and 450 mJ at 248 nm which should be sufficient to saturate the CH production.

We observed an increase by a factor of 4 at full pulse energy which is not the factor of 9 we expected from Lindner's measurements. First we checked that we are actually saturating by decreasing the pulse energy to half and observed that the signal only decreased by 5% which is a clear sign of saturation. The discrepancy between our measurement and Lindner's shows clearly that additional loss mechanisms are present which we attribute to reactions of the CH radical with dissociation products in the high density region in front of the nozzle. Furthermore, two 193 nm photons have enough energy to produce CH in the excited A state as well as to ionise bromoform. Both processes enhance the probability for unfavourable reactions and thus decrease the CH yield.

In order to investigate a potential dependence on the dissociation wavelength we changed the excimer gas and the cavity mirror (note the gain of the excimer gas is so high that the cavity only consists of one highly reflective mirror and an MgF_2 output coupler). To our surprise we saw an increase by a factor of 2 in the ground state CH production, even though the UV absorption cross section is smaller at 248 nm. Hence we operated the laser at 248 nm and saw an increase in the CH flux by a factor of 8 in total as compared to the small excimer laser operating at 193 nm. The maximum overall flux per pulse we measure is a factor of 10 lower compared to our version of Ohoyama's source. However, using helium as a carrier gas the resulting pulse is also 10 times narrower. The important thing is that the peak flux remained nearly the same and we only observed a reduced temporal width of the CH pulse. Figure 3.17 shows typical time-of-flight profiles for the photolysis source for the two different carrier gases, helium and argon. The narrow time-of-flight profile shows that the photodissociation source produces molecules at translational temperatures as low as 0.4 K (using argon as carrier gas) as compared to Ohoyama's source which was 50 K. The velocities of $1725 \, \mathrm{m \, s^{-1}}$ and $570 \, \mathrm{m \, s^{-1}}$ for helium and

argon respectively are very close to the terminal velocity of an ideal supersonic source, and so are the translational temperatures. This means that there is little residual heating involved in the dissociation process. For typical laser beam parameters and accounting for the slightly different detection efficiencies for the different velocities we can convert the photon count rate into a molecular flux. Using helium as a carrier gas we measure a flux of $1.1 \times 10^9 \, \text{sr}^{-1}$ per pulse (FWHM of 23 µs). Using argon as a carrier gas we detect a flux of $3.5 \times 10^9 \, \text{sr}^{-1}$ per pulse (FWHM of 92 µs). This flux is about ten to one hundred times less intense than the typical OH beam generated by the photolysis of nitric acid[5]. This is mainly due to the second order multiphoton process necessary for producing CH, in combination with a lower quantum yield and a smaller UV absorption cross-section (a factor of 10 less).

For most applications of molecular beams, short, intense and cold pulses are favourable because it leads to a small spatial and velocity spread of the molecules. Stark deceleration, high resolution spectroscopy or reactive scattering experiments all benefit enormously from the fact that nearly all the molecules travel with the same velocity and at a minimal spatial spread. It is therefore unlikely that we can actually make use of the larger number of molecules we get by using Ohoyama's source because the beam is nearly a hundred times hotter which results in a large velocity spread. Furthermore, the shot-to-shot stability of the photo-dissociation source is unrivalled. Unlike ablation sources where the metal target degrades over time the continuous supply of a gaseous precursor results in an extremely stable source[6]. Even small fluctuations in the dissociation laser intensity do not affect the CH yield if we operate well above the saturation energy of approximately 100 mJ per pulse. Moving the lens by up to 10% of its focal length in either direction does not change the CH flux on the few per cent level.

3.4.9 Valve Testing

A way to increase the flux of molecules is to compress the gas pulse so it matches the spatial size of the excimer laser beam. This means that we need a higher peak flux out of the nozzle, preferably in a shorter pulse such that the number of precursor molecules is increased in the dissociation volume without increasing the background pressure. In order to achieve that we need to operate the valve such that it fully opens for about 10 µs which corresponds to a spatial extent of the pulses of about 5 mm. This is quite challenging but, since the early introduction of modified fuel injector valves to create pulsed molecular beams, many groups have developed many different varieties of valves designed for specific applications.

Nearly all valve mechanisms are based on a harmonic oscillator principle with a force constant κ and an effective mass, m. The natural oscillation period of such a harmonic oscillator is given

---

[5]To my best knowledge, absolute flux measurements of such an OH source are not available in the literature. The estimate is based on private communication with G. Meijer.

[6]The noise is dominated by shot noise that arises from background laser scatter and not from fluctuations in the molecular beam intensity.

by $t_0 = 2\pi\sqrt{m/\kappa}$. This means in order to achieve a displacement of $\approx 1\,\text{mm}$ to open the valve for a time of $10\,\mu\text{s}$ one needs to exert a restoring force of the order of $10^5\,\text{N}$ onto a mass of $1\,\text{g}$, which exceeds the tensile strength of most common materials. Even and co-workers, however, miniaturised and optimised the components of a solenoid valve and achieved valve openings as short as $8\,\mu\text{s}$ when operating the valve at high gas pressures of $100\,\text{bar}$ [165]. By operating at such high pressures the restoring force exerted on the moving armature can be reduced and this allows the valve to complete its free travel of $0.1\,\text{mm}$ in $8\,\mu\text{s}$. This valve operates with a very small aperture of $0.2\,\text{mm}$ only which reduces the number of inert gas atoms that emerge from the nozzle by a factor of 16 as compared to our solenoid valve with an aperture of $0.8\,\text{mm}$. One can compensate for that by increasing the stagnation pressure to $100\,\text{bar}$. We, however, cannot increase the number of precursor molecules because bromoform is a liquid with a limited vapour pressure of $7\,\text{mbar}$ at room temperature.

There is a second effect that can limit the flow of gas out of the valve. It is well known that the solenoid valve does not open fully, and this limits the gas flow because the poppet is not completely removed from the aperture. Other types of valves might provide a larger flow which is only limited by the conductance of the nozzle. This flow is known as choked flow. Furthermore, shorter overall gas pulses decrease the amount of gas that does not interact with the excimer laser and thus reduce the gas load in to the source chamber. This makes it possible to operate at higher repetition rates.

We investigated two other valves apart from the solenoid valve. The first was a beam-bending valve (PSV Pulsed Supersonic Valve C-211, Jordan TOF Products, Inc.) which was originally conceived by Dimov [166] and then developed further by Gentry and Giese at the University of Minnesota [167]. The second valve we investigated is the Amsterdam Cantilever Piezo Valve which is based on a design by Gerlich from 1989 [168] and has been redeveloped to a commercial product by the group of Maurice Janssen in Amsterdam [169].

The Jordan Valve

The PSV Pulsed Supersonic valve, which is commonly known as the Jordan valve, seals the nozzle with a metal bar, the centre of which sits on an O-ring. A metal hairpin is rigidly attached to the valve's faceplate and forms a current loop. The static bar of the hair pin has an aperture in the middle with an O ring around it. When the valve is not operated the flexible metal bar pushes against the O ring and seals the nozzle. When a large current (up to $5000\,\text{A}$) passes through the loop for $20\,\mu\text{s}$ it generates a magnetic field that pushes the flexible metal bar from the static one and opens the $0.5\,\text{mm}$ nozzle. This results in a short gas pulse which has a nearly top-hat profile and lasts for approximately $40\,\mu\text{s}$. The top hat profile indicates that the valve fully opens and choked flow conditions prevail. It turns out that this valve gave the most intense CH beam which is approximately 3 times greater than the one produced by using the

solenoid valve.

The valve is delivering short pulses and a high intensity, but the large current through the loop leads to rapid heating of the gas which increases both the translational temperature of the resulting molecular beam and its velocity. The longer we were operating the valve the hotter the gas became which resulted in large variations of the arrival times of the molecules. Such variations are detrimental if one wants to average over thousands of pulses in high resolution spectroscopy experiments. Hence we refrained from the use of the Jordan valve.

The Piezo Valve

Using piezoelectric ceramics for the rapid actuation of a valve has a long tradition in the molecular beam community. A common design involves a large cylindrical piezo which displaces a sealing plunger if a voltage of up to 1000 V is applied [170–172]. These valves can deliver pulse widths of approximately 100 - 150 µs at repetition rates up to 100 - 1 kHz. The group of Maurice Janssen in Amsterdam developed a fast valve based on a twenty year old design by Dieter Gerlich from the Technical University in Chemnitz. It is based on a cantilever piezoelectric ceramic that seals the nozzle by pushing onto an O-ring with a blocking force of about 1-2 N. Cantilever piezos have the advantage that they can deliver large displacements of the order of 70 µm and because the piezo itself is sealing the nozzle and there is no need to displace a heavy plunger. Thus very fast oscillation frequencies are possible which results in pulses with a FWHM as short as 7 µs, measured 10 cm downstream (6 bar of helium) at repetition rates as a high as 5 kHz [169]. The nozzle has a conical shape with a full angle of 40° and a length of about 1 cm. Janssen and his colleagues measure approximately 10^{16} gas particles in the source chamber when operating at a backing pressure of 6 bar. Due to the conical shape of the nozzle they assume a full angular distribution of the supersonic expansion of 12° FWHM by referring to measurements performed by Even and Lavie using a similar nozzle [123]. We care mostly about the peak flux, which increases the number of precursor molecules in the dissociation region. The peak flux corresponds to the maximum deflection of the piezo, which is obtained using the maximum possible voltage and this results in significantly longer pulses than the reported 7 µs. Using a fast ionization gauge we measure a FWHM of 180 µs 8 cm downstream using 4 bar of argon. The pulse width decreases to 25 µs for the minimum piezo deflection which, however, results in a peak flux which is ten times smaller.

Operating the valve in fully-open mode we see an increase in CH signal of nearly a factor of 2 as compared to the solenoid valve. However, the special design of the nozzle prevents access to the high density region just in front of the aperture which typically decreases the dissociation efficiency. Furthermore, the nozzle shape, affects the temperature of the gas pulse. It restricts the full, free expansion and thus limits the cooling which results in a slightly hotter CH beam as compared to the solenoid valve. Note that this could also be due to the fact that the dissociation
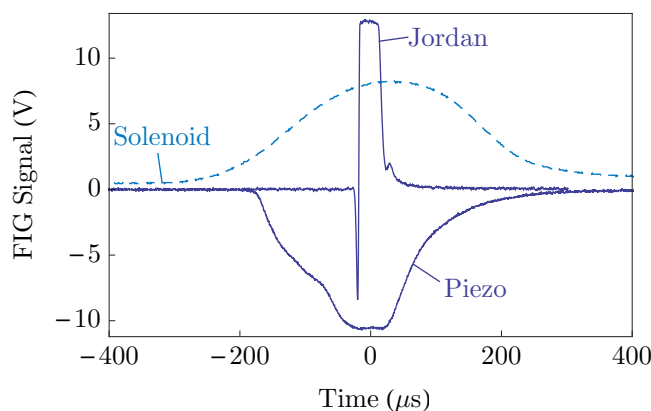
FIGURE 3.18: The signal of a fast ionisation gauge (FIG) as the pulse from three different valve types passes through it. The signal of the piezo valve has been inverted for clarity. The Jordan valve provides the pulse with the highest peak flux of precursor molecules and thus also yields the most CH molecules.

takes place in a region where most of the expansion has happened already which again limits the cooling effect. The main advantage of the nozzle shape is that it enhances the on axis flux as shown by Even and Lavie in [165].

Valve Comparison

Figure 3.18 compares the pulse amplitudes and widths of the three different valve types measured with a fast ionisation gauge. The Jordan valve produced the most intense CH beam, which we attribute to the higher precursor density in the dissociation region. However, it can only operate at a maximum repetition rate of 10 Hz and the resulting CH beam suffered from large temperature fluctuations which caused random drifting of the time-of-flight of the molecules. The piezo valve released the same peak number of precursor molecules, however the resulting CH beam had a slightly lower intensity than the Jordan valve. We attribute this to the fact that the high density area in front of the nozzle aperture is inaccessible due to the shape of the nozzle which decreases the dissociation efficiency. We have recently received an adapted version of the piezo valve which allows us to move the excimer beam close to aperture. We have not yet had the chance to test it. The advantage of the piezo valve is that it can operate at high repetition rates with minimum pumping requirements. With the solenoid valve we are currently limited to a repetition rate of 10 Hz at optimum CH flux. By optimising the piezo valve conditions we should be able to increase that to 40 Hz.

If it was possible to operate the piezo valve or the Even-Lavie valve with 7 μs pulses it would reduce the gas load by a factor of 35 as compared to a solenoid valve. This means that an experiment which is now limited to 10 Hz due to the large gas load of the solenoid valve, could run at rates as high as 350 Hz.

3.4.10 Skimmer Interference

The very first molecular beams used apertures to extract the center-line beam from a high pressure source chamber. With the invention of the supersonic source people realised that one has to be very careful where to position these apertures in order to avoid hydrodynamic shock structures and interference with gas molecules reflected from the aperture walls. To minimize such beam disruptions aerodynamic beam skimmers have been developed. The influence of these long conical apertures on the beam intensity has been studied over many decades. However, most studies that investigate the ideal position of the skimmer with respect to the nozzle were done for the case of continuous beams and the findings were simply copied to the pulsed beams without changes [165].

With modern turbomolecular pumps and fast pulsed valves one can keep the background pressure in the source chamber low enough to avoid the main problems faced by these early experiments. This means that the pressure between two pulses is low enough to move the shock wave of the supersonic expansion (zone of silence) to many cm from the nozzle. The simulations of Luria and colleagues show that in the extreme case for high pressure (100 bar) pulsed supersonic sources a skimmer placed 200 mm downstream from the nozzle can have severe effects on the beam temperature. The gas heats up at the skimmer aperture which causes the gas to expand radially and thus decreases the on-axis density. Sharp edges with a thickness of only 3 µm can reduce these effects. In addition to that the skimmer transmission for such high density beams can be as low as 1% if the diameter of the skimmer aperture is chosen too small. In direct contrast to the earlier findings of continuous beams it is thus more favourable to place the nozzle far away from the skimmer. A general rule of thumb applies: the higher the backing pressure used the larger should the distance between the nozzle and skimmer be. Furthermore, skimmers with large apertures of 3-4 mm assure efficient transmission of the order of 60% even for backing pressures as high as 100 bar. It is still very common, especially in the physical chemistry community to have nozzle-to-skimmer distances of below 2 cm and to use skimmers with apertures as small as 1 mm which can seriously affect the beam quality. In order to investigate the dependence of the CH signal as a function of the skimmer-to-nozzle distance we upgraded our source translation assembly to allow for continuous adjustment of the z-axis as well.

3.4.10.1 Skimmer to Nozzle Distance

Recently the group of Prof. Kaiser at the University of Hawai'i at Mānoa reported experiments on the chemical dynamics of the CH radical with acetylene using crossed molecular beams [173, 174]. They bubble 2.2 bar of helium through liquid bromoform and expand the mix through a piezo actuated valve of the Proch-Trickl type (large piezoelectric disk displacing a sealing plunger) with a nozzle diameter of 0.96 mm. Such a valve typically yields gas pulses of 150 µs

duration. They then dissociate the bromoform molecules with a pulsed excimer laser operating at 248 nm with an energy of 60 mJ per pulse which is focused to 4×0.7 mm right in front of the nozzle. Following the tradition of the physical chemistry community they placed a skimmer 13±1 mm downstream from the nozzle. This should have a detrimental effect on the beam quality. However, they report a very high intensity beam of CH molecules. They claim to produce a CH density of $\rho = 10^{12} \, \text{cm}^{-3}$ at $L = 4$ cm downstream from the nozzle [174] which corresponds to a flux $\Phi = \rho v L^2 = 2.7 \times 10^{18} \, \text{sr}^{-1} \, \text{s}^{-1}$ for a velocity $v = 174\,000 \, \text{cm} \, \text{s}^{-1}$. Assuming a typical FWHM of the pulse of 10 µs for a helium beam this corresponds to a staggering flux of $10^{13} \, \text{sr}^{-1}$ per pulse ($10^{18} \, \text{sr}^{-1} \, \text{s}^{-1}$), or nearly a factor of 10^4 larger than what we measure. Let's quickly put that into context of what we would expect from an ideal supersonic source. An ideal supersonic expansion of 2.2 bar helium releases $1.66 \times 10^{22} \, \text{sr}^{-1} \, \text{s}^{-1}$. The fraction of precursor molecules in the gas mix is 0.2% which yields a flux of precursor molecules of $3.3 \times 10^{18} \, \text{sr}^{-1} \, \text{s}^{-1}$. We now have to account for the fact that only a fraction of the gas pulse interacts with the excimer laser beam, which is much shorter than the gas pulse itself. The interaction time of the excimer laser with the gas pulse is $d/v = 3$ µs, where d is the width of the excimer beam along the molecular beam axis and v the velocity of the molecules. Hence the excimer beam only interacts with a fraction of $< 3/100$ of the molecular beam that emerges from the pulsed valve. Accounting for that, the total flux expected from this ideal supersonic source which dissociates every bromoform precursor molecule that interacts with the excimer laser into a CH molecule is $10^{17} \, \text{sr}^{-1} \, \text{s}^{-1}$. This means Kaiser and co-workers produce 10 times more CH than there are precursor molecules in an ideal supersonic source. We measure a flux of $4.3 \times 10^{13} \, \text{sr}^{-1} \, \text{s}^{-1}$ using argon carrier gas and assuming an interaction time of the excimer laser with the gas pulse of 9 µs, our CH quantum efficiency of 10^{-4} ties in with the measurements of Romanzin and colleagues who measured $(5 \pm 2.5)10^{-4}$ in a low pressure flow cell [153].

To summarize: our source is exactly the same as Kaiser's apart from the nozzle to skimmer distance and a lower flux by a factor of 10000. Kaiser mentions in their most recent paper that the intensity of the CH beam strongly depends on the nozzle-to-skimmer distance [174]. They mounted the valve onto vacuum compatible translation stages to optimise the CH flux. From all the considerations above we find it unlikely that they measured the right density. However, to investigate whether we could increase the flux by adjusting the skimmer-to-nozzle distance we bought a high precision ultra high vacuum compatible translation stage (VG Scienta Miniax ZXYZ1015) and attached the piezo valve to it. This means that we are now able to adjust the skimmer to nozzle distance smoothly from 0-10 cm with an accuracy of 5 µm. Furthermore, we can optimise the valve position in x and y with a resolution of 1 µm. We locked the laser on the CH transition and while we were monitoring the signal we changed the valve to skimmer distance continuously until the signal changed. We then re-optimized the excimer beam position and moved the valve again. Unfortunately we did not see a sudden increase in signal close to the skimmer, but rather a continuous decrease from a skimmer-to-nozzle distance of 50 mm onwards. This is shown in figure 3.19. We also noticed a continuous increase in the translational
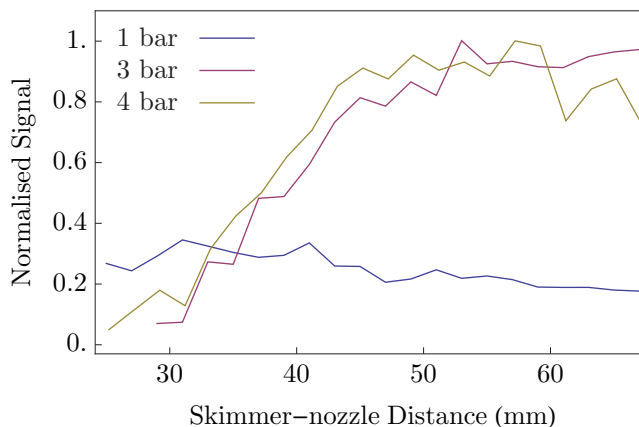
FIGURE 3.19: The normalised CH signal as a function of the skimmer-nozzle distance. We used argon carrier gas at three different stagnation pressures. This final data set was taken by fellow PhD student Darren Holland.

temperature of the molecules as we approached the skimmer which agrees with the simulations of Even and co-workers. We repeated this measurement for various stagnation pressures. For lower stagnation pressures we could approach the skimmer a bit further than $50\,\text{mm}$, but the overall signal was less.

3.5   Conclusion

We have built, tested and extensively characterised in total 4 different production methods for the CH molecule. We have identified the main limitations of the different sources and identified the production method most suitable for our purposes: the photodissociation of bromoform. It yields a CH flux of $3.5 \times 10^9\,\text{sr}^{-1}$ per pulse in a single quantum state ($J = 1/2, -, F = 1$). The time-of-flight profile has a width of $92\,\text{µs}$ measured $0.79\,\text{m}$ downstream from the nozzle which corresponds to a translational temperature of the CH molecules of $0.4\,\text{K}$ only. The molecules move at a velocity of $570\,\text{m}\,\text{s}^{-1}$ when argon is used as a carrier gas. Both the low translational temperature and the centre velocity are very close to the values of the ideal supersonic expansion. Helium, neon and krypton have been tested as well and yield similar fluxes. It is also a very stable source which yields a sufficiently high flux for high resolution spectroscopy experiments. We have further carefully calibrated the fluorescence detector which makes it possible to measure the absolute flux of CH molecules to high accuracy.

John Weinstein from the University of Reno in Nevada pointed out that the laser ablation of iodoform (CHI_3) in a buffer gas cell might be another option for a high CH yield. He measured a relative absorption of the detection laser beam tuned to the X-A transition of 0.5%. He expects to extract a beam with an intensity of 10^{12} - $10^{13}\,\text{sr}^{-1}\,\text{s}^{-1}$. For a typical buffer gas cell the molecular pulse after ablation is a few ms long which means he is aiming at generating

10^9-10^{10} sr^{-1} per pulse. The big advantage is that the CH molecules emerging from such a source travel with a speed of $200\,\mathrm{m\,s^{-1}}$. Iodoform, however, comes in powder form and it is well known that powders do not ablate well and lead to large shot-to-shot fluctuations. It might be possible to grow a crystal of iodoform or press it into a solid target.

Chapter 4

Searching for Variations of Fundamental Constants Using CH Molecules

4.1 Introduction

> *If the Lord Almighty had consulted me before embarking on creation thus, I should have*
> *recommended something simpler.*
>
> King Alfonso X of Castile

Currently we describe gravity by general relativity and the three other interactions by the standard model of particle physics. Within this theoretical framework we must consider 22 free parameters [46]. These are the Newton constant, G, the Yukawa coefficients that fix the masses of the six quarks and the three lepton flavours, two parameters for the Higgs field, four parameters for the CKM matrix, a phase for the QCD vacuum and three coupling constants. Additionally we need to add the speed of light and the Planck constant. In order to include massive neutrinos one has to add another 7 parameters. These free parameters are often referred to as fundamental constants. Fundamental because their numerical values cannot be derived from a fundamental principle. We fix these free parameters by measuring them. The failure of our theoretical model to explain these numbers can thus be seen as the failure of the model itself.

As mentioned in the introduction already theories that attempt to extend the standard model treat these parameters rather as dynamical variables which change with the evolution of the universe. In higher dimensional theories such as string theories for example the values of the fundamental constants depend on the size of the extra dimensions. Their size might change in

a similar way to the observed expansion of the universe causing the constants to change as well.

Theories of dark energy also predict variation of such constants. In particular, these theories hypothesize that a long range (nearly massless) scalar field is responsible for the observed accelerated expansion of the universe. This field couples to matter and the strength of the fundamental forces become dependent on the value of the local scalar field. Such a scalar field should be detectable through tests of the equivalence principle or fifth force experiments on Earth. So far, however, no evidence has been found in such experiments. Khoury and Weltman suggested in 2004 that the mass of the field, and thus its range, depends on the local matter density [51]. Therefore, it satisfies the constraints of equivalence principle tests, but can evolve on a cosmological scale where the matter density is typically 10^{30} times smaller. They dubbed such scalar fields chameleons. Based on this idea, Olive and Pospelov developed a model in 2008 that predicts variations in fundamental constants such as elementary particle masses and coupling constants with the local matter density [175]. By comparing the value of the coupling constants on Earth with the coupling constants in low density interstellar clouds we can test such chameleon models.

The study of the variation of constants on a cosmological scale is also a test of the equivalence principle on cosmological scales. A variation of fundamental constants implies violation of the universality of free fall, of Lorentz invariance and thus of CPT invariance. The search for such variations thus offers a unique means for testing new physics beyond the standard model and general relativity.

In particular, the test of two such constants, the fine structure constant α and the electron-to-proton mass ratio μ has attracted much interest over the last decade. The fine structure constant α as such is not a fundamental constant according to the definition presented above, but is related to the electromagnetic coupling constant of the standard model via the renormalisation group and the Weinberg angle. The electron-to-proton mass ratio is also not a fundamental constant as such, as it includes the mass of the proton which is not a fundamental particle but consists of gluons and two quarks. The gluons make up for most of the mass of the proton and μ is therefore proportional to the QCD energy scale Λ_{QCD} which is related to the strength of the nuclear force. The electron mass m_e is related to the vacuum expectation value of the Higgs field and thus to the scale of the weak nuclear force.

Why are these two constants of particular interest? Simply because their size influences the electromagnetic spectra of atoms and molecules. And if physicists have mastered a technique over the last century then it is the precise spectroscopy of atoms and molecules which approaches accuracies in the 18th decimal place. Furthermore, we can record such spectra from distant astronomical objects, compare them to laboratory values to search for differences and thus probe for variations on a cosmological scale.

How do such spectral lines shift with changing constants? Let's start with the simplest case of the Lyman-α transition in the hydrogen atom. The transition angular frequency ω for the

case of an infinitely massive nucleus can be written in terms of the fine structure constant α as

$$\omega = \frac{3}{8} \frac{m_e c^2 \alpha^2}{\hbar} , \qquad (4.1)$$

where m_e is the mass of the electron and $\hbar$ is the reduced Planck constant and c is the speed of light. The fractional change in transition frequency due to a change in the fine structure constant is thus

$$\frac{\Delta f}{f} = 2 \frac{\Delta \alpha}{\alpha} = K_\alpha \frac{\Delta \alpha}{\alpha} \qquad (4.2)$$

where $K_\alpha = 2$ is the so-called sensitivity coefficient of the transition to variations in the fine structure constant[1]. If we account for the mass of the nucleus and assume no change in the fine structure constant we can derive the sensitivity of the Lyman-α transition to variations in the electron-to-proton mass ratio $\mu = m_e/m_p$[2] by replacing the electron mass by its reduced mass,

$$\omega = \frac{3}{8} \frac{m_p m_e}{m_e + m_p} \frac{c^2 \alpha^2}{2\hbar} = \frac{3}{8} \frac{1}{1+\mu} \frac{m_e c^2 \alpha^2}{2\hbar} , \qquad (4.3)$$

where, m_p is the mass of the proton. The fractional change of the transition frequency if μ changes becomes

$$\frac{\Delta \omega}{\omega} = -\frac{\mu}{(1+\mu)} \frac{\Delta \mu}{\mu} = K_\mu \frac{\Delta \mu}{\mu} , \qquad (4.4)$$

where $K_\mu = -\frac{\mu}{1+\mu} \simeq \mu \simeq -5.4 \times 10^{-4}$ is the sensitivity coefficient of the transition to variations in the electron-to-proton mass ratio. Note that the sensitivity coefficients depend on the units that are used. It is common in the literature to use atomic units ($\hbar = m_e = e = 1$). In atomic units the sensitivity coefficients for the Lyman-α transition are then $K_\alpha^{(a.u.)} = K_\alpha^{(SI)} - 2 = 0$[3] and $K_\mu^{(a.u.)} = K_\mu^{(SI)}$. In a measurement one must compare at least two transitions that shift differently with a changing fundamental constants, i.e. only the relative sensitivity coefficient matters.

The fractional shift of an atomic transition is very insensitive to changes in μ. This is quite unfortunate because some theoretical models predict that the variation of μ is considerably larger than the variation of the fine structure constant [177]. The situation changes for the case of molecular spectra. Molecules can vibrate and rotate. The vibrational energies scale with $E_v \propto \sqrt{1/\mu}$ which gives rise to a sensitivity coefficient of $K_\mu = -1/2$. The rotational energies scale with $E_r \propto 1/\mu$ which leads to a sensitivity coefficient of $K_\mu = -1$. As will be explained

---

[1]Note, that all atomic and molecular energy levels share the same sensitivity coefficient to first order ($K_\alpha = 2$). To search for variations of fundamental constants one must therefore compare at least to two transitions with different sensitivity coefficients. In atoms such a difference can arise from second order effects such as relativistic corrections and are typically of the order of $\Delta K_\alpha = 10^{-3} - 10^{-2}$.

[2]It is common to define μ as the proton-to-electron mass ratio m_p/m_e. We, however chose this definition to be consistent with Kozlov who calculated the sensitivity coefficients for CH using the definition $\mu = m_e/m_p$ [176].

[3]The natural energy scale for atoms and molecules is the Rydberg constant which is proportional to α^2. Therefore all atoms and molecules have the same dependence on α to first order. Since it is necessary to compare at least two transitions to search for a drifting α one needs to find transitions with a large differential sensitivity coefficient ΔK_α. Two fine-structure doublet states in atoms for example typically have $\Delta K_\alpha \simeq 10^{-3}$.

later in more detail, the coupling of angular momenta in molecules leads also to large differential sensitivity coefficients ΔK for different transitions within the same molecule.

These considerations should only highlight the difference in molecular and atomic spectra and introduce the concept of sensitivity coefficients. For more complicated atoms or molecules the calculation of these sensitivity coefficients is not so trivial. There are relativistic corrections, there is coupling of angular momenta, fine and hyperfine structure. Each of these additional terms depends differently on fundamental constants. In the case of the dysprosium atom, for example, a near degeneracy between two opposite parity states leads to an enhancement of the sensitivity. The two levels move in opposite directions if α varies which results in a sensitivity of the radio frequency transition between the two states of $K_\alpha \approx 10^6$ [178]. Recently the group of Budker at Berkeley used a hot beam of dysprosium atoms to test for the temporal evolution in the fine structure constant. Their result $\Delta\alpha/\alpha = (-5.8 \pm 6.9) \times 10^{-17}$ per year is consistent with no change [179].

One can also compare two atomic clocks whose transition frequencies have different sensitivity coefficients. By comparing an aluminium and a mercury single-ion optical clock Rosenband et al. could constrain the temporal variation of the fine-structure constant to $-1.6 \pm 2.3 \times 10^{-17}$ per year [53].

Accidental degeneracies such as in dysprosium are quite rare in atoms. In molecules, however, they do occur more often due to the additional degrees of freedom. In particular, ammonia (NH_3) and the carbon monoxide molecule (CO) have been suggested as suitable candidates for a search for variations of μ [180] in the laboratory. It turns out that a certain rotational transition in CO possesses a large sensitivity of $K_\mu = -302$. A second transition in the same molecule shifts in the opposite direction with a sensitivity of $K_\mu = 202$. The combined transitions thus have a sensitivity 500 times larger than ordinary rotational transitions. Additionally, the opposite shift of the two levels rejects systematic errors that could imitate a change in μ.

The current most stringent laboratory constraint on μ-variation stems from the comparison of the Cs standard to optical clocks and was measured to be $\Delta\mu/\mu = (1.6 \pm 1.7) \times 10^{-15}$ per year [54][4]. Another measurement compared a rovibrational transition in the SF_6 molecule to the Cs frequency standard and sets a limit of $\Delta\mu/\mu = (-3.8 \pm 5.6) \times 10^{-14}$ per year [181].

Such laboratory experiments put tight constraints on the variation of fundamental constants at the present. Astronomical measurements of atomic and molecular spectra, on the other hand, can probe for variations on cosmological scales. These measurements are less precise than the current lab based methods, but probe over completely different time and length scales. Furthermore, measurements in dilute interstellar gas clouds where the matter density is usually 10^{20} times lower than on earth allows searching for chameleon fields.

In 1956, Savedoff was the first to compare astronomical spectra with laboratory spectra in order to investigate if $Z = g\mu\alpha^2$ has the same value in a galaxy 3×10^8 light years away by

---

[4]Note that the hyperfine structure of atomic transitions can be sensitive to μ.

comparing fine structure emission doublets of nitrogen and neon with the hydrogen 21 cm hyperfine line [182]. He found $\Delta Z/Z = 3.3 \pm 3.2 \times 10^{-3}$ and thus no change.

The discovery of quasars by Maarten Schmidt in 1963 stimulated George Gamov to propose a test of the constancy of the fine structure constant using such high redshift[5] objects [183]. In the same year Schmidt and his colleague John Bahcall set out to do the experiment. In contrast to Savedoff they used absorption spectra of silicon and measured $\Delta\alpha/\alpha = (1 \pm 2) \times 10^{-3}$ at a redshift of $z = 1.95$ which corresponds to a look-back time of 10.2 Gyr. Until 1999 only a handful of quasar absorption spectra have been analysed for a potential variation in α and another handful for a variation in μ. They all provide null results on the level of $\Delta\alpha/\alpha < 10^{-4}$. Uzan provides an extensive summary of these efforts in [46, 184].

It should be pointed out that the analysis of relative isotope abundances and fission products of natural reactors provided tight constraints on α variations on the 5×10^{-8} level over the last 2 billion years and thus attracted much more attention between the 1970s and 1990s [185]. A recent reanalysis of this data, however, found the positive result that the value of α has slightly decreased over the last 2 billion years ($\Delta\alpha/\alpha > 4.5 \times 10^{-8}$) with 6σ confidence [186]. The results from these natural reactors tend to be model dependent, requiring assumptions about the constancy of other parameters, as well as modelling of the nuclear reactions the actual physical conditions in the reactor.

The situation changed when high resolution telescopes, such as Keck and VLT became available by the mid to end of the 1990s. At the same time Webb and colleagues conceived the idea of the many multiplet method [187]. For over three decades observations concentrated on the measurement of the fine-structure splitting of alkali atoms (doublets) measured in gas clouds against the background light of quasars. The separation between these lines is proportional to α^2 (in atomic units). Any change in the separation of these doublets would indicate a variation in α. Webb et al., however, showed that one can increase the sensitivity by an order of magnitude by comparing doublets and multiplets of different atomic species [178, 187]. The difference in the sensitivity coefficient for different atomic species can be much larger than the relative sensitivity of a fine structure doublet that shares the same ground state. The sensitivity mainly stems from relativistic corrections which are large for the electronic ground state. These corrections scale with the square of the atomic charge. Thus heavy atoms such as Fe show a larger sensitivity than lighter atoms such as Mg. Other transitions might even shift in the opposite way due to many body effects.

By the end of the 1990s the Keck telescope in Hawai'i provided high resolution data from about 30 quasar absorption systems. The precision of some of these spectra even exceeded the

---

[5]The redshift z we are talking about here is defined by the frequency shift of an emitted frequency f_e from an object due to the expansion of the universe. We observe the redshifted frequency f_o. The redshift z is then defined as $1 + z = \frac{f_e}{f_o}$. Using a cosmological model for the expansion of the universe we can relate the redshift to the time when the observed object emitted the light. For common parameters for the matter density ratio $\Omega_m = 0.27$ and the present day Hubble constant $H_0 = 70$ km/s/Mpc a redshift of $z = 1$ corresponds to a look-back time of approximately 7.8 Gyr and a redshift of 10 to a look-back time of 13.2 Gyr.

accuracy of the available laboratory spectra at that time. The Australian group around Webb, Murphy and Flambaum analysed more and more absorption systems and concluded that α had a smaller value ten billion years ago. They measured $\Delta\alpha/\alpha = (-0.74 \pm 0.17) \times 10^{-5}$ by 2004 after analysing 143 absorbers using data from Keck [188] for redshifts of $z > 1.8$. By 2004, five years of data from VLT in Chile was accumulating which allowed them to cross-check their findings using a completely different telescope and spectrograph. The results were quite puzzling because as more and more VLT spectra were analysed it clearly showed opposing results to the Keck data for high redshift. Using VLT they found $\Delta\alpha/\alpha = (+0.61 \pm 0.2) \times 10^{-5}$ for redshifts of $z > 1.8$. They then realised that the two telescopes are probing different parts of the sky and plotted the variations along the sky for the different line of sights. Fitting to the data they found a 4.1σ significance in favour of a dipole over a monopole model [189]. This means that α not only varies over time but also over space. Even when they fitted to the data from the individual telescopes they found a dipole-like dependence of α. The two individual dipoles surprisingly pointed in the same direction and had the same amplitude. Even in the equatorial plane where the Keck and VLT look in the same directions they did not find any evidence for inconsistency. This would mean that there is a spatial gradient of the values of α throughout the universe. As Earth moves through this gradient we should see a relative annual variation of $\Delta\alpha/\alpha = 10^{-20}$ [190].

Note that this analysis was made using archival data. The first dedicated measurement to search for a variation in α using VLT is currently in progress. Webb and colleagues assume that the relative isotope abundances are similar to the ones on Earth. Agafonova and colleagues could show that this is in general not the case and that the heavy isotopes of Mg are indeed overabundant at high redshifts [191]. Molaro and colleagues re-analysed the Keck dataset of Murphy et al. [188] with and without the Mg data. The data including the Mg lines yields $\Delta\alpha/\alpha = (-4.8 \pm 1.2) \times 10^{-6}$. Without the Mg data they get $\Delta\alpha/\alpha = (-1.1 \pm 1.7) \times 10^{-6}$ [192]. They could further convincingly show that the error bars used by Murphy et al. were underestimated.

Comparing heavy to light atoms is problematic because the spectra can have completely different origins in the gas cloud. This leads to different velocity profiles and thus to relative Doppler shifts which could mimic a variation in α. There are also known calibration issues of the spectrographs. Griest et al. for example showed that the Keck spectra could be subject to calibration errors which could lead to systematic errors as large as 30 ppm per night and 120 ppm over several nights [193]. They found serious systematic errors arising from a failure to calibrate the Keck spectrograph to the precision needed, and could produce any result, from significant detections of either sign to strong null limits using a single source at $z = 2.309$. Van Weerdenburg et al. on the other hand found good agreement between Keck and VLT using H_2 and HD lines from an object at $z = 2.059$ at the accuracy level of 5×10^{-6} [194]. New spectrographs such as the ESPRESSO project or the use of femtosecond frequency combs for accurate wavelength calibration will be a major step towards solving such calibration issues [195].

Molecular hydrogen lines can be used to constrain variations in μ. It is the most abundant molecule in the Universe and has numerous UV rovibrational transitions. The main challenge using hydrogen is the difficulty in detecting it. The transitions are weak and redshifted absorbers are hidden in the so-called Lyman-α forest. Four of these systems have so far produced constraints with the highest accuracy of $\Delta\mu/\mu = (0.3 \pm 3.2_{\text{stat}} \pm 1.9_{\text{sys}}) \times 10^{-6}$ obtained by King and colleagues in 2011 [196] using VLT and an absorber at $z = 2.811$.

The positive result of the Australian group remains the only strong positive result. Nevertheless, the result stimulated great interest to search for variations of fundamental constants by comparing astronomical to laboratory spectra. More and more groups become involved and new sensitive probing methods are invented.

All the results discussed above come from transitions in the visible and UV. The most accurate astronomical measurements of cosmological variation in α or μ are obtained from observations using radio frequency and microwave transitions in molecules. The most stringent limit for μ variation at non-zero redshift has recently been obtained from absorption lines of methanol, with the result $\Delta\mu/\mu = (0.0 \pm 1.0) \times 10^{-7}$ at a redshift of $z = 0.89$ [197]. Several transitions could be observed each having a different sensitivity coefficient. By only using methanol, systematic errors due to the different velocities of different species were avoided. Kanekar and colleagues used microwave transitions in OH in combination with hydrogen lines to constrain α variation to $\Delta\alpha/\alpha = (-1.7 \pm 1.4) \times 10^{-6}$ over the last 6.7 Gyr ($z = 0.765$) [198].

Although molecules provide exceptional sensitivity there are until now no known sources for molecular microwave spectra at redshifts comparable to those where Murphy and colleagues find the largest spatio-temporal variation ($z > 1.5$). An exception are far infrared rotational lines in CO which have recently been found at an exceptionally large redshift of $z = 5.2$ which corresponds to a look back time of 12.9 Gyr [199]. However, the lines were too weak and too wide to provide accurate results. The results obtained is consistent with both the dipole and no variation, yielding a constraint of $|\Delta\alpha/\alpha| < 8 \times 10^{-6}$.

Measurements using methanol spectra (CH_3OH) in our own galaxy are extremely precise and constrain the variation in μ with matter density at the level of $|\Delta\mu/\mu| < 2.9 \times 10^{-8}$ with 1σ uncertainty [200]. Levshakov et al. also compared the inversion transitions in ammonia (NH_3) to rotational transitions in cyanoacetylene (HC_3N). The results, when interpreted as a change in μ suggest $\Delta\mu/\mu \sim 2.6 \times 10^{-8}$ with 8σ significance. However, it is now known that the spectra obtained at the 100 m telescope at Effelsberg suffered from a combination of hard and software bugs [201]. Using recent data from the Medicina 32 m telescope in Bologna and the 45 m telescope in Nobeyama they corrected this result and get the very tight constraint of $|\Delta\mu/\mu| < 3 \times 10^{-9}$ with 1σ confidence [201].

To summarise: there is some evidence for variation in constants (especially at high redshift) and some evidence against. Dedicated experiments at Keck and VLT with improved calibration techniques and measurements with other telescopes will help to confirm or refute the spatial gradient. The sensitivity of molecular spectra to variations in fundamental constants exceeds
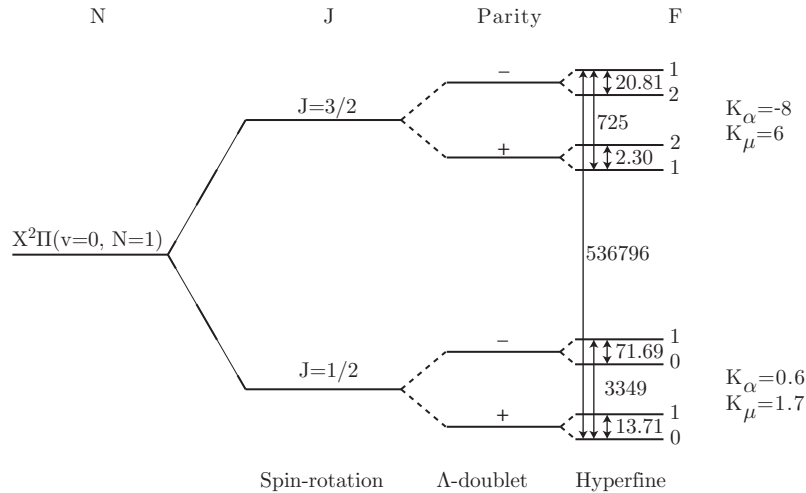
FIGURE 4.1: The level diagram of the $X^2\Pi(v = 0, N = 1)$ including fine and hyperfine structure and the sensitivity coefficients for the two Λ-doublets (averaged over the hyperfine structure, taken from [176]).

electronic transitions by up to three orders of magnitude. In addition, molecules provide multiple transitions that can even shift in opposite directions which can eliminate many systematics that originate from comparing different species. However, the laboratory frequencies of molecular spectra are often not known accurately enough or have not been measured at all. Furthermore, molecules are hard to find in outer space, particularly at high redshift.

In 2009 Kozlov pointed out that molecules with Λ-doublets can have large sensitivity coefficients to variations in both α and μ [176]. He analysed NO, LiO, CH and OH and found that the sensitivity of CH and OH is further enhanced by J-dependent decoupling of the electron spin from the molecular axis. For OH this decoupling happens in the $J = 9/2$ excited state and leads to exceptional sensitivity of $K_\alpha = -922$ for the $(J = 9/2, F = 5) - (J = 9/2, F = 4)$ transition. However, the transition frequency at $88.95\,\mathrm{MHz}$ is unlikely to be detected by any radio telescope. For CH this decoupling happens in the first excited $J = 3/2$ state. Compared to OH the sensitivity of the $J = 3/2$ transition in CH is lower with $K_\alpha(J = 3/2) = -8$, but it has been detected in cold, interstellar gas clouds already [202]. Moreover, the sensitivity coefficient of the $J = 1/2$ transition is positive $K_\alpha(J = 1/2) = +0.6$. The $J = 1/2$ doublet transition thus shifts opposite compared to the $J = 3/2$ transition. A level diagram of the $X^2\Pi(v = 0, N = 1)$ state of CH including the sensitivity coefficients is shown in figure 4.1. Two astronomical measurements recorded both lines from a single gas cloud [202, 203]. However the $J = 3/2$ transitions have not previously been measured in the lab at all and the $J = 1/2$ only to insufficient accuracy to be useful for our purposes.

We have measured all three hyperfine lines of the $J = 1/2$ Λ-doublet and all four hyperfine lines of the $J = 3/2$ Λ-doublet in order to use CH as a new, sensitive probe for variations in fundamental constants.

4.2   How to Measure the Λ-doublet Transitions in CH?

The precise measurement of transition frequencies in atoms or molecules owes much to Norman Ramsey. The techniques developed by Ramsey are based on the magnetic resonance technique which was invented by his doctoral adviser Isidor Rabi. Ramsey developed this technique further which allowed physicists to reach such high precision that it gave rise to the redefinition of the SI second [204]. Both, Rabi and Ramsey, were awarded the Nobel prize in physics (see introduction, for more details): Rabi in 1944 "for his resonance method for recording the magnetic properties of atomic nuclei" and Ramsey in 1989 "for the invention of the separated oscillatory fields method and its use in the hydrogen maser and other atomic clocks". The accuracy with which one can measure a transition frequency which is not limited by spontaneous decay is only limited by the interaction time with the electromagnetic field. So in principle longer interaction regions should lead to narrower lines. Rabi and Ramsey, however, immediately realised that in practice this was not the case because it was impossible to create completely uniform magnetic fields for their magnetic resonance experiments over long interaction times. Hence, the resonances frequently broadened far beyond the theoretical predictions [205].

Ramsey joined Harvard University in 1947 and set up his own lab. When designing his new beam apparatus he naturally wanted to maximise the spectral resolution. While struggling with the problem of how to achieve uniform magnetic fields he recalled a lecture by Philip Dee from his time at Cambridge about the Michelson stellar interferometer. Dee suggested that: "if the resolution of your telescope is not quite high enough to determine whether an object is a single or double star, simply paint the middle of the mirror black. The image will be dimmer but almost twice as sharp" [206]. It was Ramsey's ingenious idea to adapt this concept for his molecular beam apparatus. By using two pulses (two phase coherent short $\pi/2$ pulses separated by a long free evolution time T) instead of a single long π-pulse he could create an atomic interferometer which overcomes the restrictions of the traditional method and yields a linewidth which is twice as narrow. Ramsey conceived his idea as a tool for precision spectroscopy and, as it is often the case with ground-breaking inventions, they become useful beyond the initial applications. It has become *the* experimental protocol for manipulating quantum states which led to the most recent Nobel prize in physics for Serge Haroche and Dave Wineland. May it be for the manipulation of fields in cavities, of vibrating atoms and ions in traps or even of large systems that behave as artificial atoms, Ramsey's methods can be applied. It is also used in quantum information science to prepare atoms in superpositions, to build quantum gates and demonstrate quantum-computation algorithms and is especially useful to protect them against decoherence.

It is also Rabi's and Ramsey's methods that we use to measure the Λ-doublets of both the $J = 1/2$ and the $J = 3/2$ state of the ground electronic and vibrational state of CH to unprecedented accuracy. In the previous chapter the methods to produce a molecular beam of CH molecules were presented. The most versatile and stable source for high resolution spectroscopy
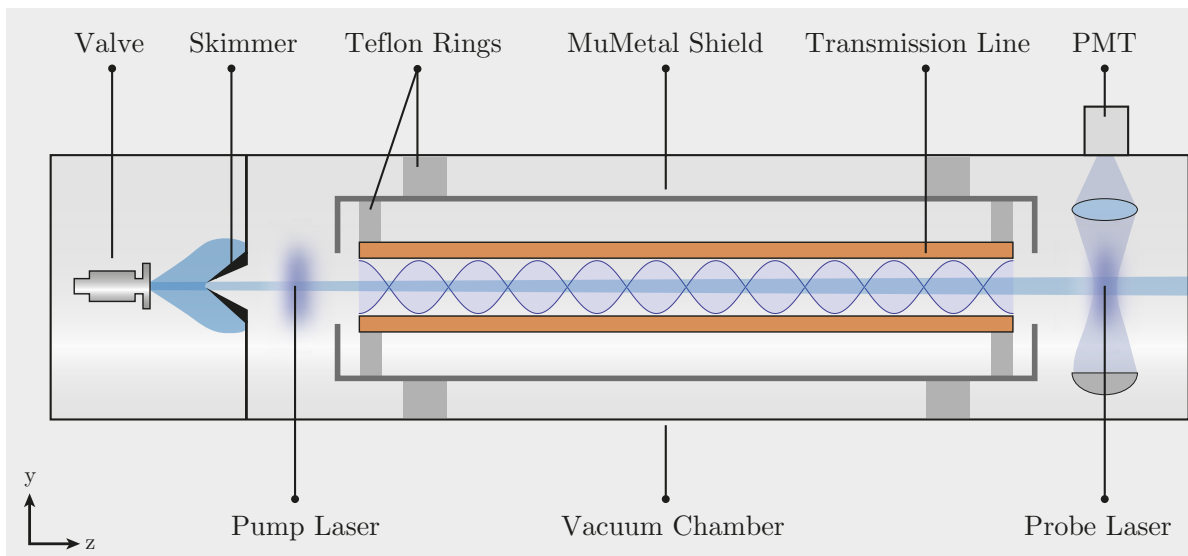
FIGURE 4.2: A sketch of the experiment to measure the Λ-doublet transitions of CH (not drawn to scale). The molecular beam is produced via photolysis of bromoform as described in the previous chapter. The beam is skimmed and passes through a state selector (pump laser). The molecules then enter a magnetically shielded interaction region where we drive the transition. Finally, the molecules are detected by laser induced fluorescence.

experiments is the photolysis of bromoform. It provides a decent flux of CH molecules, but more importantly is extremely stable, i.e. there are no drifts of the arrival time, the shot-to-shot variations are minimal and it allows changing the velocity of the molecules by using different carrier gases.

Furthermore, the detector is capable of counting the total flux of molecules with high sensitivity and good efficiency. The use of a narrow continuous wave laser enables us to address individual hyperfine levels and to record the time-of-flight profile of the molecules in a single gas pulse with a temporal resolution of $5\,\mu s$. These features are ideal preconditions for precision spectroscopy experiments. All we needed to add is a microwave interaction region to drive the Λ-doublet transitions, a state selector and a magnetic shield to screen unwanted magnetic fields. We chose a transmission line resonator as interaction region. The reasons for that will be given in section 4.2.2. All we need to know for now is that the microwaves are launched along the molecular beam axis z and form a standing wave in a transmission line. A sketch of the setup is shown in figure 4.2.

4.2.1 Driving the Λ-doublet Transition with Microwaves - Theory

Before we get started with the experiment it is useful to discuss the theory of a molecular beam resonance experiment, so that we know what to expect and can identify potential systematic errors. The Hamiltonian describing the interaction of a two-level system (atom, molecule) with an oscillating electric field can be written as $H = H_0 + H_I$ (consult your favourite quantum

optics text book ([207] for example) for all the details) where

$$H_0 = \hbar\omega_1 \left|1\right\rangle \left\langle 1\right| + \hbar\omega_2 \left|2\right\rangle \left\langle 2\right| \tag{4.5}$$

with $\left|1\right\rangle$ and $\left|2\right\rangle$ the eigenstates of the unperturbed (field-free) Hamiltonian $H_0 \left|n\right\rangle = \hbar\omega_n \left|n\right\rangle$, for $n = 1, 2$. For microwaves polarised along y the interaction is governed by the electric dipole interaction

$$H_I = -\mathbf{d} \cdot \mathbf{E}(t) = -\left(Y_{12} \left|1\right\rangle \left\langle 2\right| + Y_{12} \left|2\right\rangle \left\langle 1\right|\right) \mathbf{E}_y(t) \tag{4.6}$$

where $\mathbf{d} = -e\mathbf{r}$ is the electric dipole operator, $Y_{12} = e\left\langle 1\left|y\right|2\right\rangle$ is the matrix element of the electric dipole moment along y and $\mathbf{E}_y = \hat{y}E_0 \cos\left(\omega t + \phi\right)$ is the oscillating electric field along y. We can to express the wavefunction $\left|\psi(t)\right\rangle$ of the two-level system that interacts with electromagnetic radiation as a linear combination of the eigenstates of the unperturbed Hamiltonian with time-dependent coefficients:

$$\left|\psi(t)\right\rangle = B_1(t) \left|1\right\rangle + B_2(t) \left|2\right\rangle . \tag{4.7}$$

Substituting equations 4.6 and 4.7 into the Schrödinger equation $i\hbar\partial_t \left|\psi\right\rangle = H \left|\psi\right\rangle$ gives two coupled differential equations for the probability amplitudes B_1 and B_2. Before solving these equations it is useful to transform the coordinates into the rotating frame by $b_n = B_n e^{-i\omega_n t}$ for $n = 1, 2$. We can also neglect the fast oscillating terms proportional to $e^{\pm(\omega_2 - \omega_1 + \omega)}$ (rotating wave approximation). This approximation holds because we are dealing with excitation close to the resonance frequency $\omega_0 = \omega_2 - \omega_1$. The two coupled equations then read

$$\dot{b}_1 = i\frac{\Omega}{2}e^{-i\phi}b_2 e^{i\delta t} \qquad\qquad \dot{b}_2 = i\frac{\Omega}{2}e^{i\phi}b_1 e^{-i\delta t} \tag{4.8}$$

where we introduced the Rabi frequency $\Omega = Y_{12}E_0/\hbar$ and the detuning $\delta = \omega - \omega_0$. We can write the solutions in matrix form

$$\begin{pmatrix} b_1(t) \\ b_2(t) \end{pmatrix} = M(\Omega, t_0, t, \phi) \begin{pmatrix} b_1(0) \\ b_2(0) \end{pmatrix} . \tag{4.9}$$

where M is a 2x2 matrix

$$M(\Omega, t_0, t, \phi) = e^{it\delta/2} \begin{pmatrix} \cos\left(Wt/2\right) - (i\delta/W)\sin(Wt/2) & (-i\Omega/W)\,e^{-i\phi + \omega t_0}\sin\left(Wt/2\right) \\ (-i\Omega/W)\,e^{i\phi + \omega t_0}\sin(Wt/2) & \cos\left(Wt/2\right) + (i\delta/W)\sin\left(Wt/2\right) \end{pmatrix} \tag{4.10}$$

with $W = \sqrt{\Omega^2 + \delta^2}$ and we allowed for an arbitrary start time of the interaction t_0. The matrix M propagates the initial state in time while the system is under the influence of electromagnetic radiation. In the case when all the molecules start in state $\left|1\right\rangle$ ($b_1(0) = 1$, $b_2(0) = 0$) the

probability of finding molecules in the excited state $|2\rangle$ after an interaction time $t = \tau$ becomes

$$P_2 = |b_2|^2 = \frac{\Omega^2}{W^2} \sin^2 \left(\frac{W\tau}{2} \right) . \tag{4.11}$$

We are using a transmission line resonator which consists of two counter propagating waves along the molecular beam axis z. This means that we need to add an extra phase term in equation 4.8 which accounts for the finite velocity of the molecules with respect to the standing wave. This phase shift is $\left(A_1 e^{-ikz} + A_2 e^{ikz} \right)$, where $k = 2\pi/\lambda$, λ is the wavelength of the microwaves in the transmission line, $z = vt$ and v is the velocity of the molecules. We can account for this extra phase by defining a generalised detuning $\Delta = \delta + \Delta\omega_D$, where

$$\Delta\omega_D = \omega_0 \frac{v}{c} \tag{4.12}$$

is the Doppler shift. If we neglect the Doppler shift for the moment and set the radiation to the resonance frequency then $W = \Omega$ and the population in the excited state oscillates with a specific frequency Ω. These oscillations are known as Rabi oscillations and Ω is the Rabi frequency, after Isidor Rabi who first observed these oscillations. For the case of electronic transitions these oscillations are usually washed out by the fast spontaneous decay of the excited state. However, the spontaneous emission rate scales with the cube of the transition frequency and thus becomes negligible for transitions in the radio frequency or microwave domain on time scales of a typical molecular beam experiment (1 ms). In such a case multiple Rabi oscillations between the two levels can be observed. From equation 4.11 we can infer that if the experimental conditions are set such that $\Omega\tau = \pi$ and $\omega = \omega_0$ the population is transferred from level $|1\rangle$ to level $|2\rangle$. Hence a pulse of resonant radiation of duration $\tau = \pi/\Omega$ is called a π-pulse. If we fix the time and amplitude of the microwave pulse to $\Omega\tau = \pi$ and scan the frequency we get the typical $\text{sinc}^2(x) = \sin^2(x)/x^2$ shape of the resonance the width of which is $\Delta f \simeq 1/\tau$. In such a single pulse experiment we can reach interaction times of the order of 1 ms which yields a linewidth of approximately 1 kHz. Molecules travelling with a velocity of $600 \, \text{m s}^{-1}$ then experience a Doppler shift of $\Delta\omega_D/(2\pi) = 6.6 \, \text{kHz}$ for a transition frequency of 3.3 GHz. We are using a standing wave microwave field which consists of two counter propagating waves. Each wave produces a resonance which is Doppler shifted by $\Delta\omega_D$ with opposing sign. If the interaction is long enough to produce a lineshape which is narrower than the Doppler shift we expect to observe two resonances which are split by twice the Doppler shift.

Due to the fact that the lifetime of the excited state is extremely long the associated natural linewidth is extremely narrow. The linewidth in our experiment is thus not limited by the lifetime of the excited state but rather by the limited interaction time τ. This is what is known as transit time broadening.

We use the Ramsey method, applying two short $\pi/2$ pulses separated by a period of free evolution for a time T. The first $\pi/2$-pulse creates a superposition of population in the two

states. The superposition freely evolves at the angular frequency ω_0 of the transition for a time T. Meanwhile the microwaves evolve at an angular frequency ω. The molecular superposition and the microwave field accumulate a phase difference $\Delta\phi = (\omega - \omega_0)T$. A second $\pi/2$-pulse applied after the free evolution T completes the transfer to the excited state with a probability proportional to $\cos^2(\Delta\phi)$. By measuring the excited state population as a function of the oscillator frequency we can resolve these so called Ramsey fringes and determine the resonance frequency. It might be surprising that one can extract information about an energy interval between two states from a field free region, but it becomes obvious from the simple consideration of a Fourier transformation of a pulse sequence which is analogous to double slit interference. The sine of the diffraction angle is then replaced by the detuning $\delta = \omega - \omega_0$ and the distance between the slits by the free evolution time T. The squared Fourier transform of two rectangular pulses of duration τ separated by a time T is

$$|b_2|^2 \propto \left(\frac{\sin(\delta\tau/2)}{\delta\tau/2} \right)^2 \cos^2 \left(\frac{\delta T}{2} \right). \tag{4.13}$$

The population oscillates with a period T and has a sinc^2, single pulse envelope of width $1/\tau$. This technique not only allows for longer interaction regions and thus higher resolution but furthermore yields a 40% narrower line width as compared to the ideal single pulse experiment.

To be more precise we can use the description we developed above and propagate the initial state vector with the matrix M for the first interaction of duration τ_1, is followed by a period of free evolution for a time T, described by a matrix F and the a second pulse of radiation of duration τ_2. The free evolution is simply described by

$$F = \begin{bmatrix} e^{i\omega_0 T/2} & 0 \\ 0 & e^{-i\omega_0 T/2} \end{bmatrix}. \tag{4.14}$$

The subsequent application of the matrix M and F to the initial state vector is then

$$\begin{pmatrix} b_1(t) \\ b_2(t) \end{pmatrix} = M(\Omega_2, t_1 + T, \tau_2, \phi_2) F(T) M(\Omega_1, t_1, \tau_1, \phi_1) \begin{pmatrix} b_1(0) \\ b_2(0) \end{pmatrix}. \tag{4.15}$$

If all the population starts in the ground state ($b_2(0) = 0$) the probability of exciting the molecule becomes

$$P_2 = \frac{1}{W_1^2 W_2^2} \left(\Omega_1^2 c_2^2 s_1^2 W_2^2 + \Omega_2^2 c_1^2 s_2^2 W_1^2 + \delta^2 \Omega_1^2 s_1^2 s_2^2 + \delta^2 \Omega_2^2 s_1^2 s_2^2 \right)$$
$$- 2 \frac{\Omega_1 \Omega_2}{W_1 W_2} s_1 s_2 \left[\cos\Phi \left(\frac{\delta^2 s_1 s_2}{W_1 W_2} - c_1 c_2 \right) + \sin\Phi \left(\frac{\delta c_2 s_1}{W1} + \frac{\delta c_1 s_2}{W_2} \right) \right] \tag{4.16}$$

with

$$W_1 = \sqrt{\Delta^2 + \Omega_1^2} \qquad W_2 = \sqrt{\Delta^2 + \Omega_2^2} \qquad \Delta = \delta + \Delta\omega_D$$

$$\Phi = T\Delta + \phi_O \qquad c_{1,2} = \cos\left(\frac{1}{2}W_{1,2}\tau_{1,2}\right) \qquad s_{1,2} = \sin\left(\frac{1}{2}W_{1,2}\tau_{1,2}\right). \qquad (4.17)$$

Here we added another phase term ϕ_O which is the difference in phase of the microwave field due to a change in position of the molecules along the transmission line between the two pulses. In the ideal experiment with no Doppler shift, we set $\tau_1 = \tau_2 = \tau$, $\Omega_1 = \Omega_2 = \Omega$, $W_1 = W_2$. The lineshape given in equation 4.16 then simplifies to the one given in [205]. If we simplify this further and assume that each pulse is an ideal $\pi/2$-pulse equation 4.16 reduces to

$$P_2(\delta) = \frac{4\pi^2 \sin^2\left(\frac{X}{4}\right)}{X^4} \left[X\cos\left(\frac{X}{4}\right)\cos\left(\frac{\delta T + \phi_0}{2}\right) - 2\delta\tau\sin\left(\frac{X}{4}\right)\sin\left(\frac{\delta T + \phi_0}{2}\right)\right]^2 \qquad (4.18)$$

where $X = \sqrt{\pi^2 + 4\delta^2\tau^2}$. In a molecular beam experiment the molecules, however, travel with a velocity of about $600\,\mathrm{m\,s^{-1}}$. Hence we cannot neglect the Doppler shift. In a Ramsey experiment, the Doppler shift enters as an additional phase as indicated in equation 4.16 and thus leads to a frequency shift. The Doppler shift is suppressed to first order by using a standing wave.

Now we should investigate the effect of a non-ideal, i.e. not perfectly balanced standing wave. In a good resonator the amplitudes of the two counter propagating waves are equal. As we characterised the transmission line we realised that there is a slight imbalance ϵ between the amplitudes of the two counter-propagating waves (this will be explained further in section 4.3). We can write the electric field in such an imperfect resonator as

$$E = \frac{E_0}{2}(1 + \epsilon)\cos(kz - \omega t) + \frac{E_0}{2}(1 - \epsilon)\cos(kz + \omega t). \qquad (4.19)$$

For perfectly balanced waves the two counter propagating waves lead to two Ramsey patterns with a relative phase difference of $2kz = 2kvT$. In the experiment we observe only the sum of the two which is proportional to $\cos^2(\delta T + kz) + \cos^2(\delta T - kz)$ which is $1 + \cos(2\delta T)\cos(2kz)$ which leads to a reduction of the contrast of the Ramsey fringes, but not to a systematic frequency shift. Note that this means that the contrast vanishes for velocities that satisfy $kz = \pi/4$. For the case of an ideal standing wave the Doppler shift of equation 4.23 cancels completely. If the standing wave is not perfect and there is a small imbalance between the two waves the Doppler shift does not cancel completely but is suppressed by the imbalance factor ϵ. We can get an expression for the position dependent phase shift of the microwaves by rewriting 4.19 using trigonometric identities,

$$E = E_0\sqrt{\cos^2(kz) + \epsilon^2\sin^2(kz)}\cos(\omega t - \phi_{\mathrm{im}}) \qquad (4.20)$$

where

$$\phi_{\mathrm{im}}(kz) = \tan^{-1}\left[\epsilon \tan\left(kz\right)\right]. \tag{4.21}$$

If the standing wave is not perfect this imbalance ϵ leads to a small phase shift in the microwave field $\phi_O = \phi_{im}$. We pulse the microwaves on when the molecules are at the antinodes of the transmission line resonator, simply because the smallest phase change is near the antinodes and because most of the microwave power will be located there. This means that we choose the free evolution time between the two pulses as an integer number of antinodes, i.e. $T = n\lambda/(2v)$ where n is an integer and v is the velocity of the molecules. Hence we pulse the microwaves on when the molecules are at positions $z_1 = z_0 + \delta z_0$ and $z_2 = z_1 + (1 + \epsilon_z)n\lambda/2$, where z_0 is the position of the antinode used for the first $\pi/2$ pulse and δz_0 and ϵ_z allow for a small imperfect timing of the microwave pulses due to a small uncertainty in the velocity of the molecules. Expanding the phase 4.21 around the antinodes gives a frequency shift due to an imperfect standing wave of

$$\Delta f_O \approx \epsilon\epsilon_z \left(\frac{v}{\lambda}\right). \tag{4.22}$$

Note that this frequency shift is independent of δz_0 to first order.

There is a second contribution to the velocity-dependent frequency shift. This comes about from the Doppler shift of the individual $\pi/2$ pulses. For a travelling wave and for ideal $\pi/2$ pulses, we can expand equation 4.16 about the resonance frequency. This yields a frequency shift of

$$\Delta\omega_{D,R} = \left(1 - \frac{4}{\pi}\right)\frac{\tau}{T}\Delta\omega_D, \tag{4.23}$$

due to the finite velocity of the molecules during the individual $\pi/2$ pulses. For a standing wave this further reduced by the imbalance factor ϵ.

4.2.2 Experimental Setup

The setup is shown in figure 4.2. It provides a convenient geometry for both Rabi and Ramsey experiments. As we have learnt from the previous section the linewidth in a single pulse experiment is $1/\tau$ and the resolution of a Ramsey experiment is set by the free evolution time T. In a molecular beam experiment both times are limited by the velocity of the molecules and the size of the vacuum chamber.

4.2.2.1 Transmission Line Resonator

A common way to drive a microwave transition is the use of waveguides or microwave resonators with small apertures to feed the molecular beam through the interaction region. These structures provide very well defined electric and magnetic fields and are thus ideally suited for such purposes. For driving the $J = 3/2$ Λ-doublet transition we need radiation at about $700\,\mathrm{MHz}$.

The dimensions of a WR-1150 waveguide which supports such microwaves is $29.2 \times 14.6 \, \text{cm}^2$ which simply does not fit into our vacuum chamber. An alternative is to use a parallel plate transmission line. Simply speaking this is a coaxial cable that instead of two cylindrical conductors consists of two parallel, conducting plates. Provided the plate spacing is smaller than half the microwave wavelength, the parallel plate transmission line supports only TEM waves meaning that there is no component of the electric or magnetic field in the propagation direction. Furthermore, the boundary conditions force the electric field to be perpendicular to the metal plates similar to a plate capacitor which defines the polarisation of the microwaves very well.

The output of a microwave synthesizer for such frequencies, however, is usually into a coaxial cable. A straight forward way to connect the coaxial cable to the transmission line is to split the coaxial cable and connect the centre core to one plate and the outer shield to the other plate. We use RG-405 (non-magnetic!) semi rigid coaxial cable $(50\,\Omega)$. The characteristic impedance of such a coaxial cable is

$$Z = \frac{1}{2\pi} \sqrt{\frac{\mu}{\epsilon}} \log \frac{d}{D} \qquad (4.24)$$

where, μ and ϵ are the magnetic permeability and the dielectric constant of the insulator between the two conductors, respectively and d/D is the ratio of the diameters of two conductors. By splitting the cable one abruptly changes the ratio d/D which in turn changes the impedance of the coaxial cable. Every change in impedance along a transmission line leads to reflections and interference between the incoming and reflected wave, which affects the coupling efficiency onto the plates. The same happens at the output of the parallel plate transmission line which can lead to very complex interference patterns and thus to a very complicated field distribution. By keeping the coupling region short and the splitting small compared to the wavelength we hoped to minimise the impedance mismatches. A small splitting means also a small spacing between the plates and hence we decided the minimum distance between the plates to be $d = 7\,\text{mm}$ which in turn fixed the width of the plates to $D = 53\,\text{mm}$ to achieve an impedance of $Z = \sqrt{\mu/\epsilon}(d/D) = 50 \, \Omega$. The length of the transmission line is limited by the length of the vacuum chamber to about $L = 50\,\text{cm}$. However, even for such a small splitting we found that only about one percent of the incident power was transmitted through the transmission line at $3.3\,\text{GHz}$ and the transmission was extremely sensitive to the shape and position of the in- and output couplers. Simply by changing the angle of the coax cable slightly we could change the coupling efficiency by a factor of 10. This was unsatisfactory and means that although the coupler is only about a tenth of the wavelength it has significant impact on the coupling efficiency. For low frequencies on the other hand (between 10 and $200\,\text{MHz}$) nearly perfect coupling could be observed. We tried to change the geometry of the coupler, to add trimming capacitors and to use a balun to balance the impedance, but nothing improved the coupling to our satisfaction. Hence we decided to leave one end open circuited so that a resonator is formed and produce a well defined standing wave. By cutting the length of the plates such
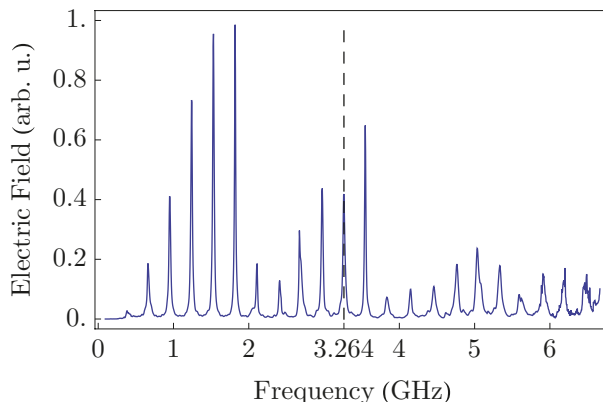
FIGURE 4.3: We excite the transmission line with one port of a vector network analyser. We then measure the electric field inside the transmission line resonator as a function of the frequency with a small antenna attached to the other port of a vector network analyser. If the plates are cut to the right length there is a resonance exactly at the resonance frequency of the molecules. The width of the resonance is about $30\,\mathrm{MHz}$. The dashed line shows the approximate transition frequency of the $(1/2^+, 1) - (1/2^-, 0)$ line at $3.264\,\mathrm{GHz}$.

that $L = nc/(2f)$, where n is an integer, c the speed of light and f the approximate transition frequency of the Λ-doublet match the resonant frequency of the transmission line to that of the molecule. We checked this by exciting the transmission line with one port of a vector network analyser (Agilent 8722ES) and measured the transmitted power as a function of the frequency with an electric field antenna placed between the plates and attached to the second port of the network analyser. A plot of the transmission as a function of the applied frequency is shown in figure 4.3. We found that fine adjustment to the length of the resonator was necessary to tune the resonance of the transmission line exactly to the resonance frequency of the molecules. This means that the point of reflection at each end is not exactly the end of the plates. We further noticed that the exact shape and location of the coupler influences both the width and location of the resonance peak. The end caps of the magnetic shield also influence the resonance considerably. It is thus of utmost importance to check the resonance frequency when the plate structure is in its final setup inside the vacuum chamber.

We also probed the electric field with an antenna attached to a microwave power meter which was mounted on a motorised translation stage. By scanning the position of the power meter along the transmission line we could produce a field map of the standing wave inside the resonator. We found that terminating the transmission line with a short between the plates produced significant distortion of the standing wave towards the end of the plates.

The field map showed a standing wave that was consistent with a wavelength of $9\,\mathrm{cm}$ which is the expected wavelength for $f = 3.3\,\mathrm{GHz}$. Later measurements using the molecules as field-probes revealed a wavelength of $11.9\,\mathrm{cm}$. This means that the wave vector of the microwaves was angled with respect to the molecular beam axis resulting in an effective longer wavelength. The coupler thus launched a higher order mode which was travelling with an angle of $\approx 40°$ with respect to the molecular beam even though the plate spacing is smaller than half the

wavelength. The higher-order mode is one that zig-zags between the open sides of the transmission line, reflecting from the impedance change at these open sides. The molecules experienced an effectively longer wavelength of the microwaves which led to a smaller Doppler shift $\Delta f_D = \Delta \omega_D/(2\pi) = v/\lambda$. By reducing the width of the plates we fixed that problem. Narrower plates provide a sharp cut-off for such higher order modes. Hence for the final measurements we used plates with a width of 30 mm and reduced the distance between the plates to 5 mm to reduce fringe fields.

4.2.2.2 Controlling Magnetic Fields

To screen the interaction region against ambient magnetic fields we surround the plates with a high permeability nickel-iron based alloy (MuMetal) cylinder which reduces the ambient magnetic field by approximately a factor of 1000. The shielding factor S for static magnetic fields (the ratio of the magnetic field outside of the shield to the field inside a single-layer shield) is $S \approx \mu t/D = 1000$, where $\mu \approx 10^5$ is the relative permeability of the material the shield is made of, $t = 1.5$ mm the thickness and $D = 15$ cm the diameter of the shield [208]. Note that this is the transverse shielding factor for magnetic fields perpendicular to the cylinder axis. The axial shielding factor is usually worse. However, we benefit from the coincidence that the magnetic field in our lab along this direction is a factor of 10 smaller than in the other two directions.

The $J = 3/2$ Λ-doublet transitions are nearly a thousand times more sensitive to magnetic fields as compared to the $J = 1/2$ transitions. Hence for these measurements we added a second layer of magnetic shielding which extended into the state selection area. A sketch of this setup is shown in figure 4.4. For well separated shields the shielding factor then becomes $S = S_1 S_2 \left[1 - (D_1/D_2)^2 \right] \approx 3 \times 10^5$ [208]. We measured the shielding factor for the single and two layer shield with a three axis fluxgate gaussmeter (Bartington) to be better than 1000 and 10000, respectively despite apertures for the molecular and laser beams. De-gaussing coils are wound between the shields to be able to demagnetise them. We drive these coils with a 50 Hz sine wave that saturates the shields and then slowly ramp the H-field to zero [209].

Furthermore, we added two pairs of coils in order to be able to apply well controlled magnetic fields in x and y. The coils are made from four metal rods which run along the transmission line. The metal rods are connected such that a homogeneous magnetic field is created along the entire transmission line when a current flows through them. A solenoid wound along the transmission line provides a uniform field along z. The assembly consisting of the plates, field coils, magnetic shields and de-gaussing coils is then centred in the vacuum chamber. We carefully align the position of the plates using a laser beam that enters the chamber centrally, goes through the skimmer and hits the valve nozzle.
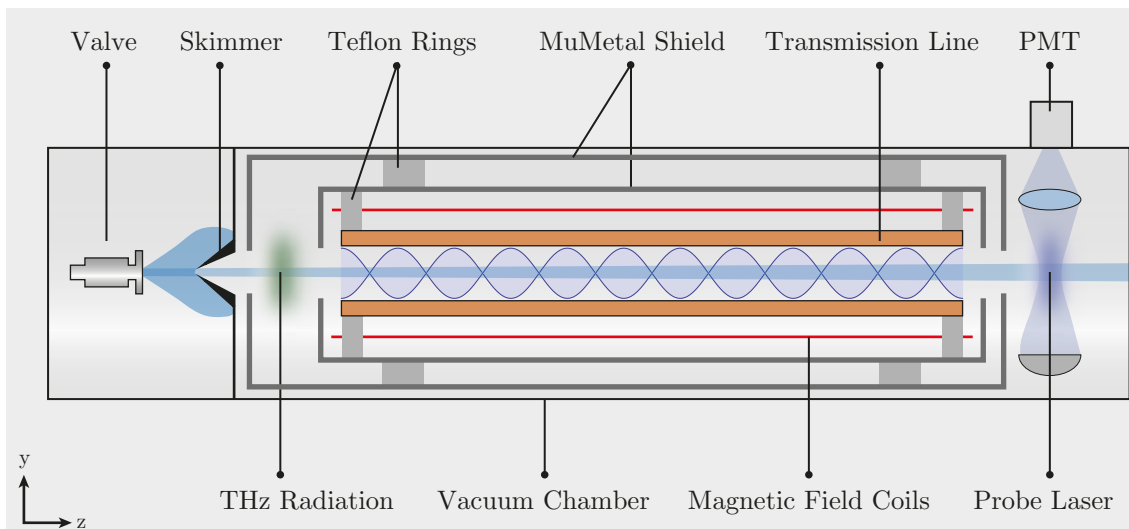
FIGURE 4.4: For the measurement of the $J = 3/2$ Λ-doublet we added a second layer of magnetic shielding that extends into the state selection region and added magnetic field coils. We replaced the optical pumping laser with resonant THz radiation to selectively transfer population from the $J = 1/2$ to the $J = 3/2$ state.

4.2.2.3 Microwave Electronics

The microwaves for driving the Λ-doublet transitions are generated by a Gigatronics Synthesized Signal Generator 7100 (synth) which is phase locked to a GPS frequency reference (Quartzlock E8-X). The GPS antenna is installed on the roof of our laboratory to assure good reception which is essential for a stable lock. We monitor the GPS signal strength on a computer via a RS232 interface using the freely available WinOncore software. We have good visibility to at least 8 (typically 10) satellites which allows an accurate calculation of the local time. The E8-X then locks its internal 20 MHz reference oscillator to the GPS signal and provides a phase-locked 10 MHz sine wave or 1 pulse per second TTL which can be used as a frequency or time reference. The typical short term stability is given as an Allan variance of $< 2 \times 10^{-10}$ for time scales on the order of 1 s and as low as $< 2 \times 10^{-12}$ for long terms $> 10^4$ s. We use the 10 MHz sine wave output and amplify it before connecting it to the external lock port of the synth. The lock of the synth is cross-checked against a counter which is also locked to the stable 10 MHz signal. If the 10 MHz signal is removed from the synth the counter shows frequency shifts of up to 1 kHz for synth output frequencies in the GHz range. We could not detect any influence of the RF amplifier on the stability of the lock. The phase locked microwave output is then connected to the transmission line cavity through a fast, TTL activated, high isolation switch (Mini Circuits ZASWA-2-50DR), a coaxial DC-Block and an SMA vacuum feedthrough. The switch output is monitored on an oscilloscope using a fast diode (Agilent).

4.2.2.4 State Selector

We measure the population in one specific Λ-doublet state as a function of the microwave frequency. Our molecular beam source creates an equal amount of molecules in the two Λ-doublets of the $J = 1/2$ ground state. If we drove a π-pulse with an initially equal population in both states we only swap the population and can not detect any change in signal due to the interaction with the microwaves. Hence the first step is to create an imbalance between the populations in the two states. We can do so by means of optical pumping. We take part of our detection laser and let it interact with the molecules before they enter the transmission line. We lock the laser to the $R_{22}(1/2)$ line of the $A^2\Delta(v = 0) \leftarrow X^2\Pi(v = 0)$ transition, for example, which depletes the $(1/2^-, 1)$ level (see level diagrams 2.4 and 4.1). We use the short hand (J^p, F) to label the levels from now on. Hence without resonant microwaves we cannot detect any CH molecules in our detector because they were all pumped away into a dark state. We now need to apply the microwaves while the molecules are flying through the transmission line and measure the fluorescence signal in our detector as the microwave frequency is scanned. This technique is known as molecular beam laser-microwave double-resonance spectroscopy.

Approximately 95% of the CH molecules are created in the $J = 1/2$ ground state. With such little signal in the $J = 3/2$ state a measurement of the Λ-doublet would be extremely challenging. We therefore populate the $J = 3/2$ state by driving the $J = 1/2$ to $J = 3/2$ transition with resonant THz radiation near $533\,\text{GHz}$. We generate this so-called mm-wave radiation with a commercial amplifier multiplier chain (VDI AMC 331). The AMC generates the 54th harmonic of its input frequency (between 9.3 and 13.9 GHz, 13 dBm (13 mW)) which corresponds to an output scan range of 500-750 GHz. The mm-waves are launched into a free-space Gaussian beam by a WR-1.5 diagonal gain horn (gain of 26 dB, 84% Gaussicity). The beam waist radius at the horn output is $1\,\text{mm}$, the E-field polarisation is along y with a maximum power output of typically -20 dBm ($10\,\mu\text{W}$) and a full 3 dB bandwidth angle of 10 degrees. The output radiation can be modulated via a TTL input and attenuated with a control voltage. The beam is collimated with a teflon lens ($f = 30$ mm) to a diameter of $1\,\text{cm}$ enters the vacuum chamber through a quartz window and intersects the molecular beam orthogonally at $z = 24\,\text{cm}$.[6] An excellent overview of the technology and optical elements for microwaves, millimeter and submillimeter waves is provided in Goldsmith's book about Quasioptical Systems [210]. The teflon lens is mounted on a 3-axis translation stage to optimise beam position and collimation. For the $J = 3/2$ measurement we use the Gigatronics 7100 for generating the fundamental frequency for the AMC and a second synth (HP 8656B) to generate the $700\,\text{MHz}$ for driving the Λ-doublet transitions in the $J = 3/2$ state.

---

[6]Note that reflective elements such as curved mirrors are preferred in the THz community because they prevent back-reflections and mirrors are usually more efficient (less loss). A number of different materials exists for focusing THz radiation. Tsurupica or TPX (polymethylpentene) for example have a similar refractive index ($n = 1.52$) for THz and visible light, which facilitates alignment procedures. Both materials are highly transparent to THz radiation. However, due to the high price of these lenses we preferred to make teflon lenses in our own workshop.
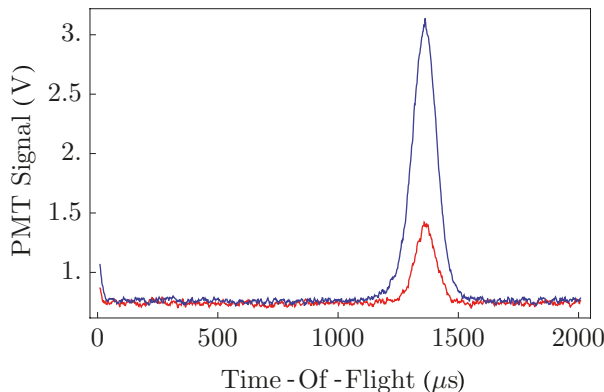
FIGURE 4.5: CH signal at the detector without (blue) and with (red) optical pumping laser.

4.3   Measuring the $J = 1/2$ Λ-doublet

4.3.1   First Preparations

When we add the optical pumping laser at $z = 24\,\mathrm{cm}$ the signal at the detector decreases by approximately 75% as shown in figure 4.5. This means that part of the molecules return to the initial state after optical pumping which is expected due to the large Franck-Condon overlap of the A-X transition. The pump laser typically has a power of $50\,\mathrm{mW}$ in a $6 \times 3\ \mathrm{mm}^2$ beam which is reflected to increase the intensity and the interaction time. For the probe beam we use about $5\,\mathrm{mW}$ in a beam of similar size. Now we have depleted the population in the negative parity state which allows us to measure an increased population in that state by driving molecules from the positive to the negative parity state using the microwaves.

First we pulse the microwaves on for a short time ($\tau = 15\,\mathrm{\mu s}$) when the molecules are in the middle of the interaction region (at an antinode) and scan the microwave frequency over the resonance with an arbitrarily chosen power (0 dBm for example). The short pulse results in a very broad resonance and thus can easily be detected. For the case that we did not detect anything we changed the power of the microwaves, but usually we could detect a small resonance. If the power is too high it can result in very odd-shaped resonances. If that is the case we lower the power by factors of two until we see a nice resonance that resembles a sinc^2 function. We then fix the resonance frequency to the centre of the peak and scan the microwave power to record Rabi oscillations which then allows us to find the exact power needed to drive a π-pulse. Such Rabi oscillations are shown in figure 4.7 on the left.

We then use the molecules as a field probe to create a map of the standing wave electric field. We fix the pulse length, microwave power and frequency and scan the time when the microwaves are pulsed on. Due to the standing wave the electric field amplitude varies along the transmission line. Therefore, less molecules are transferred when the microwaves are pulsed on and the molecules are at a node in the transmission line. This allows us to identify the field maxima with high accuracy. To be more precise, the transition probability on resonance is $P = \sin^2(\frac{\Omega\tau}{2})$,

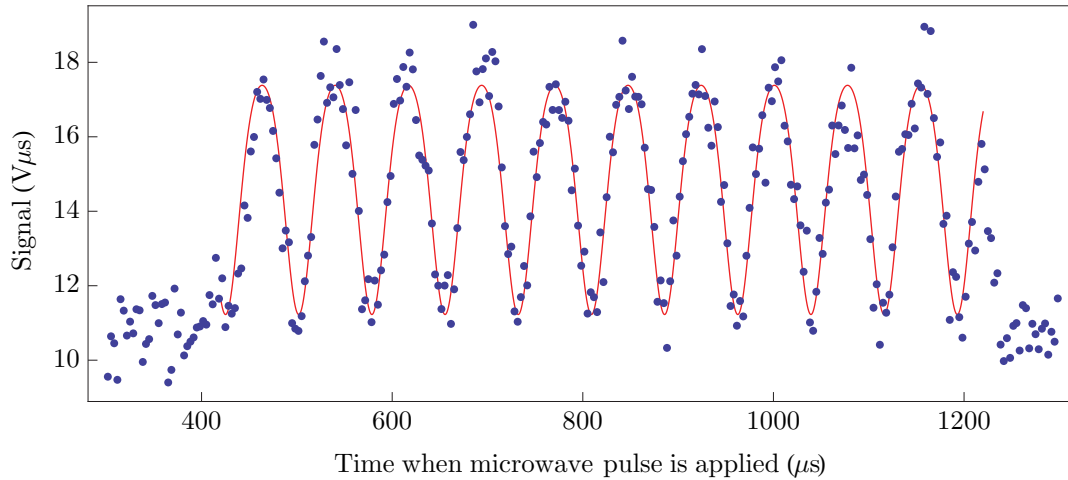FIGURE 4.6: We can use the molecules to create a field map of the standing wave inside the transmission line. The microwaves are pulsed on for a short time (15 µs) with the power of the microwaves set such that we apply a π-pulse when the molecules are at the centre antinode. We then record the fluorescence as a function of the delay time when the microwaves are pulsed on. We fit the model of equation 4.25 (red line) to the data (blue dots) which allows us to determine the positions of antinodes to high accuracy. We can determine the wavelength in the resonator from the fit to 8.99 ± 0.01 cm which agrees well with the expected wavelength at 3.335 GHz.

and since the Rabi frequency is proportional to the electric field, $\Omega = \Omega_{\max} \cos \left[2\pi \left(z - z_0 \right) / \lambda \right]$. Note that we set $\Omega_{\max} \tau = \pi$ in the experiment. To account for the fact that the molecule possess a finite velocity distribution we use an averaged Rabi frequency $\Omega_a \tau = q \Omega_{\max} \tau = q\pi$ with $q < 1$. Figure 4.6 shows such a field map obtained using the molecules as probes. Here we used the $(1/2^+, 1) - (1/2^-, 1)$ transition and fit the function (red line)

$$ S = S_0 + A \sin^2 \left(q \frac{\pi}{2} \cos \left(\frac{2\pi \left(vt - vt_0 \right)}{\lambda} \right) \right) \tag{4.25} $$

to the data (blue dots), where we used $z = vt$, with $v = 570 \, \text{m s}^{-1}$ determined from the experiment. The offset S_0, the amplitude A, the initial time t_0, the wavelength λ and q are fitting parameters. We determine the wavelength of the microwaves from the fit to be $\lambda = 8.99 \pm 0.01$cm which agrees well with the expected wavelength at 3.335 GHz.

Once we know the positions of the field-maxima we record Rabi oscillations at each antinode position to check if the power to drive a π-pulse varies along the transmission line. Note that the most precise way to record a field map is to do a full power scan for each position along the transmission line. We then fit to the Rabi oscillations and plot the power needed to drive a π-pulse for each position. We found that it gave exactly the same result for the antinode positions as the much simpler and shorter version described above. The plot on the left of figure 4.7 shows a power scan of the microwaves for an interaction time $\tau = 15$ µs at the centre antinode and the frequency on resonance. The blue dots are the data and the red line is a fit using the model $S = S_0 + A \sin^2(\alpha x)$, where x is the independent variable proportional to the square root of power, and S_0, A and α are fitting parameters. The data fit well to this model.
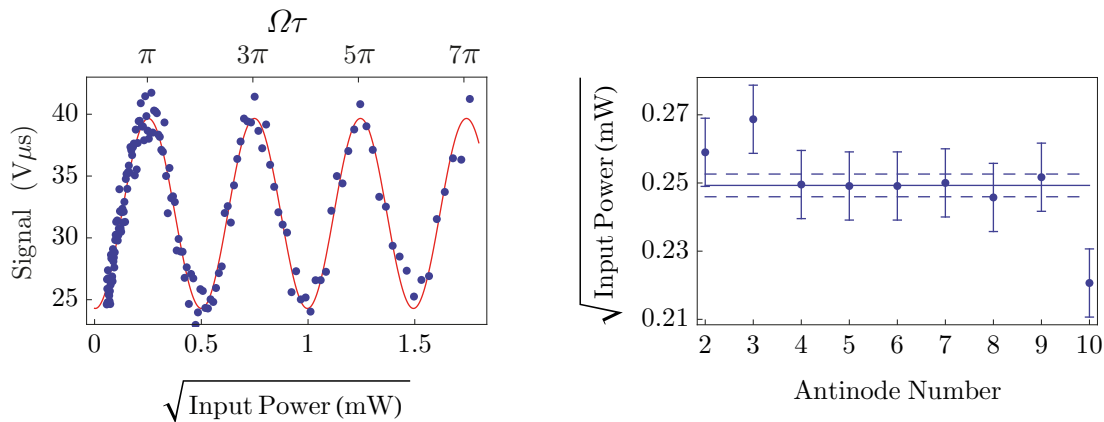
FIGURE 4.7: Left: When the molecules are at the centre antinode we apply a 15 µs microwave pulse and record the fluorescence as the microwave power is scanned. We observe Rabi oscillations. Right: We repeat this measurement for each antinode and plot the power needed to drive a π-pulse for each antinode. The solid line is the mean of all the data points and the two dashed lines are the 1σ standard errors.

The right hand side of figure 4.7 shows the power needed to drive a π-pulse for each antinode. We can clearly see that the microwave field has a uniform amplitude in the central region.

Note that the input coupler severely influences the reflection which can lead to distortions of the standing wave close to the end of the plates. The field map thus also serves as an analysis tool to check for any inhomogeneities along the transmission line. Only if a fit to the standing wave reproduces the exact free space wavelength and the amplitudes to drive a π-pulse do not vary significantly at different antinodes we proceed. Otherwise the plates are removed and the coupling behaviour is inspected again with the vector network analyser.

Once we have roughly determined the resonance frequency we start to increase the microwave pulse length which gradually narrows the resonance. For molecules travelling at $570\,\mathrm{m\,s^{-1}}$ the interaction time is limited by the length of the plates (48 cm) to 840 µs. For such long interaction times the resonance becomes narrow enough to resolve the Doppler splitting of $2\Delta f_D$ (due to the standing wave we observe two resonances which are split by twice the Doppler shift). By taking the mean of the two centre frequencies we can extract the Doppler free resonance frequency. Figure 4.8 shows such single pulse data for an interaction length of $\tau = 387$ µs about the centre of the transmission line. The red line is a fit using equation 4.11. For the fit we fix the interaction time τ to the one used in the experiment. It is remarkable that the lineshape fits so well which indicates that the linewidth is only limited by the interaction time and does not suffer from any inhomogeneous broadening. The single pulse data also reveals that there is a small imbalance between the two counter propagating waves of 8% which results in unequal amplitudes of the lineshape.
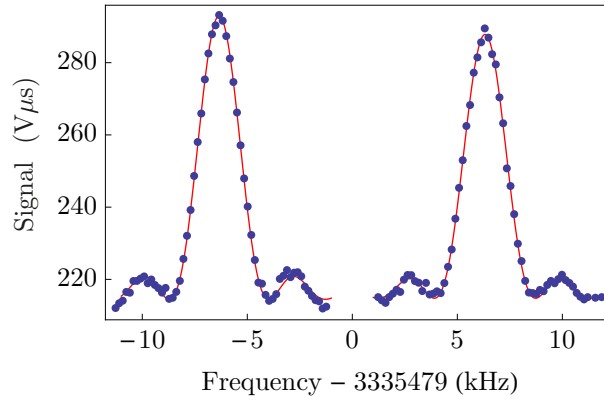
FIGURE 4.8: We apply a single long pulse of $\tau = 387$ µs duration about the centre antinode and record the fluorescence as a function of the microwave frequency. We fit equation 4.11 and extract the centre frequency for each peak. The mean of the two centre frequencies gives the Doppler free resonance frequency 3335479349 ± 7 Hz for the $(1/2^+, 1) - (1/2^-, 1)$ transition.

4.3.2 Measuring the $J = 1/2$ Λ-doublet Using Ramsey's Method of Separated Oscillatory Fields

As mentioned in section 4.2.1 we know that Ramsey's method provides us with an even narrower resonance and makes our measurement less susceptible to systematic frequency shifts. We know the exact positions of the antinodes and thus exactly when to pulse on the microwaves to drive the two $\pi/2$ pulses, in order to benefit from the suppression of systematic shifts described in the previous section. From our field map measurements we also know the exact power that is needed to drive a $\pi/2$-pulse at each antinode.

The experimental sequence is illustrated in figure 4.9. For each molecular pulse we set the microwaves to a specific frequency and pulse them on twice with a power set to drive a $\pi/2$-pulse. The first pulse is applied when the molecules are near one of the antinodes and the pulses are separated by a free evolution time $T = n\lambda/(2v)$, where n is an integer, λ is the wavelength of the microwaves and v is the velocity of the molecules. The detector then measures the population in a single hyperfine component of the negative parity Λ-doublet state for the specific microwave frequency. For the next molecular pulse we step the frequency and repeat the measurement. The resulting Ramsey fringes for $\tau = 15$ µs and a free evolution time of $T = 428$ µs is shown in figure 4.10. The top plot in figure 4.10 shows a wide frequency scan and reveals the Ramsey fringes modulated by an envelope which is determined by the single pulse duration τ. The bottom plot is a narrower scan about the transition frequency and shows the $\cos^2(\delta T)$ oscillation. The solid line is a fit to the model $aP_2(\delta) + b$ where a and b are constants and P_2 is given by equation 4.18. We set $\Delta\phi_O = 0$, τ and T to the values used in the experiment and thus only leave the scale factor a the offset b and resonance angular frequency ω_0 as fit parameters. The model fits the data exceedingly well, demonstrating the exquisite degree of control achieved in this experiment. From our single, long pulse measurement we know the transition frequency
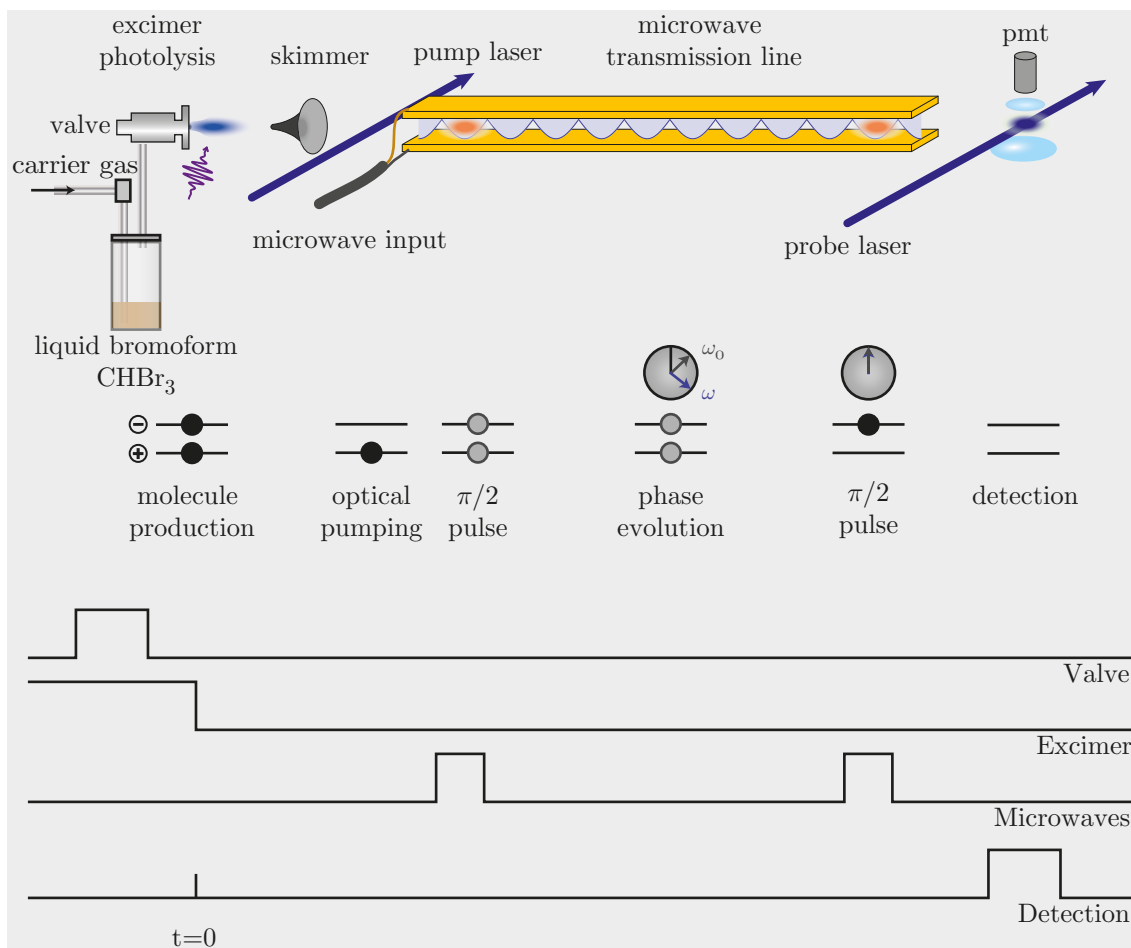
FIGURE 4.9: The experimental sequence for a Ramsey experiment. The molecules are produced at time $t = 0$ with equal population in each Λ-doublet state. Molecules in the $(1/2^-, 1)$ state get pumped into a dark state by the optical pumping laser which has the same frequency as the probe laser. The molecules then enter the transmission line resonator. We apply a pulse of microwaves ($\tau = 15\mu s$) with a power set such that $\Omega\tau = \pi/2$ when the molecules are located at an antinode well within the plates. The microwaves are blocked using a fast switch for a time $T = n\lambda/(2v)$ and are pulsed on again for a second $\pi/2$-pulse thereafter. We then detect the population in the $(1/2^-, 1)$ state as a function of the microwave frequency via laser induced fluorescence. Cheers to Dr. Smallman for drawing such a nice skimmer.

to better than $10\,\mathrm{Hz}$ which is much less than one fringe period. Hence we know which one of these fringes is the central fringe whose centre is the resonance frequency. Additionally, we can unambiguously determine the central fringe and thus the resonance frequency by repeating the experiment for three different free evolution times T. Note that the phase of the standing wave changes by π from one antinode to the next. This means that the fringe pattern gets inverted for a free evolution time that corresponds to an odd number of antinodes. This means that for a sequence of three Ramsey experiments with free evolution times that correspond to n, $n+1$ and $n+2$ number of antinodes the $n+1$ fringes will be inverted with respect to the n and $n+2$ case. For three subsequent Ramsey experiments performed in such a particular way there is only one unique frequency at which two fringe maxima line up with one minimum - the resonance frequency. Figure 4.11 shows Ramsey data for the $(1/2^+, 1) - (1/2^-, 1)$ transition, taken for
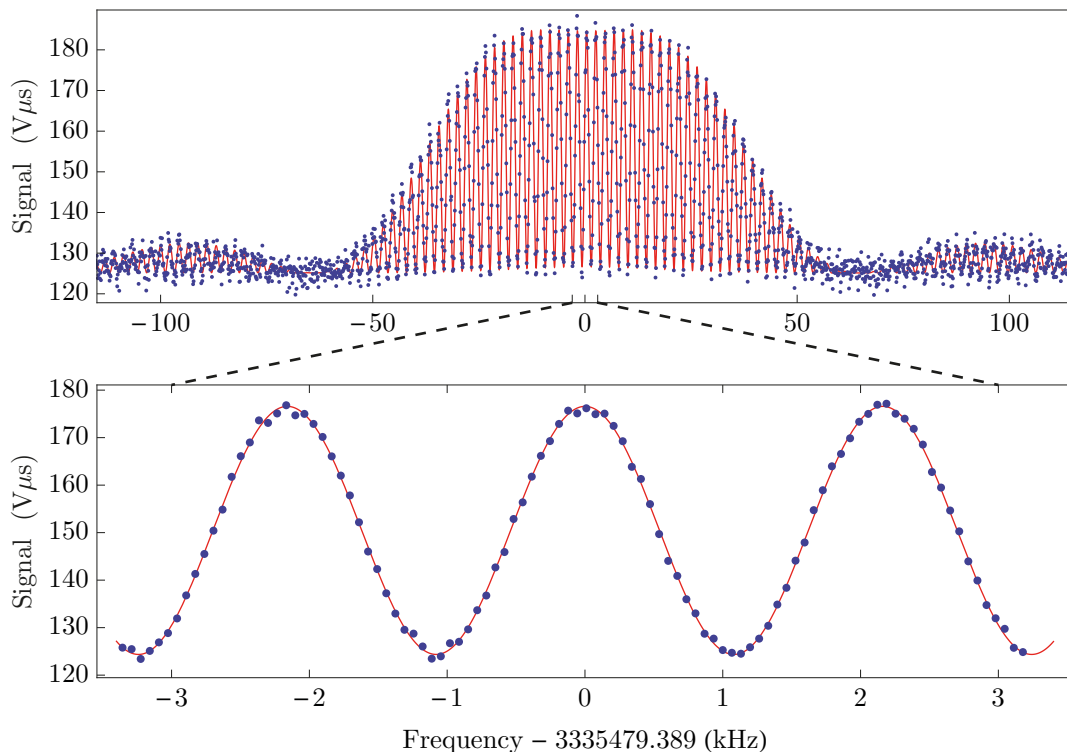
FIGURE 4.10: The dots represent the population in the $(1/2^-, 1)$ state as a function of the microwave frequency measured using Ramsey's technique of separated oscillating fields. The solid lines are a fit to the data using equation 4.18. Here, we measure the $(1/2^+, 1) - (1/2^-, 1)$ transition. Top: wide frequency scan for $\tau = 15$ µs and a free evolution time of $T = 428$ µs (5000 points per scan, averaged over 10 scans at a repetition rate of 10 Hz). The first $\pi/2$-pulse is applied when the molecules are located at the third antinode and the second when they reach the ninth antinode. Bottom: A narrower frequency scan for the same transition (500 points per scan, binned, averaged 30 scans at a repetition rate of 10 Hz).

three different free evolution times. From the fits we can extract the transition frequencies for each measurement which give the consistent results of 3335479389 ± 1 Hz, 3335479391 ± 2 Hz and 3335479389 ± 2 Hz for a free evolution time of 458 µs, 380 µs and 302 µs, respectively.

4.3.3 Systematic Frequency Shifts Related to Magnetic Fields

Now we have measured the transition frequency, but we still need to check for potential, systematic frequency shifts. Here we discuss frequency shifts related to magnetic fields.

A magnetic field splits each F level into its $(2F + 1)$, M_F Zeeman sublevels. The $(1/2^\pm, 1)$ levels thus split into three sublevels which are labelled $M_F = -1, 0, 1$. As mentioned in chapter 2.6 the $J = 1/2$ states are extremely insensitive to magnetic fields. Therefore all $J = 1/2$ transitions are extremely insensitive to magnetic fields. Earth's magnetic field of 50 µT would split the single pulse lineshape into two components separated by 1 kHz which is comparable to the linewidth (see figure 4.8). A single-layer MuMetal shield is thus enough to reduce broadening of the line due to magnetic fields to insignificant levels.
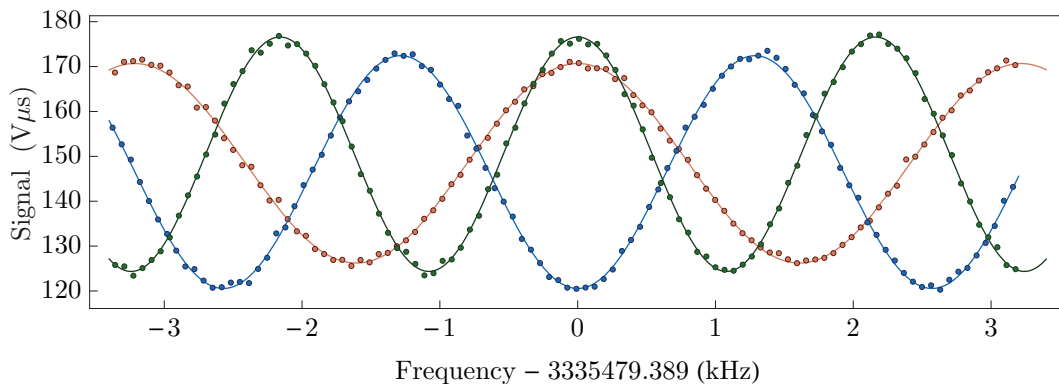
FIGURE 4.11: We use three different free evolution times to identify the central fringe and thus the transition frequency. Green: $458\,\mu s$ Blue: $380\,\mu s$. Red: $302\,\mu s$.

The $M_F = \pm 1$ components of the two parity states shift, in this approximation, by the same amount. This means that the two $\Delta M_F = 0$ transitions, for example, should not shift at all. This is similar to the magnetically insensitive transitions that are commonly used in atomic clock experiments. A more precise treatment including higher order terms, however, reveals a small parity dependent component of the Zeeman shift. The matrix elements of the entire Zeeman Hamiltonian are given in [107] (and see chapter 2 for more details). Evaluating the parity dependent terms for the $(1/2^+, 1)$-$(1/2^-, 1)$ transition gives a Zeeman splitting for the two π-components ($\Delta M_F = 0$, magnetic field parallel to the polarisation of the microwaves) of $\pm 36\,\mathrm{Hz}\,\mu T^{-1}$. We measured the $\Delta M_F = 0$ splitting by applying a magnetic field parallel to the electric field and using long single microwave pulses ($\tau = 500\,\mu s$) to find the transition frequency. The linewidth was thus narrow enough to reveal the Zeeman splitting for magnetic fields of the order of $100\,\mu T$. The results of this measurement are shown in Figure 4.12. The linear fits to the data give two Zeeman components shifted by $\pm 23\,\mathrm{Hz}\,\mu T^{-1}$ which is about 40 % less than expected. The discrepancy is probably due to uncertainty in the relevant parameters of the effective Hamiltonian, since not all of them have been measured.

For linearly polarised microwaves and a small magnetic field, there is a symmetry in the splitting and amplitudes of the Zeeman sublevels, and therefore no systematic frequency shift of the mean frequency. In a Ramsey experiment the lineshape consists of a sum of two Ramsey patterns proportional to $\cos^2(\delta T + \Delta\omega T) + \cos^2(\delta T - \Delta\omega T)$, where $\Delta\omega$ is the Zeeman shift. This is equivalent to $1 + \cos(2\delta T)\cos(2\Delta\omega T)$. If the splitting is symmetric it does not lead to a net phase shift of the fringes and thus to a systematic frequency shift. However, the amplitude of the Ramsey fringes oscillates with $\cos(2\Delta\omega T)$ as the magnetic field is tuned. Circularly polarised microwaves preferably populate one M_F sub-level which causes an asymmetric splitting and unequal amplitudes of the Zeeman sub-levels. This results in a systematic frequency shift. In the parallel plate transmission line, however, circular polarisation components are strongly suppressed.

In order to investigate any magnetic field dependent frequency shifts we apply magnetic fields as large as $50\,\mu T$ and do not observe any frequency shift on the $1\,\mathrm{Hz}$ level. Note that
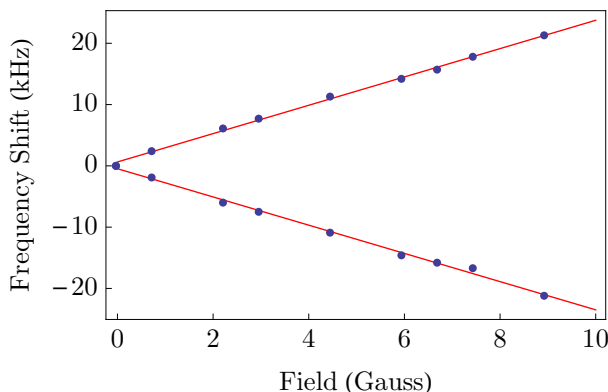
FIGURE 4.12: Zeeman splitting of the $J = 1/2$ Λ-doublet transition as a function of the applied magnetic field ($1G = 100\,\mu\text{T}$). The magnetic field is applied along y parallel to the polarisation of the microwaves. Hence only the two $\Delta M_F = 0$ components can be addressed by the microwaves. The fits yield a splitting of $\pm 23\,\text{Hz}\,\mu\text{T}^{-1}$.

such magnetically insensitive transitions can be extremely useful for precision measurements in molecules or for preserving long-term coherence of molecular qubits [211].

4.3.4 Systematic Shifts Related to Electric Fields

The Stark interaction of CH has been presented in section 2.5. All the $(1/2^\pm, 0)$ and $(1/2^\pm, 1)$ levels shift by exactly the same amount of $\Delta E_S^\pm/h = \mp 17.9$ Hz/(V/cm)^2. A plot of this theoretical frequency tuning as a function of the applied electric field is shown in figure 4.13 on the left. The transition frequencies thus shift quadratically by $2E_S/h \approx 36$ Hz/(V/cm)^2. To measure the Stark shift we apply a DC voltage to one of the plates of the transmission line via a bias tee and record the transition frequency obtained from a fit to long single pulse data. The frequency shift as a function of the applied electric field magnitude is shown in figure 4.13. We fit the quadratic function $\Delta f = a(x - b)^2 + c$ (red line) to the data (blue dots), where a, b and c are constants. The fit gives a Stark shift a of 32.98 ± 0.04 Hz/(V/cm)^2. The small discrepancy with the theoretical prediction might stem from a combination of a slightly larger plate spacing and a smaller actual voltage on the plates. It should be pointed out that the main goal of this measurement is not to reach high absolute accuracy but rather to measure the change in the Stark shift upon reversing the applied field. If there is an unknown field in the interaction region (e.g. due to patch potentials on the plates) in addition to the applied field, the Stark shift will change when the applied field is reversed. We saw no such change. We can use this information to set an upper limit to uncontrolled Stark shifts of $ab^2 = 0.1$ Hz.

4.3.5 Velocity Dependent Frequency Shifts

The single pulse data revealed that the standing wave in the transmission line is not perfect, i.e. there is a small imbalance between the two counter-propagating waves of approximately
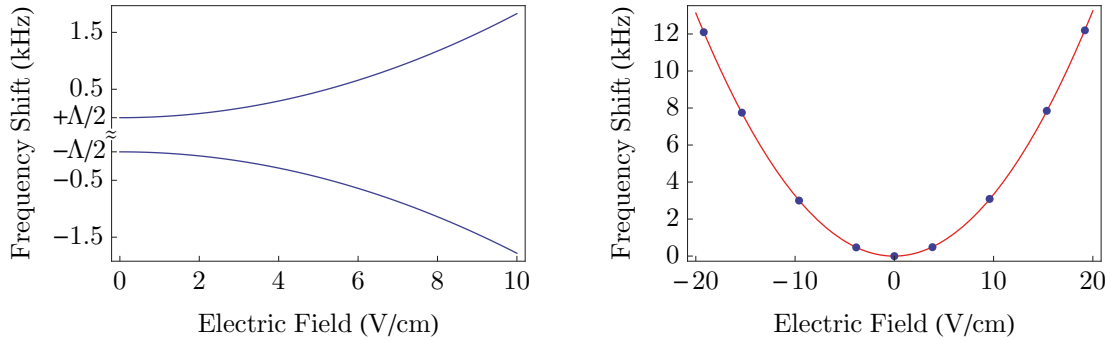
FIGURE 4.13: Left: The Stark tuning of the Λ-doublet states. Note that in the low field limit all the hyperfine levels $(1/2^\pm, 0, 1)$ shift by exactly the same amount of ∓ 17.9 Hz/(V/cm)^2. Right: Measured frequency shift of the $(1/2^+, 1) - (1/2^-, 1)$ transition.

8%. The molecular beam pulse has a finite velocity distribution. When we use argon as a carrier gas the FWHM of the pulse at the detector is typically $\Delta t = 90\,\mu$s which corresponds to a spatial length of the pulse of $\Delta x = v\Delta t = 5.1$ cm which is of a similar size to the distance between two minima in the standing wave. The slowest molecules will therefore experience a considerably different phase and magnitude of the electric field as compared to the ones in the centre of the pulse. We can illustrate this effect by dividing the time-of-flight profile into 10 μs slices and plot the apparent transition frequency as a function of the arrival time. Such a plot is shown in figure 4.14 on the right. The blue dots are the transition frequencies we obtain by fitting to the Ramsey spectra for each time-of-flight slice. The red line is a fit of $\Delta f = 1/(2\pi T)\left(\phi_{\rm im}(kL + kz_0) - \phi_{\rm im}(kz_0)\right)$, where $\phi_{\rm im}(z)$ is given in equation 4.21, $L = vT$ and $z_0 = vt_0$ where t_0 is the time at which the first microwave pulse is applied. The velocity is related to the time of flight $t_{\rm tof}$ via $v = D/t_{\rm tof}$, where D is the distance between source and detector. In the fit, we have fixed the imbalance factor ϵ to 0.08. We can clearly see that the model predicts the large frequency shifts due to the change in phase at the nodes of the standing wave. This means that we need to gate the time-of-flight profile narrowly about the most likely arrival time $t_{\rm tof}$ so that we only use molecules that are sufficiently close to the antinodes in the analysis. The part of the time-of-flight profile we typically use is shown as the shaded area in figure 4.14. Such a plot is a very fast and easy way to find potential timing errors. If we do not time the $\pi/2$ pulses such that the molecules are at an antinode we see large gradients of the transition frequencies across the whole time-of-flight profile.

If we gate narrowly about the most likely arrival time we can make use of the approximation 4.22 and expect a residual velocity dependent, systematic frequency shift $\Delta f \simeq \epsilon\epsilon_z(v_0/\lambda) \approx$ 0.04 Hz/(m/s), where $\epsilon = 0.08$ is the imbalance factor and $\epsilon_z = 0.05$ is the fractional error in the position of the second antinode.

A second velocity dependent shift was introduced in section 4.2.1. This is the residual Doppler shift due to the detuning of the $\pi/2$ pulses $\Delta f_{D,R} = (1 - 4/\pi)\,(v_0/\lambda)\,(\tau/T)$ which is suppressed by the imbalance factor $\epsilon = 0.08$. For typical experimental parameters of $\epsilon = 0.08$, $\tau = 15\,\mu$s and $T = 450\,\mu$s, we expect a shift of -0.01 Hz/(m/s).
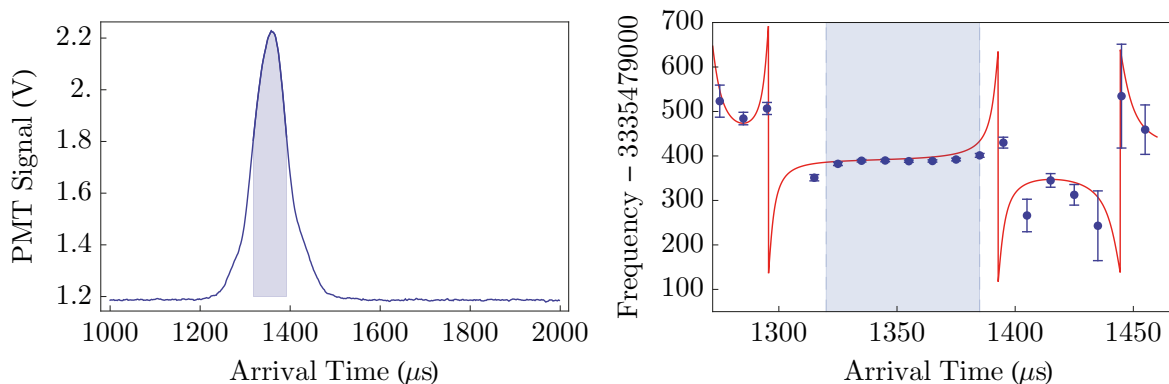
FIGURE 4.14: Left: A typical time-of-flight profile from a Ramsey experiment. The interaction with the microwaves distorts the profile slightly from the ideal Gaussian shape. The shaded region is the typical gate we use when analysing the Ramsey spectra. Right: Velocity dependent frequency shift due to the finite extent of the molecular pulse. This shows that it is necessary to use only those molecules that are within an interval of $t_0 \pm \Delta t$, where t_0 is the most probable arrival time and $\Delta t = 0.02 t_0$.

We control these velocity dependent shifts by measuring all the frequencies for at least three different velocities. Using krypton, argon and helium as carrier gases we obtain molecular beam velocities of $415\,\mathrm{m\,s^{-1}}$, $570\,\mathrm{m\,s^{-1}}$ and $1710\,\mathrm{m\,s^{-1}}$. For each velocity and transition frequency we produce a field map and measure the power needed to drive a π-pulse for each antinode. We start at antinode three, for example, and record at least four Ramsey patterns using antinodes six through nine for the second $\pi/2$ pulse. All these measurements agree within their uncertainties and we take the weighted mean as the final result (figure 4.15 on the left). We then repeat these measurements using antinode four and five to initialise the Ramsey sequence. The mean transition frequencies for different starting antinodes, however, do not agree within their uncertainties (see the right hand side plot in figure 4.15). For each carrier gas we took at least three Ramsey spectra for each starting antinode. The left hand side plots in figure 4.16 show Doppler shift data for the three different starting antinodes: three (blue), four (red) and five (green) for the three $J = 1/2$ transitions. The solid lines are linear fits to the data. The right hand side plots of figure 4.16 show the extrapolated zero-velocity frequencies for each starting antinode. The error bars are the 1σ standard errors of the individual zero velocity frequencies obtained form the linear fits. By extrapolating to zero-velocity the position dependent Doppler shift disappears and all measurements agree within their uncertainties. The solid lines are the weighted means of the extrapolated frequencies which give our final result. Table 4.1 gives an overview of the final measured frequencies and the systematic and statistical errors for each transition.
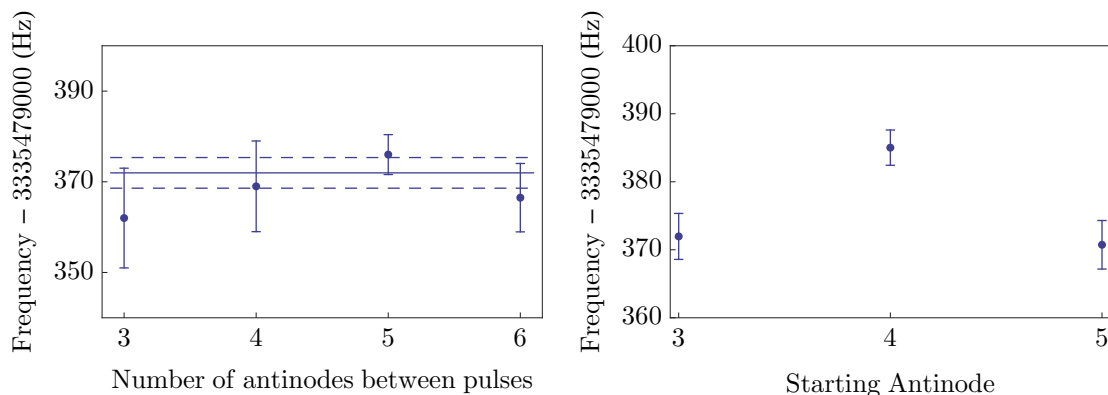
FIGURE 4.15: Left: The transition frequencies for the $(1/2^+, 1) - (1/2^-, 1)$ hyperfine line using antinode three for the first $\pi/2$-pulse. The data agree for different free evolution times T. The experiment using a free evolution equivalent to five antinodes was repeated twice which results in a smaller errorbar. The data sets agree within their uncertainty and the solid line represents the weighted mean. The dashed lines show the 1σ standard error. We repeat this experiment for different starting antinodes (shown on the right). Right: A systematic frequency shift that depends on which antinode we use for the first $\pi/2$ pulse.

4.3.6 Other Systematic Frequency Shifts

Blackbody radiation, for example, is long known to shift atomic hyperfine states whose control is extremely important for atomic clocks [212]. For atoms the blackbody radiation acts like a DC field that Stark shifts the hyperfine levels. Hence only the amplitude of the field is important. Rotational and vibrational transitions in molecules are in the same range as the typical emission spectrum of a black body at $300\,\mathrm{K}$. Therefore, electric dipole allowed transitions are possible. Typical absorption rates for light molecules are on the order of $1\,\mathrm{s}^{-1}$ and $10^{-3}\,\mathrm{s}^{-1}$ for rotational and vibrational transitions, respectively [213]. Shifts of rotational transitions due to blackbody radiation are on the order of tens of mHz and a few mHz for vibrational transitions. For our spectroscopy experiments at the Hz level this has no significance. These effects are further suppressed by the fact that the energy density of the black body radiation is very small at the Λ-doublet transition frequencies. However, experiments that aim to detect variations of fundamental constants in the laboratory must perform spectroscopy on the 10^{-13} fractional uncertainty level. Frequency shifts due to black body radiation thus can play a significant role in such experiments.

To test for any systematic dependence on the microwave power we performed Ramsey experiments with $\pi/2$-pulses as short as $4\,\mu\mathrm{s}$. Hence we increased the power of the microwaves by a factor of 16 and did not detect any change in the measured transition frequency at the $3\,\mathrm{Hz}$ level. We could therefore rule out any systematic shifts related to the microwave power. Furthermore, we investigated potential systematic shifts which depend on the frequency and power of the probe laser, but these were negligible.

The use of a molecular beam and the associated low density prevents any collisional broadening or density related systematic shifts on the current level of accuracy. An error budget for
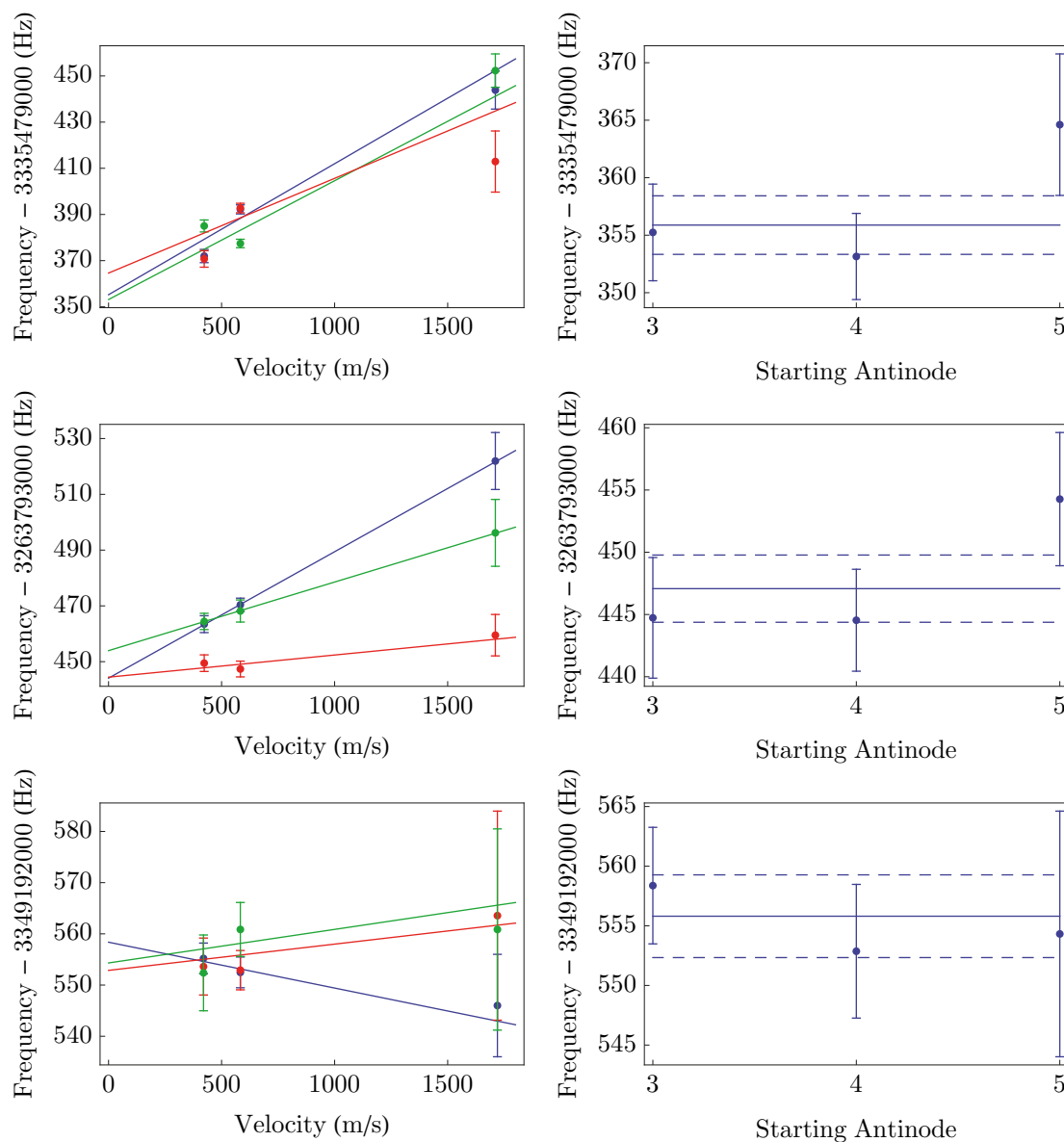
FIGURE 4.16: Left: Velocity dependence of the measured frequency for the three $J = 1/2$ transitions. Each data point is an average of at least three Ramsey experiments for each carrier gas and starting antinode (the antinode we use for the first $\pi/2$-pulse). We use antinodes three (blue), four (red) and (five) to initialise the Ramsey sequence. Each antinode gives a slightly different slope. Right: All the extrapolated zero-velocity frequencies agree within the 1σ uncertainties of the linear fits to the Doppler data.

	$(1/2^+,1)-(1/2^-,1)$	$(1/2^+,0)-(1/2^-,1)$	$(1/2^+,1)-(1/2^-,0)$
Transition Frequency (Hz)	3335479356	3349192556	3263793447
Stark Shift (Hz/(V/m)^2)	32.98(7)	32.98(4)	33.01(5)
Residual Electric Field (V cm^{-1})	-0.07(1)	-0.05(1)	-0.05(1)
Error Due To Electric Fields (Hz)	0.2	0.1	0.1
Zeeman Splitting (Hz nT^{-1})	0.023(2)	-	-
Error Due To Magnetic Fields (Hz)	0	0	0
Error Due To Microwave Power (Hz)	0	0	0
Error Due To Laser Detuning (Hz)	0	0	0
Max. Doppler Gradient (Hz/(m/s))	0.06(1)	0.05(1)	0.01(1)
Stat. Error of Zero Velocity Freq. (Hz)	3	3	3

TABLE 4.1: The error budget for the $J = 1/2$ measurements. All the systematic errors are negligible on the current accuracy level of one part per billion. The final error bar is determined by the 1σ standard error of the extrapolated zero-velocity Doppler fits.

each transition is given in table 4.1.

4.3.7   Summary

Let us quickly recall the measurement procedure to summarise the previous section. We use a magnetically shielded transmission line resonator for microwaves to measure the $J = 1/2$ Λ-doublet of CH. For each transition we use a separate pair of plates cut to exactly the right length to make sure that the resonance of the transmission line resonator occurs at the transition frequency. This assures a well balanced standing wave for each measurement. The resonance of the transmission line is more than 30 MHz wide which is 1000 times wider than a typical scan used for a measurement. Hence variations of the microwave power within a narrow frequency scan are negligible. A laser tuned to the A-X transition empties one of the doubled states via optical pumping. We can typically pump out over 75% of the initial population in the $(1/2^-,1)$ or $(1/2^-,0)$ state, depending on which transition we measure. The molecules then enter the transmission line resonator where we drive the transition using either single long pulses or two short pulses. We then measure the transferred population as a function of the microwave frequency via laser induced fluorescence to determine the transition frequency. The single long pulses are used to roughly determine the transition frequency and to perform systematic checks. We measured the Zeeman splitting of the $(1/2^+,1)-(1/2^-,1)$ transition and the Stark shift of all three transitions. This allows us to set limits to systematic frequency shifts due to residual magnetic and electric fields inside the interaction region. We repeat the Stark shift measurements for each pair of plates.

Using single short pulses we probe the electric field inside the transmission line resonator with the molecules and measure the wavelength of the microwave field. This allows us to determine the exact position of the antinodes which is important for the subsequent measurements using Ramsey's method of separated oscillatory fields. We repeat this measurement for each transition. There are in total eleven antinodes available for driving the $\pi/2$-pulses. The first and last two are omitted to make sure we pulse the microwaves on when the molecules are well inside

Transition	Frequency (Hz)
$(1/2^+, 1) - (1/2^-, 1)$	3335479356 ± 3
$(1/2^+, 0) - (1/2^-, 1)$	3349192556 ± 3
$(1/2^+, 1) - (1/2^-, 0)$	3263793447 ± 3

TABLE 4.2: The measured $J = 1/2$ Λ-doublet frequencies with 1σ uncertainties.

the magnetic shield. We then measure the transitions using Ramsey's technique and perform further systematic checks. In particular, we apply magnetic fields to look for any additional phase shifts in the Ramsey data. However, we do not observe any frequency shifts on the $1\,\mathrm{Hz}$ level for magnetic fields as large as 0.5 G.

Furthermore, we test for systematic shifts that depend on the power of the microwaves by using $\pi/2$-pulses as short as $4\,\mu\mathrm{s}$. We do not observe any shift. We also do not observe any frequency shifts that depend on the probe laser detuning.

However, we do measure a small Doppler shift whose gradient depends on which antinode is used to apply the first $\pi/2$-pulse. After extrapolating to zero-velocity the results for the different antinodes all agree and we take the weighted mean of the zero-velocity values as the final frequencies. These final frequencies with their 1σ standard errors are given in table 4.2. They are in agreement with the previous best laboratory measurements and with astrophysical measurements, and are 300 times more precise than any of these.

4.4 Measuring the $J = 3/2$ Λ-doublet

The splitting between the $(F_2, J = 1/2)$ and $(F_1, J = 3/2)$ of CH is approximately $530\,\mathrm{GHz}$ which corresponds to a temperature of $25\,\mathrm{K}$. The molecular beam has a translational temperature of $0.4\,\mathrm{K}$. The rotational temperature is normally close to the translational temperature [214]. Assuming a thermal distribution of the molecular energies we expect a negligible fraction of the molecules to populate the $J = 3/2$ state. In order to see if we can detect any CH molecules in the $J = 3/2$ state we tuned the probe laser to the $R_{11}(3/2)$ line of the A-X transition. We detect a fluorescence signal which is only about four per cent of the one we get from the $J = 1/2$ state. Neglecting the small difference in the transition dipole moment this corresponds to a rotational temperature of about $8\,\mathrm{K}$. To reach the same statistical uncertainty as for the $J = 1/2$ measurements, we would need to average for at least 25 times longer, which is unrealistic. We could have used one of the discharge sources which create a hotter beam and thus provide more population in the $J = 3/2$ state. Then we would have to cope with large shot-to-shot fluctuations, an increased velocity spread, a faster beam with large variations in the most likely arrival time and thus the central velocity. We therefore decided to coherently drive population from $J = 1/2$ to $J = 3/2$ with radiation near $530\,\mathrm{GHz}$, which we call THz radiation or mm-waves.
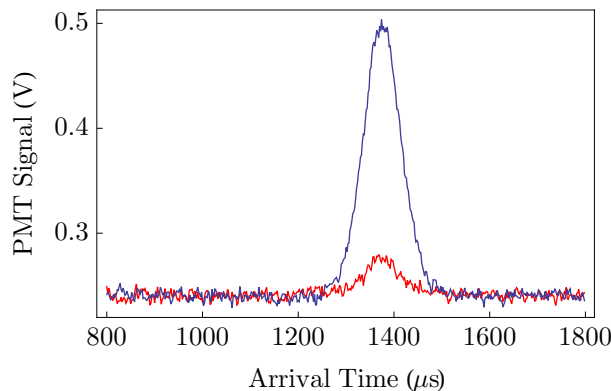
FIGURE 4.17: A time-of-flight profile of CH in the $J = 3/2$ state with (blue) and without (red) the THz radiation applied. The THz beam crosses the molecular beam orthogonally just before the start of the transmission line resonator. We can increase the population in the $J = 3/2$ state by a factor of nine corresponding to about 40% of the initial $J = 1/2$ population. The detection laser is locked to the $R_{11}(3/2)$ line of the A-X transition.

The experimental details for driving this transition will be discussed in the following chapter. All we need to know for the moment is that we replaced the pump laser beam with radiation from an amplifier multiplier chain (AMC). We can now selectively populate either the $(3/2^+, 1)$ or $(3/2^+, 2)$ state depending on which transition frequency we would like to measure. Figure 4.17 shows a time-of-flight profile of CH in the $J = 3/2$ state with (blue) and without (red) the THz radiation applied. We can increase the signal in the $J = 3/2$ state by nearly one order of magnitude.

The $J = 3/2$ state is approximately 1000 times more sensitive to magnetic fields as compared to the $J = 1/2$ state. Hence we added a second magnetic shield that extends into the state preparation region. This prevents Zeeman splitting of the lowest mm-wave transition which improves the transfer efficiency. We further added magnetic field coils which permit applying homogeneous magnetic fields in each direction. We can thus precisely measure the Zeeman splitting and limit potential systematic frequency shifts.

As before the plates are cut to the right length and the coupling is checked with the vector network analyser. We measured the FWHM of the transmission line resonance to be $75\,\text{MHz}$ which is about twice the size as in the $J = 1/2$ case. All the hyperfine components of the $J = 3/2$ state lie within only $20\,\text{MHz}$ which allows us to use the same plates for all measurements.

Using the molecules we create a field map to determine the exact position of the antinodes and measure the power needed to drive a π-pulse for each antinode in the same way as described above. We then increase the length of the pulse until we can clearly identify the two Doppler components. This gives us a rough estimate for the transition frequency. Analogous to the $J = 1/2$ measurements we then use Ramsey's technique to measure each of the four transition frequencies.

4.4.1 Systematic Shifts Related to Magnetic Fields

For small magnetic fields we can neglect the coupling of different F states and the Zeeman shift is $\Delta E = g_i \mu_B B M_F$, with the g_i-factors for each state i given in table 2.1. For the states of interest they are $g(3/2^{\pm}, 1) = 1.08$ and $g(3/2^{\pm}, 2) = 0.648$ which corresponds to a shift of the energy levels $\Delta E/h = 15.1 M_F$ Hz nT^{-1} for $F = 1$ and $\Delta E/h = 9.07 M_F$ Hz nT^{-1} for the $F = 2$ state. The contribution of the rotation and the nuclear spin to the molecular g-factor is small and thus can be neglected. Parity dependent effects are also small and shall be neglected.

From angular momentum selection rules it follows that the $(3/2^+, 1) - (3/2^-, 1)$ transition splits into a total of six lines (two π, two σ^+ and two σ^- transitions). The $\Delta M_F = 0$ lines do not shift to first order. However, due to mixing of the hyperfine levels there is a quadratic (second order) Zeeman shift of 0.119 Hz/(mG)^2. The $\Delta M_F = \pm 1$ transitions shift linearly by ± 1.5 kHz/mG.

The $(3/2^+, 2) - (3/2^-, 2)$ transition splits into 12 components. For small magnetic fields there are two lines that do not shift, two lines that shift quadratically with -0.11 Hz/(mG)^2, four lines that shift linearly with a positive gradient of 0.907 kHz/mG and four lines that shift with a negative gradient of the same magnitude. A plot of the large and low field Zeeman tuning of this transition is shown in figure 4.18 on the left.

The $(3/2^+, 1) - (3/2^-, 2)$ and the $(3/2^+, 2) - (3/2^-, 1)$ transitions split into a total of nine lines, respectively, with the largest gradient being 1.5 kHz/mG. The frequency shifts of all the components for large and small fields are shown in figure 4.18 on the right.

The Zeeman structure of these transitions is very complex and we thus need good control over magnetic fields and ideally need to measure the residual magnetic fields in the interaction region with high accuracy.

We generate magnetic fields along x and y using two pairs of magnetic field coils. Along z we use a solenoid. The first step is to calibrate the magnetic field coils and check the homogeneity of the field inside the magnetic shields. We perform both measurements with a fluxgate magnetometer (Bartington) and measure 0.079 ± 0.003 mG/mA along x, 0.145 ± 0.005 mG/mA along y and 1.15 ± 0.01 mG/mA along z. The homogeneity of the magnetic field in the interaction region is better than 2% for the x and y coils better than 3% for the solenoid along z. Note that we had to remove the transmission line cavity in order to measure the magnetic fields. Copper is diamagnetic with a magnetic susceptibility of 10^{-5}. Therefore its influence onto the magnetic field is small for the small magnetic fields we apply.

The first transition we investigated was the $(3/2^+, 2) - (3/2^-, 2)$ transition near 701 MHz. We used long single pulses of 780 μs duration and measured the splitting of the transition as a function of the magnetic field. By reversing the applied magnetic field we measured the residual magnetic field in a specific direction, averaged over the interaction region. The data are shown in figure 4.19. Note that before we reverse the magnetic field we de-magnetise both shields to make sure that no residual magnetic flux is pinned in the shields. We checked for systematic
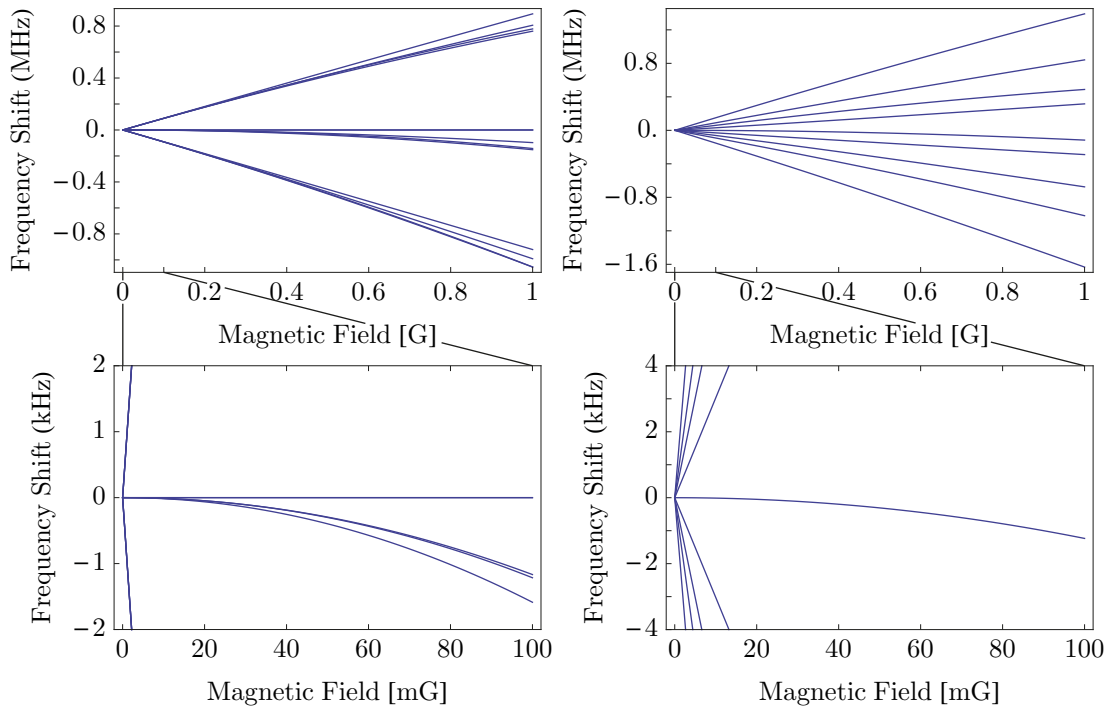
FIGURE 4.18: Left: The Zeeman tuning of the $(3/2^+, 2) - (3/2^-, 2)$ transition for large (top) and small magnetic fields (bottom). Right: The Zeeman tuning of the $(3/2^+, 1) - (3/2^-, 2)$ transition for large (top) and small magnetic fields (bottom).
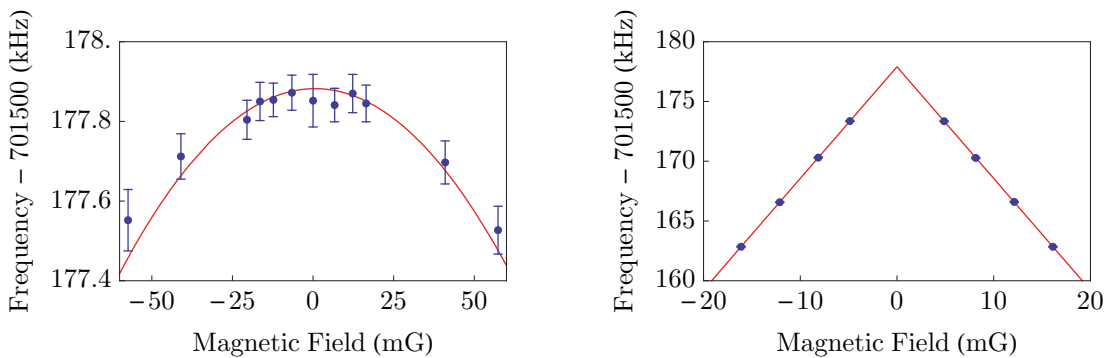
FIGURE 4.19: We use single, long pulses of $780\,\mu s$ duration to find the transition frequency as a function of the applied magnetic field for each direction of the magnetic field. Measuring the change in the Zeeman shift upon reversal of the magnetic field sets an upper limit to uncontrolled magnetic fields. Left: The Zeeman shift of the $(3/2^+, 2) - (3/2^-, 2)$ $\Delta M_F = 0$ transition when we apply a magnetic field along y (parallel to the polarisation of the microwaves). Right: The Zeeman shift of the $(3/2^+, 2) - (3/2^-, 2)$ $\Delta M_F = \pm 1$ transition when we apply a magnetic field along x. We always measure the component that shifts to lower frequency. This is the $\Delta M_F = +1$ component for negative values of the field and the $\Delta M_F = -1$ for positive values.

shifts related to the de-magnetisation procedure by measuring the transition frequency before and after, but could not detect any change. However, we detected a small residual magnetisation of the shields after we applied magnetic fields which can result in a systematic frequency shift. The de-magnetisation procedure efficiently removed the residual magnetisation.

When we apply a field along y (parallel to the polarisation of the microwaves) we can only drive the five π-transitions, three of which shift quadratically. This is shown in figure 4.19 on the left. We fit a quadratic function of the form $\Delta f = a(B - b)^2 + c$ to the data and infer a quadratic Zeeman shift of $a = -0.126 \pm 0.008$ Hz/(mG)^2 which agrees well with the theoretical prediction of -0.11 Hz/(mG). The offset of the parabola b amounts to 0.6 ± 1.5 mG which is consistent with zero and gives a 1σ upper bound for the residual magnetic field in the interaction region along y of 2.1 mG. To improve the upper bound we analyse single pulse data more carefully. Any magnetic field present in the interaction region would broaden the lineshape. The $\Delta M_F = 0$ transitions of the $(3/2^+, 2) - (3/2^-, 2)$ line shift, however, only to second order with an applied magnetic field. Hence in order to get a better estimate for residual fields along y we used single pulse data on the $(3/2^+, 2) - (3/2^-, 1)$ transition. For this line the three $\Delta M_F = 0$ transitions possess large shifts of -605, 0, and 605 Hz/mG with relative amplitudes of (9:12:9). We apply a single long pulse of 780 µs and record the lineshape. We then fit the lineshape from equation 4.11 with the interaction time floating as a free fitting parameter and get 783 ± 21 µs which is consistent with the time used in the experiment and with no broadening. The error in the measured linewidth provides us with an upper limit to the broadening which we can use to set an upper limit to the residual magnetic field. To be more precise we fit a model that consists of three lines which are separated by the Zeeman shift and leave the magnetic field as a fitting parameter. This yields a residual magnetic field of 0.38 ± 0.18 mG which is consistent with zero and gives a 1σ upper bound of 0.56 mG for residual magnetic fields along y.

When we apply magnetic fields along x and z we drive the $\Delta M_F = \pm 1$ transitions which have a large linear Zeeman shift. We measure the four components that shift with the same negative slope and fit a linear model $\Delta f = aB + c$ for each sign of B (see figure 4.19 on the right). The fit gives a linear slope of -0.934 ± 0.003 kHz/mG and a residual magnetic field along x of 0 ± 0.03 mG. We observe a 3 % discrepancy between our measurement and the theoretical prediction of 0.907 kHz/mG which is of the same size as the measured homogeneity of the magnetic field and the absolute accuracy of the magnetometer we used to calibrate the magnetic field coils. When we apply a field along z we get a slope of 0.83 ± 0.1 kHz/mG with a residual field of 0.05 ± 0.2 mG.

To determine the final frequencies we use Ramsey's technique. However, the Zeeman structure is complicated and higher order effects may lead to a systematic shift. Three $\Delta M_F = 0$ transitions of the $(3/2^+, 2) - (3/2^-, 2)$ line, for example, all shift quadratically to lower frequency which leads to a systematic frequency shift of the order of 10 Hz/(mG)^2. Therefore, we need to check if the transition frequencies measured using Ramsey's technique shift with small applied magnetic fields. We use exactly the same timing as in a single pulse experiment.
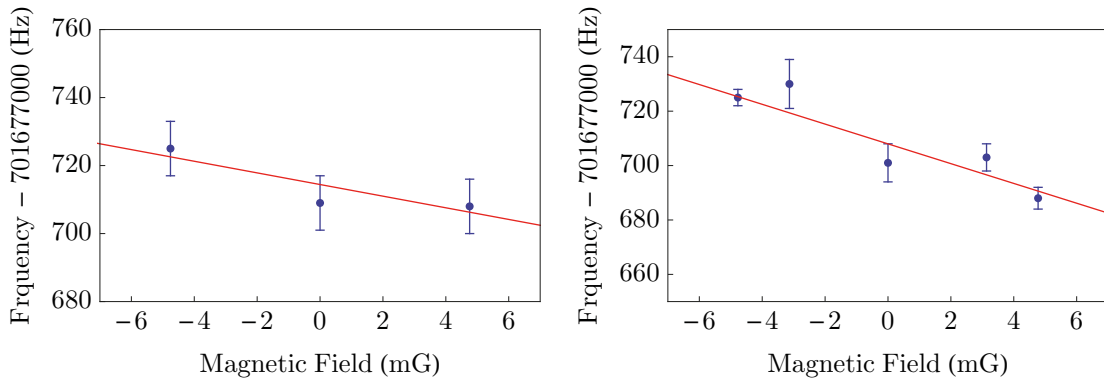
FIGURE 4.20: We check for systematic frequency shifts in a Ramsey experiment by measuring the transition frequency as a function of the applied magnetic field in x (left) and y (right). The red lines are linear fits to the data to determine the maximum possible slope. By multiplying the slope with the largest upper limit of the measured magnetic fields we determine the systematic uncertainty due to residual magnetic fields.

The molecules thus probe exactly the same interaction region for which we know the residual magnetic field very precisely. We then plot the transition frequency as a function of the magnetic field and find the maximum possible gradient (df/dB) by fitting a linear model to the data. This is shown in figure 4.20. To find upper limits to the gradient we take the slope of the linear fit and add or subtract the 1σ error of the fit depending on the sign of the slope. For the $(3/2^+, 2) - (3/2^-, 2)$ transition we measure a maximum gradient of -1.7 ± 1.26 Hz/mG along x, -3.6 ± 0.5 Hz/mG along y and -0.54 ± 0.28 Hz/mG along z. Adding the (1σ) error bar to the slope and multiplying it with the maximum upper limit for the magnetic fields gives an upper limit for systematic frequency shifts due to residual magnetic fields of 0.1 Hz along x, 2 Hz along y and 0.2 Hz along z. Adding these uncertainties in quadrature gives a total uncertainty due to uncontrolled magnetic fields of 2 Hz. We assume the same systematic uncertainty for the $(3/2^+, 1) - (3/2^-, 1)$ due to the analogous Zeeman structure.

The $(3/2^+, 1) - (3/2^-, 2)$ transition is substantially different from the $(3/2^+, 2) - (3/2^-, 2)$ transition with many more non-degenerate components and large Zeeman shifts. We therefore repeated the Zeeman measurement for this line. For this transition we could not rule out gradients as large as 10 Hz/mG along x, 20 Hz/mG along y and 5 Hz/mG along z. Multiplying these by the upper limits to the residual field gives a systematic uncertainty of 11 Hz. Because the $(3/2^+, 2) - (3/2^+, 1)$ transition resembles the Zeeman structure of the $(3/2^+, 1) - (3/2^-, 2)$ we assume the same systematic uncertainty.

4.4.2 Systematic Shifts Related to Electric Fields

Analogous to the $J = 1/2$ measurement we measure the Stark shift of the $(3/2^+, 2) - (3/2^-, 2)$ transition to rule out any systematic frequency shift due to stray electric fields or residual
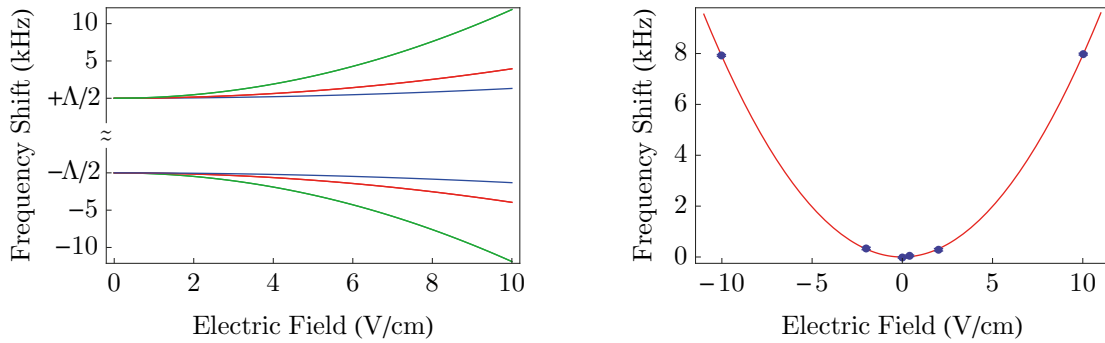
FIGURE 4.21: Left: Theoretical Stark shift of the two $J = 3/2^{\pm}, F = 2$ states. The different M_F sublevels shift differently. The $(F = 2, M_F = 0)$ levels shift by $\mp 13.2 \text{ Hz}/(\text{V/cm})^2$ (blue), the $F = 2, M_F = \pm 1$ levels shift by $\mp 39.5 \text{ Hz}/(\text{V/cm})^2$ (red), the $F = 2, M_F = \pm 2$ shift by $\mp 118.9 \text{ Hz}/(\text{V/cm})^2$ (green). $\Lambda \approx 701.7 \text{ MHz}$. Right: The measured Stark shift of the $(3/2^+, 2, M_F = \pm 1) - (3/2^-, 1, M_F = \pm 1)$ transition. The measured Stark shift of $79.1 \pm 0.3 \text{ Hz}/(\text{V/cm})^2$ agrees well with the theoretical prediction.

potentials on the plates. Note that contrary to the $J = 1/2$ transitions we need to account for the hyperfine structure in the calculation of the Stark shift of the $J = 3/2$ levels (see chapter 2.5 for more details). The left hand side plot in figure 4.21 shows the Stark shift of the $(3/2^{\pm}, 2, M_F = \pm 1)$ levels. The measurement of the Stark shift of the $(3/2^+, 2, M_F = \pm 1) - (3/2^-, 2, M_F = \pm 1)$ transition is shown in figure 4.21 on the right. A parabolic fit of the form $\Delta f_S = a(E - b)^2 + c$ reveals a Stark shift of $a = 79.1 \pm 0.3 \text{ Hz}/(\text{V/cm})^2$ with an offset of $b = -0.014 \pm 0.016 \text{ V cm}^{-1}$. Multiplying the 1σ upper bound of the electric field ($b_{\max} = -0.03$) with the measured Stark shift gives a systematic uncertainty related to uncontrolled electric fields of 0.2 Hz.

4.4.3 Velocity Dependent Frequency Shifts

Also similar to the $J = 1/2$ measurement we get the final statistical error by repeating the zero-field measurements for at least three different carrier gases. This permits controlling systematic shifts which depend on the velocity of the molecules. We do not see a spatially varying velocity dependence as in the case of the $J = 1/2$ measurement. The largest gradient we measure is $0.03 \pm 0.01 \text{ Hz}/(\text{m/s})$. We get the final frequency of each transition by extrapolating to zero velocity. The uncertainty of the fit is our final statistical error bar. Note that the 530 GHz transition is also subject to a small Doppler shift which has to be accounted for when the carrier gas is changed. This will be dealt with in more detail in the next chapter.

4.4.4 Other Systematic Effects

Analogous to the $J = 1/2$ measurement we checked for frequency shifts that depend on the power of the microwaves and the probe laser detuning, but could not detect any shifts at the

current accuracy level. An overview of the various effects that contribute to final error bar is given in table 4.3.

4.4.5   Summary

There is hardly any initial population in the $J = 3/2$ Λ-doublets. We therefore, selectively populate the $3/2^+$ doublet state in either the $F = 1$ or $F = 2$ hyperfine component using resonant THz radiation. We typically transfer 40% of the initial $(J = 1/2^-, 1)$ population into the $J = 3/2$ state and proceed with the measurement of the transition analogous to the $J = 1/2$ case. The $J = 3/2$ transitions are particularly sensitive to magnetic fields and we thus added a second layer of magnetic shielding to prevent large systematic frequency shifts. We also added magnetic field coils. This allowed us to apply uniform magnetic fields along each direction x, y and z. Using long, single microwave pulses we measured the shifts of the $J = 3/2$ transitions as a function of applied magnetic field in all three directions. Reversal of the applied magnetic field measures the residual field in each direction, averaged over the interaction region. All the residual fields are consistent with zero and the measurements provide upper limits to uncontrolled magnetic fields. We then measure the transition frequencies using Ramsey's technique as a function of applied magnetic field and determine the largest gradients. Multiplying the gradients with the upper limits of residual field in each direction provides us with a final systematic uncertainty. The systematic uncertainty is negligible for the two $\Delta F = 0$ transitions whereas for the two $\Delta F = 1$ transition it contributes $11\,\text{Hz}$ to the final measurement uncertainty. Similar to the $J = 1/2$ case we measure a small velocity dependence of the order of 0.03 Hz/(m/s) which we correct for. The 1σ standard error of the zero-velocity frequency gives the final statistical uncertainty. The final transition frequencies with the systematic uncertainties added in quadrature are given in table 4.4.

4.5   Constraining Changes of α and μ

We can now combine these lab measurements with existing astronomical data to set bounds on possible variations of α and μ. The astronomical spectra we use are from interstellar gas clouds in our own galaxy where the density is typically 10^{19} times smaller than on Earth. Hence we can constrain variations of fundamental constants with matter density. These clouds are highly dynamic objects and the atoms and molecules within possess a complex velocity profile. This leads, in general, to complicated spectra with many Doppler shifted components. For spectra from very distant objects the redshift of spectral lines due to the expansion of the universe is another factor that must be accounted for. This makes it necessary to compare at least two spectral lines from each source to cancel the Doppler shift. In order to achieve high sensitivity to changes in fundamental constants the two transitions should have very different sensitivity

	$(3/2^+,2)-(3/2^-,2)$	$(3/2^+,1)-(3/2^-,1)$	$(3/2^+,1)-(3/2^-,2)$	$(3/2^+,2)-(3/2^-,1)$
Transition Frequency (Hz)	701677682	724788315	703978340	722487624
Stark Shift (Hz/(V/cm)^2)	78.3(6)	-	-	-
Residual Electric Field (V cm^{-1})	-0.02(2)	-	-	-
Uncertainty Due To Electric Fields (Hz)	0.1	0.1	0.1	0.1
Largest Zeeman Gradient (Hz nT^{-1})	0.036(5)	-	-	0.20(4)
Uncertainty Due To Magnetic Fields (Hz)	2	2	11	11
Uncertainty Due To Microwave Power (Hz)	0	0	0	0
Uncertainty Due To Laser Detuning (Hz)	0	0	0	0
Max. Doppler Gradient (Hz/(m/s))	0.03(2)	-0.03(2)	0.01(1)	0.03(2)
Stat. Error of Zero Velocity Freq. (Hz)	6	16	18	11

TABLE 4.3: Overview of the contribution of the systematic and statistical errors for the individual transitions. We use the same plates for all the measurements. We therefore only measured the Stark shift for one transition to set an upper limit to residual electric fields. Contrarily to the $J = 1/2$ measurement we have to account for additional systematic frequency shifts for the two $\Delta F = 1$ transitions.

Transition	Frequency (Hz)
$(3/2^+, 2) - (3/2^-, 2)$	701677682 ± 6
$(3/2^+, 1) - (3/2^-, 1)$	724788315 ± 16
$(3/2^+, 1) - (3/2^-, 2)$	703978340 ± 21
$(3/2^+, 2) - (3/2^-, 1)$	722487624 ± 16

TABLE 4.4: The measured $J = 3/2$ Λ-doublet transition frequencies with their 1σ uncertainties.

FIGURE 4.22: A false colour image of the giant molecular cloud W51 taken with the Spitzer space telescope [216]. The infrared array camera detects radiation at a wavelength of 3.6, 4.5, 5.8 and 8 μm and is displayed as red colour. At this wavelength polycyclic aromatic compounds (hot soot or dust) emit after being excited by strong ultraviolet radiation from massive hot stars. Emission at 24 and 70 μm is shown in green.

coefficients, ideally of opposite sign. We spectra from six different interstellar gas clouds. In two of these sources both, the $J = 1/2$ and $J = 3/2$ Λ-doublet transitions are observed together and in the other four the $J = 1/2$ transition of CH is observed together with the ground state $J = 3/2$ Λ-doublet transition of OH. The first time the $J = 3/2$ Λ-doublet of CH has ever been measured was in the astronomical survey conducted by Ziurys and Turner in 1985 [202]. They pointed both the 300 m dish at Arecibo and the 91 m telescope at NRAO, Greenbank towards W51, a giant molecular cloud (84×114 pc) and active nursery for new massive stars. It is located towards the Aquila constellation in the northern sky and lies along the Sagittarius arm of our galaxy (Galactic coordinates: $l = 49.5$, $b = -0.4$). It is one of the most active star forming regions in our galaxy, first discovered in a large radio survey conducted by Gart Westerhout in 1958 [215]. A false colour image of W51 from the Spitzer space telescope is shown in figure 4.22. The mechanisms that lead to the rich chemical diversity in such clouds (over 120 different molecular species have been detected so far) are only poorly understood. The molecules range in size from 2-13 atoms and are mainly organic in nature. The CH molecule plays a central role in these reaction dynamics [217]. Molecular spectra are also important for determining

the temperature and the total gas density throughout the gas cloud. Hence, molecules are a convenient means to obtain a better understanding of the physical conditions in these sources. Ziurys and Turner aimed to get more precise measurements of the column densities of CH by measuring the excited $J = 3/2$ state in addition to the $J = 1/2$ transitions. They succeeded in finding CH in W51 and a number of other clouds including W43, W3 and OriB. The $J = 3/2$ data from W51 remains the only published data set to date [202, 218].

They measured the $J = 3/2$ transitions at exactly the same location in the cloud as Genzel and colleagues six years earlier which allows us now to compare these transition frequencies to the frequencies we measured in the lab.

The astronomical spectra are plotted in terms of velocities. As a rule of thumb one can remember that for a wavelength of $1\,\text{mm}$ a velocity of $1\,\text{km}\,\text{s}^{-1}$ corresponds to $1\,\text{MHz}$. For the CH $(1/2^+, 1) - (1/2^-, 1)$ transition at a wavelength of $89.9\,\text{mm}$, $1\,\text{MHz}$ corresponds to $89.9\,\text{km}\,\text{s}^{-1}$. The line widths of a typical astronomical spectrum of CH has a FWHM of approximately $10\,\text{km}\,\text{s}^{-1}$. Astronomers can typically determine the centre of the line to an accuracy of $0.1\,\text{km}\,\text{s}^{-1}$ which corresponds to a frequency uncertainty of $1\,\text{kHz}$ for the $J = 1/2$ transitions. For our purpose of testing the variation of fundamental constants the lab frequencies should be known to higher accuracy than the astronomical measurements which was not the case until now.

In general, astronomers measure a Doppler shifted transition frequency $f_a' = f_a (1 - v_s/c)$, where f_a is the rest-frame transition frequency of the molecules, v_s is the relative velocity between the molecules and the observer and c is the speed of light. The velocity profile of the source is usually not known so the spectra are plotted with respect to a known nominal frequency f_n. This is usually the accepted value for the transition at the time of the measurement, is specified in the publication and carries no uncertainty. The frequency measured at the telescope's receiver is then $f_a' = f_n (1 - v_m/c)$, where v_m is the measured velocity determined from the data with respect to f_n. The two equations then give

$$\frac{1}{c}(v_m - v_s) = \left(1 - \frac{f_a}{f_n}\right)(1 - \epsilon) \tag{4.26}$$

where $\epsilon = v_s/c$. By using the difference of two transition frequencies which have the same velocity v_s we can get rid of the Doppler shift. Any additional difference in the frequencies is then due to a change in fundamental constants. This is of course only true if the two transitions shift by a different amount due to variations in constants, i.e. they have different sensitivity coefficients K. Suppose that the rest frequency in the molecular cloud deviates from the lab frequency due to a change in the fine structure constant α by $f_a = f_l (1 + K_\alpha(\Delta\alpha/\alpha))$, where f_l is the lab frequency for the transition. The difference in the measured velocities then is

$$\frac{1}{c}(v_{m,1} - v_{m,2}) = \frac{\Delta v_{12}}{c} = \left(\frac{f_{l,2}(1 + K_{2,\alpha}(\Delta\alpha/\alpha))}{f_{n,2}} - \frac{f_{l,1}(1 + K_{1,\alpha}(\Delta\alpha/\alpha))}{f_{n,1}}\right)(1 - \epsilon) \tag{4.27}$$

We can see that ϵ is only a minute correction to $\Delta v_{12}/c$ for non-relativistic speeds v_s and we can thus neglect it. We can further assume that $K f_{l,i}/f_{n,i} \approx K$ because the sensitivity coefficients are only known to about 1% accuracy and the ratio of f_l/f_n is known to a few parts per million level or better. Rearranging the equation then yields the expression

$$\frac{\Delta \alpha}{\alpha} = \frac{1}{(K_{2,\alpha} - K_{1,\alpha})\, c} \left[\frac{\Delta v_{12}}{c} + \left(\frac{f_{1,l}}{f_{1,n}} - \frac{f_{2,l}}{f_{2,n}} \right) \right] . \tag{4.28}$$

Note that the total uncertainty in determining $\Delta \alpha / \alpha$ is governed by the uncertainty in determining Δv_{12}. The uncertainty in determining Δv_{12} is typically 100% or more. The error in the sensitivity coefficients, however is only a few per cent and thus negligible. For the case when the uncertainties in the lab frequencies are small compared to the astronomical observations we can write the total uncertainty in determining a variation in α as

$$\delta \left(\frac{\Delta \alpha}{\alpha} \right) = \frac{\delta(\Delta v_{12})}{c} \frac{1}{K_{2,\alpha} - K_{1,\alpha}} \tag{4.29}$$

In CH the transitions also depend on the electron-to-proton mass ratio μ. Everything that has been derived so far is analogous for the case of μ-variation. To obtain bounds on the variation it is common to assume that there is either a change in α or a change in μ but not in both simultaneously. If instead we allow both constants to change, we obtain

$$\frac{\Delta \alpha}{\alpha} = -\frac{\Delta \mu}{\mu} \frac{K_{\mu,2} - K_{\mu,1}}{K_{\alpha,2} - K_{\alpha,1}} + \frac{1}{K_{\alpha,2} - K_{\alpha,1}} \left[\frac{\Delta v_{12}}{c} + \left(\frac{f_{1,l}}{f_{1,n}} - \frac{f_{2,l}}{f_{2,n}} \right) \right] . \tag{4.30}$$

All we now need to do is to extract Δv_{12} from the astronomical spectra. There are currently only two published spectra of the $J = 3/2$ transition available [202, 218]. They are both taken in W51 but with different telescopes. To accurately extract Δv_{12} from the published $J = 1/2$ and $J = 3/2$ spectra we digitise them and fit Gaussian profiles to the spectra. We fit multiple Gaussians to spectra that contain multiple velocity components or hyperfine components. Figure 4.23 on the left shows the astronomical data (blue dots) and the multi Gaussian fits (red line) which we use to find the centre of the lines. As mentioned by Ziurys and Turner the qualitative similarity between the excited- and ground-state spectra in terms of the velocity distribution of the CH molecules in W51 strongly indicates that both spectra stem from the same region in the cloud [202]. This is very important because different parts of the cloud may possess different velocities and thus different Doppler shifts. We digitise all the datasets and find that a function consisting of the sum of three Gaussians fits the data best. We get the centre for each Gaussian and find Δv_{12}. For the sensitivity coefficients we take the ones calculated by Kozlov [176] which are reproduced in table 4.5. We calculate $\Delta \alpha / \alpha$ for each combination of hyperfine transitions (single $J = 3/2$ and three $J = 1/2$) individually and take the weighted mean and standard deviation of the individual results. Assuming that only one constant changes at a time this
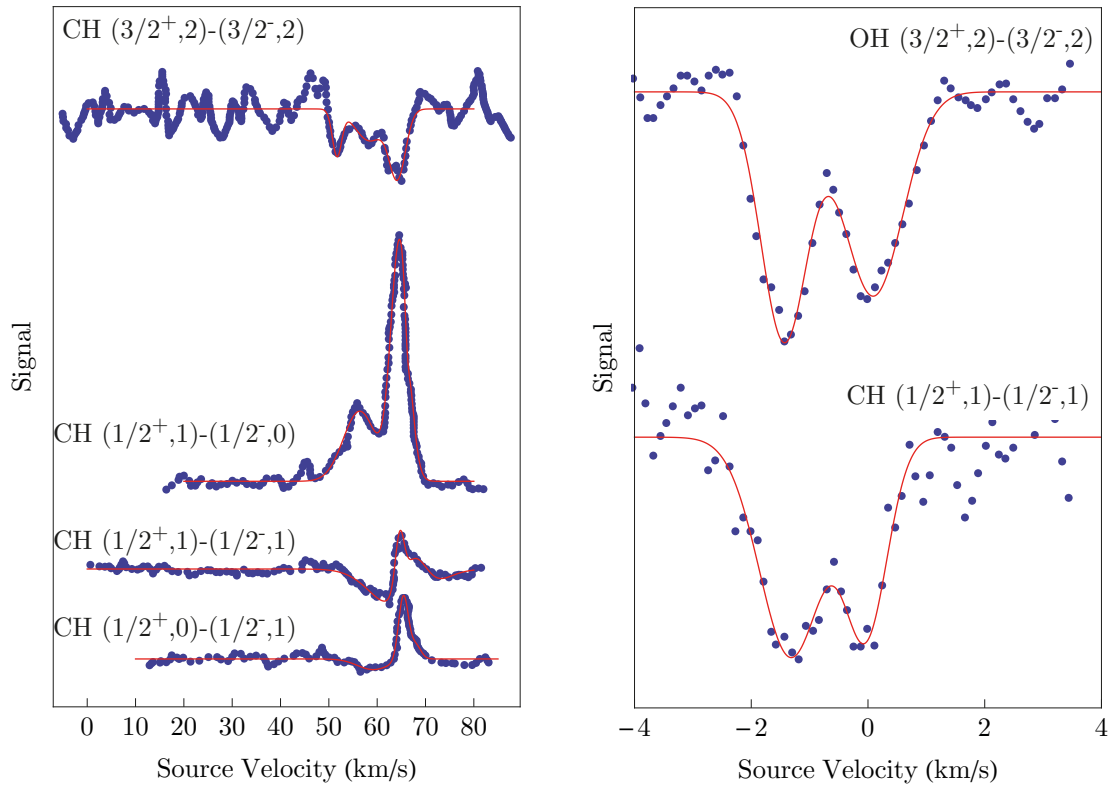
FIGURE 4.23: Examples of astronomical data we use to determine Δv_{12}. Left: Ziurys and Taylor measured the $(3/2^+, 2) - (3/2^-, 2)$ transition towards W51 [202]. We compare these data to all three $J = 1/2$ transitions measured by Genzel and colleagues [203]. The peculiar lineshape is further analysed by Turner [218]. He comes to the conclusion that the absorption feature in the $J = 1/2$ spectra at about $60\,\mathrm{km\,s^{-1}}$ stems from a dense cloud in front of the cloud that emits at $67\,\mathrm{km\,s^{-1}}$. Right: We also use data from Rydbeck and colleagues who recorded CH and OH spectra in the Orion spiral arm features towards the continuum source Cassiopeia A. The similar velocity profile indicates that both spectra originate from the same region in the cloud and that OH and CH have similar velocities in the cloud.

Transition	K_α	K_μ	f_l	f_n
$(1/2^+, 1) - (1/2^-, 1)$	0.62	1.7	3335.479356	3335.481
$(1/2^+, 0) - (1/2^-, 1)$	0.63	1.69	3349.192556	3349.193
$(1/2^+, 1) - (1/2^-, 0)$	0.59	1.71	3263.793447	3263.794
$(3/2^+, 2) - (3/2^-, 2)$	-8.44	6.15	701.677682	701.677
$(3/2^+, 1) - (1/2^-, 1)$	-8.07	5.97	724.788315	724.788
$(3/2^+, 1) - (1/2^-, 2)$	-8.66	6.32	703.978340	704.175
$(3/2^+, 2) - (1/2^-, 1)$	-8.37	6.17	722.487624	722.303

TABLE 4.5: The sensitivity constants of the CH transitions, the current best lab frequencies f_l and the nominal frequencies f_n used by the astronomers.

Transition	K_α	K_μ	f_l	$f_n(1972)$
$(3/2^+, 2) - (3/2^-, 2)$	-1.14	2.55	1667.358996	1667.35903
$(3/2^+, 1) - (1/2^-, 1)$	-1.14	2.55	1665.401803	1665.40184
$(3/2^+, 1) - (1/2^-, 2)$	-1.02	2.49	1720.529887	1720.52998
$(3/2^+, 2) - (1/2^-, 1)$	-1.27	2.61	1612.23101	1612.23101

TABLE 4.6: The sensitivity coefficients for the OH transitions, the current best lab frequencies f_l and the nominal frequencies f_n used by the astronomers

gives the final result of

$$\frac{\Delta\alpha}{\alpha} = -2 \pm 1.5 \times 10^{-7} \qquad \text{and} \qquad \frac{\Delta\mu}{\mu} = 4 \pm 3 \times 10^{-7}. \qquad (4.31)$$

If both constants change we can constrain the combination of a variation in α and μ by

$$\frac{\Delta\alpha}{\alpha} = 0.49\frac{\Delta\mu}{\mu} + \left(-2 \pm 1.5 \times 10^{-7}\right). \qquad (4.32)$$

It is not ideal that the data were taken with different telescopes with a time difference between the measurements of six years. The limits we provide, however, clearly demonstrate the potential of this technique for obtaining tight constraints on variations in fundamental constants with the benefit that systematic errors are heavily suppressed by comparing transitions in a single molecular species.

The shortage of $J = 3/2$ data prompted us to investigate other species with similar velocity profiles in the same and other clouds as well. It is known that clouds with CH usually contain OH as well and that they are well mixed with very similar lineshapes and velocity components. We identified 5 such sources in our galaxy. One of the spectra is shown in figure 4.23 on the right. The OH lab frequencies and sensitivity coefficients we use are given in table 4.6. The results of all of these data sets and their constraints are given in table 4.7. As shown in figure 4.23, in each source there are multiple velocity components and/or hyperfine components. We therefore get several different values for the velocity difference Δv_{12}. Their standard deviation is typically several times the individual uncertainties of the fits. First of all this might simply be due to the fact that the transitions were not observed simultaneously with the same receiver, beam size, system temperature and velocity resolution. Violation of any of these conditions leads to shifts in the line centres which are referred to as Doppler noise. For the data presented in table 4.7 we assume that these velocity shifts due to instrumental imperfections are of random nature. We can circumvent these problems with dedicated measurements instead of using archival data. However, for the case of CH-only data residual Doppler noise may still arise from kinetic temperature fluctuations within the molecular cloud (the J=3/2 state lies 25 K above the J=1/2 state). If we compare CH spectra to other molecular spectra unavoidable Doppler noise is caused by velocity gradients across the molecular cloud and/or by spatial segregation. The different optical depths for different transitions is also a problem. Finally, the underlying
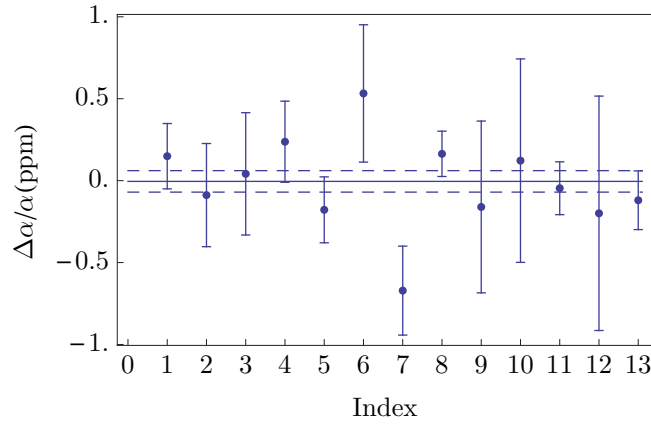
FIGURE 4.24: The value of $\Delta\alpha/\alpha$ and its error bar for each velocity component used to in table 4.7. The values 7-13 are all the possible combinations of CH and OH lines given in references [225, 226].

velocity profiles may not be Gaussian.

All these effects, however, should vary randomly for different clouds. By averaging over a statistically significant data sample we can minimise the influence of the Doppler noise. Other systematic frequency shifts caused by external electric and magnetic fields and the cosmic black-body radiation-induced Stark effect have been shown to be small ($\approx 1 \text{ m s}^{-1}$) [219].

Taking the weighted mean of all of these constraints we arrive at the final results of

$$\Delta\alpha/\alpha = (0 \pm 0.7) \times 10^{-7} \qquad \text{and} \qquad \Delta\mu/\mu = (0.1 \pm 1.4) \times 10^{-7} \qquad (4.33)$$

with 3σ upper bounds of $|\Delta\alpha/\alpha| < 2.1 \times 10^{-7}$ and $|\Delta\mu/\mu| < 4.3 \times 10^{-7}$. All the data we used to derive this result is plotted in figure 4.24. Unfortunately, current chameleon theories do not predict any specific value for changes in fundamental constants as a function of the surrounding matter density and we thus cannot constrain any of these theories yet. However, this work can be regarded as a test of the Einstein equivalence principle of local position invariance.

4.5.1 Summary

By comparing our lab-based measurements of the Λ-doublet frequencies with astronomical spectra obtained from interstellar gas clouds within our own galaxy we constrain the variation of the fine-structure constant α and the electron-to-proton mass ratio μ with matter density. The $J = 1/2$ and $J = 3/2$ transitions are highly sensitive to changes in such fundamental constants and thus provide a sensitive means to constrain such variations. Furthermore, the two transitions shift with different sign and amount with changes in α or μ which allows to cancel the Doppler shift in a relative measurement. The shortage of $J = 3/2$ data prompted us to compare the CH $J = 1/2$ transitions to the ground state Λ-doublet transitions of OH. The comparison of two different molecular species, however, is prone to systematic velocity offsets that stem

Source	Transition 1	Transition 2	v (km/s)	Δv_{12} (km/s)	$\Delta v'_{12}$ (km/s)	$\frac{\Delta\alpha}{\alpha}10^{-7}$	$\frac{\Delta\mu}{\mu}10^{-7}$	Ref
G111.7-2.1 (CasA)	CH (3264,3335,3349)	OH (1667)	-1.4,0	-0.01(0.09)	-0.08(0.11)	1.5(2.0)	-3.1(4.1)	[220, 221]
G265.1+1.5 (RCW36)	CH (3264,3335)	OH (1612,1665,1667,1721)	6.8	0.06(0.19)	0.04(0.16)	-0.9(3.1)	1.8(6.7)	[222]
G174.3-13.4 (Heiles2)	CH (3264,3335,3349)	OH (1612,1665,1667,1721)	5.8	0.00(0.19)	-0.02(0.19)	0.4(3.7)	0.9(7.9)	[221, 223]
G6.0+36.7 (L124N)	CH (3264,3335,3349)	OH (1665,1667)	2.5	0.05(0.13)	-0.12(0.13)	2.4(2.5)	-5.0(5.3)	[221, 223]
G49.5-0.4(W51)	CH (702)	CH (3264,3335,3349)	65	-0.7(0.4)	-0.5(0.4)	-1.8(2)	3.6(4)	[202]
G30.7-0.0(W43)	CH (702)	CH (3264,3335,3349)	92	1.07(1.2)	1.44(1.1)	5.3(4.2)	-10.8(8.5)	[203, 224]
G174.3-13.4 (Heiles2)	CH (3264,3335)	OH (1665,1667)	5.9,6.3	0.13(0.06)	0.02(0.04)	-0.5(0.8)	1(1.8)	[225, 226]

TABLE 4.7: Analysis of the astronomical data. The columns are: the direction of the source, the transitions used (labelled by the frequencies of the hyperfine components in MHz), the velocity component(s) used, the measured velocity difference, the velocity difference corrected for any differences between the nominal and laboratory frequencies, the derived values of $\Delta\alpha/\alpha$ and $\Delta\mu/\mu$, the references where the spectra are given. The (1-σ) uncertainties are given in parentheses.

from chemical and spatial segregation in the molecular cloud instead of a variation in fundamental constants. The densities of CH and OH, however, are governed by similar gas-phase production and destruction mechanisms which lead to similar abundances in interstellar gas clouds and hence to a similar Doppler profile of the emitted spectra. A recent survey in TMC-1 supports this argument showing that the CH and OH abundances are well correlated [227]. We could demonstrate the high sensitivity of this method to variations in fundamental constants by setting the most stringent upper limit on α variation with matter density to date.

4.5.2   Outlook

Note that the data presented in table 4.7 are not the only sources where CH has been detected. However, we only used those for which the original spectra were presented in the publications. Rydbeck and colleagues published an extensive survey of CH in our galaxy in 1976 in which they list over 20 different galactic sources [221]. With new dedicated observations in these already known sources we could improve our limits and reduce the influence of Doppler noise considerably. Moreover, we could extend Rydbeck's survey to search for CH lines from the $J = 3/2$ transitions that originate from the same sources to make use of the full sensitivity of CH to variations in fundamental constants.

Recent data taken with the $100\,\mathrm{m}$ telescope at Effelsberg show that it has become possible to determine the line centre of the $(1/2^+, 1) - (1/2^-, 1)$ and the $(1/2^+, 1) - (1/2^-, 0)$ transitions with a precision of $0.003\,\mathrm{km\,s^{-1}}$ and $0.004\,\mathrm{km\,s^{-1}}$ which is nearly twenty times more accurate than the data we used to provide the constraints above (figure 4.23) [226]. The accuracy of these data also exceeds the previous best lab frequency values by a factor of three and seven, respectively [228]. Hence with dedicated astronomical measurements, and assuming a three times worse accuracy for determining the centre of the $J = 3/2$ transition, constraints below the 10^{-8} level are possible using the new laboratory measurements presented above. This of course requires to control the random Doppler noise on the same level.

Sakai and colleagues found a small velocity offset between two different hyperfine components in a single CH spectrum [226]. Using our new measurements we can correct their value and indeed the offset disappears.

It would be very interesting to find CH molecules at high redshift to probe for temporal variations of fundamental constants as well. A promising candidate for such a search would be the well known absorbing system at redshift $z \approx 0.89$ towards the radio source PKS 1830-211 [229, 230]. The microwave radiation stems from a high redshift ($z = 2.507$) quasar which passes through a spiral galaxy at $z \approx 0.89$. The galaxy acts as a gravitational lens and splits the image of the quasar into two components and an Einstein ring. By analysing the radio spectrum Wiklind and Combes realised that there is a large number of molecules present in this galaxy which imprint their spectrum onto the broad emission of the quasar [231]. So far over

Source	Redshift	Molecules Detected
Cen A	0.002	CO, OH, NH_3, CN, HCO^+, HCN, N_2H^+, CS, H_2CO, C_3H_2
3C293	0.045	CO, HCO^+, HCN
4C31.04	0.060	CO, HCO^+, HCN
PKS 1413+135	0.247	CO, HCO^+, HCN, CN, HNC
B 1504+377	0.673	CO, HCO^+, HCN, CN, HNC
B 0218+357	0.685	CO, NH_3, H_2O, HCO^+, HCN, CS, H_2CO, H_2S
PKS 0132-097	0.765	OH
PKS 1830-211	0.886	> 40 species including CH

TABLE 4.8: Extra galactic sources for radio- and microwave spectra of molecules.

40 species have been detected in this system, including CH via the lowest mm-wave transition at 530 GHz [232]. A list of the extragalactic sources for molecular spectra following [232, 233] (excluding H_2 and CO, for which many more systems exist) is given in table 4.8. The intensity of the CH lines, especially of the $J = 3/2$ transitions, is usually quite low (ten times weaker than OH lines) which requires the use of large telescopes. The 100 m telescope at Effelsberg covers the entire frequency range between the two Λ-doublets and thus is ideal for further studies. The 100 m telescope of NRAO at Green Bank covers the frequency range from 0.29 to 2.6 GHz and is thus suitable for measuring both transitions at moderate redshifts. The 300 m telescope at Arecibo is also an option. An even larger radio telescope with a single 500 m dish is being built in China's Guizhou province. The construction of the expanded very large array in New Mexico will be completed soon and provide very high sensitivity and resolution. By 2024 the square kilometer array, built in Australia, New Zealand and South Africa is expected to be operational. It will have a collecting area of $10^6 \, m^2$ and thus will provide unprecedented sensitivity to frequencies between 0.07 and 10 GHz.

Other molecules that can provide multiple transitions with different sensitivity coefficients should be considered as well. Methanol, has already been shown to be an excellent probe for μ-variation which does not need any other molecular species to fix the Doppler shift.

Similar to CH the states in the OH molecule are Λ-doubled. All the hyperfine components of the $J = 3/2$ ground state of OH have been measured to very high accuracy already [234] and have been used to constrain a variation in the combined quantity $g_p(\alpha^2/\mu)^{1.849}$ at a redshift of $z \approx 0.247$ [235]. These measurements are however limited to the 10^{-4} level because the sensitivity coefficients of the individual hyperfine components are very similar. The closest other state with a significantly different sensitivity coefficient lies too high in energy to be excited in cold molecular clouds. It might be possible to find excited state OH in the warm (100 K) and dense star-forming regions that surround protostars. However, the emerging spectra will be broad and complicated. Kanekar and colleagues thus used the 21 cm line of hydrogen to calibrate the OH spectra which increased their sensitivity to below the ppm level for a system at $z = 0.765$ [198].

Kozlov and Levshakov have recently proposed to use the tunneling and rotational transitions

of the hydronium ion (H_3O^+) to limit μ-variation [219]. Hydronium has already been detected in interstellar gas clouds and, similar to ammonia, possesses an inversion transition which is very sensitive to variations in μ. The inversion occurs when the oxygen atom tunnels through the plane of the hydrogen atoms which leads to an inversion splitting of the rotational lines. However, in contrast to ammonia ($1.3\,\text{cm}^{-1}$) this splitting is very large ($55.3\,\text{cm}^{-1}$) and is thus observed in the submillimeter-wave region. Furthermore, there are several transitions with opposite sensitivity to μ. In contrast to ammonia the constraint is then based on only one molecular species. Preliminary results constrain $|\Delta\mu/\mu| < 2 \times 10^{-7}$ in our own galaxy. With new high-precision instruments such as ALMA, SOFIA, CCAT and others this can be improved even further. However, the laboratory frequencies have to be improved as well. The isotopologues of the hydronium ion possess similar sensitivities. Currently, however there are no laboratory frequencies available for these ions.

Another potential candidate that provides three strong transitions at 27.6, 25.1 and 10.5 GHz is the linear C_3H molecule with large sensitivity coefficients that range from -5 to +19 [236]. This molecule has already been observed in the absorber system towards PKS 1830-211 but the laboratory frequencies are not known for these transitions yet.

Molecular spectra in the microwave and far infrared provide a sensitivity to variations in fundamental constants that can surpass optical spectra by as much as three orders of magnitude. Furthermore, molecules provide multiple transitions that shift by a different amount, or even in opposing direction. Hence there is no need to compare spectra of different species which makes this technique relatively immune to systematic errors. However, there are currently only very few molecular spectra available from high redshift objects. Additionally, the laboratory frequencies of particularly suitable molecules are often not known accurately enough in order to be useful for tests of variations of fundamental constants. Our new measurements of the Λ-doublets of the $J = 1/2$ and $J = 3/2$ states adds another molecule to the list of sensitive and abundant species and will help to improve constraints. A search for new sources of CH spectra at high redshift is no longer hindered any more by inaccurate lab frequencies. With new, high precision telescopes such as the EVLA it will become possible to find CH at high redshift and use it to tightly constrain variations of fundamental constants.

Finally it should be mentioned that it is widely recognised that abundances of molecules can show significant variations within a molecular cloud as well as between one cloud and another [226]. This is also why one has to be extremely cautious to compare more than one molecular species to search for variations of fundamental constants. Understanding the origin of this chemical segregation is currently an important topic in astrochemsitry. Furthermore, the most abundant molecule H_2 is difficult to observe and thus astronomers rely on other species to trace its distribution through molecular clouds [237]. The CH Λ-doublet emission lines have long been considered as a good tracer of H_2, especially in translucent clouds where the densities are quite low. However, until now the poor rest frequencies of CH limited its usability. With the new rest frequencies provided by our measurement CH can now be used more reliably as

a tracer for H_2 and will also help in elucidating an unexpected velocity offset between CH and CO which was recently detected by a survey conducted by Chastain and colleagues [237].

Chapter 5

Measuring the Lowest Millimetre-Wave Transition Frequency of CH

> *Somewhere, something incredible is waiting to be known.*
>
> Carl Sagan

5.1 Introduction

This chapter describes a measurement of the frequency of the transition between the two F-manifolds, i.e. from $(F_2, J = 1/2)$ to $(F_1, J = 3/2)$ (see level diagram of 4.1). As mentioned in the previous chapter our molecular beam source produces CH molecules at a low translational temperature of $0.4\,\mathrm{K}$. The rotational temperature is similar. This means that only a small fraction of the molecules populate the excited $J = 3/2$ state which lies about $25\,\mathrm{K}$ above the ground $J = 1/2$ state. Therefore we populate the $J = 3/2$ state with radiation from an amplifier multiplier chain (AMC) which enabled us to observe the $J = 3/2$ Λ-doublet transitions for the first time directly in the lab (see previous chapter). We can use our setup, however, not only to transfer population, but also to measure this lowest far-infrared transition of CH with unprecedented accuracy. This is especially interesting because new high-precision instruments such as ALMA or the Herschel Space Observatory provide exceptional resolution in the far-infrared and have very recently delivered the first CH spectra of the $J = 1/2 - J = 3/2$ lowest mm-wave transition from the high redshift absorber PKS 1830-211 [232] and from sources in our own galaxy [238–241]. Herschel has now run out of liquid helium to cool its detectors. However, the new CCAT is currently being built in Chile and will provide extremely fast data acquisition rates and thus is a perfect instrument to conduct large surveys to search for new sources for

molecular spectra. Once new sources have been found the unrivalled sensitivity of ALMA can be used to record high resolution spectra.

The first to directly measure any far-infrared transition of CH in the lab were Evenson, Radford and Moran in 1971 using the absorption of a water vapour laser in an oxyacetylene flame. They detected the pure rotational transition $(J = 5/2, N = 2) - (J = 7/2, N = 3)$ at 2.5 THz [242]. In 1978, Hougen and colleagues succeeded to measure the $(J = 1/2, N = 1) - (J = 3/2, N = 1)$ transition for the first time using optically pumped far-infrared lasers, a low-pressure methane/atomic fluorine flame within the laser cavity and a strong magnetic field to Zeeman shift the molecules into resonance with the far-infrared laser [243]. These measurements significantly improved the indirect measurements of the Λ-doublet frequencies also. In 1983 Brown and Evenson extended the work by Hougen et al. using the same method. They were able to derive precise molecular constants from their measurements [244]. The uncertainties of these measurements were limited by the accuracy of the then available gaussmeters to a few MHz. By the mid 1980s Evenson, Jennings and Petersen developed a tunable far-infrared spectrometer by mixing two CO_2 lasers in a a so-called MIM (metal-insulator-metal) diode [245]. This technique provided a couple of microwatts of far-infrared radiation which Davidson, Evenson and Brown used to measure the CH lines with a tenfold improvement in accuracy. They measured the rotational transitions up to N=5, however refrained from publishing their results because they could not detect the lowest mm-wave transition. By 2000 new far-infrared sources such as the backward wave oscillator have become available. Amano used such a source to measure the $(J = 1/2, N = 1) - (J = 3/2, N = 1)$ transition to accuracies that range from 30 to 100 kHz [246]. This stimulated Davidson et al. to publish their results as well and to compile an accurate set of rotational transition frequencies and molecular parameters for CH [247].

As mentioned earlier CH has also been detected in interstellar space via mm-wave transitions. Ossenkopf, for example, recorded a high resolution spectrum of the $(1/2^+, 1) - (3/2^-, 2)$ (notation as in previous chapter (J^p, F)) transition in CH from the iris nebula (NGC7023) with a FWHM of below $2 \, \text{km} \, \text{s}^{-1}$ using Herschel [241]. The centre of this line can be determined to better than one part in a hundred to below $20 \, \text{m} \, \text{s}^{-1}$ which corresponds to a frequency uncertainty of approximately 10 kHz. This is three times more precise than Amano's lab measurement. This clearly shows that even higher precision is needed to be able to use the lowest mm-wave transitions to search for variations of fundamental constants.

5.2 Experimental Setup

A sketch of the setup used to measure the lowest mm-wave transition in CH is shown in figure 5.1. We use an amplifier multiplier chain (AMC) to drive and measure this transition frequency. It multiplies a low frequency input by a factor of 54. This low frequency input is generated by a synthesizer which can easily be phase-locked to a relative frequency uncertainty of 10^{-12} using
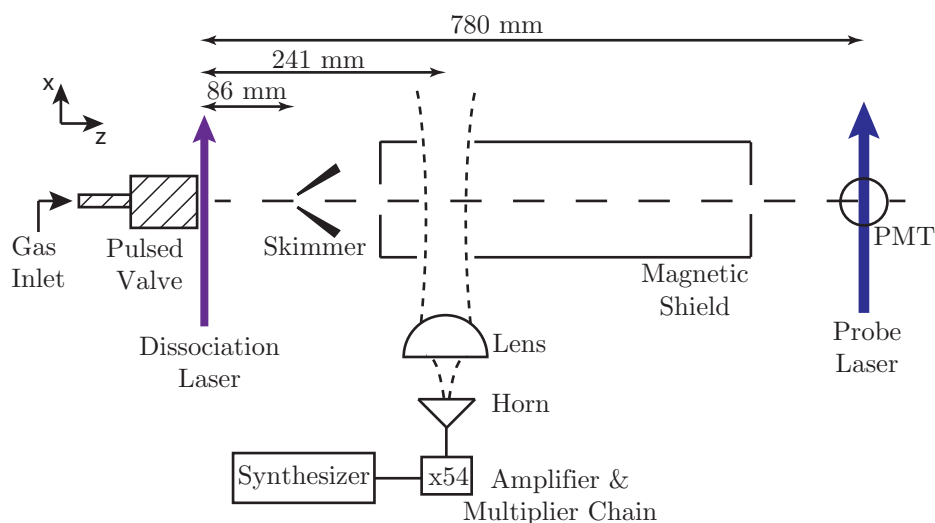
FIGURE 5.1: A sketch of the experimental setup used to measure the lowest mm-wave transition in CH.

standard techniques such as the 10 MHz GPS phase lock described in the previous chapter. A backward wave oscillator typically provides larger tunable frequency range and more output power, but is much more difficult to frequency stabilise.

A plano-convex spherical teflon lens focuses the mm-wave beam which is launched by a diagonal horn antenna to a beam waist of 5.3 mm. The mm-wave beam enters the vacuum chamber through a quartz window. It should be noted that the only way to measure the output of the AMC is the interaction of the radiation with the molecules. We thus have to trust the manufacturer's manual regarding the output power and mode size.

The region where the molecules interact with the mm-wave beam is magnetically shielded. We use external magnetic field coils to measure the residual magnetic fields in the interaction region of the THz radiation with the molecular beam.

5.3 Driving The Millimetre-Wave Transition

5.3.1 Matrix Elements

The theory for driving such a transition is very similar to the case of driving a Λ-doublet transition. The only difference is a slightly different transition dipole matrix element and that the electric field which is driving the transition stems from a Gaussian beam. We can write the transition dipole matrix elements between the two states ($d = \langle 1 | \mathbf{d} | 2 \rangle$) in terms of the Wigner

rotation matrix $\mathcal{D}$ using a pure Hund's case (a) basis as:

$$d = \mu_e \left\langle J, \Omega, I, F, M_F \left| (\mathcal{D}_{00})^* \right| J', \Omega', I, F, M_F' \right\rangle =$$

$$= \mu_e (-1)^{F+M_F-\Omega+I+F'+1} \begin{pmatrix} F & 1 & F' \\ -M_F & 0 & M_F' \end{pmatrix} \sqrt{(2F+1)(2F'+1)} \cdot$$

$$\cdot \begin{Bmatrix} J & F & I \\ F' & J' & 1 \end{Bmatrix} \sqrt{(2J+1)(2J'+1)} \begin{pmatrix} J & 1 & J' \\ -\Omega & 0 & \Omega' \end{pmatrix}. \tag{5.1}$$

As outlined in chapter 2 a Hund's case (a) basis is not appropriate for CH. To account for that we have to use the proper parity-symmetrised basis states (see chapter 2 for details). This allows us to calculate the matrix elements for each M_F component of the transition. The obtained matrix elements are: $(0.29\mu_e, 0.33\mu_e$ and $0.29\mu_e)$ for the three M_F components of the $(1/2^-, 1, M_F) - (3/2^+, 2, M_F')$ line and $(0.17\mu_e$ and $-0.17\mu_e)$ for the two possible M_F components of the $(1/2^-, 1, M_F) - (3/2^+, 1, M_F')$ transition, where μ_e is the permanent electric dipole moment of CH ($\mu_e = 1.46$ D). We concentrate on these two hyperfine components because those are of most relevance to the experiment.

5.3.2 The Millimetre-Wave Beam

The lens we use to collimate the mm-wave beam is a spherical-concave teflon lens, with a radius of $r = 12.7$ mm. The thickness of the lens is 15.85 mm and the radius of curvature thus $R = 13$ mm. The refractive index of teflon at 535 GHz is 1.435 [210]. The focal length of this lens in air is then $f = R/(n-1) = 29.9$ mm (back-focal length 11.9 mm). This results in a beam with a waist of 5.3 mm at the position of the molecules (beam waist at the horn apex: 1 mm, distance from lens to horn apex: 21.2 mm, distance from horn to molecular beam: 239 mm). The output power of the AMC at 535 GHz is 13 µW. The fractional power reflected at each surface is $(n - 1/(n+1))^2$, where $n = 1.4$ is the refractive index of teflon and $n = 2.1$ is the refractive index of the quartz window. The fractional power absorbed in a material of thickness l is $e^{-\alpha l}$, with $\alpha = 0.13 \, \text{cm}^{-1}$ for teflon and $\alpha = 0.1 \, \text{cm}^{-1}$ for quartz. We therefore deliver 7 µW of power to the molecular beam in a beam whose waist is 5.3 mm. The electric field in a Gaussian beam of power P and waist w is $E_0 = \sqrt{4P/(\pi\epsilon_0 c w^2)}$ which for our beam parameters is $10.9 \, \text{V m}^{-1}$. The Rabi frequency at the centre of the beam is $\Omega_0 = d \cdot E_0/\hbar$. For the $(1/2^-, 1) - (3/2^+, 2)$ transition we thus get a Rabi frequency of $\Omega_0 = 2\pi \times 23.1 \, \text{kHz}$ for the $M_F = 1$ to $M_F = 1$ component and $\Omega_0 = 2\pi \times 26.7 \, \text{kHz}$ for the $M_F = 0$ to $M_F = 0$ component. Molecules moving at the speed of argon ($570 \, \text{m s}^{-1}$) through the centre of the mm-wave beam interact for about $\tau = 2w/v \simeq 20 \, \text{µs}$ which yields $\Omega_0 \tau = 0.92\pi$. So, by coincidence, the power of the mm-wave beam should just be enough to drive a π-pulse.

5.3.3 Lineshape

In the limit of small excitation, the transition probability scales as the square of the electric field amplitude at the resonance frequency. The molecules experience a time-dependent electric field $E(t) = E_0 e^{-v^2 t^2 / w^2} e^{-i\omega t}$, where v is the speed of the molecules and ω is the oscillation frequency of the electric field. The expected line shape is then the Fourier transform $E(\omega_0) \propto e^{-w^2 \delta^2 / (4v^2)}$, where $\delta = \omega - \omega_0$ is the detuning from the resonance angular frequency ω_0. The transition probability $|E(\omega_0)|^2$ is a Gaussian function whose FWHM is $\Delta f = \sqrt{2 \ln 2} \frac{v}{\pi w} = 40\,\text{kHz}$. However, we expect to drive a π-pulse which is not in the limit of small excitation. A numerical solution of the Schrödinger equation gives also a Gaussian line shape with a slightly smaller FWHM of 39 kHz.

We still need to account for the Doppler broadening due to the curved wave-fronts of the Gaussian beam. The Doppler broadening is $\Delta f_D = \frac{v}{\lambda} \frac{w \ln 4}{R} = 40\,\text{kHz}$, for $R = 0.16\,\text{m}$. If we add this in quadrature to the transit-time broadening of 40 kHz we expect a total FWHM of the line shape of 57 kHz.

We can also include that into the numerical model. At time t, the molecules are at position vt, where the k-vector of the mm-wave beam is at an angle vt/R, where R is the radius of curvature. The Doppler shift is then $\Delta f_D = v^2 t / (\lambda R)$, with λ the wavelength of the mm-waves. This can be included as a frequency chirp δ_D in the Schrödinger equation and also yields a width of 57 kHz for molecules moving at $570\,\text{m}\,\text{s}^{-1}$ and with a radius of curvature of the mm-wave beam $R = 0.16\,\text{m}$.

Finally we need to take account for the fact that the different M_F components have slightly different Rabi frequencies. This leads to a small decrease in the expected transfer efficiency. Averaged over all three Rabi frequencies of the $(1/2^-, 1) - (1/2^+, 2)$ transition we expect to transfer 74% of the initial ground state population for the mm-wave beam intensity given above.

5.4 Results

The experiment is done in the following way. First we position the AMC box with its horn output central and perpendicular to the molecular beam axis with the polarisation axis of the electric field along y. We lock the detection laser to the $R_{11}(1/2)$ line of the A-X transition and look for depletion of the fluorescence signal as the mm-wave frequency is scanned. We usually detect a depletion of 10%. We then fix the mm-wave frequency to the transition frequency and optimise the position of the box by minimising the signal. After that we add the lens at about one focal length distance from the horn. We adjust the position of the lens using a three-axis translation stage such that it minimises the signal which results in beam waist of $w = 5.3\,\text{mm}$ at the position of the molecular beam. We then scan the mm-wave frequency again to check if the

transition frequency has changed due to small changes in angle of the mm-wave beam. After this optimisation procedure we can typically transfer 40% of the initial $J = 1/2$ population as shown in figure 5.2 on the right for the $(1/2^-, 1) - (3/2^+, 2)$ transition. The blue dots are the data and the red line is a Gaussian fit. The fact that we cannot reach the full expected transfer efficiency of 74% can be attributed to a lower mm-wave beam power. The fit yields a FWHM of 59 ± 0.6 kHz. This agrees well with the expected width of 57 kHz presented in the previous section. The small discrepancy might be due to a slightly smaller beam waist as expected. Figure 5.2 on the left shows the depletion signal without a magnetic shield in the interaction region. We can clearly see that the transition splits due to the Zeeman effect into five components. As explained in chapter 2 the, $J = 1/2$ levels do not shift to first order, whereas the $(3/2^+, 2)$ components shift by $9.07 M_F$ Hz nT^{-1}. The fact that we measure a value that is close to the ideal expected linewidth we conclude that magnetic fields are suppressed to insignificant levels. Broadening due to the Zeeman effect is thus negligible.

After we have optimised the depletion and found the transition frequency we lock the detection laser to the $R_{11}(3/2)$ line of the A-X transition to detect the increase in signal as the mm-wave frequency is scanned. This is shown in the lower panel of figure 5.2.

In order to measure the transition frequency we need to perform systematic checks as well. Although we do not measure any excessive broadening of the lineshape we need to consider systematic shifts due to the Zeeman effect. We measure a magnetic field component along z of 13 nT with the components along x and y at least ten times smaller. The linear Zeeman splitting in this field is only 120 Hz. Furthermore, this linear splitting should not shift the line centre, because for a linearly polarised mm-wave beam, the shifted components are symmetric about the line centre (as shown in figure 5.2).

To verify this we apply an external field along x, y and z using external field coils.[1] When we applied fields of approximately 1 G along x and y we could not detect any frequency shifts. When we applied a field along z we measured a quadratic shift. We fit a parabola of the form $\Delta f(x) = a(x - b)^2 + c$ to the data and extract a quadratic shift of $a = -0.093 \pm 0.005$ kHz/A^2 where A is the current through the solenoid along z in ampere. The offset $b = 0.04 \pm 0.46$ A yields an 1σ upper limit to magnetic field related shifts of $ab^2 = 0.04$ kHz. The data and fit are shown in figure 5.3.

To control frequency shifts that depend on the velocity of the molecules we measure the transition frequency using three different carrier gases. We use krypton, argon and neon for these measurements, with velocities of 420 m s^{-1}, 570 m s^{-1} and 800 m s^{-1}, respectively. A plot of the transition frequency as a function of the velocity is shown in the left panel of figure 5.4. We made this measurement twice for two different angles (red, blue) of the mm-wave beam. We fit a linear model to the data which reveals a frequency shift of -0.049 ± 0.002 kHz/(m/s)

---

[1] The well calibrated magnetic field coils used in the previous chapter do not extend into the state selection region. We thus added external coils, outside the vacuum chamber. Note that these external field coils are very efficient in magnetising the shields. Thus, before changing the applied magnetic field one has to de-gauss the shields.
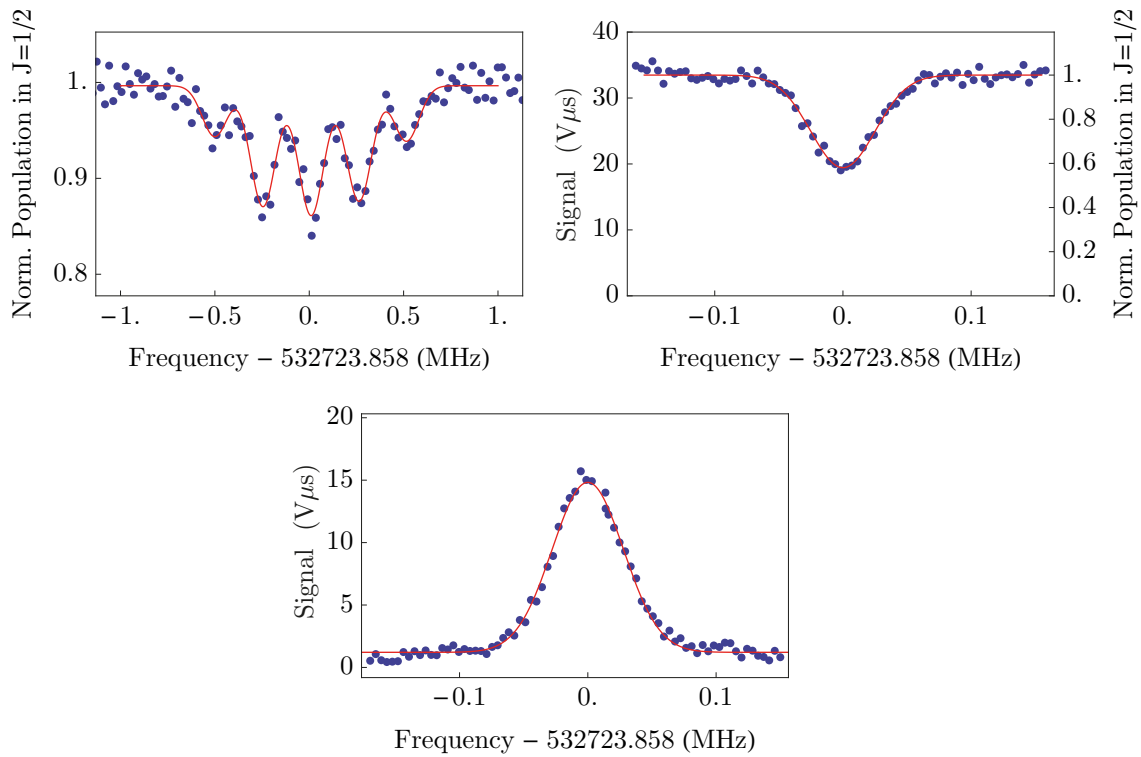
FIGURE 5.2: Left: The $(1/2^+, 1) - (3/2^-, 2)$ measured by scanning the mm-wave frequency while the detection laser is locked to the $R_{11}(1/2)$ line of the A-X transition. The transition is split into five components by the Zeeman effect because of the ambient magnetic field in the lab. The red line is a fit that consists of five Gaussian functions. Right: The same spectrum but with a magnetic shield screening the interaction region. Please note the different scan range. The FWHM of the transition is 59 kHz which agrees well with the expected linewidth presented in the previous section. Bottom: We lock the detection laser to the $R_{11}(3/2)$ line of the A-X transition and detect an increase in signal as the mm-wave frequency is scanned across the lowest mm-wave transition $(1/2^-, 1) - (3/2^+, 2)$.

FIGURE 5.3: Measurement of the Zeeman shift of the $(1/2^-, 1) - (3/2^+, 1)$ transition to control magnetic field related frequency shifts. We apply currents as large as 20 A through an external solenoid. We fit a parabola to the data and extract a limit for residual magnetic fields along z which allows us to constrain magnetic field related frequency shifts.

FIGURE 5.4: Left: We measure the transition frequency as a function of the velocity by changing the carrier gas. We use krypton, argon and neon which yield $420\,\mathrm{m\,s^{-1}}$, $570\,\mathr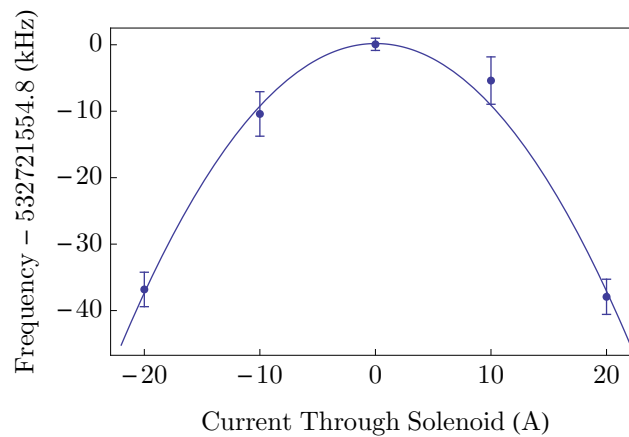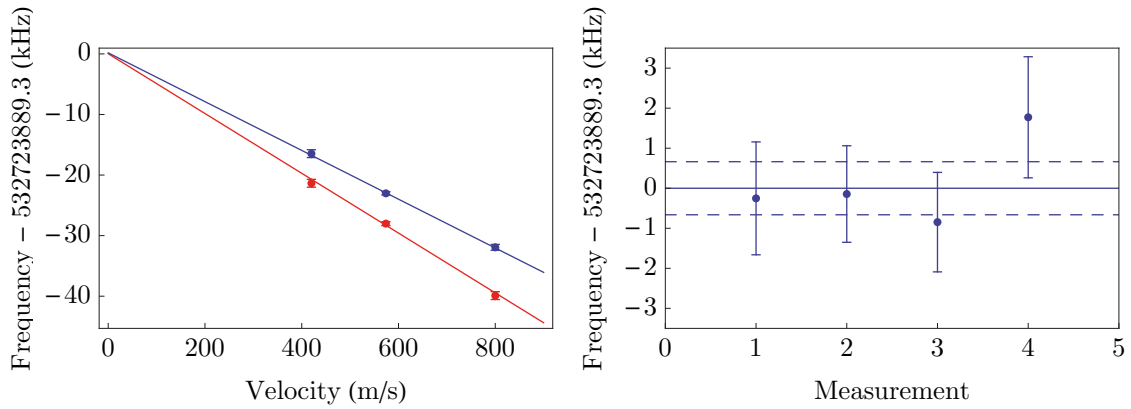m{m\,s^{-1}}$ and $800\,\mathrm{m\,s^{-1}}$, respectively. The difference between red and blue is a slightly different angle of the mm-wave beam with respect to the molecular beam (we moved the AMC box). Right: We repeat this measurement for each angle and thus get four extrapolated frequencies (only two are shown in the left panel). The weighted mean of all four extrapolated zero-velocity frequencies yields the final transition frequency (solid line). The $\pm 1\sigma$ error is shown as dashed lines. The final frequency is 532723889.3 ± 0.7 kHz

Transition	Frequency (kHz)
$(1/2^+, 0) - (3/2^-, 1)$	536795569.5 ± 0.6
$(1/2^+, 1) - (3/2^-, 1)$	536781856.3 ± 0.6
$(1/2^+, 1) - (3/2^-, 2)$	536761046.3 ± 0.6
$(1/2^-, 0) - (3/2^+, 1)$	532793274.6 ± 0.6
$(1/2^-, 1) - (3/2^+, 2)$	532723889.3 ± 0.6
$(1/2^-, 1) - (3/2^+, 1)$	532721588.6 ± 0.6

TABLE 5.1: Final transition frequencies of all six components of the lowest mm-wave ($J = 1/2 - J = 3/2$) transition. The uncertainties are slightly smaller than the individual measurements quoted above because there are more measurements than independent frequencies.

for the data shown in red and -0.040 ± 0.002 kHz/(m/s) for the data shown in blue. The gradients correspond to an angle of about $2.5°$ between the molecular beam and the mm-wave beam. The extrapolated zero velocity transition frequencies with the 1σ uncertainties of the linear fits are shown in the right panel of figure 5.4. The solid line is the weighted mean of the four extrapolated frequencies with the $\pm 1\sigma$ standard error shown as dashed lines. Together with the Λ-doublet transition frequencies from the previous chapter we can now provide improved frequencies for all six lines of the lowest mm-wave transition in CH. We have also measured the $(1/2^-, 1) - (3/2^+, 1)$ transition in the same way to be 532721588.5 ± 1.4 kHz. The final frequencies are given in table 5.1.

5.5 Summary

We measured the lowest mm-wave transition between the $(N = 1, J = 1/2)$ and the $(N = 1, J = 3/2)$ states in CH to unprecedented accuracy using a molecular beam and resonant mm-waves
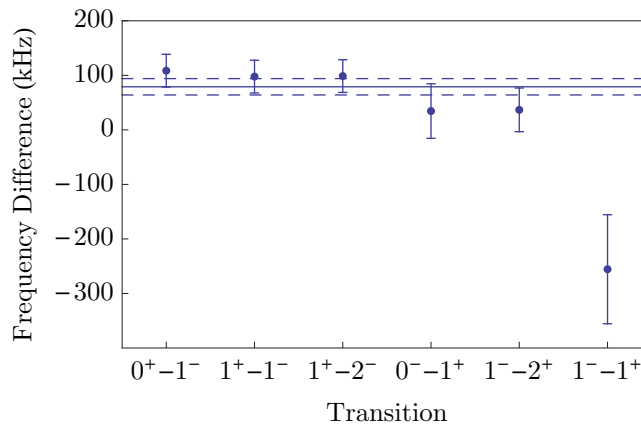
FIGURE 5.5: Difference between the results of Amano [246] and our results. The difference for each transition frequency is shown. The transitions are labelled (F^p, F'^p), where no prime denotes the $J = 1/2$ state and the prime the $J = 3/2$ state. The error bars are entirely due to the uncertainty in Amano's measurement. Our results differ from Amano's by as much as 3.6 standard deviations. Taking the weighted mean (solid blue line) we find a difference of 79 ± 15 kHz indicating an uncontrolled systematic error in those previous measurements (1σ standard error shown as dashed lines).

in combination with laser induced fluorescence detection. Compared to the previous best values for these transitions provided by Amano [246] our results are between 50 and 150 times more precise. Our measurements differ from Amano's by as much as 3.6 standard deviations. A plot of the difference between the transition frequencies obtained by Amano and our measurements is shown in figure 5.5. Taking the weighted mean of all the differences we find a discrepancy of 79 ± 15 kHz. This indicates an uncontrolled systematic error in those previous measurements.

In our measurement systematic frequency shifts are negligible apart from a small velocity dependence. We control these velocity shifts by measuring the frequencies for three different carrier gases.

5.6 Outlook - The Sensitivity of the Lowest Millimeter-Wave Transition to Variations in Fundamental Constants

It has been shown by de Nijs and colleagues that the mm-wave transitions, similar to the Λ-doublet transitions, are sensitive to variations in fundamental constants. The sensitivity coefficients to variations in α and μ are $K_\alpha = 1.57$ and $K_\mu = -0.22$ [248]. Note that there is a small differential sensitivity for transitions that start from different parity states in the $J = 1/2$ ground state. The new, sensitive telescopes that have and will become available are ideal instruments to look for CH at high redshift. Using ALMA, for example, Muller and colleagues recorded the very first spectrum of CH at a redshift of $z = 0.89$ [232]. These measurements together with new radio astronomical data of the Λ-doublet transitions in the $J = 1/2$ and/or

the $J = 3/2$ state from the same cloud would be an ideal way to test for variations in fundamental constants, to very high precision.

Chapter 6

A Microwave Trap for Polar Molecules

[...] we never experiment with just one electron or atom or (small) molecule. In thought experiments, we sometimes assume that we do; this invariably entails ridiculous consequences[...]

Erwin Schrödinger

6.1   Introduction

The statistical uncertainty in a measurement of frequency f, can be described by

$$\sigma \propto \frac{1}{Q\sqrt{N}}, \qquad (6.1)$$

where Q is the quality factor of the transition, given by $Q = f/(\Delta f)$, with Δf the width of the transition and N is the total number of detected events (e.g. detected photons per shot over a given period of time). For the Λ-doublet measurements, for example, Δf is limited by the interaction time to $\Delta f \simeq 1/\tau = 2\,\text{kHz}$, $N \simeq 10\,000\,\text{s}^{-1}$ gives a statistical uncertainty of $\sigma = 6 \times 10^{-9}t^{-1/2}$. This is only true in the absence of any other noise sources, for example of electronic noise or laser scatter. We can infer that by increasing the interaction time we can increase the quality factor and thus decrease the statistical uncertainty linearly. So to improve any frequency measurement which is not limited by spontaneous decay it is beneficial to increase the interaction time with the electromagnetic field in order to decrease the linewidth Δf. This is, of course, the basic idea behind an atomic fountain which achieves interaction times of the order of one second. For frequency measurements in molecules this is very challenging due to the lack of efficient cooling techniques. Although one can decelerate molecules to rest using

Stark decelerators the molecules remain relatively hot. Once released from the decelerator, they quickly expand which decreases the number of molecules available for the measurement drastically. Nonetheless, efforts are under way to measure the inversion doublet transition frequency in ammonia to very high precision in a molecular fountain [55].

It has recently been shown that direct laser cooling of molecules is possible [72, 249–251]. This technique, however, will be limited to a few molecular species only [71]. It has recently been suggested that laser cooling of a slow, effusive buffer gas beam could be sufficient to build a fountain of YbF molecules [252]. This could improve the sensitivity of a measurement of the electric dipole moment of the electron by three orders of magnitude. The final temperature in laser cooling experiments is, however, still too high ($\approx 200\,\mu$K) to explore the rich physics of long-range and anisotropic dipole-dipole interactions between polar molecules. In order to cool a gas of polar molecules to ultra cold temperatures (below $1\,\mu$K) for a large variety of different molecular species it is thus necessary to find a very general and very efficient cooling technique.

A large variety of molecules can be produced with temperatures in the range of $10\,$mK to $1\,$K either by decelerating a supersonic beam [81] or by capturing the low velocity tail of an effusive buffer gas cell [81, 82, 214]. Collisional cooling in a trap is the natural extension and can serve as such a very general cooling technique. Evaporative cooling, for example, led to the observation of Bose-Einstein condensation [58, 253], degenerate Fermi gases [59] and the realisation of the first quantum simulator using ultracold atoms in an optical lattice [67]. This technique relies on the selective removal of the most energetic particles from the trap. The remaining particles thermalise through elastic collisions which results in an overall colder and denser sample. This process is highly efficient and yields very low temperatures. It has recently been demonstrated that this technique is not only limited to atoms, but can also be applied to diatomic molecules. In particular, a sample of hydroxyl radicals (OH) has been cooled by microwave-forced evaporative cooling in a magnetic trap [90]. The cooling typically reaches an end when inelastic collisions start to heat the sample and lead to unintended trap loss.

Another collisional cooling technique is sympathetic cooling, i.e. one can overlap a cold sample of molecules with ultracold laser-cooled atoms and let them thermalise. Sympathetic cooling is commonly used in cold atom and ion research [254–257]. To sympathetically cool molecules with ultracold atoms the rate of elastic collisions must be sufficiently high. Hence it is of great advantage to overlap the atoms and molecules in a trap so they can interact for a long time.

The first trapped sample of diatomic, polar (heteronuclear) molecules was created by direct loading of CaH molecules into a magnetic trap inside a cryogenic buffer gas cell [76]. The CaH molecules were produced via laser ablation and cooled via collisions with cold helium buffer gas inside a copper cell (held at 0.3 K). The copper cell was located inside the bore of two superconducting magnet coils in anti-Helmholtz configuration. Molecules with their magnetic moments oriented anti-parallel to the magnetic field (in a weak-field-seeking state) could thus be trapped in the field-free region in the centre. The trap depth is determined by the magnetic moment of the molecules ($\approx 1\mu_B$) and the magnetic field strength. By applying $3\,$T this results

in a trap depth of $2\,\mathrm{K}$.

Similar to magnetic trapping, polar molecules can be confined in an electric field minimum generated by a quadrupole electrode geometry. Only molecules with their permanent electric dipole moment oriented anti-parallel to the electric field (in a weak-field-seeking state) are trapped. The molecules gain potential energy in an applied electric field, i.e. they possess a positive Stark shift. The trap depth is governed by the Stark interaction and is typically of the order of 0.3 to $1\,\mathrm{K}$ for typical electric field strengths achievable in the lab $(100\,\mathrm{kV\,cm^{-1}})$. The first to demonstrate trapping of polar molecules ($\mathrm{ND_3}$) using electrostatic fields were Bethlem and colleagues in the year 2000 [258]. Note that trapping does not necessarily mean having a potential energy minimum at a single location in space. In 2007 a storage ring for polar molecules has been demonstrated that is able to confine molecules to a circular orbit on which the molecules can travel a distance of up to a mile [259, 260].

The great advantages of the magnetic and electrostatic traps are that they are relatively easy to implement and yield deep potential wells of the order of $1\,\mathrm{K}$ which is ideally suited to capture molecules from a buffer gas cell or a Stark decelerator. The great disadvantage, however, is that these traps only work for molecules which are not in their ground state.

The absolute ground state of an atom or molecule is always lowered by an external perturbation, i.e. an atom or molecule in its ground state will be attracted by a field maximum. If the molecules are trapped in an excited state inelastic collisions can eject the molecules from the trap by de-exciting them to the lower-lying ground state. These traps are therefore not suitable to achieve cooling via collisions with a cold buffer gas or evaporation. For some particular molecules, as in the case of the OH radical, the elastic to inelastic cross-section happens to be very large and collisional cooling can even be achieved if the molecules are trapped in an excited state.

A much more general way to achieve collisional cooling is to trap the molecules in their absolute ground state, which prevents a potential loss due to inelastic collisions in the first place. As mentioned already earlier, the ground state of a polar molecule is high-field-seeking. This means that its potential energy decreases as the electric/magnetic field increases, i.e. it possesses a negative Stark shift. Using static electric or magnetic fields it is, however, not possible to create an electric field maximum in free space (in three dimensions), because the largest electric/magnetic field is near the electrodes/magnets. It can even be shown that there exists no combination of static electric, magnetic and gravitational fields that can produce a stable trap for ground state atoms or molecules [261]. In two dimensions such a field maximum can be created. In a cylindrically symmetric trap the atoms or molecules can be confined radially but not axially or vice versa. Fast switching between these two configuration can confine the molecules in their ground state near the trap centre. Such traps are commonly known as ac traps. The basic principle of an ac trap is similar to a Paul trap for charged particles which was invented by Wolfgang Paul and Hans Dehmelt who were awarded the Nobel Prize in Physics in 1989 "for the development of the ion trap technique". Compared to electrostatic traps, ac

traps are very shallow. Such traps provide depths of a few mK and a trapping volume of approximately 10^{-3} cm^3 [87]. Molecules confined in an ac trap are subject to a micromotion at the switching frequency (small amplitude) superimposed on a low frequency macromotion (large amplitude). Tokunaga and co-workers could show that collisions with ultracold atoms lead to unstable trajectories and thus to considerable trap loss before the molecules are cooled [91].

Strong optical light fields have also been demonstrated to trap molecules [262]. Such traps are commonly used in cold atom research and rely on the electric dipole interaction of atoms or molecules with strong laser light that is far detuned from a resonance. The use of a free-space laser beam allows to trap atoms or molecules in their ground state. The trapping potential arises from the interaction of the (induced) dipole moment with the intensity gradient of a strong, focused laser beam. Since the light is very far detuned from any resonance, optical excitations to untrapped states can be kept extremely low. Typical trap depths are below 1 mK and the trapping volume is 10^{-5} cm^3 [263]. The small volume and trap depth makes it very difficult to load large samples of polar molecules from a molecular beam into such traps. However, with high power fibre lasers available nowadays this situation might change. These lasers provide exceptionally high power (500 W) and mode quality which could allow one to couple the light into an optical cavity. This can increase the trap volume and can lead to very deep traps of the order of (0.1 K).

An alternative approach to an optical trap for ground state atoms has been demonstrated in Chris Westbrook's group in 1994 [264]. They used a spherical microwave cavity tuned near the ground state hyperfine transition of caesium. This created a magnetic field maximum in the centre of the cavity in which the atoms could be confined. Due to technical difficulties, however, they could not trap the caesium atoms in their absolute ground state. Nonetheless, Spreeuw and colleagues could demonstrate the basic working principle of such a microwave trap for ground state atoms or molecules. DeMille and co-workers took this idea further and pointed out that one could use the same principle to trap molecules in their absolute ground state [265]. The large wavelength of the microwaves results in a large trap volume (1 cm^3) and the ac Stark interaction with low lying rotational transitions in molecules can lead to very deep traps ($\approx$ 1 K). To reach such large trap depths one must amplify high power microwaves (2 kW) in a resonator to reach electric field strengths of order of 3 MV m^{-1}. DeMille proposed to use a Fabry-Pérot type resonator, the open geometry of which allows for easy trap loading and overlapping with ultracold atoms. The molecules are trapped in their high-field-seeking ground state which should, in principle, eliminate inelastic collisions during evaporative or sympathetic cooling. The polarisation of the molecules in the strong electric field leads to extraordinary large elastic collision cross-sections due to the long-range dipole-dipole interaction [265].

More detailed calculations at a later stage, however, showed that under certain circumstances the presence of a microwave field can lead to considerable inelastic collisions between atoms and molecules [266] and molecules and molecules [267, 268]. A strong microwave field ($\mu E_0 \approx hB$) close to a rotational transition at $f \approx 2B$, where μ is the permanent electric dipole moment, E_0

is the electric field strength of the microwaves and B is the rotational constant of the molecules produces a dressed state, i.e. a superposition of multiple rotational states. The strong dipole-dipole interaction then induces inelastic (state-changing) collisions mediated by the microwave field.

Molecule-molecule and molecule-atom systems can also undergo chemical reactions, even at ultracold temperatures and the reaction rate can increase with increasing dipole-dipole interactions [268].

From all these traps presented above we decided that the most favourable candidate for reaching ultracold temperatures through collisional cooling is the microwave trap. Although the microwave field induced collisional losses may be a disadvantage, the problem can be minimised by operating the trap with a large detuning from resonance. DeMille proposed the idea of a microwave trap nine years ago, but nobody has actually built a working version yet. However, a lens and a decelerator using microwaves have recently been used to manipulate the motion of ammonia molecules [269, 270].[1] A decelerator based on an open Fabry-Pérot resonator for microwaves has also been suggested, but has not been realised yet [272]. In the group of Takamasa Momose at the University of British Columbia in Vancouver, an alternative approach to decelerate molecules using microwaves has been realised. Instead of using normally conducting copper as in [269] they have built a prototype decelerator based on a closed cylindrical, superconducting cavity which operates at cryogenic temperatures [273]. The possibility to use superconducting mirrors in an open geometry for trapping will be discussed in more detail in section 6.7.1.

Our efforts to build and characterise a microwave trap have been stimulated by DeMille's original paper and David Glenn's efforts to built such a trap [265, 274].

6.2 Initial Design Considerations and Basic Working Principle

The very first restriction in terms of designing the microwave cavity was that it should be general (for many species) and deep (provide a trap depth of the order of $1\,\mathrm{K}$). We also restricted ourselves to the use of ohmic (not superconducting) materials, although using superconducting material might be a very attractive future development for microwave traps. The use of normal conducting metals requires high input power ($2\,\mathrm{kW}$) as will be discussed later more quantitatively. Such power levels are commercially available through travelling wave tube or klystron amplifiers commonly used for satellite communication. These amplifiers can typically operate in the frequency range of $2 - 18$ GHz. This, therefore, limits also the frequency range at which we can operate a microwave trap. Note also that the trap volume is approximately $V \simeq (\lambda/2)^3$ which should not exceed $1\,\mathrm{cm}^3$. The large mode of low frequency traps would lead

---

[1]It is worth noting that Hill and Gallagher showed the deflection of a molecular beam of CsF molecules with resonant microwaves already in 1975 [271].

to a smaller electric field strength and thus decreases the trap depth. Furthermore, the trap for the molecules would be considerably larger than the typical size of a magneto-optical trap for atoms we plan to use for sympathetic cooling experiments. Hence we decided to use a Ku-Band klystron (CPI-VKU7791J) which generates up to $2\,\mathrm{kW}$ of microwave power between 14 and 14.5 GHz. We preferred to use a klystron because they typically deliver a higher CW-output power than travelling wave tube amplifiers. The microwave trap setup should also be open, for easy trap loading with molecules and/or atoms and good optical access. Furthermore, it should be compact and compatible with our existing setup that produces ultracold lithium atoms for sympathetic cooling experiments.

The basic working principle of the trap is that the microwave field couples low lying rotational levels in polar molecules. The energy shift of level $|i\rangle$ of a polar molecule in the presence of an oscillating electric field $\mathbf{E}(t) = E_0\hat{\epsilon}\cos(\omega t)$ is given by second order perturbation theory as

$$\Delta E = -\sum_j \frac{\left|\langle j\left|-\frac{1}{2}E_0\mathbf{d}\cdot\hat{\epsilon}\right| i\rangle\right|^2}{\hbar\omega_{ij} - \hbar\omega} - \sum_j \frac{\left|\langle j\left|-\frac{1}{2}E_0\mathbf{d}\cdot\hat{\epsilon}\right| i\rangle\right|^2}{\hbar\omega_{ij} + \hbar\omega} \tag{6.2}$$

where $\hbar\omega_{ij}$ is the transition energy and $\mathbf{d}$ is the dipole moment operator. Here we have to sum over all states $|j\rangle$ that have a non-zero transition matrix element with state $|i\rangle$. Although perturbation theory is strictly only valid for small electric fields ($\mu E_0 < hB$, with μ the permanent electric dipole moment of the molecule, E_0 the electric field strength and B the rotational constant in units of frequency) it illustrates the important features and basic principles of the microwave trap. If we assume state $|i\rangle$ to be the rotational ground state, its energy will decrease in an electric field (will be trapped) if the microwave field is red-detuned from the transition frequency ($\Delta = \omega - \omega_{ij} < 0$). If the frequency of the microwave trap is blue-detuned ($\Delta > 0$), the sign in equation 6.2 changes, the ground state will become low-field-seeking and thus will not be trapped. From equation 6.2 we can also infer that by tuning the microwave frequency closer to the transition frequency we can increase the trap depth. For optical traps this is usually not such a good idea because it leads to an increased scattering rate and thus to rapid heating due to fast spontaneous decays. Rotational states on the other hand have very long spontaneous decay lifetimes, which can exceed the trap lifetime and thus allows to operate the trap very close to resonance. The trap depth for strong fields close to frequencies $\omega/(2\pi) \approx B$ can be approximated by the DC Stark shift to $\Delta E \simeq -(\mu/2)\,E_0$ [265], where μ is the dipole moment of the molecule. As will be discussed in more detail later we can typically achieve electric fields of $E_0 = 3\,\mathrm{MV\,m^{-1}}$ in a high power microwave cavity which results in a trap depth of approximately 0.4 K per Debye of dipole moment (for $\mu E_0 \geq hB$).

A more rigorous treatment of the microwave trap using the dressed state formalism and including more than one state can be found in [265, 274]. As the ground state decreases in energy with increasing electric field a multi-photon transition will become possible between the ground and excited states which gives rise to avoided crossings. This means that if a molecule adiabatically follows the energy curve through such an avoided crossing it will be lost from the trap.

DeMille and co-workers, however, could show that by using circularly polarised microwaves one can circumvent this problem. In such a case the absorption of one or multiple photons can only occur if the angular momentum selection rules are obeyed. For the very simple case of $^1\Sigma$, rigid rotor molecules with quantum numbers J (total angular momentum) and M (the projection of the total angular momentum onto the internuclear axis), for example, these selection rules forbid any multiphoton transitions from the ground $|J = 0, M = 0\rangle$ state.

From these consideration we can infer that the trap geometry should be open for easy access, provide a large electric field of about $3\,\mathrm{MV\,m^{-1}}$, operate at the highest frequency available from high power amplifiers, and provide circularly polarised microwaves. An open Fabry-Pérot resonator can fulfil all these requirements. Because of the importance of such resonators in masers and later in lasers, this type of resonator has been extensively studied experimentally and theoretically. Schawlow and Townes initially proposed using Fabry-Pérot interferometers, as they called them, for infrared and optical masers [275]. Fox and Li then provided the first extensive theoretical description, most of which we are still using today [276, 277]. The importance of such resonators in maser and laser science has led to the fact that this topic has become subject of numerous textbooks. Saleh and Teich, for example, provide a very nice general introduction [278] and a great overview especially for the microwave and mm-wave domain is provided by Goldsmith [210].

A simple open resonator, or cavity, is comprised of two highly reflective mirrors each having a radius of curvature (R_1, R_2 respectively) separated by a length L. Electromagnetic radiation confined between two such mirrors will reflect multiple times and interfere. Only waves whose round-trip phase change is an integer multiple of 2π will interfere constructively and form a standing wave. This leads to the well known frequency spectrum of a Fabry-Pérot cavity. If we monitor the transmitted power as a function of the frequency we measure discrete, narrow peaks separated by the free spectral range FSR $= c/(2L)$. The width of the individual peaks depends on the quality of the mirrors, i.e. their reflectivity. Dielectric mirrors that are used nowadays for cavities in the optical domain are very lossy at microwave frequencies. Hence we use metal mirrors. The reflectivity r of a metal mirror can be determined by [279]

$$r = \frac{1 - k\delta\cos\theta_i}{1 + k\delta\cos\theta_i},\tag{6.3}$$

where $k = 2\pi/\lambda$ is the wave number, θ_i is the angle of incidence, $\delta = \sqrt{2/(2\pi f\mu_0\sigma)}$ is the skin depth for non-magnetic ($\mu_r = 1$) good conductors ($\epsilon_r = 1$) with $\mu_0 = 4\pi \times 10^{-7}$ the permeability of free space, f the frequency of the microwaves and σ is the DC conductivity of the metal.[2] The highest bulk conductivity of all the elements is that of silver. It surpasses that of copper by about 5%. Bulk silver mirrors would be expensive and silver plating of a

---

[2] An electromagnetic field induces an AC current density on the surface of the conductor. This current density decreases exponentially with increasing depth from the surface. The depth below the surface at which the current density has decreased to $1/e$ of its original value is defined as the skin depth δ.

substrate usually introduces extra losses on the few per cent level [280]. So we decided to use copper instead. Using the recommended resistivity $\sigma = 1/\rho = 5.8 \times 10^7$ S m^{-1} (International Annealed Copper Standard, IACS) of copper at 293 K from [281] a frequency of 14.5 GHz and normal incidence ($\theta_i = 0$) the skin depth is $\delta = 0.55\,\mu$m which corresponds to a reflectivity $r = 0.999666$. Note, however, that surface effects can have significant impact on the reflectivity and lead to considerable discrepancies of the actual surface resistance compared to the one calculated from the conductivity of the bulk material. This discrepancy typically becomes worse for higher frequencies, especially for copper [282]. Furthermore, a layer of copper oxide on the surface reduces the conductivity typically by about 8% [280]. It could also be shown that a surface roughness of the order of the skin depth can reduce the surface conductivity by up to 15% [283]. Hence care must be taken when machining and preparing the mirrors.

For any wave to be a stable mode in a cavity, i.e. the distribution of the electromagnetic field inside the cavity is not changing over time, the mirrors must obey the condition:

$$0 < \left(1 - \frac{L}{R_1}\right)\left(1 - \frac{L}{R_2}\right) < 1\,. \tag{6.4}$$

We limit ourselves to the lowest order modes in such a cavity (fundamental modes) which are commonly denoted as TEM$_{m=0,n=0,q}$ modes. These modes have the lowest loss in a cavity and have the smallest size and thus produce the largest electric field.

We have to keep in mind that the cavity should fit into our ultracold lithium setup in which we can test the basic working principle with ultracold lithium atoms. This will also be the setup in which we will aim to sympathetically cool molecules with ultracold lithium atoms. We can cool the atoms in a standard magneto optical trap to ultracold temperatures. The atoms can then be transferred into a magnetic trap (magnetic field coils in anti Helmholtz configuration) which is mounted on a translation stage. This movable trap can transport the atoms into a science chamber in which we plan overlap the magnetic trap with the microwave trap. A picture of the setup is shown in figure 6.1. The height of the science chamber is chosen such that large magnetic field gradients needed to tightly confine the atoms can be achieved. This severely restricts the length of the microwave cavity. Hence we set the length of the cavity to accommodate three antinodes at 14.5 GHz which corresponds to approximately 34 mm. We want the waist of the fundamental Gaussian mode to be in the centre which demands $R_1 = R_2 = R$. The waist of this mode is determined by the radius of curvature of the mirrors and the length of the cavity L to:

$$w_0 = \sqrt{\frac{\lambda z_0}{\pi}} \qquad \text{with} \qquad z_0 = \frac{L}{2}\sqrt{2\frac{R}{L} - 1}\,. \tag{6.5}$$
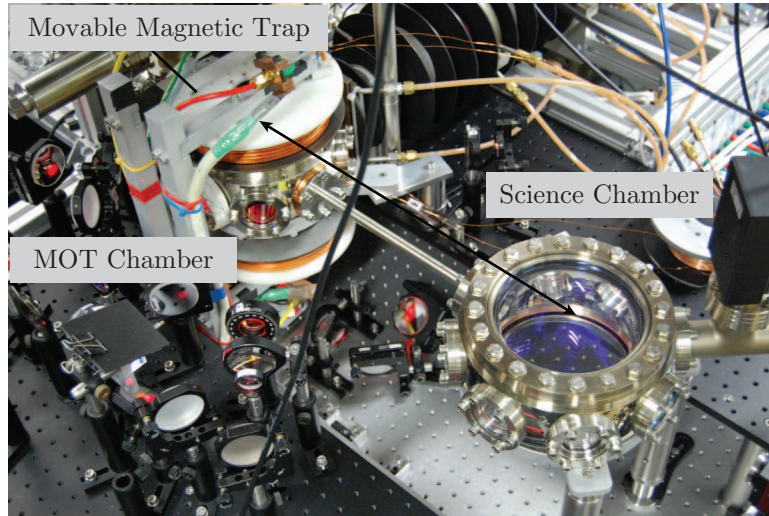
FIGURE 6.1: The lithium setup has been developed by Aisha Kaushik, Rich Hendricks, Sean Tokunaga and Jakob Stack. A cloud of cold, laser-cooled lithium atoms can be transferred between the MOT chamber and the science chamber by using a strong magnetic trap, which is fixed to a motorised translation stage. The microwave trap will be mounted in the science chamber.

Hence small cavities comprised of mirrors with a small radius of curvature produce a tight focus in the centre of the cavity. The size of the mode at the position of the mirrors ($z = \pm L/2$) is:

$$w_m = w(L/2) = w_0 \sqrt{1 + \left(\frac{L}{2z_0}\right)^2} \tag{6.6}$$

If the mode size at the mirror surface is comparable to the size of the mirrors, some of the microwave power will be lost per round trip. This so-called diffractive loss due to the finite size of the mirrors per round trip is:

$$\alpha_d = 2e^{-\frac{D^2}{4w_m^2}}, \tag{6.7}$$

where D is the diameter of the mirrors. As will be explained later, loss per round trip directly translates into lower intra-cavity field and thus lower trap depth. The loss due to the finite size of the mirrors should therefore be small compared to the losses due to the finite reflectivity of the mirrors $\alpha_r = 2\,(1 - r) = 6.58 \times 10^{-4}$. We need to allow for a gap between the mirrors in order to load atoms or molecules into the trap as well. We fixed this distance $d = L - 2\left(R - \sqrt{R^2 - D^2/4}\right) \geq 5$ mm. For our cavity we use a radius of curvature of $R = 73$ mm and a diameter of the mirrors of $D = 85$ mm which yields a diffraction loss of $\alpha_d = 2.6 \times 10^{-6}$ and a gap between the mirrors of $d = 7$ mm for a cavity length of $L = 34.34$ mm. The resonance frequency for such a cavity is given by:

$$f_c = \frac{c}{2L}\left[p + \frac{m + n + 1}{\pi}\cos^{-1}\left(1 - (L/R)\right)\right] \tag{6.8}$$

where p is the number of antinodes in the cavity. For generality we include the frequencies of the transverse modes (m and n) as well. Note that in contrast to optical cavities the Gouy phase term can be of considerable size and has to be included in further calculations. The wavelength resonating in the cavity is thus $\lambda_c = c/f_c$).

In the experiment we typically measure the reflected or transmitted power of the cavity as a function of the frequency. Assuming we measure in transmission the line shape we expect is a Lorentzian of the form [278]

$$\frac{I_t}{I_i} = \frac{t_1 t_2}{1 - \sqrt{r_1 r_2}} \frac{1}{1 + 4\frac{\sqrt{r_1 r_2}}{(1 - \sqrt{r_1 r_2})} \sin^2(\phi/2)} \tag{6.9}$$

where I_t and I_i are the transmitted and incident light intensities, t_1 and t_2 are the transmission coefficients of the mirrors, r_1 and r_2 the reflection coefficients of the mirrors and ϕ the phase shift imparted on the wave by a single round trip. The transmission reaches its maximum at $\phi/2 = \pi$ and the FWHM of the resonance peak is:

$$\Delta f = \frac{c}{2L\mathcal{F}} \qquad \text{with} \qquad \mathcal{F} = \frac{\pi (r_1 r_2)^{1/4}}{1 - \sqrt{r_1 r_2}} \tag{6.10}$$

where we have defined the finesse of the cavity $\mathcal{F}$ and assumed high reflectivity mirrors. We can measure the width of a transmission peak Δf and the frequency at which the cavity resonates f. The ratio $f/\Delta f$ is known as the quality factor Q of the cavity which is related to the finesse by $Q = 2L\mathcal{F}f_c/c$. For the parameters presented above ($L = 34.34$ mm, $R = 73$mm, $r_1 = r_2 = 0.999666$) we expect a quality factor $Q_0 = 31291$. This is often referred to as the unloaded quality factor of the cavity. We need to lower the reflectivity of one mirror to couple power into the cavity which lowers the quality factor. This is known as the loaded quality factor Q_l.

By measuring the width and the resonance frequency we can determine the total round-trip losses of the cavity. The quality factor is also related to total internal energy in the cavity. To be more precise it is defined as the resonance angular frequency times the ratio between the total stored energy inside the cavity U to the total power loss. Hence the width of the resonance is a direct measure of the total energy that is stored in the electromagnetic field inside the cavity. If we are constantly feeding power into the system and a steady state is reached the total power lost must be equal to the input power P_i. The quality factor in this steady state is thus

$$Q = 2\pi f \frac{U}{P_i}. \tag{6.11}$$

The total stored energy in the cavity is related to the electric field inside the resonator of volume V via:

$$U = \frac{1}{2}\epsilon_0 \int_V |E|^2 dv. \tag{6.12}$$

The electric field in a standing wave Gaussian beam in cylindrical coordinates is:

$$E(r, z, t) = E_0 \frac{w_0}{w(z)} e^{-r^2/w^2} e^{ik\rho^2/(2R)} e^{-i\phi} e^{i\omega t} \cos(kz). \tag{6.13}$$

The total stored energy in a resonator of length $L = q\lambda/2$ becomes:

$$U = \frac{1}{8} \epsilon_0 E_0^2 \pi w_0^2 L. \tag{6.14}$$

If we plug this into equation 6.11 the quality factor becomes

$$Q = \frac{f}{\Delta f} = \frac{\pi^2 f \epsilon_0 E_0^2 w_0^2 L}{4P_i} \tag{6.15}$$

which gives us an expression for the electric field inside the cavity:

$$E_0 = \sqrt{\frac{4P_i Q}{\pi^2 f \epsilon_0 w_0^2 L}} = \sqrt{\frac{8P_i \mathcal{F}}{\pi^2 \epsilon_0 c w_0^2}}. \tag{6.16}$$

A small waist, large input power and high reflectivity mirrors therefore maximise the electric field inside the cavity.

A common way in the literature to express the quality factor is in terms of the losses per round trip. The loss per round trip due to finite resistivity (reflectivity) of the mirrors is $\alpha_r = 2(1 - r)$. The quality factor of this ideal cavity is then given by:

$$Q_0 = 2\pi \frac{2L}{c/f_c} \frac{1}{\alpha_r}. \tag{6.17}$$

Note that for long cavities the factor $2L/(c/f_c)$ is simply the number of antinodes. For short cavities whose size is comparable to the wavelength the Gouy phase term is large and the exact value for f_c must be used. Equation 6.17 is a very useful way to express the quality factor because now we can add other potential losses in the cavity and check how they affect the quality factor. As mentioned earlier already we need to lower the reflectivity of one mirror so that we can couple power into the cavity. This effectively introduces an additional loss α_c. The resulting quality factor is known as the loaded quality factor:

$$Q_l = 2\pi \frac{2L}{c/f} \frac{1}{\alpha_r + \alpha_c}. \tag{6.18}$$

When the loss introduced by the coupling equals the losses in the cavity $\alpha_c = \alpha_r$ the cavity is said to be critically coupled, meaning that 100% of the input power is coupled into the cavity. At this point the quality factor is half of its unloaded value Q_0. Note that we assumed that all the loss in the cavity is due to the finite resistivity in the mirrors. This also means all the input power is finally dissipated as resistive heat in the mirrors. For an input power as large as $2\,\mathrm{kW}$ this leads to significant heating of the mirrors and an efficient cooling scheme for the mirrors is

thus obligatory.

For a mirror diameter of $D = 85\,\text{mm}$ the losses due to the finite size of the mirrors is $\alpha_d = 2.6 \times 10^{-6}$ and thus can be neglected.

The surface roughness of our mirrors can be another source of loss. This can considerably affect the surface conductivity of the mirrors and thus their reflectivity. This effect was first studied by Samuel Morgan in 1949 [284]. He found that the presence of regular grooves or scratches whose dimensions are comparable to the skin depth can increase the surface resistance by up to 60 %. Measurements performed by Hernandez and colleagues could confirm this although to a somewhat smaller, but still significant level [283]. Incoherent scattering (diffusive reflection) from a mirror that has a surface roughness leads to an effective reduction in the mirror reflectivity. The reduction factor is similar to the one derived from electron or X-ray diffraction where it is known as the Debye-Waller factor:

$$r = r_0 e^{-2\epsilon_{\text{rms}}^2 k^2}, \tag{6.19}$$

where ϵ_{rms} is the root-mean-square roughness of the surface. This scattering affects the reflectivity if the lateral correlation length λ_c of the surface roughness is of the order of the wavelength, specifically $\lambda_c k > 4\pi^2$ [285]. Such a large scale variation is not expected if the mirrors are fabricated using a modern CNC lathe.

Since most experiments were done at atmospheric pressure, the absorption of microwaves by water vapour must be considered. Zhevakin and colleagues gave a comprehensive analysis of the absorption of electromagnetic radiation in the atmosphere [286]. At a wavelength of $2\,\text{cm}$ they measured an absorption coefficient of 0.01 dB/km for a water density of $7.5\,\text{g}\,\text{m}^{-3}$. This corresponds to a round trip loss of about $\alpha_w \simeq 10^{-7}$ which is negligible. Note, that at a later stage of the experiment, we also measured the width of the transition under vacuum and did not detect any change.

Therefore the main loss we expect is due to the finite surface resistance of the copper mirrors, which is expected to deviate from the ideal bulk conductivity due to non-ideal surface conditions. Assuming that we can achieve the perfect surface conductivity as calculated from the bulk dc conductivity and assuming critical coupling we can now calculate the expected electric field inside such a cavity: using $Q_l = Q_0/2 = 15646$, $P_i = 2$ kW, $w_0 = 14.3$ mm a resonance frequency of $f = 14.5$ GHz and a cavity length of $L = 34.34$ mm the electric field is $E_0 = 3.8$ MV m^{-1}.

6.3 Aperture Coupling a Fabry-Pérot Resonator

We decided to use a single aperture, drilled into the centre of one mirror to couple microwave power into the cavity. We deliver the high power microwaves through a rectangular waveguide

which is attached centrally to the back of one mirror. The size and wall thickness of the hole then determine the amount of power which is coupled into the cavity. We did not pursue the idea of antenna coupling because of the high power requirement which would necessarily lead to discharges close to the antenna-mirror interface. Coupling into the cavity via an array of sub-wavelength holes has also been suggested [265, 274]. This, however, requires elaborate safety measures which come with handling free-space high power microwave beams. Furthermore, an array of coupling apertures prevents effective cooling of the mirrors, which is crucial due to the large resistive heating.

The theory describing the diffraction of electromagnetic waves by a circular hole (small compared to the wavelength) in a perfectly conducting screen has been developed by Hans Bethe in 1944 [287]. A nice introduction to this theory can also be found in chapter 9.5 of Jackson's book [279] or chapter 4.13 in Collin's book [288]. This theory is based on the simple principle that the hole can be modelled as an effective dipole, i.e. an electric dipole perpendicular to the plane of the hole and a magnetic dipole in the plane of the hole. A rectangular waveguide propagates a TE_{10} mode, which has no component of the electric field in the direction of propagation. This means the electric dipole of the hole cannot be excited, i.e. the coupling is governed by the transverse magnetic field (H_x, where x is along the long side of the waveguide) in the waveguide and the magnetic dipole of the hole. The dipole moment of the hole is [279]:

$$P_{m,x} = \alpha_m H_x = \frac{4r^3}{3} H_x \,, \tag{6.20}$$

where α_m is the magnetic polarisability of the hole, r is the radius of the aperture and H_x, to a first approximation, is the transverse magnetic field that would be present in the absence of the hole. However, because we are dealing with large coupling to a cavity we need to include the fields that are transmitted and reflected by the hole as well. Mongia and Arora deal with this problem in detail [289]. The interested reader will find the books by Collin [288, 290] also very useful. The magnetic dipole moment can then be written as

$$P = \alpha_m \left(H_i + H_r - H_c \right) \tag{6.21}$$

where $H_i = H_x = 2A \sin(\pi x/a) \cos(k_0 z)$ is the incident magnetic field from the waveguide, with A its amplitude, a the long dimension of the waveguide and k_0 is the guided wavenumber in the waveguide. H_r is the reflected magnetic field produced in the waveguide by the radiating dipole, and H_c is the cavity field. We can use equation 4.124 from Collin's book to get H_r:

$$H_r = -\frac{2iP\mu_0\omega}{ab}, \tag{6.22}$$

where μ is the permittivity of free space, ω the angular frequency and a and b are the long and short dimension of the waveguide, respectively. For the field inside the cavity H_c we can consult chapter 7.9 in Collin's book where he deals with the excitation of a cavity of arbitrary

geometry. In particular the final result is given in equation 7.131a. The field in the cavity is $H_c = h_n H_n$ where H_n is the TEM$_{003}$ mode we want to excite and h_n is given by:

$$h_n = \frac{k_0^2 P H_n}{k_n^2 - k_0^2(1 + \frac{1-i}{Q_n})}, \tag{6.23}$$

where k_n is the wavenumber for the particular mode we want to excite, k_0 is the wavenumber in the waveguide and Q_n is the quality factor for mode n. We can see that the reflected field depends on the magnetic dipole moment which depends on the reflected field. We are therefore looking for a self-consistent solution. We can now plug the standard expression for a TEM$_{00}$ mode of a Fabry-Pérot cavity into equation 6.23.[3] Assuming that the hole is in the centre ($\rho = 0$) and at $z = -L/2$, h_n becomes:

$$h_n = \frac{ik_0^2 P}{k_n^2 - k_0^2(1 + \frac{1-i}{Q_n})} \frac{w_0}{w_m} H_x, \tag{6.24}$$

where $w_m = w(z = -L/2)$ is the waist size at the position of the mirror. The cavity field H_c at the position of the aperture then becomes:

$$H_c = \frac{-k_0^2 P}{k_n^2 - k_0^2(1 + \frac{1-i}{Q_n})} \frac{4}{\pi w_m^2 L} = c_1 P, \tag{6.25}$$

where c_1 is a constant.

Now we have expressions for all the fields we need for equation 6.21. Assuming that the amplitude of the incident wave $A = 1$, $H_i(x = a/2) = 2$ we get the final expression for the dipole moment:

$$P = \frac{2\alpha_m}{1 + \frac{2i\alpha_m}{ab} - \alpha_m c}. \tag{6.26}$$

In the experiment we measure the reflected power relative to the incident wave as function of the frequency. So we can plug the expression obtained for the dipole P back into 6.22 to get the expression for the reflected field relative to the incident wave (assumed to have an amplitude of 1):

$$H_r = 1 - \frac{4i}{2i + \frac{\pi w_m^2 L}{4\alpha_m} - \frac{4ab}{\pi w_m^2 L k_g} \frac{k_0^2}{k_n^2 - k_0^2\left(1 + \frac{1-i}{Q}\right)}} \tag{6.27}$$

Note that until now we have neglected the finite wall thickness of the hole. Ralph Levy suggests that one can account for the finite thickness of the aperture by treating the hole as a waveguide below the cut-off frequency [291]. This effectively changes the polarisability α_m of the aperture to:

$$\alpha_{m,t} = \alpha_m e^{-\frac{2\pi A_m t}{\lambda_c}\sqrt{1 - \left(\frac{\lambda_c}{\lambda}\right)^2}}, \tag{6.28}$$

---

[3]$H_n = H_x \frac{w_0}{w_z} \exp\left[-\rho^2/w(z)^2\right] \cos(k_n z + k_n \rho^2/(2R(z)) - \phi(z))$, where ϕ is the Gouy phase. Note, that if you want to use equation 6.23, H_n has to be properly normalised such that $\int_V |H_n|^2 dV = 1$, where V is the volume of the cavity. Here we can make use of the fact that the cavity is tuned to resonance ($kL = n\pi$).
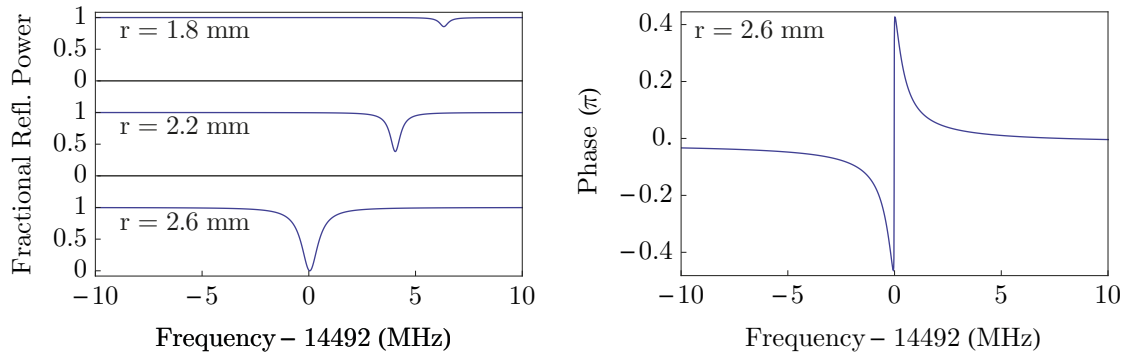
FIGURE 6.2: Left: Theoretical reflected power (normalised to the input power) as a function of the microwave frequency for different coupling hole radii (wall thickness 1.5 mm). The size of the coupling aperture affects the FWHM of the resonance and the slightly affects frequency at which the cavity resonates. A hole with radius $r = 2.6$ mm critically couples the cavity. The lineshape resembles the familiar Lorentzian function. Right: The phase $1/\pi \arg(H_r)$ of the reflected field as a function of the microwave frequency for the critically coupled hole radius of 2.6 mm. The phase is an extremely sensitive measure for the coupling. For perfect critical coupling the change in phase at the resonance frequency is exactly π. We see that $r = 2.6$ mm still slightly undercouples the cavity.

where λ is the free space wavelength, $\lambda_c = 3.412r$ is the cut-off wavelength, and for the case when $t/r > 0.2$, and the factor $A_m t = 1.0064t + 0.0819r$. These equations allow us to plot the reflected power ($|H_r|^2$) and the phase as a function of the frequency and the coupling aperture radius and are shown in figure 6.2. Figure 6.3 shows how the quality factor, the reflected power, and the intra-cavity field vary with the hole radius. As expected, the Q-factor decreases as the hole size increases because the hole represents a source of loss out of the cavity. The fractional reflected power also decreases as the hole size increases because a bigger hole transmits more of the incident power. When $r = 2.6$ mm, the cavity is critically coupled, meaning that all the power is coupled into the cavity. This happens when the transmission through the hole is equal to the sum of all the other losses. Since the losses are doubled at this point, the Q-factor has fallen to half of its maximum value. If the hole size is increased any further, the reflected power starts increasing again, while the Q-factor continues to fall. The intra-cavity electric field depends on the transmission through the hole and on the Q-factor and is maximised when $r = 2.395$ mm. For this hole size 11% of the incident power is reflected.

6.4   Experimental Setup - The First Prototype

Our first prototype cavity was designed to accommodate five antinodes. We realised at a later stage that the space in the ultracold lithium science chamber is very limited and a shorter cavity (three antinodes) was necessary. This is also why the previous calculations were presented for a cavity which accommodates three antinodes.

We use a vector network analyser (VNA) for all the measurements (Agilent 8722ES). This
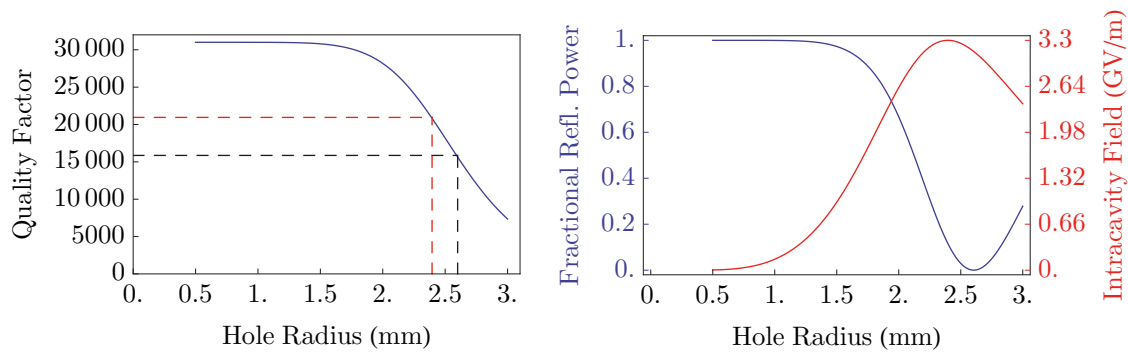
FIGURE 6.3: Left: The quality factor decreases as the aperture radius is increased. The red dashed line marks the quality factor and radius at which the electric field in the cavity reaches its maximum. The black dashed line shows the quality factor and hole radius at critical coupling. Right: Fractional reflected power (blue) and the electric field inside the cavity (red) as a function of the hole radius.

device allows to completely characterise an unknown microwave circuit by measuring its S-parameter matrix [292]. This matrix has four elements S_{11}, S_{21}, S_{12} and S_{22}. The VNA measures the reflected or transmitted signal relative to the incident signal, and the S parameters give these ratios of the incident to either the reflected or transmitted signal. S_{11} measures the ratio of the reflected to the incident signal and S_{21} measures the ratio of the transmitted to the incident signal, if the structure is excited by port 1. S_{12} and S_{22} are the same ratios, if the structure is excited by port 2. Modern VNAs house their own signal generator to excite the circuit, directional couplers, bridges and splitters to separate the forward and reflected signals. The difference between a scalar and vector network analyser is that a VNA can not only measure the magnitude of a reflected or transmitted signal but also its phase. The detection system is typically also more elaborate and more sensitive. A good introduction to the basics of a vector network analyser can be found on the web [293].

A sketch of the entire first prototype cavity is shown in figure 6.4. It consists of two spherical mirrors with a radius of curvature of $R = 73$ mm. The material we use for the mirrors is oxygen-free copper (OFC103) which is rated to a DC bulk conductivity of 101% IACS. So we expect a finesse of $\mathcal{F} = 9461$ and an unloaded quality factor of $Q_0 = 51330$. The mirrors are machined in our workshop on a CNC lathe. Both mirrors have a recess in the back to accommodate a standard UBR 140 flange of a WG 18 waveguide. The wall thickness of these first mirrors at the position of the hole was 2.25 mm. Both mirrors are fixed into precision holders made from aluminium. One of the holders is attached to a translation stage which is equipped with a differential micrometer. The translation stage is bolted to an aluminium plate. The second mirror and its aluminium holder is rigidly attached to the aluminium plate as well. The angular alignment of the mirrors with respect to each other is checked with a vernier caliper to an accuracy of better than 0.5×10^{-3} rad. We attach the waveguides to the mirrors and connect the system to the VNA via standard N-type or SMA to waveguide adapters. The first spectrum we recorded is shown in figure 6.5. We drilled only a very small hole (hole radius $r = 1.25$ mm, wall
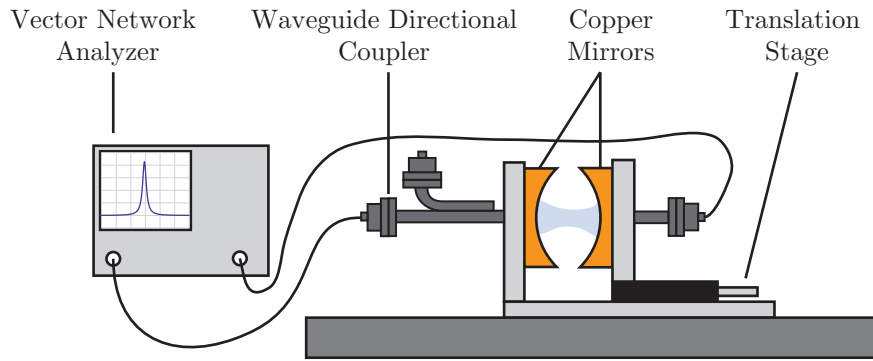
FIGURE 6.4: Our first prototype cavity. The two copper mirrors are mounted in precision aluminium holders. The alignment and cavity length is measured with a vernier caliper. One of the mirrors is mounted on a translation stage. Both mirrors share the same aluminium base plate. The base plate is fixed to a breadboard. We excite the cavity via one port of a vector network analyser through a waveguide directional coupler. By drilling a small aperture in the second mirror we can measure in transmission.

thickness $t = 2.25$ mm) into one of the mirrors to extract the unloaded quality factor and excited the cavity using port 1 of the VNA. We measured the cavity field with an antenna inside the cavity. The antenna was connected to port 2 of the VNA and its coupling was chosen to be very small so that the influence of the antenna on the cavity mode is kept to a minimum. The VNA also allows to record the phase as a function of the microwave frequency which is shown in the right panel of figure 6.5. We fit a Lorentzian line shape ($L(f) = a(w^2/4)/\left[(f - f_0)^2 + (w^2/4)\right]$) to the field magnitude data. The fit yields a FWHM of $w = 0.371$ MHz which corresponds to an unloaded quality factor of $Q_0 = 40419$ (finesse $\mathcal{F} = 7462$). This is about 20% lower than the ideal unloaded quality factor for this geometry. Hence the surface resistance was slightly higher, which is not surprising since we neither etched away the surface oxide layer nor polished the mirrors to get a better surface finish. At a later stage we removed the oxide layer in an acetic acid bath and could improve the quality factor to 46000 and thus to within 8% of the ideal quality factor. Recently we found that by etching away the top layers and applying a soft polish we can prepare mirrors that possess a reflectivity very similar to the one calculated from the dc-conductivity of the bulk material. Figure 6.5 on the right shows that the phase of the microwaves changes by π when the microwaves are scanned throught the resonance. A wide transmission spectrum of an undercoupled cavity with a slightly larger aperture, i.e. 40 % of the incident power is coupled into the cavity, is shown in figure 6.6.

We wanted to see if we can indeed critically couple the cavity with only a single coupling hole. Therefore, we continuously increased the size of the coupling hole and measured the reflected power. Note that care must be taken when drilling the hole since sharp edges and remaining burr can affect both coupling and the quality factor. We thus decided to use electrical discharge machining instead of drills. We machined a hole with a radius of $r = 1.95$ mm into the mirror and measured the reflected power (S$_{11}$ parameter) with the VNA. Reflection measurements are more challenging than transmission measurements because the cavity does not produce a Lorentzian
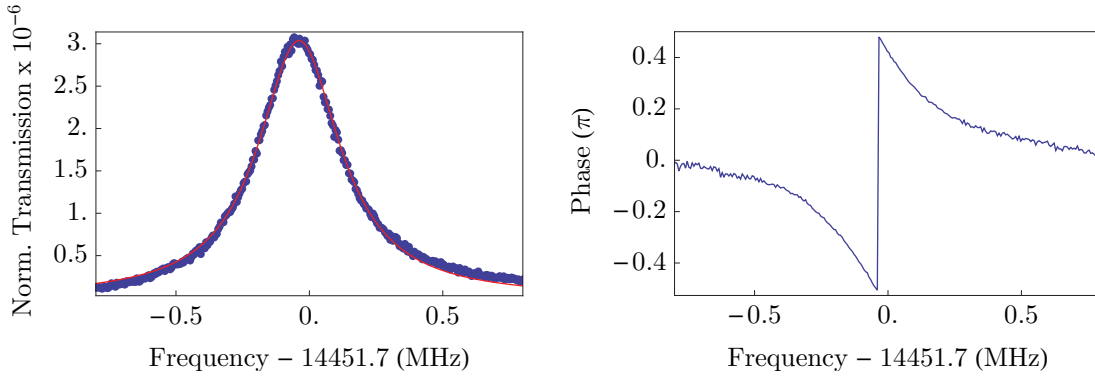
FIGURE 6.5: Left: A transmission spectrum of a very weakly coupled cavity (hole radius $r = 1.25$ mm, wall thickness $t = 2$ mm). We excite the cavity using port 1 of the VNA and record the power inside the cavity with a probe antenna which is connected to port 2 while the frequency is scanned. We fit a Lorentzian line shape (red line) to the data (blue dots). The antenna couples only very weakly to the cavity field as indicated by the small amplitude of the peak which is normalised to the input power. Right: The phase of the microwave field as the frequency is scanned.
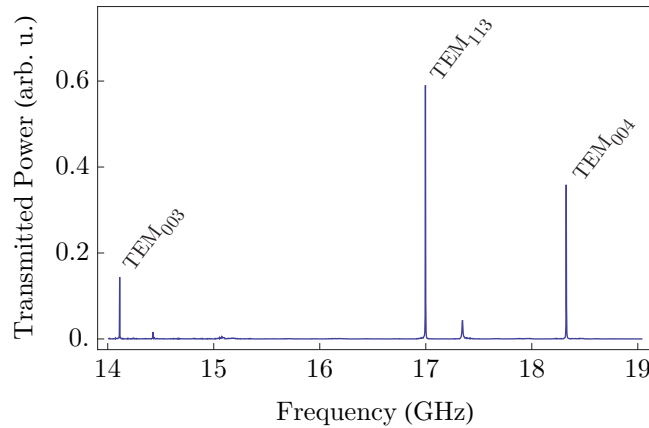

FIGURE 6.6: Wide frequency spectrum of an undercoupled cavity (40 % of the incident power is coupled into the cavity) of length 35.3 mm. We use a small aperture in the second mirror to measure in transmission. The spectrum shows that it is possible to excite higher order transverse modes in the cavity. The number of higher order modes depends on the size of the aperture.

dip on a flat background. The resonance is superimposed by an interference pattern produced by the non-ideal waveguide system we use to couple the microwaves into the cavity. Each element, the cables of the VNA, the coaxial coupler and the waveguides produces reflections (especially at the connections) which give rise to a complicated interference pattern. We blocked the cavity so that the resonance disappears and recorded the standing wave. We then subtracted this background from the measurement with the cavity unblocked. As we found out later this can lead to an over- or underestimation of both the coupling and the quality factor by as much as 10%. If the cavity is on resonance there is no standing wave (the cavity is impedance matched). By subtracting the standing wave we artificially shift the zero-level which appears as an increase in coupling. The background subtraction thus caused a systematic error in extracting

the coupling from a reflection measurement. One can solve this problem by taking the mean of the standing wave as the real zero value, relative to which one must measure the fractional reflected power. It is also possible to eliminate the standing wave by calibrating the VNA up to the point of the cavity with one- and two-port networks that have known characteristics. We terminate the end of the waveguide with a short and a load for example and thus can remove the standing wave by calibrating the VNA. For these early measurements, however we did not have the proper equipment to perform such a calibration.

We fit a Lorentzian to the reflection measurements and can extract the coupling for a given hole radius. For a reflection measurement it is convenient to rewrite equation 6.27 in terms of the coupling coefficient K and the unloaded quality factor Q_0. Following [294] we can write the fractional reflected power ($|H_r|^2$) as

$$|H_r|^2 = 1 - \frac{4K}{(1+K)^2} \frac{\omega_0^2 \left(1 + K^2\right)/(2Q_0)^2}{(\omega - \omega_0^2)^2 + \omega_0^2 \left(1 + K\right)^2/(2Q_0)^2}, \tag{6.29}$$

which is a Lorentzian dip in the reflected power of amplitude $4K/(1 + K)^2$. The microwave angular frequency is ω and the resonance angular frequency is ω_0. If $K < 1$ the cavity is said to be undercoupled and if $K > 1$ it is overcoupled. This definition of K allows us to relate the loaded to the unloaded quality factor by $Q_l = Q_0/(1+K)$. For the phase we get the expression:

$$\phi(\Omega) = \tan^{-1}\left(\frac{2KQ_0\Omega}{1 - K^2 + \Omega^2 Q_0^2}\right), \tag{6.30}$$

where $\Omega = (\omega/\omega_0) - (\omega_0/\omega)$. This allows us to extract both K, Q_0 and the loaded quality factor Q_l from either a magnitude or a phase measurement. Figure 6.7 shows such a measurement. The left panel shows a magnitude measurement and the right panel shows a phase measurement. By fitting equation 6.29 (red line) to the data (blue dots) we can extract $Q_0 = 37121 \pm 119$ from the magnitude measurement. In the right panel of figure 6.29 we fit equation 6.30 (red line) to the data (blue dots) and thus can extract $Q_0 = 41242 \pm 446$ from the phase measurement. For the coupling factor we get $K = 0.05395 \pm 0.0001$ and $K = 0.0523 \pm 0.0004$ from the magnitude and phase measurements, respectively. The disagreement between the two measurement methods is due to the background subtraction which can affect the quality factor of the magnitude measurement in reflection. However, the unloaded quality factor from the phase measurement agrees well with the transmission measurement of the minimally coupled cavity shown in figure 6.5. A coupling factor of $K = 0.0523$ corresponds to a fractional power coupled into the cavity of $4K/(1+K)^2 = 0.19$. By increasing the coupling into the cavity we have also decreased the quality factor by about 5.4% to $Q_l = Q_0/(1 + K) = 39192$.

We next increased the coupling aperture in small steps and measured the coupling and quality factor for each aperture radius. The result of these measurements are shown in figure 6.8. We can clearly see that for larger hole diameters the experiment deviates considerably from the ideal case shown as the solid red line. We attribute this to an additional loss due to the presence
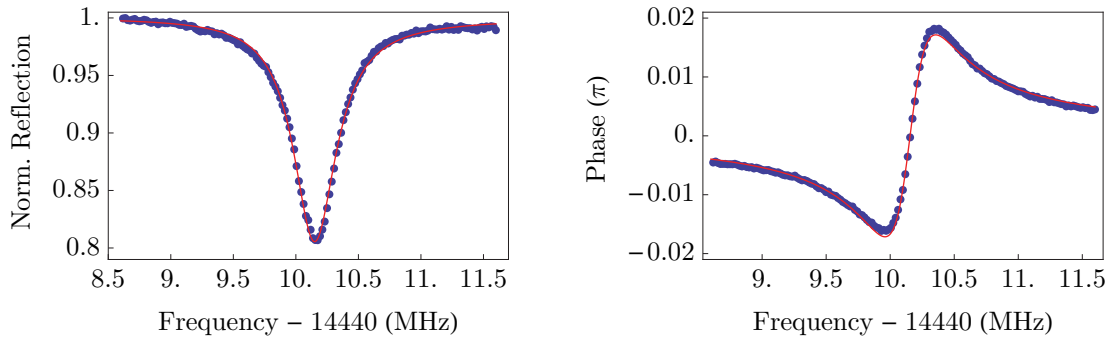
FIGURE 6.7: Left: The fractional reflected power (normalised to the input power) as a function of the frequency. The solid red line is a fit of equation 6.29 to the data (blue dots). Right: The phase of the microwave field as a function of the frequency. The red line is a fit using equation 6.30 to the data (blue dots).
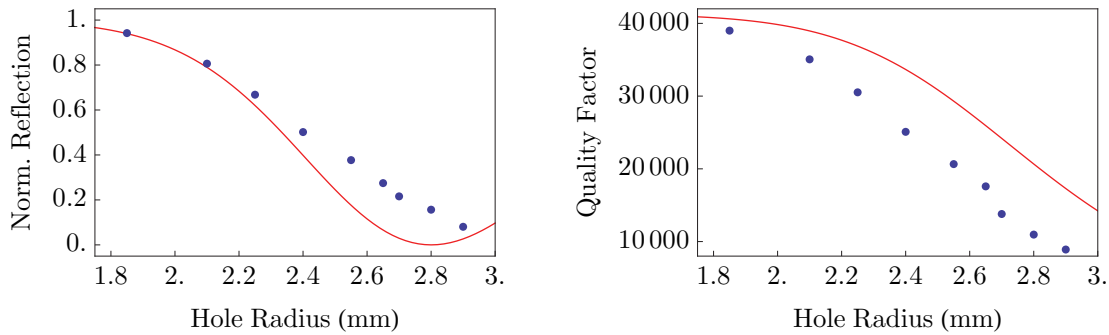

FIGURE 6.8: Left: As the hole diameter is increased the reflected power decreases. The blue dots are the data and the red line is a plot of $|H_r|^2$, where H_r is defined in equation 6.27. The wall thickness of the hole is set to $t = 2.25$ mm and $Q_0 = 41000$ is the measured unloaded quality factor. Right: Measurement of the quality factor as function of the hole size (blue dots). The ideal, theoretical quality factor extracted from a fit to $|H_r|^2$ is shown as a red line.

of a hole in the centre of the mirror and to the background subtraction error. This also means that the loaded quality factor at critical coupling is not half of the unloaded quality factor as in the ideal case, but less (see the right panel of figure 6.8). For the geometry presented above we couple over 90% into the cavity at a quality factor which is a quarter of the unloaded quality factor.

In order to minimise the aperture radius needed for critical coupling we built another cavity with a reduced wall thickness of $t = 1.5$ mm. In this cavity we could couple 93% of the incident power into the cavity with a loaded quality factor of $Q_l = Q_0/2.49$. In our final version of the cavity we aim to reduce the wall thickness even further.

6.4.1 Cooling the Mirrors

All the input power is finally dissipated as resistive heat in the mirrors. We thus need to cool the mirrors. By cooling the mirrors with liquid nitrogen, instead of water, we benefit from the fact

that the resistivity of the copper mirrors decreases as the temperature decreases. This increases the quality factor which allows us to lower the input power while keeping the intra-cavity field at the same level. To investigate the effect of cooling on the quality factor and coupling we designed cooling blocks for the cavity and a small vacuum chamber to prevent condensation on the mirrors. It is also at this point that we realised that we needed to shorten the cavity length so that the trap is compatible with our existing lithium setup. Hence from now on all the data is taken with a cavity whose mirrors have a radius of curvature of $R = 73$ mm and a diameter of $D = 85$ mm which results in a length of 34.34 mm for a cavity that can accommodate three antinodes at a resonance frequency of 14.5 GHz. The diffraction losses for this geometry are $\alpha_d = 2.6 \times 10^{-6}$. The waist in the centre is $w_0 = 14.3$ mm. The ideal quality factor assuming a surface resistivity equal to the dc resistivity of the bulk material of $1.72 \times 10^{-8} \Omega \, \text{m}^{-1}$ is $Q_0 = 31300$ (finesse $\mathcal{F} = 9420$). Without any further chemical treatment or polishing the maximum achieved quality factor we measured was 28300 which is about 10% lower than in the ideal case. This geometry allows a gap of 7 mm between the mirrors, which is large enough for loading molecules and/or atoms.

The electrical resistivity of an ideal, chemically pure metal is caused by scattering of the electrons either by phonons and/or by collisions with the metal atoms themselves, i.e. the resistivity is inversely proportional to the mean free path of the electrons in the material. This intrinsic resistivity goes to zero for $T \to 0$ K. To first order (the change in temperature is not too large) a linear approximation can be used

$$\rho_i(T) = \rho_0 \left[1 + \alpha \left(T - T_0 \right) \right], \tag{6.31}$$

where $\rho_i(T)$ is the intrinsic resistivity at a temperature T, ρ_0 is the resistivity at the initial temperature T_0 and α is the so-called material specific temperature coefficient of resistance. For low temperatures, however, the resistivity is dominated by impurities or defects in the metal and becomes nearly constant with temperature. Following Matthiessen's rule the two contributions to the total resistivity can be added together [281]:

$$\rho(c, T) = \rho_0(c) + \rho_i(T), \tag{6.32}$$

where we assume that the resistivity due to impurities $\rho_0(c)$ is a linear function of the concentration c of the type of impurity. A more precise expression for the intrinsic, ideal resistivity of a metal as a function of the temperature is given by the Bloch-Grüneisen formula [281]:

$$\rho_i(T) = \frac{C}{m\Theta} \left(\frac{T}{\Theta} \right)^5 \int_0^{\Theta/T} \frac{z^5 e^z}{\left(e^z - 1 \right)^2} dz, \tag{6.33}$$

with T the temperature, $C = 1.62 \times 10^{-3}$ a normalisation constant chosen such that $\rho_i(T = 293) = 1.72 \times 10^{-8} \, \Omega \, \text{m}$, $m = 63.5$ is the relative atomic mass of Copper in atomic mass units,
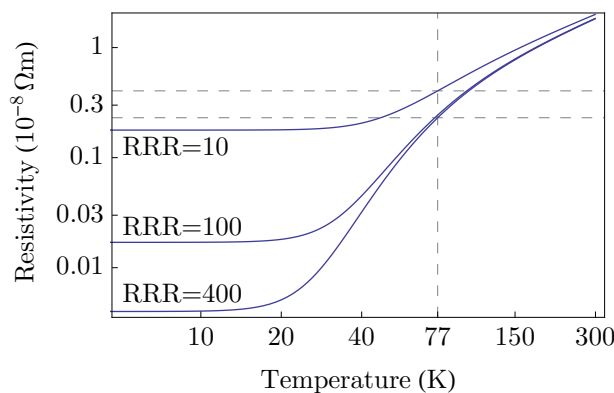
FIGURE 6.9: A plot of equation 6.32 using equation 6.33 for three different RRR values. C is chosen such $\rho_i(T = 293) = 1.72 \times 10^{-8} \ \Omega\,\mathrm{m}$, $\Theta = 310.8$ K and $m = 63.5$ is the relative atomic mass of Copper in atomic mass units.

$\Theta = 310.8$ K is the Debye temperature of copper [281]. The value of $\rho_0(c)$ determines what is known as the RRR (residual resistivity ratio) value of copper (RRR $= \rho(c, 273\,\mathrm{K})/\rho(c, 4\,\mathrm{K})$). The RRR values of copper vary from several tens (telephone wire) to several thousands (ultra high purity, annealed copper). A typical value for good oxygen-free copper lies in the several hundreds. A plot of equation 6.32 using 6.33 for three different RRR values is shown in figure 6.9. From this graph we can infer that we do not need to use very high purity copper because the resistivity at 77 K hardly changes for copper with an RRR $= 100$ or RRR $= 400$. Assuming we have material with an RRR $= 100$ we can increase the conductivity of the mirrors by a factor of 7.6 and thus the reflectivity of the mirrors by $\sqrt{7.6} = 2.7$ by cooling the mirrors to 77 K. The finesse and quality factor thus increase by a factor of 2.7. This would allow us to lower the input power by the same amount which relaxes the cooling requirements. The ultimate case for using superconducting mirrors will be discussed in section 6.7.1.

To investigate the effect cooling has on the quality factor we attached cooling blocks to the cavity and put the setup under a rough vacuum ($10^{-2}\,\mathrm{mbar}$). A sketch of this setup is shown in figure 6.10. We connected the cooling blocks via flexible tubing to a dewar filled with liquid nitrogen. By producing a small overpressure in the dewar we created a continuous flow of liquid nitrogen through the whole system to assure good cooling without creating too much turbulence which could produce vibrations. We monitored the temperature of the mirrors with thermocouples that were attached to the back of the mirrors at two different locations. To feed microwaves into the vacuum chamber we simply bolted a waveguide against a quartz window. A second waveguide on the vacuum side coupled to the air-side waveguide via an evanescent wave through the window and was bolted to the back of one mirror. A 3 mm thick window leads to a transmission loss of about 20% of the input power. For this proof-of-principle experiment this loss does not cause any problems. For the final high-power version, however, such high losses can not be tolerated.

Figure 6.11 shows how the fractional reflected power of an undercoupled cavity changes as
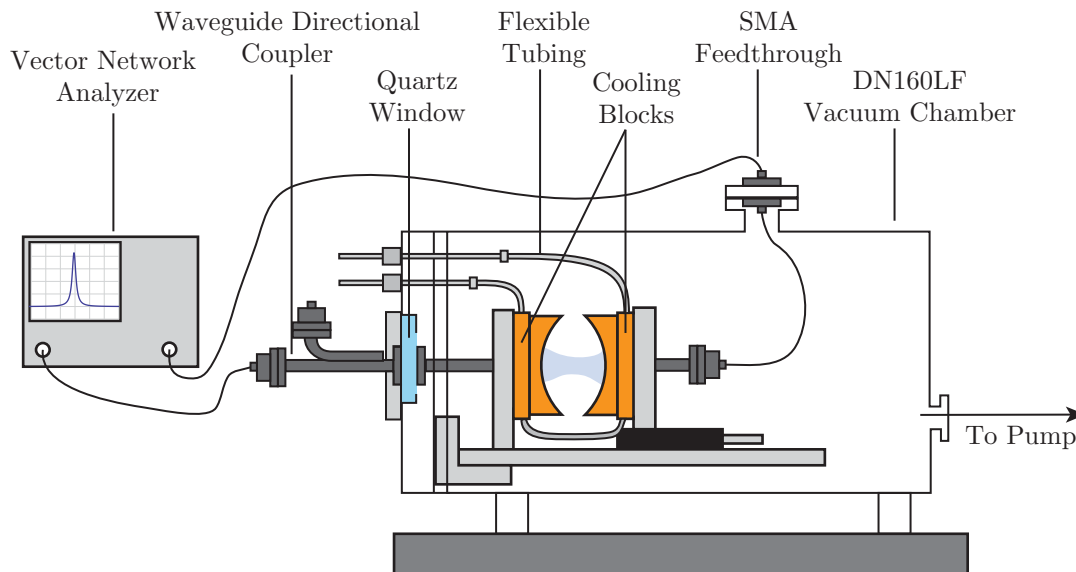
FIGURE 6.10: A sketch of the setup we used to measure the quality factor and coupling as a function of the temperature.

the temperature is reduced from $293\,\text{K}$ to $77\,\text{K}$. The cavity is undercoupled to minimise the influence of the hole in this measurement. We also reduced the number of points per frequency scan and did not average the spectra to reduce the influence of vibrations on the measurement (i.e. to keep the scanning time to a minimum). With this change in temperature, the quality factor increased by a factor of 1.9 and the fractional power coupled into cavity increased by a factor of 1.2. The discrepancy of 30% between the expected increase in quality factor of 2.7 and 1.9 can be attributed to the fact that the surface resistivity is higher than the resistivity of the bulk material. In fact it is common to measure the surface resistivity of a material by measuring the quality factor of a (closed) cavity (see [295] and the references therein, for example). We can include the higher surface resistivity into equation 6.32 by assuming an effectively lower RRR value of the surface. This higher resistivity corresponds to an RRR of about 10 and an extra loss per round trip of $\alpha_{\text{surf}} = 1.5 \times 10^{-4}$.

Machining of the bulk copper material leads to a local deformation of the lattice structure, also known as work hardening. This can increase the defect density and the number of dislocations in the lattice structure of the metal. Machining can also lead to the formation of new grain boundaries. Electrons might scatter at these grain boundaries which increases the resistivity. Furthermore, impurities are introduced into the copper lattice when it is machined. In general, such a worked surface layer can lead to large deviations of the actual surface conductivity from the ideal surface conductivity, which is derived from the bulk dc conductivity. It also influences the low temperature behaviour of metals [296, 297]. This, in addition to the expected increased resistivity due to the surface roughness mentioned earlier, can explain why we observe a lower improvement factor. This deviation increases even further for very low temperatures and high
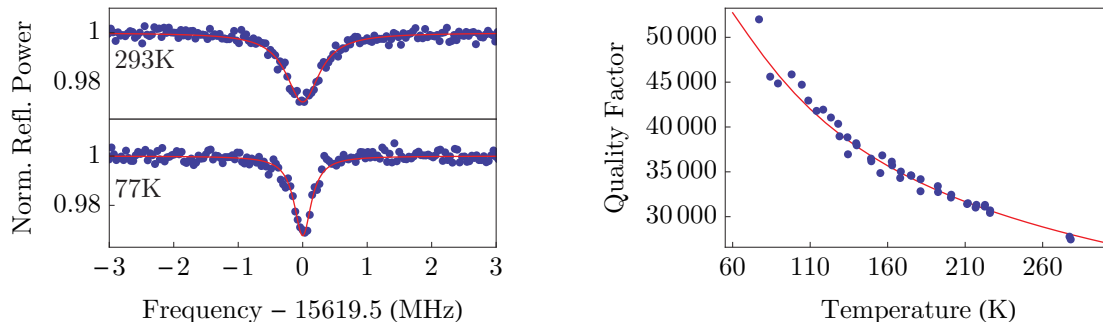
FIGURE 6.11: Left: The fractional reflected power measured as a function of the frequency for two different temperatures (293 K, 77 K). Right: The measured quality factor (blue dots) as a function of the temperature. The red solid line is a fit using equations 6.32 and 6.33 assuming a worse copper quality RRR ≈ 10 due to the influence of the surface conditions on the conductivity. This models the non-ideal surface conditions as an effective deterioration of the copper quality.

frequencies when the mean-free-path of the electrons becomes comparable to the skin depth. This effect is known as the anomalous skin effect.

To chemically etch away the machined layers Thorp suggests a mixture of phosphoric acid, nitric acid and acetic acid [296]. This chemical treatment should be followed by annealing (heating to high temperature 790 °C) in a hydrogen atmosphere which reduces the oxygen content in the copper and removes the dislocations in the metal lattice. Finally, electro-polishing may be used to reduce the macroscopic surface roughness. This should make it possible to obtain the ideal quality factor as calculated from the bulk dc resistivity for both room temperature and at 77 K. For the final ultra-high vacuum version we plan to treat the copper this way to improve the quality factor even further.

6.5   Finite-Difference Time-Domain (FDTD) Simulation of the Cavity

We could not explain why the quality factor at critical coupling was less than half of the uncoupled quality factor. This means that there is an additional loss which depends on the hole size. This loss is not due to an increase in the coupling, but seems to be an additional diffraction loss which increases as the coupling aperture increases. In particular, we wanted to understand if the shape or size of the mode changes with increasing hole diameter, because this could affect both the volume and depth of the trap.

We therefore started to simulate the cavity numerically using software which is based on the finite-difference time-domain (FDTD) method. The basic mathematical model behind FDTD methods goes back to a seminal paper by Courant, Friedrichs and Lewy from 1928 in which the authors introduced the idea of the finite difference scheme to solving differential equations [298].

One replaces the differential quotients of Maxwell's equations by difference quotients defined on a mesh of finite density. Kane Yee took this idea further and used this approximation to discretise Maxwell's equations in the time and spatial domains [299]. One then solves the equations numerically and derives the distribution of the electric and magnetic fields at each time step. Although this method is straightforward and easy to implement (directly follows from the differential form of Maxwell's equations) the development of FDTD methods was hindered by the need to discretise the simulation space on sub-wavelength scales, with very small time steps. Therefore, even small problems required large amounts of computer memory and time. By the 1990s computer memory became cheap enough and FDTD has since become a standard technique for solving Maxwell's equations for arbitrary structures.

First we tried an open source software package developed by the group of Prof. Joannopoulos at MIT called MEEP (for MIT Electromagnetic Equation Propagation). This is a very powerful software package which can yield transmission and reflection spectra, the resonant modes, frequencies and field patterns in nearly arbitrary structures. However, it can only produce transmission and reflection spectra by Fourier transformation of the response to a short excitation pulse. A cavity, however, is continuously fed with input power. In order for power to be built up in the cavity the field needs to bounce on the order of 10^4 times between the mirrors. The short excitation pulse, however, decayed before enough power could build up. Furthermore, it only supports lossy materials in the resonant mode solver which is not able to deliver any information about the S-parameters of the system. We therefore abandoned the use of MEEP and looked for an alternative.

We found two commercial solutions to be suitable for our purposes. One was the RF Module of COMSOL Multiphysics and the other CST Microwave Studio. The first is not based on FDTD but rather on finite element modelling which works in the frequency domain only. Furthermore, COMSOL requires more in-depth knowledge whereas Microwave Studio is quite easy to use. We thus decided to use Microwave Studio which provides both a powerful frequency and time domain solver. Both software solutions need to run on designated high-performance workstations or even on a computer cluster. Our first trials on a normal computer failed due to the lack of memory which is needed to store the fields at each mesh cell and at each point in time. Figure 6.12 shows the actual model used in the simulations. The length of the cavity is set such that three antinodes fit into the cavity at a resonance frequency of 14.5 GHz. We excite the structure through a waveguide port and record the S_{11} parameter and electric fields as a function of the frequency for a series of different aperture sizes. We then fit a Lorentzian function to each S-parameter plot and extract the coupling and quality factor for each aperture radius. The fractional reflected power as a function of the aperture radius is shown in the left panel of figure 6.13 (blue dots). We compare this to the analytical model presented in section 6.3 and find good agreement. In the right panel of figure 6.13 we compare the simulated quality factor (blue dots) to the quality factor predicted by the analytical model. We can clearly see a discrepancy. At critical coupling the quality factor has decreased by a factor of three which is
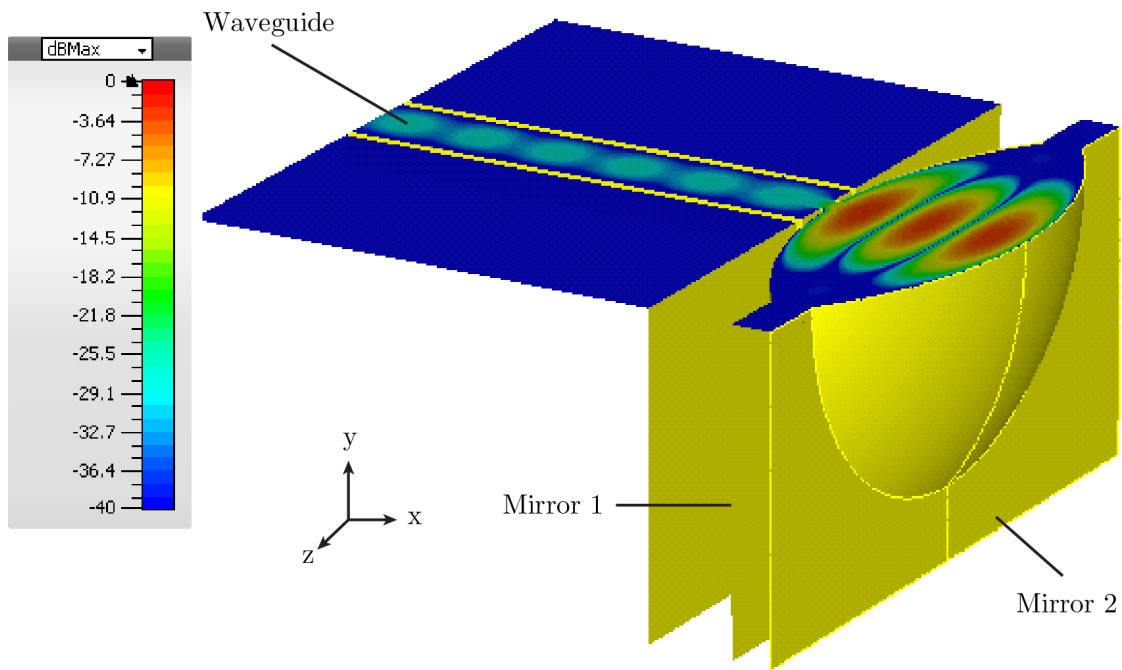
FIGURE 6.12: A central cut through the model drawn in Microwave Studio with a logarithmic plot of the electric field inside the cavity. The aperture radius is 2.2 mm with a wall thickness of 1 mm. We excite the structure through a waveguide port (frequency domain solver) and the software calculates the field at each mesh cell until a steady-state criterion is met. We can also monitor the reflected field magnitude (S_{11} parameter). The software solves the linear equation system for a single frequency at a time until the relative residual has reached the specified size (10^{-9} in this case). One can decrease the simulation time considerably by enabling the broadband frequency sweep option. This uses as few frequency samples as required for reaching a stop-criterion. We set this stop-criterion by the S-parameter error threshold to 0.01. This means that if the S-parameter does not change by more than 0.01 between two successive frequency samples the simulation stops. Defining symmetry planes reduces the computation by a factor of 4. We find that for the most accurate results one needs to check the adaptive tetrahedral mesh refinement option. The mesh is then adaptively optimised for each frequency sample. A single S-parameter scan (10 MHz about the resonance frequency) with the electric field calculated at the resonance frequency takes then about 2 hours on an Intel Xeon 3 GHz (12 cores) workstation with 64GB of RAM.

similar to what we observed in the measurements. The aperture therefore introduces an extra loss which is not accounted for in our analytical model. In the left panel of figure 6.14 the simulated quality factor is plotted as a function of the fractional reflected power. We can clearly see that when the fractional reflected power drops below 10% (most of the incident power is injected into the cavity) the Q-factor starts to fall more rapidly. It is therefore not ideal to operate the cavity at critical coupling but rather with a slightly smaller hole that corresponds to a fractional reflected power of 10%. In the right panel of figure 6.14 the frequency shift of the resonance as a function of the hole radius is shown. Compared to the analytical model the simulation (blue dots) predicts a stronger dependence between the resonance frequency and the
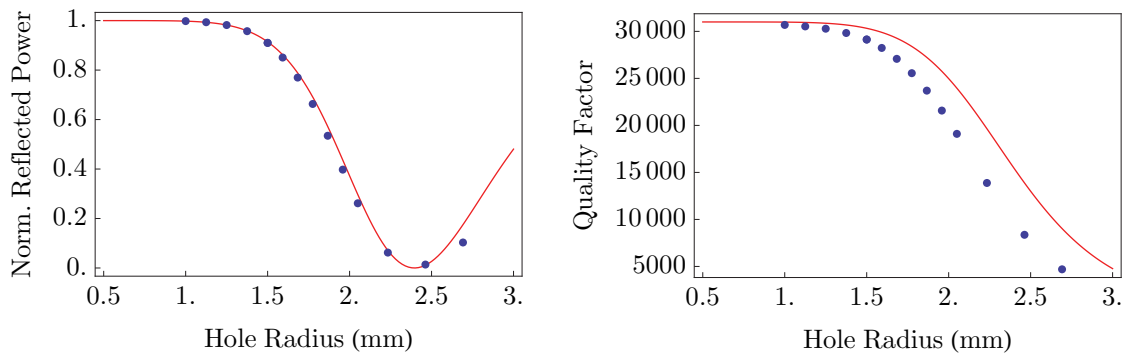
FIGURE 6.13: Left: The reflected power normalised to the input power (fractional reflected power) as a function of the aperture radius as predicted by the simulation (blue dots) and the analytical theory (red line). Right: The quality factor as a function of the aperture radius extracted from the simulations (blue dots) and the analytical theory (red line).
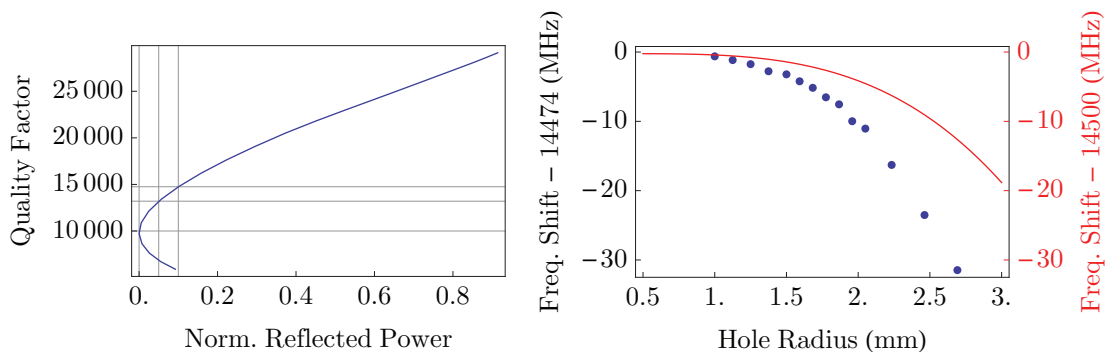

FIGURE 6.14: Left: The quality factor plotted against the fractional reflected power as predicted by the simulation. The intra-cavity field does, not peak at critical coupling but for a slightly under-coupled cavity. Right: The cavity resonance frequency shifts as the hole radius increases. Compared to the analytical model the simulations show a stronger dependence and a constant offset of about 26 MHz

hole size, and it predicts an offset of about 26 MHz (solid red line).

Microwave Studio can also calculate the fields inside the cavity. Figure 6.15 shows a cut through the actual model drawn in Microwave Studio. The central plane shows the electric field calculated in the centre of the cavity. We can also compare the contour-plots of the electric field for different hole sizes to look for any differences and anomalies that could explain the rapid decrease in the quality factor for large coupling apertures. A comparison of the electric field for an aperture radius of 1.1 mm and 2.2 mm for the two waveguide axes is shown in figure 6.16. The electric field values are plotted on a logarithmic scale so that even small variations in the field magnitude can be seen. The comparison shows that a larger aperture leads to a larger mode, especially along the short axis of the waveguide. A larger mode leads to an increase in diffraction losses and thus to a decrease in the quality factor. Figure 6.16 shows the effect of the hole size on the mode even more clearly. Here we plot the normalised field across the antinode in the centre ($x = 0$) of the cavity along y and z. Especially along the short waveguide axis the
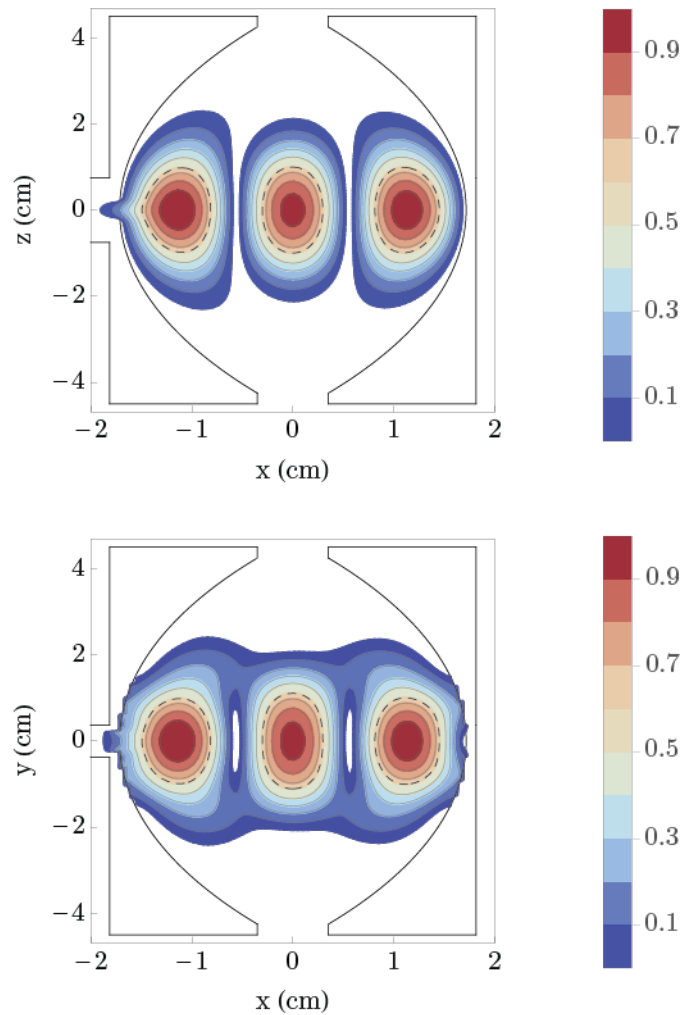
FIGURE 6.15: Top: A contour plot of the electric field in the centre of the cavity (along the long waveguide axis at $y = 0$) for a hole radius of $2.23\,\text{mm}$ and a wall thickness $t = 1\,\text{mm}$. The contours are plotted relative to the field maximum. The dashed contour shows the $1/e$ radius (waist) of the electric field. Bottom: The electric field in the centre of the cavity, along the short waveguide axis ($z = 0$).

aperture causes higher order diffraction maxima to appear, the relative size of which depends on the aperture radius. This causes higher diffraction losses for larger hole sizes, which explains why the quality factor for critical coupling is somewhat smaller than half the unloaded quality factor. We therefore need to operate at a slightly smaller aperture size in order to maximise the intra-cavity field. This leads to a reflection of about 10% of the incident power. The klystron amplifier has a built-in circulator which can handle this amount of reflected power.

To compare the simulations with measurements we have recently built a high precision cavity. A photograph of the mirrors and the assembled cavity is shown in figure 6.18. This cavity consists of two mirrors which are separated by a high precision spacer. Every time we increase the aperture size, we have to disassemble the cavity. The high precision spacer ensures that changes in the cavity length and alignment of the mirrors with respect to each other are kept to a minimum. We increase and measure the aperture with a wire eroder to an accuracy of better
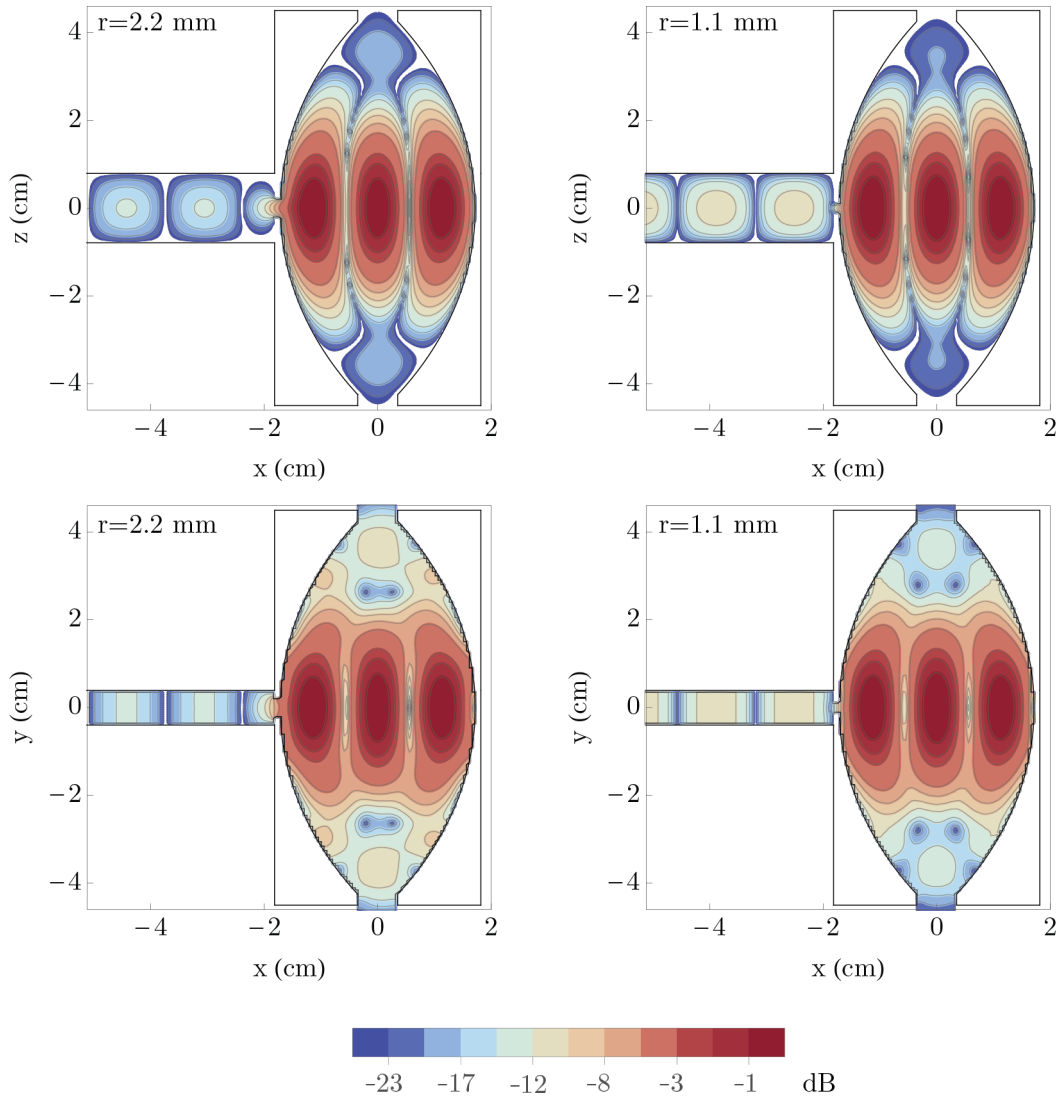
FIGURE 6.16: Top: Logarithmic contour plot of the electric field in the centre of the cavity, along the long axis of the waveguide for two aperture sizes. Bottom: Logarithmic contour-plot of the electric field in the centre of the cavity, along the short axis of the waveguide for two aperture sizes. Each contour-plot is normalised to the maximum field value inside the cavity.

than $5\,\mu m$. We can also measure the exact shape of the mirrors and the wall thickness of the aperture with a high precision profilometer to an absolute accuracy of better than $10\,\mu m$. Preliminary data in this setup show striking agreement between measurement (fractional reflected power and quality factor as a function of aperture size) and simulations.

6.6 The Final Ultra High Vacuum Version of the Microwave Trap

Ultimately the lifetime of the molecules in a trap will be limited by collisions with background gas molecules. An estimate for the trap lifetime τ_l due to background gas collisions is $\tau_l \approx 10^{-8}/p$
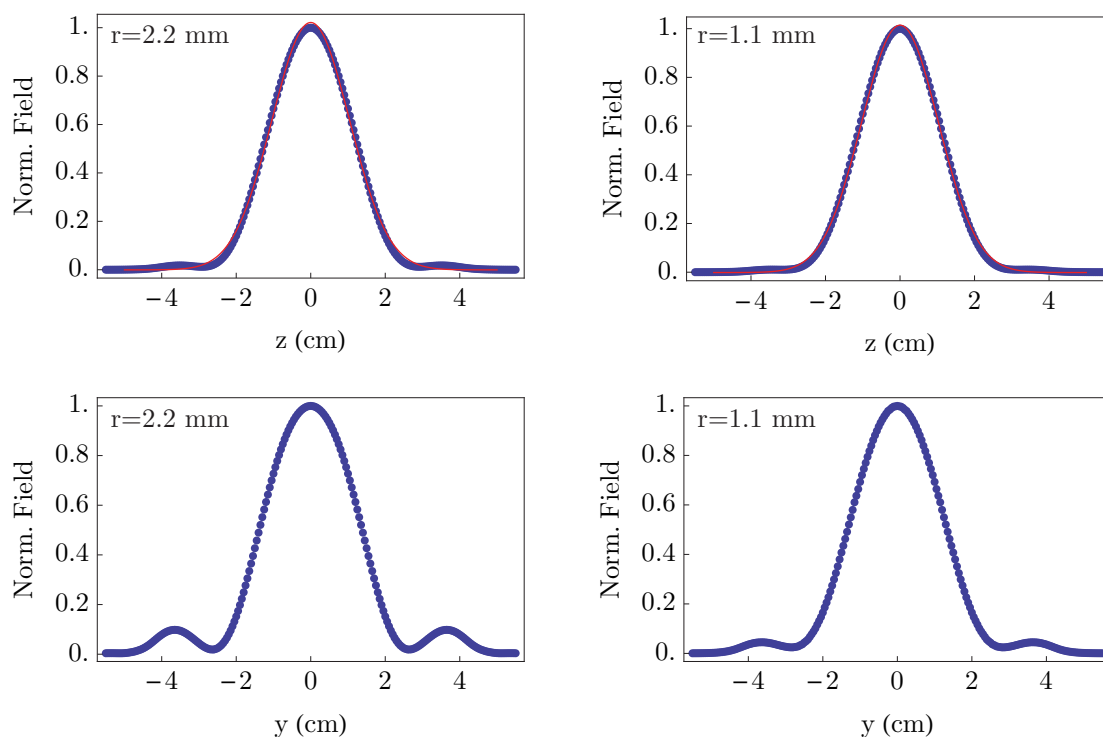
FIGURE 6.17: Top: Simulated normalised electric field magnitude across the centre of the cavity and along the long axis of the waveguide ($x = 0$, $y = 0$) for two different aperture sizes. The blue dots are the data and the red line is a Gaussian fit. The fit yields a beam waist radius $w_0 = 1.47\,\mathrm{cm}$ ($r = 2.2\,\mathrm{mm}$) and $w_0 = 1.46\,\mathrm{cm}$ ($r = 1.1\,\mathrm{mm}$). Gaussian beam theory predicts a waist of $1.43\,\mathrm{cm}$ for this geometry. Bottom: The normalised electric field magnitude across the centre of the cavity and along the long axis of the waveguide ($x = 0$, $z = 0$) for two different aperture sizes. We can clearly see that the aperture causes diffraction to the sides of the main peaks. The relative size of these side peaks increases as the hole size increases.
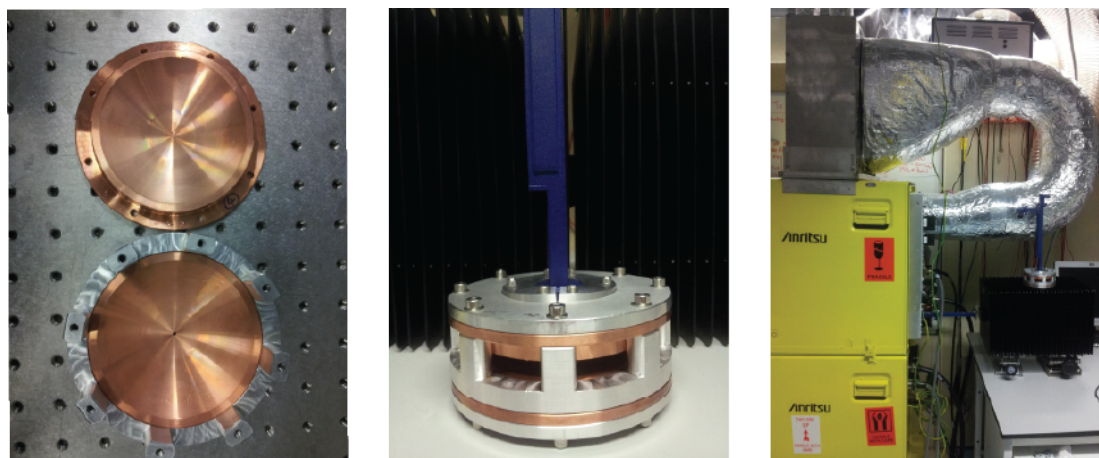
FIGURE 6.18: Left: Two cavity mirrors, one mounted in the high precision spacer. Middle: The assembled cavity with the directional coupler attached to the input mirror. Right: The assembled cavity on top of the high power load and next to the klystron amplifier.

seconds where p is the background pressure in mbar (1 mbar = 100 Pa). To achieve trap lifetimes of the order of one minute we therefore need to operate the microwave trap in ultra-high vacuum conditions ($< 10^{-9}$ mbar). This is our first constraint for the final version. We chose a 8.0" spherical octagon vacuum chamber from Kimball Physics (MCF800-SphOct-G2C8) to house the microwave trap. As mentioned earlier we plan to test the microwave trap with ultracold lithium atoms first. The atoms are delivered by a movable magnetic trap from a separate chamber. The trap depth and thus the number of atoms critically depends on the magnetic field gradient and thus on the separation of the magnetic field coils. We therefore need to minimise the height of the vacuum chamber. A spherical octagon combines good optical access, large internal volume and minimum height. The external dimensions of the trap are thus determined by the size of the spherical octagon. As pointed out earlier, all the power we inject into the cavity will ultimately be lost through resistive heat in the mirrors. Hence efficient cooling under ultra-high vacuum conditions is obligatory. We plan to use liquid nitrogen to cool the mirrors, because it increases the conductivity and thus relaxes the input power requirements, which again relaxes the cooling requirements. The latent heat of evaporation of liquid nitrogen (the amount of energy needed to induce the phase-change from liquid to gas) is $L = 200$ kJ kg^{-1} and the density is $\rho = 0.8$ kg l^{-1}. To dissipate $P = 1$ kW of microwave power in the mirrors we need to achieve a liquid nitrogen flow of $F = P/(L\rho) = 22.5$ l h^{-1}. To achieve efficient cooling the liquid needs to be evaporated on the hot surface which produces about 260 l min^{-1} (16 m^3 h^{-1}) of nitrogen gas which has to be removed from the cooling area without causing any significant overpressure in the cooling blocks which will reside inside the vacuum chamber to reduce heat transfer from ambient air. We need excellent thermal contact between the cooling blocks and the mirrors, without sacrificing on the alignment of the mirrors with respect to each other and to the waveguide which feeds the cavity with microwaves from the klystron amplifier. Furthermore, we need to keep the overall geometry open so that we have good optical access to the atoms and molecules. The cooling process should not generate excessive noise or vibrations on the mirrors and be very effective in removing the heat from the mirrors. The cooling with liquid nitrogen also demands for thermal breaks to the vacuum chamber to prevent heat transfer to the cooling blocks and mirrors. The vacuum feedthrough for the microwaves must be low loss and compatible with the ultra-high vacuum and high power requirements. After exiting the vacuum chamber the waveguide must turn through 90°, so that the magnetic field coils that transport the atoms into the trap can slide over the chamber without needing to increase the distance between the coils. The waveguide is connected to one of the mirrors and thus needs a thermal break to prevent condensation and heat transfer.

The technical drawings of the final design are shown in figures 6.19 and 6.20. The heart of the setup consists of the two cooling blocks and the two cavity mirrors which are connected to the top flange of the vacuum chamber via two thin-walled stainless steel tubes. Note that stainless steel (316) and copper have very similar thermal expansion coefficients, which makes sure that no cracks develop where the steel tube is connected to the copper cooling block. This

is also crucial to maintain ultra-high vacuum conditions when cooling to low temperatures. The two cooling blocks are connected via hollow legs so that a constant flow of liquid nitrogen through the whole system can be achieved. The cooling blocks have a total internal volume about $300\,\mathrm{cm}^3$ which allows us, in principle, to operate the trap for about one minute at full power without refilling. However, we plan to continuously supply liquid nitrogen through a tube that goes into the bottom cooling block.

The mirrors sit on the cooling blocks and are positioned with precision dowel pins. This assures good axial alignment of the two mirrors. The tilt and yaw of the mirrors is set by the alignment of the cooling blocks with respect to each other and must be better than 10^{-3} radian. The cavity length is also pre-defined by the cooling blocks and cannot be changed. The microwaves are fed into the cavity through a waveguide system which consists of two parts: A standard WG 18 waveguide is connected to a short custom-built, silver plated invar waveguide. The invar waveguide sits in an adapter flange which is welded into the rotatable DN160CF flange of the vacuum chamber after the silver plating. The standard waveguide is then welded to the custom-built one to form a good vacuum seal. The thermal conductivity of invar is about forty times lower than that of copper (standard waveguide material) and thus serves as a thermal break between the cooling block and the room-temperature waveguide system. In order to minimise electrical losses the invar waveguide is plated with a thin layer of silver (the thickness should be several skin depths). Nearly all the parts have been manufactured in our workshop and we are currently only waiting for the silver plating of the invar waveguide to be completed. Once this is done the parts will be assembled in a custom-made support structure to assure good alignment of the individual parts and brazed together in a vacuum furnace in a single manufacturing step.

The mirrors are machined on a CNC lathe in our workshop. We measure the profile and the wall thickness of the mirrors with micrometer accuracy. Only if they have a smooth profile without any defects we proceed. The mirrors are cleaned and electro-polished to remove the work hardened top-layer of the mirrors and to improve the surface finish. The mirrors are then annealed in our vacuum furnace to release stress in the material and to decrease the defect density. We also plan to inspect the surface roughness with an electron microscope and measure it with a white-light interferometer, to select the ones with the best surface finish. The mirrors are then mounted on the cooling blocks and the alignment is checked. First we will test the cavity in a separate chamber for its ultra-high vacuum compatibility and we will then mount it in the ultracold lithium setup, where we will trap ultracold lithium atoms.

6.7   Future Directions - A Superconducting Cavity

As discussed in the previous sections, the conductivity, and thus the reflectivity, of the mirrors increases as the temperature is lowered. In metals such as copper, silver or gold the electrical
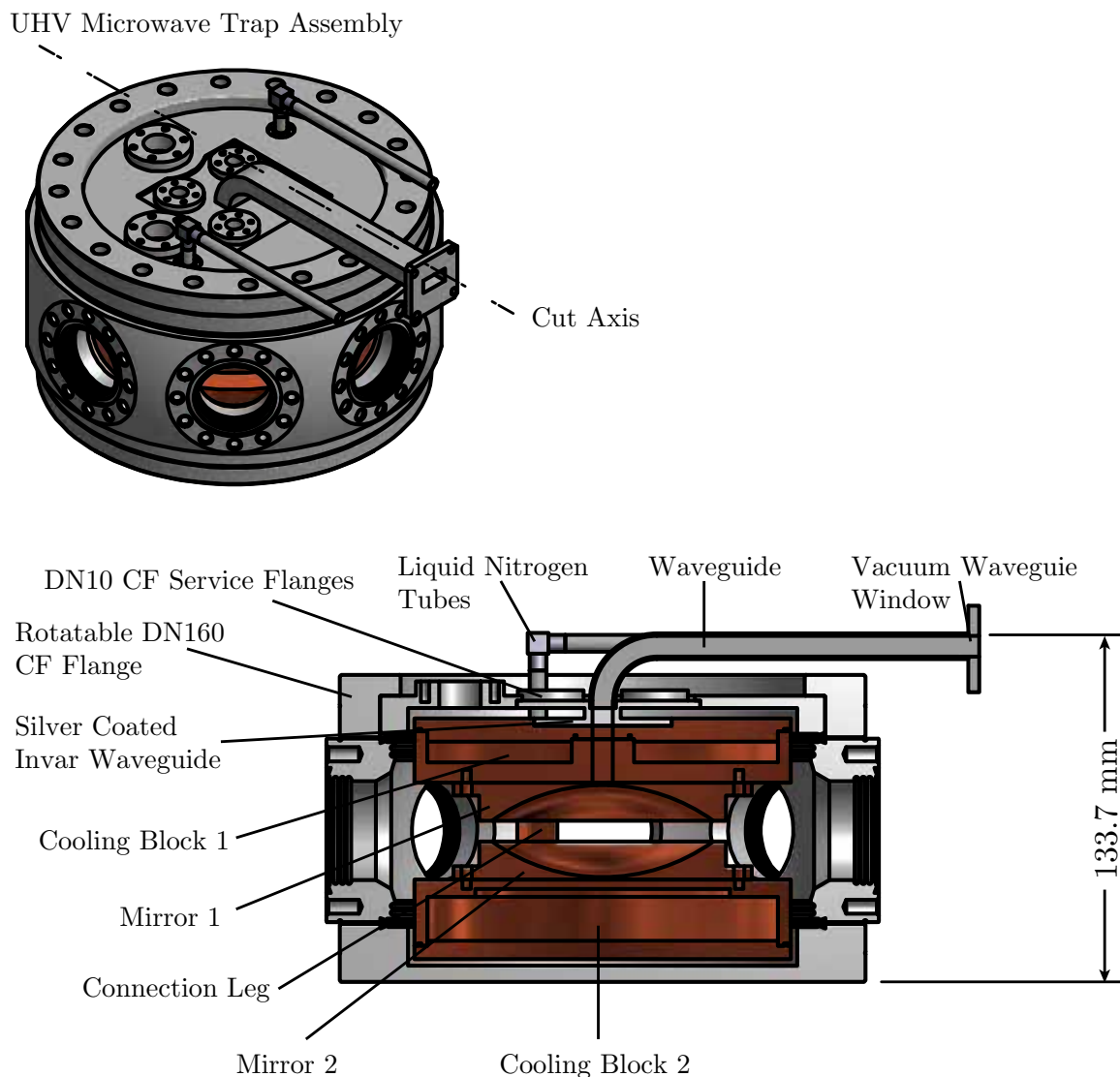
FIGURE 6.19: Top: A 1:4 scale drawing of the ultra-high vacuum assembly. Bottom: A 1:3 drawing of a central cut through the chamber. The cavity and cooling blocks are attached to the top flange of the vacuum chamber via two thin-walled stainless steel tubes. This provides the thermal break necessary to keep external heat transfer from the outside to a minimum. The mirrors are located with precision dowel pins to provide good axial alignment and can be removed from the setup without the need to disassemble everything. The angular alignment of the mirrors with respect to each other is predefined by the alignment of the cooling blocks and must be better than 10^{-3} radians. The waveguide that feeds the cavity with high power microwaves from the klystron consists of two parts: First, a room-temperature part which combines a standard WG-18 waveguide bend with an ultra-high vacuum compatible, high power waveguide window which is glued into the flange of the standard waveguide. This standard waveguide is connected (welded) to a custom-built silver-plated invar waveguide which is bolted to the cooling block through the DN10CF service flanges. This assures good electrical contact of the waveguide to the cavity. A waveguide bore in the cooling block then guides the microwaves to the cavity mirror.
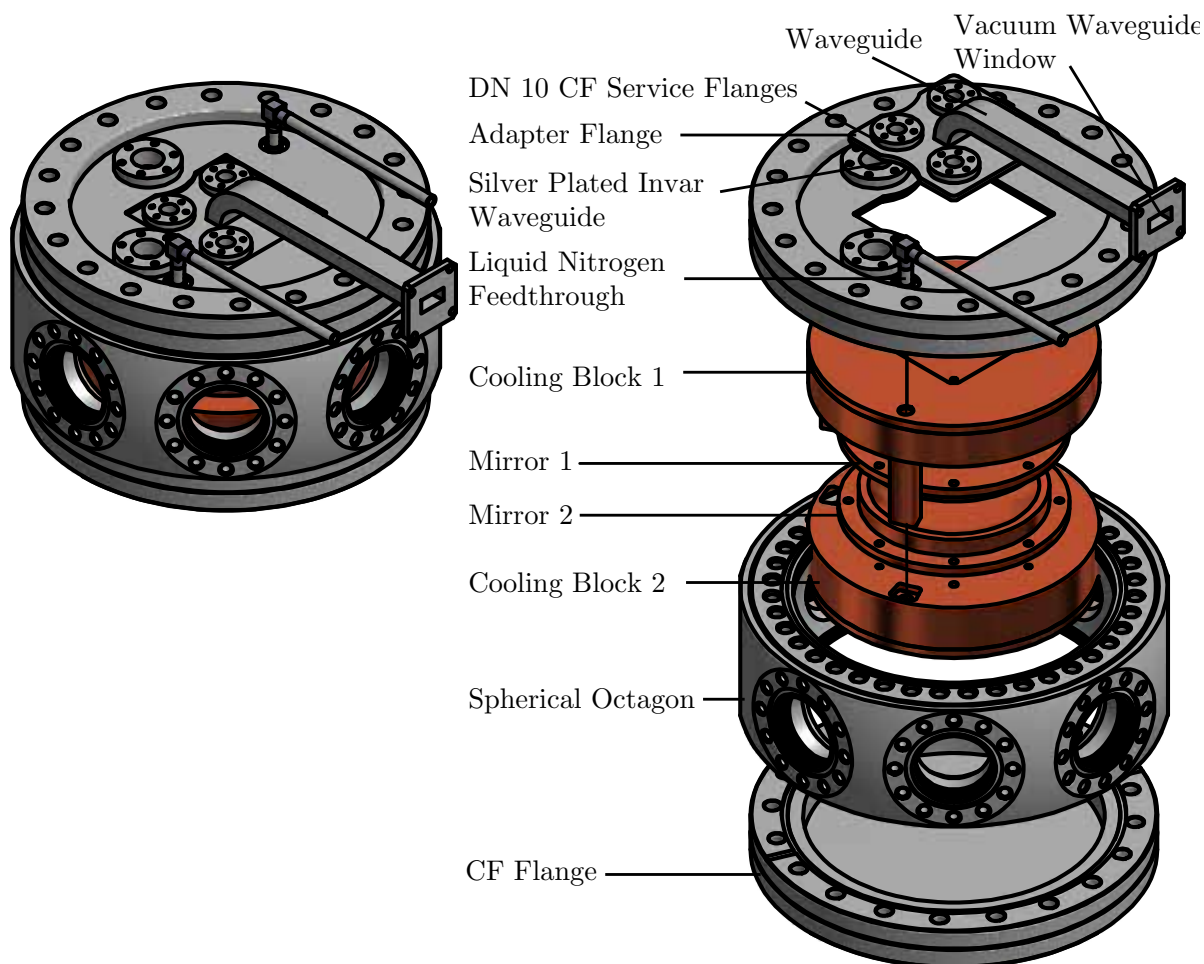
FIGURE 6.20: Left: A 1:3 scale drawing of the assembly. Right: An exploded view showing all the individual parts.

resistance eventually levels off to a constant value which is determined by impurities in the metal lattice. Some materials, however, undergo a phase transition below a certain critical temperature T_c, at which the dc electrical resistance suddenly vanishes. The first to observe such a phase transition was Heike Kamerlingh Onnes from Leiden University. He was awarded the Nobel prize in physics "for his investigations on the properties of matter at low temperatures which led, inter alia, to the production of liquid helium". Onnes could show that the resistance of pure platinum and gold wires decreased with temperature and reached a constant value for temperatures as low as $1.15\,\mathrm{K}$. He attributed this finite resistivity to a small amount of impurities which remain even in pure gold. He therefore turned his attention to mercury which he hoped to purify to higher degree than gold. After a "painstaking" purification process he succeeded to show that the resistance of mercury disappears for low temperatures, but to his surprise not gradually but very abruptly. He immediately realised that mercury must have undergone a phase transition to a previously unknown state which he called superconductivity.

Meissner and Ochsenfeld discovered that superconductors expelled applied magnetic fields in 1933. Heinz and Fritz London were able to explain this effect theoretically and thus gave

the first phenomenological description of superconductivity. By 1950, Vitaly Ginzburg and Lev Landau, provided a profound phenomenological description of superconductivity. The explanation of what happens on the microscopic level, however, remained elusive until 1957 when John Bardeen, Leon Neil Cooper and John Robert Schrieffer explained the superconducting current by assuming that the electrons form pairs (Cooper pairs) via interactions with phonons [300]. Ginzburg, Landau, Bardeen, Cooper and Schrieffer would sooner, or later, receive the Nobel prize in physics for their contributions to explain superconductivity. More and more materials were investigated and by the end of the 1980s Bednorz and Müller realised that certain semiconducting oxides became superconducting at temperatures as high as 35 K. This stimulated great interest and led to the first samples that became superconducting at liquid nitrogen temperatures by 1987 using a compound of yttrium, barium copper and oxygen (YBCO).

For ac fields the situation is slightly different. Similar as for the case of a normal conductor the surface resistance is related to the conductivity of the bulk material by

$$R_{\mathrm{surf}} = \frac{1}{\lambda_L \sigma}, \tag{6.34}$$

where the typical length scale is not the skin depth, but the London penetration depth $\lambda_L = \sqrt{m_e/(\mu_0 n_c e^2)}$, with m_e the electron-mass, μ_0 the vacuum permeability, n_c the density of the cooper pairs and e the elementary charge. In general a current in a superconductor is carried by both Cooper pairs and unpaired electrons. At 0 K all electrons in the material are condensed into Cooper pairs. As the temperature increases the density of Cooper pairs decreases to zero as the critical temperature is approached. Our aim here is to describe the temperature dependence of the surface resistance.

The conductivity therefore consists of a normal conducting part σ_n and a superconducting part σ_s. The unpaired electrons obey Ohm's law and the corresponding current density J_n is

$$J_n = \sigma_n E_0 e^{-i\omega t}, \tag{6.35}$$

where, σ_n is the normal conductivity of the material, E_0 is the amplitude of the electric field which is oscillating at an angular frequency ω. Halbritter found an expression to describe the normal part of the ac resistance as a function of the temperature [301]. Below the critical temperature normal, free electrons are created by thermal breakup of Cooper pairs. He described this break-up process similar to a semiconductor by introducing a gap parameter $\Delta(T)$ which is half of the energy gap between the BCS ground state of the electrons and the free, normal state of the electrons:

$$\sigma_n \propto e^{-\frac{\Delta(T)}{k_B T}}, \tag{6.36}$$

Now to the superconducting part σ_s. Cooper pairs move without resistance through the superconducting material, but they possess a small inertial mass. An alternating driving field leads to a constant acceleration and deceleration of the Cooper pairs ($m_e \dot{v} = -2eE_0 e^{-i\omega t}$). By

integration we get the velocity and thus the current density:

$$J_s = n_c e v = n_c e \int -2e E_0 e^{-i\omega t} dt = i \frac{2 n_c e^2}{m_e \omega} E_0 e^{-i\omega t} = i \sigma_s E_0 e^{-i\omega t} \tag{6.37}$$

The total current density is then

$$J = J_n + J_s = \sigma E_0 e^{-i\omega t}, \tag{6.38}$$

with the complex conductivity $\sigma = \sigma_n + i\sigma_s$. The surface resistance is then given by [302]

$$R_{\text{surf}} = Re\left(\frac{1}{\lambda_L(\sigma_n + i\sigma_s)}\right) = \frac{1}{\lambda_L}\frac{\sigma_n}{\sigma_n^2 + \sigma_s^2} \simeq \frac{1}{\lambda_L}\frac{\sigma_n}{\sigma_s^2}. \tag{6.39}$$

Equation 6.39 shows that the surface resistance of a superconductor for ac fields depends on the normal conductivity of the bulk material. We can rewrite the last expression of equation 6.39 by using $\sigma_s = \frac{1}{\mu_0 \lambda_L \omega}$ and arrive at the final expression for the surface resistance of a superconductor, often denoted as R_{BCS}, as a function of the microwave frequency and the temperature:

$$R_{\text{BCS}}(\omega, T) \propto \lambda_L^3 \omega^2 e^{-\frac{\Delta(T)}{k_B T}}. \tag{6.40}$$

For temperatures $T/T_c < 1/2$ we can approximate $\Delta(T) \simeq 1.76 k_B T$. The important results therefore are: the surface resistance scales with the cube of the London penetration depth, with the square of the microwave frequency and decreases exponentially with temperature.

Similar to normal conductors, the resistance will reach a small residual value R_{res}, which is independent of the temperature and determined by the density of impurities and lattice distortions. Frozen-in magnetic flux in the bulk material can also contribute to this value. Hence the total surface resistance is:

$$R_{\text{surf}} = R_{\text{BCS}} + R_{\text{res}} \tag{6.41}$$

Both parts R_{BCS} and R_{res} can be as low as a few nΩ compared to mΩ for normal, ohmic materials such as copper.

6.7.1 High Q Superconducting Cavities

From the very beginning of linear particle accelerators rf cavities have been used to accelerate electrons and protons to very high velocities. These cavities are made from copper and water cooled to remove the heat dissipated in the cavities. The need to generate large electric fields to accelerate particles close to the speed of light means that accelerators based on copper cavities can only be used at a very low duty cycle to prevent melting of the copper due to the large resistive heating. Therefore it is advantageous to use superconducting ones. The low dissipation

in the superconducting cavity walls allows to the accelerator to operate continuously. Superconducting cavities face a physical limitation: the microwave magnetic field must stay below the critical field at which superconductivity breaks down (200 mT for niobium). This limits the maximum acceleration fields to $50\,\mathrm{MV\,m^{-1}}$, while normal conducting copper cavities reach up to $150\,\mathrm{MV\,m^{-1}}$. Niobium is used because it has the largest critical temperature of all elements ($T_c = 9.2$ K), and is available in large quantities at high purity. Although certain alloys can have very high critical temperatures, their rf properties at large electric and magnetic fields are worse or they can not be manufactured in large quantities. Promising materials such as Nb_3Sn ($T_c = 18$ K) or MgB_2 ($T_c = 40$ K) are currently under investigation by many research groups. Such accelerator cavities could in principle be adapted to decelerate or guide polar molecules in their high-field seeking ground state. The manufacturing process is well established, and the geometry of such accelerator cavities is already ideally suited for molecular beam experiments. They can accommodate a vacuum tube, the electric field has a maximum along the beam axis and is homogeneous. By operating at higher frequencies (20 GHz) one can decrease the size of the cavities and thus create a very compact decelerator with an unprecedented phase-space acceptance. The molecules climb a potential hill due to the Stark effect which is large due to a strong interaction with the molecular dipole moment. In order to dissipate the gained energy one can simply modulate the input power.[4]

In the atomic physics community the group of Jean-Michel Raimond and Serge Haroche at ENS in Paris have pioneered the use of superconducting microwave cavities to study the light-matter interaction at the most fundamental level. They started with a free-space millimeter-wave beam in 1977 to drive transitions between two sodium Rydberg levels [303] and gradually upgraded their interaction region to gain better and better control over the interaction. By 1982 they had built a room temperature cavity for radiation at 162 GHz with a quality factor of $Q = 10000$ [304] and finally built their first superconducting cavity in 1983 using niobium [305]. This allowed them to observe the intriguing effect that the mere presence of two highly reflecting mirrors can change the spontaneous emission lifetime of atoms. Since 1983 the group in Paris has perfected the production of high-Q superconducting cavities in order to study the interaction of light and matter at the most fundamental level. By 2007 they succeeded in building a cavity that can store light for up to 130 ms which corresponds to a finesse of 4.6×10^9 the highest that has ever been achieved in any frequency domain [306]. This persistent approach to perfection culminated in Serge Haroche being awarded the Nobel Prize in Physics in 2012.

The group in Paris uses a Fabry-Pérot cavity which they operate at a frequency of 51 GHz. This frequency is too high for our purposes because we need to be red-detuned from the closest rotational transition, which for most molecular species we use in our lab is in the 20 - 40 GHz range. From equation 6.40 we know that by operating at a lower frequency we decrease the surface resistance quadratically. However, it should be pointed out that the finesse of the cavity presented in [306] is not limited by the conductivity but rather by diffraction loss, i.e. due to

---

[4]Note the quality factor should not be too high because decay of the electric field would take too long.

the finite size of the mirrors. They achieve the above stated maximum finesse at a temperature of 0.3 K. Unfortunately, we have no means of reaching such low temperatures. Typical closed-cycle cryocoolers possess 3 W of cooling power at 4.2 K. By using a traditional helium bath cryostat we can reach about 2.2 K by decreasing the pressure above the helium bath. This way up to 30% of the helium evaporates and cools the remaining liquid. Going below the Λ-point results in large helium loss rates and is thus not an option (we do not have a helium recovery system). The latent heat of vaporisation of liquid helium is $21 \, \mathrm{kJ \, kg^{-1}}$ and has a density of $\rho = 0.12 \, \mathrm{kg \, l^{-1}}$. If we want to dissipate an input power of 2 W we would need about $3 \mathrm{l \, h^{-1}}$ of liquid helium.

In this temperature range the finesse will mainly be limited by the surface resistance R_{BCS} of the mirrors. Assuming the exponential dependence on the temperature measured by Kuhr and colleagues [306] and an increase in conductivity by $(51/15)^2 \approx 12$, due to the ratio of the frequencies, we could achieve a finesse of 7.3×10^8 at $T = 2.2$ K and 2.56×10^7 at $T = 4.2$ K. This corresponds to an increase in finesse of about 30000 or 1000 in finesse compared to the copper cavity at 77 K. In order to achieve a comparable intra-cavity field we therefore need to couple 30 mW or 1 W into the cavity.

Note that this is for the ideal case that we indeed benefit from the full increase in conductivity by operating at lower frequency. Furthermore, by operating at such low frequencies we need about twice the mirror size to keep the diffraction losses small. However, the Paris design is a nearly closed cavity (the spacing between the mirrors is encompassed by an aluminium ring) which reduces the diffraction losses considerably and increases the finesse by nearly a factor of 100 as demonstrated in [307]. We on the other hand need optical access to detect the molecules, once they are trapped. We might be able to carefully image the molecules through small apertures in such rings. Furthermore, the Paris group has no coupling apertures in their latest version of the cavity. Such coupling irises are detrimental to the surface quality and reduce the finesse by as much as a factor of 400, even for a very small aperture that corresponds to a coupling of below 1% [306–309]. Hence we need to find new ways to critically couple such a cavity.

In view of all these complications we decided to pursue the copper version, but the superconducting version remains a very interesting option. Especially because it would perfectly complement a cold effusive or hydrodynamically enhanced buffer gas which operates already at 4 K.

A very interesting aspect of this cavity is that one can get access to a regime at which the molecules are strongly coupled to the cavity field. This means that the cavity can influence the way the molecules scatter the microwave radiation. This is a very intriguing effect and can be used to cool the centre of mass motion of the molecules in the trap, also known as cavity cooling. This cooling scheme, opposing to traditional laser cooling, does not rely on a closed transition. The effect is based on Doppler cooling but due to preferential scattering, in contrast to preferential absorption. The cavity affects the off-resonant (large detuning) scattering of the

molecules in the cavity field and one can exploit this effect to cool the molecules to very low temperatures [310, 311]. Although the momentum kick of a scattered microwave photon is very small, one can make up for it by increasing their number. For optimum cooling conditions the cavity must be detuned from the injected field by $\Delta = \kappa/\sqrt{3}$, where $\kappa = 1/\tau$ is the cavity decay rate ($Q = \omega\tau$) [312]. A characteristic momentum damping rate is given by

$$\beta \approx -\frac{3\sqrt{3}}{2}\left|\frac{U_0\alpha}{\kappa}\right|^2 \omega_r \tag{6.42}$$

with

$$U_0 = -\frac{\omega_c\chi}{2\epsilon_0 V} \qquad\qquad \alpha = \sqrt{\frac{P}{2\kappa\hbar\omega_p}} \qquad\qquad \omega_r = \frac{\hbar k^2}{2m_p} \tag{6.43}$$

where ω_c is the angular frequency of the cavity, χ is the polarisability of the molecules, V is the cavity volume, P is the power injected into the cavity, ω_p is the angular frequency of the photons, k is the wavenumber of the microwave photons and m_p is the mass of the particles. The great advantage of using molecules in microwave fields is that their polarisability χ can be extremely large even for a very large detuning from a resonance ($\chi \approx 10^5 4\pi\epsilon_0 \text{Å}^3$). If we operate the cavity at about 19.5 GHz the polarisability for the CaF molecule for example is about $\chi = 50000\ 4\pi\epsilon_0 \text{Å}^3$. For a cavity volume of about $1\,\text{cm}^3$, assuming that we can critically couple $1\,\text{W}$ into a cavity that has the same unloaded Q as the group in Paris, the decay rate would be $\kappa = 50$ Hz (adjusted for the lower resonance frequency and coupling) and for a mass of the CaF molecule of 59 amu we get an average cooling rate $\beta = 50$ mHz. The typical time the molecules have to spend in the cavity to experience a large cooling force is of the order of $1/\beta = 20$ s. Therefore, cavity cooling could only work once the molecules are trapped already.

Note that U_0 is known as the coupling constant. It has the dimension of a frequency and describes the optical potential created by a single photon and the shift of the cavity resonance due to the presence of a particle (the change in refractive index). Although this is very small for a microwave cavity ($U_0 \approx 30 \times 10^{-9}$ Hz) we can compensate for that by a large number of photons $|\alpha|^2$ and a high quality factor (small κ), such that $|U_0|\,\alpha \gg \kappa$ and enter the regime of strong coupling. Although this is extremely challenging one can get extremely efficient cooling to below the photon-recoil limit.

6.8   Trap Loading

Before concluding this chapter we discuss how we plan to load the microwave trap with molecules. As a first step we will test the basic working principles by trapping ultracold lithium atoms, which we can already produce in a magneto-optical trap and transport into the microwave trap using a moveable magnetic trap. In the science chamber we overlap the microwave trap with

the magnetic trap, ramp down the magnetic trap and increase the microwave trapping field. A similar scheme works of course also for molecules that possess a magnetic moment.

Recent results show that laser cooling and slowing for certain molecules (SrF, YO, CaF) is possible [72, 249, 251, 313]. This is also the most promising loading technique for the microwave trap. With laser cooling, molecules can be cooled to the Doppler temperature $T_D = \hbar\Gamma/(2k_B) \approx 0.2$ mK, where $\Gamma \approx 2\pi 10$ MHz is the damping rate. Laser cooling relies on specific selection rules that allow for quasi-closed transitions. One such selection rule demands that the lower state is a rotationally excited state ($N = 1$) which is low-field-seeking in a red-detuned microwave trap. In order to trap the molecules in their ground state one needs to transfer the molecules via optical pumping or resonant microwaves (π-pulse) to the ground state. Note, that for the same reason that laser cooling uses the first rotational ground state (parity selection rule) optically pumping via an excited electronic state into the ground state is forbidden. However, the presence of the microwave fields breaks this selection rule. This is therefore a very convenient way to accumulate the molecules over time. The fact that the molecules are already cold relaxes the requirements for the trapping fields considerably. This means that the input power for the copper cavity can be lowered to a few watts. For the superconducting cavity we could work at $4\,\mathrm{K}$ which is the temperature at which buffer gas sources operate and use just a few mW of input power. Once the molecules are trapped, the temperature is low enough and the density high enough that evaporative cooling could be used to cool the sample to quantum degeneracy.

Laser cooling will always be limited to very few species which possess Franck-Condon factors near unity. For other molecules, especially polyatomic molecules, direct loading into a deep trap is also possible. Slow buffer gas beams with an effusive velocity distribution and a most probable velocity of $40\,\mathrm{m\,s^{-1}}$ have been demonstrated already [314]. The low velocity tail of such a beam can be filtered using an electric or magnetic guide [82, 89] and accumulated in the microwave trap via optical pumping. The molecules confined in such a way will still be too hot ($\approx 1\,\mathrm{K}$) for evaporative cooling. However, electro-optic cooling, single photon cooling schemes [88, 89, 315], sympathetic cooling with ultracold atoms, or even cavity cooling can be used to cool the molecules to temperatures where evaporation becomes effective.

Loading the trap from a Stark-decelerated supersonic beam is also possible. Molecules with low-lying Λ or Ω-doublets are preferred for Stark deceleration because the mixing of these levels leads to a large linear Stark shift which simplifies the deceleration. The requirement that the microwave trap is red-detuned from the closest transitions rules out most of the species that have been Stark decelerated already. However, ammonia ($\mathrm{NH_3}$) is an attractive candidate. Ammonia molecules have been decelerated already [316] using a traditional Stark decelerator and by using a closed cylindrical microwave cavity [270]. By axially aligning the cavity with the Stark decelerator one can use the microwave fields as the last stages of a Stark decelerator and trap the molecules in the centre. The molecules can be focused through a small aperture in one of the mirrors. Alternatively one can simply attach the Stark decelerator as close as possible

to the microwave cavity (orthogonally oriented to the Stark decelerator) and let the molecules fly into the trapping region. The molecules can be pumped into the high-field-seeking ground state with a resonant microwave pulse which is spatially overlapped with the trapping field.

Alternatively one can use a microwave decelerator to decelerate the molecules in their high-field-seeking ground state. One could even conceive trapping the molecules at the end of the microwave decelerator. Such decelerators are typically closed cylindrical cavities which makes the detection and further cooling challenging. Therefore a separate open Fabry-Pérot type cavity as a trap for good optical access would ideally complement such a decelerator.

In 2007 Matthews and colleagues proposed that one could produce molecules at zero velocity by dissociating a suitable precursor molecule. A supersonic beam of precursor molecule (NO_2 or H_2S for example) is initially cooled in expansion. Further downstream the molecular beam intersects a resonant laser beam which dissociates the molecule. One can break the O_2 bond of NO_2 molecule, for example, which results in an atomic and a molecular fragment. The recoil of the oxygen atom can decelerate and even stop the NO fragment [317]. Zhao and colleagues and later Trottier and colleagues could show that one can indeed decelerate and stop molecules in a molecular beam via photodissociation [85, 318]. This technique can be a relatively simple way to load and test the microwave trap.

6.9   Conclusion and Outlook

In this chapter, the development of a new kind of trap for ground-state polar molecules has been presented. From a general overview of the various, existing trapping techniques we concluded that collisional cooling is most likely to work in a microwave trap which obviates the problem of inelastic collisions. Furthermore, the trap provides a deep trapping potential for a large variety of molecules.

This was followed by a theoretical description of the basic working principle of an open Fabry-Pérot resonator for microwaves and an analytical model for coupling the cavity using an aperture was compared to first measurements. We found that at critical coupling the quality factor was lower than expected. We therefore investigated the coupling and intra-cavity fields by performing FDTD simulations using Microwave Studio and could show that the aperture influences the mode inside the cavity and leads to extra losses. By operating the cavity slightly below critical coupling we can circumvent this problem. We demonstrate that it is possible to couple over 90% of the injected power into the cavity by only using a single coupling aperture and still retain the high finesse needed for a deep trapping potential. We could further show that the quality factor increases when the mirrors are cooled with liquid nitrogen. Non-ideal surface conditions, however, influenced the low-temperature behaviour which led to a discrepancy of 30% between the expected and measured quality factor. We have identified ways to improve the surface quality of the cavity mirrors which will allow us to reach near-perfect quality factors at

room temperature and at 77 K for our final version. We have built a high precision cavity which we are currently using to compare measurements (coupling and quality factor as a function of the aperture size) with the predictions of the FDTD simulations. Preliminary results show striking agreement. We have also designed a final ultra-high vacuum compatible, high power version of the cavity which is currently built and assembled in our workshop. The alternative approach of using a superconducting cavity has also been discussed. The use of such a cavity, especially in combination with a laser-cooled molecular beam from a cryogenic buffer gas cell, is a very promising future direction to reach very high densities of trapped polar molecules at low temperatures. Once the molecules are confined, the microwave trap is the ideal starting point for secondary cooling processes such as sympathetic or evaporative cooling which can cool the molecules to quantum degeneracy. Some specific ways to load the trap have briefly been discussed as well.

We are currently testing the high-power stability of the cavity and finishing the new high precision measurements of the coupling and quality factor as a function of the aperture size. Once the ultra-high vacuum version is completed we will test the microwave trap with ultracold lithium atoms while a suitable molecular beam apparatus for trap loading is being developed. This will most likely consist of a cryogenic buffer gas beam of either CaF or SrF molecules which can be slowed and cooled using laser light.

Chapter 7

Towards a Magneto-Optical Trap for Polar Molecules

One has to do something new in order to see something new.

Georg Christoph Lichtenberg

7.1 Introduction

With laser cooling techniques one can routinely cool an atomic gas from hundreds of kelvin to below a few µK within a few milliseconds. The momentum of a single photon ($p_{ph} = \hbar k$) is relatively small ($1eV/c = 5.3 \times 10^{-28}$ kg m s^{-1}) compared to the momentum of an atom moving at thermal speed ($p_a \approx 10^{-23}$ kg m s^{-1}). When an atom absorbs a photon that is resonant with one of its electronic transitions it recoils from the impact of the photon and slows by $\hbar k/m$. We therefore, typically need to scatter approximately $10^4 - 10^5$ photons to slow an atom to rest. Some atoms possess specific transitions which, after excitation, decay back to the initial state only. The atom can go through the same absorption and emission cycle again using the same laser. Molecules, however, can vibrate and rotate and thus possess a more complex internal structure. Once a molecule has been excited by the laser beam it can decay to many possible vibrational and rotational states in the ground electronic state. Therefore, in general, one can only scatter a few photons before the molecule is optically pumped into a dark state which cannot be addressed by the same laser.

However, there are exceptions. In his paper of 2004, Di Rosa pointed out that for some carefully selected molecules it might be possible to scatter enough photons to cool them to sub-millikelvin temperatures [71]. He identified three criteria a molecule must meet: it must have a strong transition (short excited state lifetime) which allows high scattering rates, a highly diagonal Franck-Condon matrix (the potential curves of the ground- and excited state must be

very similar) and no intermediate electronic state to which the molecule could decay. Ideally the Franck-Condon overlap between the lowest vibrational state of the first electronically excited state and the lowest vibrational state of the ground electronic state should be close to unity. Therefore, if the molecule is excited with a resonant laser beam the probability for it to return to the same vibrational state in the ground electronic state is close to unity. Di Rosa suggested a number of molecules that meet these criteria: BeH, MgH, CaH, SrH, BaH, NH, BH, AlH, AlF and AlCl. For most of these molecules one still needs to close leaks to one or two vibrational states in the ground electronic state and to other rotational states. Furthermore, the hyperfine structure needs to be addressed as well. In 2008 Stuhl and co-workers took Di Rosa's idea a step further. The decay to rotationally excited levels in the ground electronic and vibrational state must satisfy the total angular momentum selection rule $\Delta J = 0, \pm 1$. This means that for a Franck-Condon factor of unity and without hyperfine structure one needed already three lasers to address the three rotational branches. Stuhl et al. pointed out that if the angular momentum of the ground state J'' is greater than the angular momentum of the excited state J' then two of these three decay channels are forbidden [319]. If one chooses a molecule which has no nuclear spin one can also get rid of hyperfine splitting. Stuhl and colleagues identified TiO and TiS in their ground states and metastable FeC, ZrO, HfO, ThO and SeO as good candidates. They first concentrated their efforts on TiO but later switched to YO which allows higher scattering rates, has a better Franck-Condon factor and a superior dipole moment of 4.5 D. Recently, they could show laser cooling of the transverse temperature of a beam of YO molecules to about 2 mK which is still a factor of 20 higher than the Doppler limit of 116 µK.

The first to show that laser cooling of molecules can indeed work was the group of DeMille at Yale in 2010 [72]. They cooled the transverse temperature of a molecular beam of SrF molecules from 50 mK kelvin to a few millikelvin by scattering about 1000 photons [72]. They also demonstrated the slowing of a beam of SrF molecules using radiation pressure two years later [250].

Recently, the slowing and cooling of a CaF beam from a few kelvin to a few millikelvin has been demonstrated in our lab [251]. When slowing a molecular beam using radiation pressure, the laser beam counter-propagates to the molecular beam. This means that the laser frequency must be detuned by the Doppler shift. As the molecules slow down the velocity and thus the Doppler shift changes. Zhelyazkova and colleagues tackled this problem by chirping the frequency of the lasers. The standard technique used for slowing atoms is to shift the atomic resonance with a spatially varying magnetic field, i.e. by using a Zeeman slower. The ground states of CaF and SrF are $^2\Sigma$ states. The first excited rotational state thus splits into two spin-rotation components with a total angular momentum of $J = 1/2$ and $J = 3/2$. Each doublet is again split due to the interaction of the fluorine nuclear spin with the unpaired electron. One must address all these levels to keep the molecule in the cycling transition. In a magnetic field each hyperfine state splits into a number of Zeeman sub-levels, each of which tunes differently in a magnetic field. It is thus extremely challenging, if not impossible, to use a Zeeman slower. In this regard a magneto-optical trap seems very challenging as well.

However, if one uses a molecule that has no fine-structure (singlet states), no orbital angular momentum (Σ states) and, no or only small hyperfine structure one can circumvent all these problems and, in principle, build a Zeeman slower and a magneto-optical trap.[1]

Let us summarise the conditions for a simple laser cooling scheme for diatomic molecules: a strong transition (excited state lifetime of < 100 ns), Franck-Condon factor of the main transition ($A(v' = 0) - X(v'' = 0)$) close to unity, no unpaired spin (singlet states), no orbital angular momentum (Σ ground state), no (or small) hyperfine structure. By browsing through the list provided by Di Rosa [71] we find NH, BH, AlH, AlF and AlCl to be suitable candidates. We can add ScF, CS and BeO to this list, although only very limited spectroscopic data is available for these molecules which makes them unattractive. The dipole moment of AlH is too small to be useful. So is the dipole moment of NH in its ground-state. The transitions for AlF and AlCl are both in the deep UV at 227.5 and 261.5 nm respectively. We do not have any lasers available to access these transitions. This leaves the ^{11}BH molecule whose A-X transition is at 433.4 nm. BH is a very simple molecule with only six electrons and thus has been subject of considerable theoretical and experimental interest since 1931 (see [320] and references therein). We can find all the transition frequencies needed in the literature [321, 322] and also some information on how to produce a molecular beam [320, 323].

It has a reasonable dipole moment of 1.3 D [324][2] and an upper state lifetime between 127 and 159 ns [325–328]. The ground state of BH is a $^1\Sigma^+$ and the first excited state is $^1\Pi$. For the specific case of a $A^1\Pi \leftarrow X^1\Sigma^+$ transition the parity selection rule that restricts the rotational branching is fulfilled for $J' = J'' = 1$. This is due to the orbital angular momentum in the excited state which leads to a Λ-doubling of the $J' = 1$ state into two closely spaced opposite parity states. Luh and Stwalley constructed RKR (Rydberg-Klein-Rees [103–105]) potentials using the spectroscopic data obtained by Johns and co-workers [321] and calculated the Franck-Condon factors [329]. A plot of the RKR potentials for the ground- and first electronically excited state is given in figure 7.1. The relevant Franck-Condon factors ($f_{v'v''}$) are $f_{00} = 0.9987$, $f_{01} = 0.27 \times 10^{-3}$, $f_{02} = 0.9827 \times 10^{-3}$ and $f_{03} = 0.2335 \times 10^{-7}$. This means that we could scatter 3700 photons with one repump laser and nearly 5×10^7 photons with two repump lasers. A schematic, showing the laser cooling scheme for BH is given in figure 7.2.

Although ground state BH has no spin or orbital angular momentum, the boron and hydrogen nuclei carry a nuclear spin of $I = 3/2$ and $I = 1/2$ respectively. The interaction of the nuclear spins with the rotation of the molecule leads to a small splitting of the $J'' = 1$ level that we plan to use for laser cooling. The interaction of the nuclear electric quadrupole moment of the boron nucleus with the electric field gradient (mainly produced by the electrons) leads

---

[1]Note that even for such a toy-model molecule a standard atomic MOT will not work because of dark Zeeman sub-levels in the ground-state. These dark levels have to be re-mixed by either modulating the polarisation of the laser beams or by applying a time-varying electric field, as was pointed out by Stuhl and co-workers [319].

[2]The effective electric dipole moment due to the large rotational constant $\mu_{\text{eff}} = -\mu(\partial E_{\text{stark}}/\partial E)$ obtainable in an electric field of $300 \, \text{kV cm}^{-1}$ is only 0.2 D. This is unfortunate and might not be enough to study strong dipole-dipole interactions at low temperatures. However, the simple structure of BH makes it very valuable as a toy-model molecule to explore new cooling techniques.
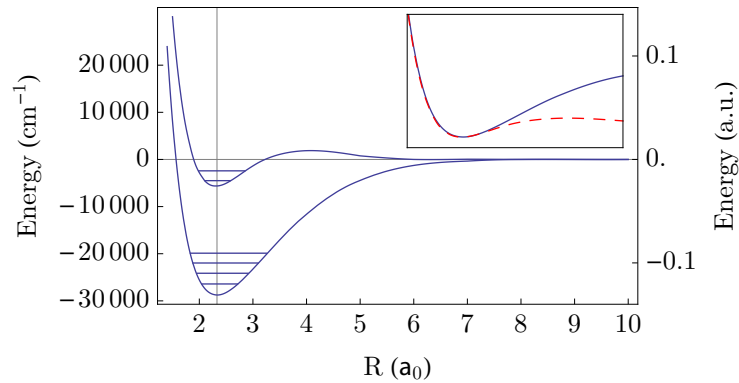
FIGURE 7.1: The binding energy as a function of the internuclear distance R for the two electronic states $X^1\Sigma^+$ and $A^1\Pi$ of BH [329]. The horizontal lines show vibrational energies. The vertical grid line shows the equilibrium internuclear distance $r_e = 2.33$ a_0 of the ground-state with a_0 the Bohr radius. The inset shows the two potentials on top of each other (ground state in blue, excited state as the red dashed line). This shows the striking similarity of the two potential curves which leads to a Franck-Condon factor near unity for the $v'' = 0 - v' = 0$ transition.
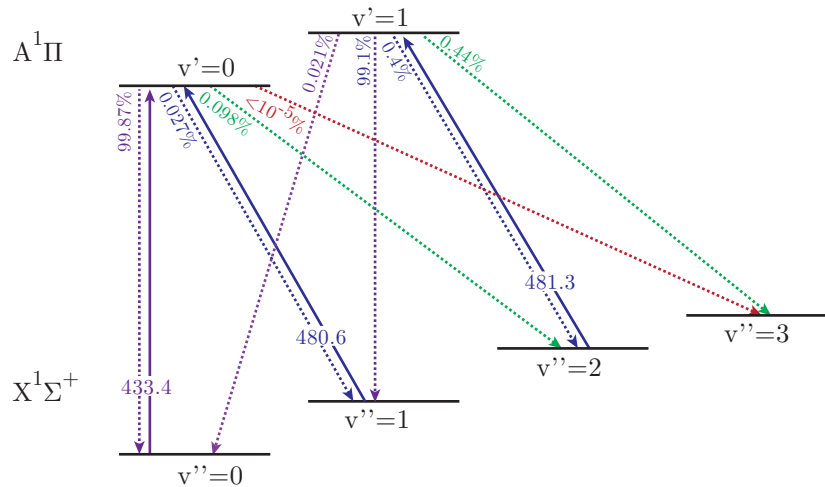

FIGURE 7.2: The laser cooling scheme for BH. The solid lines show the repump lasers with the wavelength in nano meters. The dashed lines show the possible decay channel from the excited state. The Franck-Condon factor, as calculated by Luh and Stwalley [329] for each decay route is given in percent.

to a small splitting of the $J'' = 1$ into three components $F_1 = 1/2$, $3/2$ and $5/2$. The size of the splitting is governed by the electric quadrupole coupling constant $eqQ = -6.6$ MHz [330] (calculated, see [107] for details). There is also a small contribution from the nuclear magnetic dipole moment of the boron nuclei to this splitting. In addition, the magnetic dipole moment associated with the hydrogen nuclear spin $I = 1/2$ leads to a small splitting of each F_1 level. This leads to a total of 6 levels with quantum numbers ($F = F_1 \pm 1/2$). All the splittings are similar to the natural linewidth of the A-X transition and thus can be addressed by a single laser frequency. A level diagram, showing the hyperfine splitting of the $J'' = 1$ state is shown in the lower panel of figure 7.3. The top panel shows the rotational lines of the A-X transitions relevant to our experiment.

The scattering rate for an ideal two-level system is given by [331]

$$R = \frac{I/I_{\text{sat}}}{1 + I/I_{\text{sat}} + 4(\delta/\Gamma)^2}\Gamma/2\,, \tag{7.1}$$

where I is the laser intensity, δ is the detuning from the resonance frequency, Γ is the spontaneous decay rate of the excited state and $I_{\text{sat}} = \pi hc\Gamma/(3\lambda^3)$ is the saturation intensity for the transition ($1.7\,\text{mW\,cm}^{-2}$). The fact that we do not have an ideal two-level system but need to close two vibrational leaks means that the maximum scattering rate of $\Gamma/2$ is reduced to an effective scattering rate $\Gamma_{\text{eff}} = \Gamma N_e/(N_e + N_g) \approx \frac{1}{3}\Gamma$, where N_e and N_g is the number of excited and ground states respectively.[3] The number of scattered photons we need to slow the molecules to rest is

$$n_{ph} = \frac{mv}{h/\lambda}\,, \tag{7.2}$$

which amounts to 5500 photons, assuming $m = 12$ amu, a speed of $420\,\text{m\,s}^{-1}$ (supersonic beam using krypton) and $\lambda = 433$ nm. By cooling the valve to $120\,\text{K}$ we can decrease the speed of the supersonic beam to about $260\,\text{m\,s}^{-1}$. Alternatively, by using xenon as a carrier gas and cooling the valve to $170\,\text{K}$ we can reduce the velocity to about $200\,\text{m\,s}^{-1}$. For a beam of BH molecules travelling at $200\,\text{m\,s}^{-1}$ we can reduce the number of photons we need to scatter to slow the molecules to rest to about 2600. This means that by closing the leakage to $v'' = 2$ only we should be able to slow the molecules to rest (assuming that we can trust the calculated Franck-Condon factors of Luh and Stwalley). Compared to CaF, SrF or YO, where at least 12 frequencies are needed, the laser cooling scheme for BH is very attractive. The largest possible deceleration force one can exert on a particle of mass m using scattering of resonant laser light is

$$F_{\max} = ma_{\max} = \hbar k\Gamma_{\text{eff}}. \tag{7.3}$$

---

[3] The total number of ground-state M_F levels we can address and transfer to the A state is 16. Assuming we are using two repump lasers we get 48 levels in total (3×16 for each vibrational state). The total number of excited states is 20 (the F_1 splitting is larger due to the orbital angular momentum in $^1\Pi$ state and we therefore can only connect to one F_1 level). This gives an effective scattering rate of $\Gamma_{\text{eff}} = (20/68)\Gamma \approx \Gamma/3$
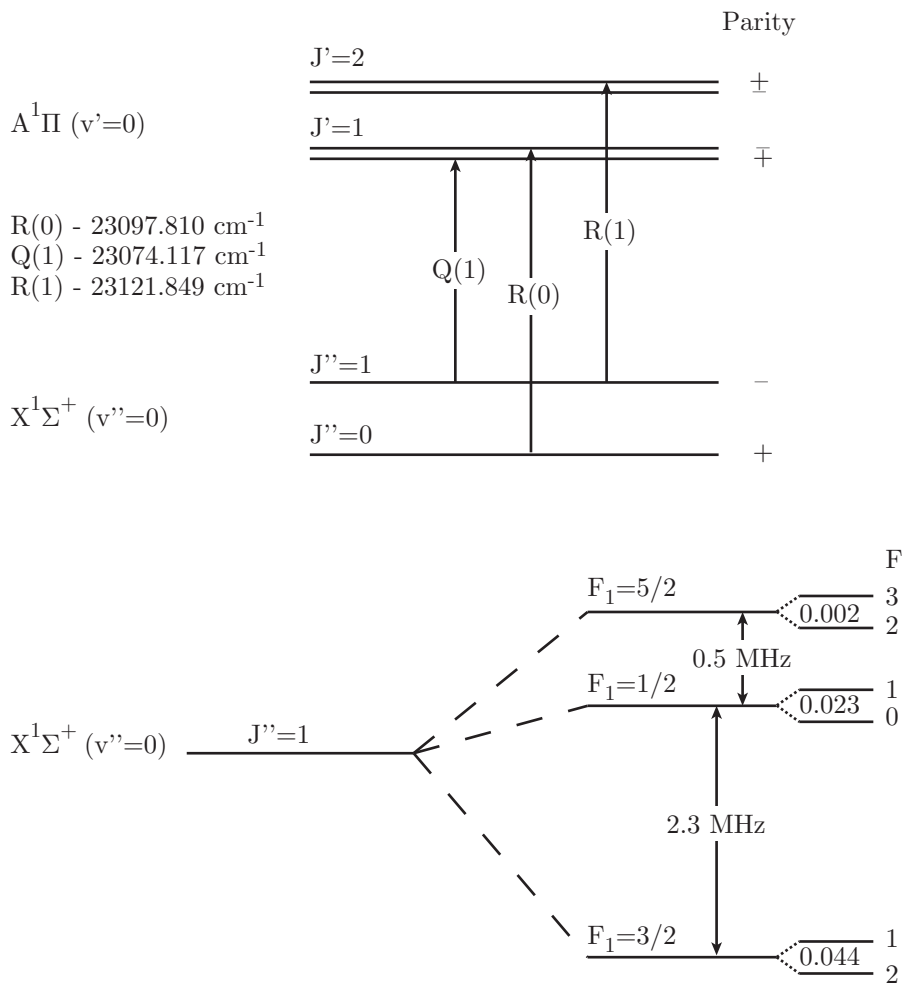
FIGURE 7.3: Top: The A-X $(0-0)$ transitions and frequencies of BH. Note that due to the Λ-doubling in the excited state the parity selection rule needed to restrict the rotational branching is met for $J' = J'' = 1$, i.e. for all Q transitions. Bottom: The splitting of the $J'' = 1$ level of the ground $X^1\Sigma^+(v'' = 0)$ level is due to the interaction of the nuclear moments of boron and hydrogen with the rotation of the molecule. The frequencies were calculated by Mike Tarbutt using the hyperfine constants provided in [330] (all frequencies are in MHz). The larger splitting is due to the electric quadrupole moment of the boron (^{11}B) nucleus ($I = 3/2$) which couples to the rotation and leads to three F_1 states. Each F_1 state is again split due to the interaction with the hydrogen nuclear spin ($I = 1/2$). Note that we get the analogous splitting in each $J' = 1$ parity state. The splitting is, however, much larger (≈ 100 MHz) due to the interaction of the nuclear spin with the orbital angular momentum.

For an effective scattering rate of $\Gamma_{\text{eff}} = \Gamma/3$, with $\Gamma = 2\pi \times 7\,\text{MHz}$ the time to slow the molecules to rest is given by $t_0 = v/a_{\max} = 2.3$ ms with the corresponding stopping distance $z_0 = v^2/(2a_{\max}) = 0.49$ m. Note that this is for the worst case scenario for a beam with a velocity $v = 420\ \text{m s}^{-1}$. If we can reduce the velocity to $200\,\text{m s}^{-1}$ the time to slow the molecules reduces to $t_0 = 1.1$ ms and the stopping distance to $z_0 = 0.11$ m.

It is also possible to use a Zeeman slower to keep the molecules in resonance with the laser beam as they slow down. The excited state is a $^1\Pi$ state and the interaction of the orbital angular momentum with an applied magnetic field thus large. According to [107] the Zeeman shift in the $J' = 1$ level is given by

$$\Delta E_{\text{Zeeman}} = g_L \mu_B B \frac{\Lambda^2}{J(J+1)} M_J, \qquad (7.4)$$

with $g_L = 1$, μ_B the Bohr magneton and B the applied magnetic field strength. Ignoring the small hyperfine splitting the $M_J = \pm 1$ levels thus shift by $7\,\text{GHz T}^{-1}$. Therefore, at a field of $0.14\,\text{T}$, the Zeeman shift is equal to the Doppler shift of molecules moving at $420\,\text{m s}^{-1}$. The molecular g-factor of the ground electronic state is close to zero ($\Lambda = 0$). A small Zeeman shift comes from the nuclear magnetic moments of boron and hydrogen, but this is almost 2000 times smaller than the Zeeman shift of the excited state.

The prospect of laser cooling a supersonic beam using a Zeeman slower and a magneto-optical trap to either the Doppler temperature $T_D = h\Gamma/(2k_B) = 30$ µK or even to the recoil temperature $T_r = (h/\lambda)^2/(2mk_B) = 4$ µK seemed so appealing to us that we started to investigate molecular beam sources for BH molecules.


7.2 A Molecular Beam of BH Molecules

BH molecules were first produced by Lochte-Holtgreven and van der Vleugel in 1931. They used a discharge tube filled with BCl_3 and H_2 and could record the very first spectra of the A-X transition [332]. This production technique was used until Bauer, Herzberg and Johns produced BH via flash-photolysis of a parent molecule in 1964. They used borine carbonyl (H_3BCO) as a precursor and recorded the first absorption spectra of BH [333]. Bauer and colleagues prepared the borine carbonyl by mixing one part of diborane B_2H_6 with three parts of CO in a glass bulb: "the bulb was allowed to stand for one or two weeks at room temperature to allow the equilibrium to be established" [333]. Johns, Grimm and Porter used flash-photolysis of borine carbonyl and diborane in a gas cell [321]. Dufayard and Nedelec produced BH molecules by an rf discharge of 10% diborane in helium in a spectroscopy cell [327]. Gustafsson and Rittby bombarded diborane with high energy electrons in a static gas cell [328] and Pianalto and colleagues used a microwave discharge through a mixture of diborane and helium in a quartz tube [334]. Douglass, Nelson and Rice produced BH by excimer photolysis (193 nm, 20 mJ) of

borine carbonyl in a reaction cell [325]. Fernando and Bernath simply used a hollow cathode discharge. The hollow cathode was made of B_4C and a discharge through argon gas produced BH molecules even without any H_2 added to the argon [322]. Gilkison, Viteri and Grant were the first to produce a supersonic beam of BH molecules by photodissociation of diborane in 2004. They seeded 5% diborane in 3 bar of H_2 and expanded it through a solenoid valve. The output of an excimer laser (193 nm, 50 mJ) was focused into the supersonic expansion right in front of the nozzle exit [335]. This is exactly the same method we used for producing CH, apart from the different precursor. They also found that a significant flux could be produced via dc-discharge of diborane [336]. They used both a continuous discharge nozzle and a pulsed dc-dielectric discharge similar to the one used by Even and Lavie [123].

Diborane is extremely flammable, forms explosive mixtures in air, can ignite spontaneously at room temperature, and is highly toxic. Short term exposure causes lung congestion (it hydrolyses to boric acid), burns, kidney and liver damage and ultimately death (LC50 (rat): 40 ppm). Therefore, it is not a pleasant precursor to work with. Although it is straightforward to synthesize, we preferred to order it diluted (1%) in argon in a gas bottle.[4] Diborane is unstable and decomposes to produce hydrogen and higher boranes, so its shelf life is limited. Elaborate safety precautions must also be taken. After all the safety equipment had been installed, we could finally try to create a molecular beam.

The single photon absorption cross section of diborane at 193 nm is only 4.4×10^{-20} cm^2 which is about 100 times smaller compared to bromoform [337, 338]. The absorption cross-section decreases exponentially to zero for longer wavelengths [337, 339]. Therefore, it is necessary to operate at the shortest wavelength possible. The quantum efficiency for the reaction

$$B_2H_6 + h\nu \rightarrow 2(BH_3)^* \tag{7.5}$$
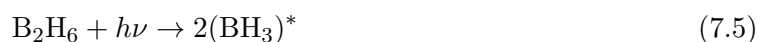
has been measured to be 0.06 [337]. It may, in fact, be higher than this, because fast secondary reactions of the excited BH_3 with other photolysis products to higher boranes prevents the measurement of the primary BH_3 products [340]. The secondary dissociation

$$(BH_3)^* \rightarrow BH + H_2 \tag{7.6}$$

$$(BH_3)^* + h\nu \rightarrow BH + H_2 \tag{7.7}$$
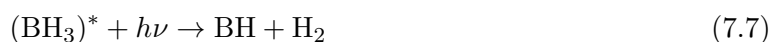
are likely reaction paths for the production of BH. The small absorption cross-section means that we need a high intensity to saturate the BH production. One advantage is that diborane is light and a gas which prevents clustering in the supersonic expansion. In combination with the fact that there might be a single photon reaction path via excited BH_3, the dissociation of diborane is an attractive way for to make a highly intense molecular beam of BH.

After little optimisation of the source parameters we were able to detect our first BH signal

---

[4]Note that a higher concentration might lead to a more intense molecular beam, but the rather restrictive health and safety regulations in the UK limits us to use a concentration below 1%.
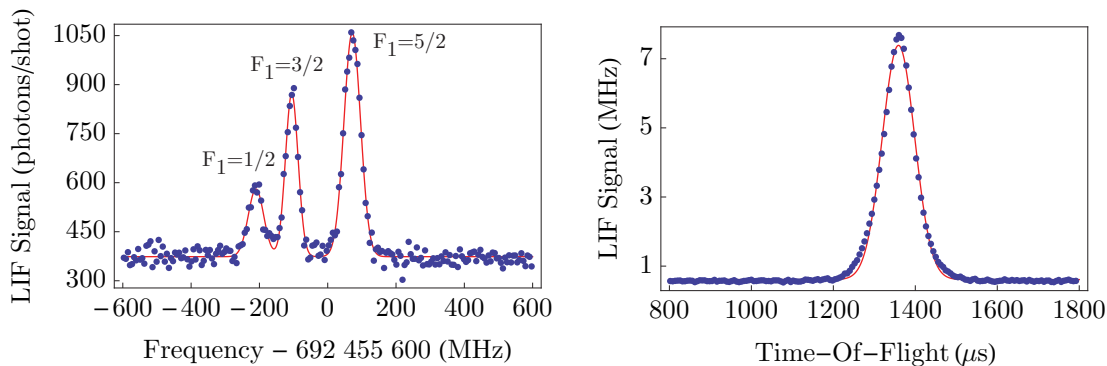
FIGURE 7.4: Left: A frequency scan over the $R(0)$ line of the $A^1\Pi(v' = 0) \leftarrow X^1\Sigma^+(v'' = 0)$ transition of BH. We can clearly identify the three hyperfine components corresponding to the $F_1 = 3/2$, $1/2$ and $5/2$ states of the $A^1\Pi$ excited state. We fit three Gaussian profiles (red line) to the data (blue dots). The fit yields a FWHM of 53, 44 and 57 MHz with relative amplitudes of approximately $1/6$, $2/6$ and $3/6$. Right: Time-of-flight profile of the molecular beam. We fit a Gaussian profile (red) to the data (blue dots). The central arrival time of 1360 µs corresponds to a velocity of $570\,\mathrm{m\,s^{-1}}$ and the FWHM of 93 µs to a transverse temperature of 0.4 K

using a focused excimer beam operated at 193 nm with a pulse energy of 100 mJ. A spectrum of the R_0 line near 433.4 nm (692.454 923 THz) is shown in figure 7.4. The intensity of the beam source is similar to that of the CH source. However, to convert the number of photons per shot into a number of molecules we would need to measure the signal as a function of the probe laser intensity. For the beam presented in figure 7.4 the field plates from the CH measurement were still in place. This restricts the solid angle of the molecular beam and thus reduces the molecular flux we measure by about a factor of three. Assuming similar parameters as for CH we can assume a molecular flux of $3 \times 10^9\,\mathrm{sr^{-1}}$ per pulse.

As pointed out in the introduction to this chapter, a simple scheme for laser cooling molecules requires the lower state of the quasi-cycling transition to be a rotationally excited state. The rotational constant of BH in the electronic ground-state is $B = 12.021\,\mathrm{cm^{-1}}$ (360 GHz) which corresponds to a temperature of 17 K [324]. The first rotationally excited state lies approximately $2B$ above the ground state. This means that for our cold supersonic beam which has a temperature of 0.4 K, we expect very little population in that state. We therefore need to transfer population from the ground-state into the first rotationally excited state by driving the mm-wave transition. The amplifier-multiplier chain we used to drive population from the $J = 1/2$ to the $J = 3/2$ state in CH can provide the necessary radiation.

The setup we use to drive and measure this transition is exactly the same as for the measurement of the lowest mm-wave transition in CH, presented in chapter 5. The mm-wave beam is collimated with a teflon lens, enters the vacuum chamber through a quartz window and intersects the molecular beam at right angle. The interaction region is shielded from ambient magnetic fields with a single layer mu-metal shield. We lock the detection laser to the $F_1 = 5/2$ peak of the $R(0)$ line of the $A^1\Pi(v' = 0) \leftarrow X^1\Sigma^+(v'' = 0)$ transition and record the fluorescence as a function of the mm-wave frequency. Such a depletion spectrum is shown in figure 7.5.
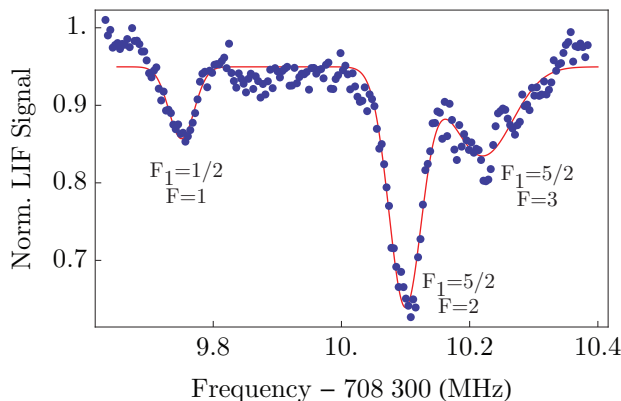
FIGURE 7.5: Spectrum of the $J = 0 - J = 1$ rotational transition of BH. We lock the probe laser to the $R(0)$ line of the $A^1\Pi(v' = 0) \leftarrow X^1\Sigma^+(v'' = 0)$ transition (to the largest $F_1 = 5/2$ peak). We then record the fluorescence as the frequency of the mm-waves is scanned. The structure is part of the hyperfine structure of the rotationally excited (J=1) state. When the mm-waves are resonant with the molecules, they get pumped into the rotationally excited state ($J'' = 1$) and the fluorescence in the probe region decreases. This way we can transfer nearly 40% of the ground-state population into the first, rotationally excited state. We fit three Gaussian profiles (red line) to the data (blue dots).

We fit three Gaussian profiles (red line) to the data (blue dots). The fit yields three resonance frequencies at 708309751 ± 37 kHz, 708310100 ± 15 kHz and 708310220 ± 54 kHz. They correspond to excitation of the $(J'' = 1, F_1 = 5/2, F = 2, 3)$, $(J'' = 1, F_1 = 1/2, F = 1)$ and $(J'' = 1, F_1 = 1/2, F = 0)$ states respectively. Comparing this to the calculated level diagram in figure 7.3 we observe a small discrepancy. The $F_1 = 5/2 - F_1 = 5/2$ splitting is smaller than expected, and the splitting of the $F_1 = 5/2$ state is larger than expected. This means that the hyperfine constants calculated by Sauer and colleagues [330] are not accurate enough to predict the small hyperfine structure of BH to this level of precision. With the precise measurement of this rotational transition we can measure these molecular constants of BH for the first time and to very high accuracy. Figure 7.5 also shows that we can transfer nearly 40% of the initial ground-state population into the $J'' = 1$ rotationally excited state. Similar to the CH measurement we are limited to a transfer efficiency of 40% due to the low output power of the AMC. Unfortunately the output power drops to a minimum of about $1\,\mu W$ at exactly the frequency we need. We have now replaced the quartz window with a teflon window which should reduce the Fresnel losses by about 15-20% percent.

7.3 Measuring the Franck-Condon Factors of the A-X Transition

We cannot expect the Franck-Condon factors Luh and Stwalley calculated to be accurate on the 10^{-4} level. Such high accuracy is necessary to determine the number of repump lasers
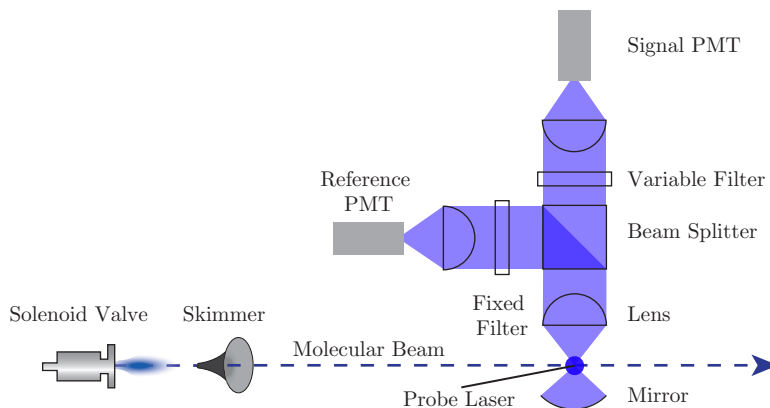
FIGURE 7.6: The setup we use to measure the Franck-Condon factors of the $A^1\Pi \to X^1\Sigma^+$ transition in BH. The molecules are excited with a resonant laser beam. The fluorescence light emitted by the molecules is composed of different spectral components with relative intensities determined by the Franck-Condon factor. To analyse the relative magnitude of each spectral component, i.e. to measure the Franck-Condon factors, we use various bandpass filters in front of the photomultiplier tube (Signal PMT). We use a beamsplitter to direct part of the fluorescence light onto a reference PMT which allows us to normalise the signal for each molecular beam pulse. The measurement is insensitive to variations in the molecular beam or laser intensity.

needed for laser cooling. Douglass, Nelson and Rice measured the ratio of the Einstein emission coefficients $A_{01}/A_{00} = 0.0051 \pm 0.0007$ which gives rise to a leakage to $v'' = 1$ of about 0.5%. This means that even with one laser it should be possible to scatter about 200 photons. As we can infer from the calculated Franck-Condon factors by Luh and Stwalley, it seems that the leakage to $v'' = 2$ is larger than the leakage to $v'' = 1$. To verify this and to make sure which and how many repump lasers we need we are currently measuring the Franck-Condon factors to an accuracy of better than 10^{-4}.

Recently, the Franck-Condon factors of the YbF molecule have been measured in our group [341]. We use a very similar technique to measure the Franck-Condon factors of BH. A sketch of the setup is shown figure 7.6. The fluorescence emitted by the molecules is collimated and directed onto a beamsplitter cube which divides it into two components. Each component is focused, spatially filtered and detected by a photomultiplier tube (PMT). A bandpass filter (FWHM of 10 nm) centered at 430 nm in front of the reference PMT is used to reduce ambient background light. We use bandpass filters centred at 430 nm, 480 nm, 530 nm and 600 nm in the signal arm to analyse the different spectral components of the $A^1\Pi(v' = 0) \to X^1\Sigma^+(v'' = 1, 2, 3)$ fluorescence light. We measure the transmission through all optical elements and calibrate the signal PMT at each wavelength. This allows us to measure the relative sensitivity of our detection system at each wavelength. The probe laser is modulated (on/off) between subsequent beam pulses to subtract any remaining background light. Each filter is used in random order and orientation. By using the ratio of the signal and reference the measurement is immune to fluctuations in the molecular beam or laser intensity. Preliminary data runs show that we can reach a relative sensitivity of 10^{-4} after 30 minutes of averaging. We are still taking the final

data sets at the moment but preliminary data reveals that one repump laser will not be enough to slow BH to rest. This is unfortunate, but with only three frequencies in total, the prospect of using a Zeeman slower and to create a magneto-optical trap makes BH still a very interesting candidate for laser cooling.

7.4   Conclusion and Outlook

In this chapter the prospect for direct laser cooling of BH molecules has been discussed. The highly diagonal Franck-Condon factors and the absence of large hyperfine structure makes it possible to laser cool BH with minimal experimental effort. The ground electronic state is insensitive to magnetic fields, whereas the excited state can be tuned using modest magnetic fields. This allows us to use a Zeeman slower and build a magneto-optical trap for BH. For other molecules such as SrF, CaF or YO the large number of levels involved in the cooling process precludes such a straight-forward approach. With a maximum of three laser frequencies we will be able to slow and cool BH molecules to the Doppler temperature of $30\,\mu K$ or even to the recoil temperature of $4\,\mu K$. The large rotational constant of $360\,GHz$ means that we can not fully polarise the molecules in typical electric fields obtainable in the lab ($\mu_{\mathrm{eff}} = 0.2$ D in $300\,kV\,cm^{-1}$). This might be to small to study strong dipole-dipole interactions at low temperatures. However, the possibility to laser cool molecules from a supersonic beam to such low temperatures and the prospects of building a magneto-optical trap were so appealing to us that we started to investigate ways to create BH. It turns out that both production and detection techniques are very similar to what we were using for CH. Analogous to CH we could produce BH via photo-dissociation of a precursor molecule (diborane). This allowed us to realise a supersonic beam of BH molecules in relatively short time.

A necessary precondition for laser cooling is that the lower state of the cooling cycle is a rotationally excited state. Due to the large rotational constant and the low temperature of the molecular beam we could not detect any population in the first rotationally excited state $J'' = 1$. However, we could demonstrate the coherent population transfer from the ground to the first rotationally excited state using resonant mm-waves. Finally, the setup we use to measure the Franck-Condon factors of BH to determine the exact number of repump lasers has been presented.

Once the Franck-Condon measurement is completed we will start investigating cycling on the $Q(1)$ transition. Without repump lasers we should already be able to scatter on the order of 100 photons. To prevent optical pumping into dark M_F levels we will need to add a magnetic field which re-mixes these dark Zeeman levels back into the cooling cycle. At the same time we can develop the laser system necessary for closing the vibrational leaks. Once we can lock all lasers to the right frequencies we aim to counter-propagate the laser beams with the molecular beam to demonstrate laser slowing. This will keep us busy until the construction of the Zeeman slower

will be completed. Once we have achieved laser-slowing we can capture the BH molecules in a magneto-optical trap. This will allow to cool the molecules to the recoil temperature of $4\,\mu K$. This will also be the ideal starting point to explore new sub-Doppler cooling schemes for polar molecules. We could investigate cavity cooling, single-photon cooling or electro-optical cooling. Furthermore, we can transfer the molecules into their absolute ground state and confine them in an optical dipole trap. We can then initiate forced evaporative cooling which could allow us to reach quantum degeneracy.

Chapter 8

Conclusions and Future Directions

> *[...] Then felt I like some watcher of the skies*
> *When a new planet swims into his ken;*
> *Or like stout Cortez when with eagle eyes*
> *He star'd at the Pacific - and all his men*
> *Look'd at each other with a wild surmise -*
> *Silent, upon a peak in Darien.*
>
> John Keats

In this thesis I described a number of advances in cold molecule physics. The lowest-lying Λ-doublet transitions of CH are exceptionally sensitive to variations in fundamental constants such as the fine-structure constant α or the electron-to-proton mass ratio μ. To be able to use CH as a sensitive probe for such variations new laboratory measurements of these transitions were needed. We therefore investigated the optimum method for producing an intense, pulsed, supersonic beam of cold CH molecules. We have investigated four different sources for CH based on a dc discharge, dc discharge-reaction, laser ablation and photodissociation. The photodissociation of bromoform yielded an intense beam with 3.5×10^9 CH molecules per steradian per shot in a single quantum state with an exceptional shot-to-shot stability. This beam has a translational temperature of $400\,\text{mK}$ and a velocity that is tuneable between 400 and $1800\,\text{m s}^{-1}$ and is thus ideally suited for high resolution spectroscopy experiments.

Using a novel spectroscopic method we could measure the lowest-lying Λ-doublet transitions of the $(F_2, J = 1/2)$ and $(F_1, J = 3/2)$ states of CH to unprecedented accuracy. By comparing these new laboratory measurements to radio-astronomical observations, we could test the hypothesis that fundamental constant may differ between the high and low density environments of the Earth and the interstellar medium of the Milky Way. We found no variation and set upper limits of $|\Delta\alpha/\alpha| < 2.1 \times 10^{-7}$ and $|\Delta\mu/\mu| < 4.3 \times 10^{-7}$.

We could also measure the lowest mm-wave transition in CH to unprecedented accuracy.

These transitions are also sensitive to variations in fundamental constants.

With new dedicated astronomical measurements, especially of the excited $F_1, J = 3/2$ Λ-doublet and at high red-shift it will become possible to measure temporal and/or spatial drifts in fundamental constants with exceptional sensitivity, free from common systematic errors. The new laboratory measurements are also of great importance to astronomers who use CH as a tracer for other atoms or molecules and to reveal the gas and reaction dynamics in such clouds. With our new measurements we could already remove the systematic velocity offset between different hyperfine components found by Sakai and co-workers [226].

I have also described the development of a novel type of trap for polar molecules. Trapping the molecules is essential for further cooling to ultracold temperatures. The trap uses a high intensity microwave field in a Fabry-Pérot resonator which will enable us to create a very deep trap for molecules in their absolute ground state. A prototype resonator allowed us to determine the optimum geometry and coupling conditions to maximise the electric field inside the resonator. The final ultra-high vacuum compatible high power version is currently being assembled in our workshop and will be tested with ultracold lithium atoms. The trap is applicable to a large variety of polar molecules, straightforward to load and an ideal means to accumulate molecules. Once the molecules are trapped further cooling, either sympathetically via collisions with ultracold atoms, evaporation, cavity cooling or electro-optical cooling will be possible.

Finally, I presented the development of a cold supersonic beam of BH molecules. This molecule appears to be particularly well-suited to direct laser cooling due to its favourable rotational structure and Franck-Condon factors. The laser cooling concept is described, and a first spectroscopic investigation of the relevant molecular structure is presented. We are currently measuring the Franck-Condon factors to determine the exact number of re-pump lasers needed for efficient laser-cooling. We will then use a Zeeman slower to slow the molecules from a supersonic beam and add magnetic field coils to investigate a magneto-optical trap for polar BH molecules.

Bibliography

[1] D. Bernoulli. *Hydrodynamics*. Strassburg: Johann Reinhold Dulsecker, 1738 (see p. 15).

[2] R. Boyle. *New Experiments Physico-Mechanical Touching the Spring of the Air, and its Effects, Made, for the most part, in a New Pneumatical Engine*. London: Miles Flesher, 1682 (see p. 16).

[3] J. Dalton. *A new system of chemical philosophy*. Manchester, 1808 (see p. 16).

[4] M. Gay-Lussac. "Memoir sur la combinaison des substances gazeuses, les unes avec les autres". In: *Mémoires de la Société d'Arcueil* 2 (1809), pp. 207–234 (see p. 16).

[5] A. C. Avogadro. "Essai d'une manière de déterminer les masses relatives des molécules élémentaires des corps, et les proportions selon lesquelles elles entrent dans ces combinaisons". In: *Journal de Physique, de Chimie et d'Histoire Naturelle* 73 (1811), pp. 58–76 (see p. 16).

[6] J. Herapath. "On the causes, laws and phenomena of heat, gases, gravitation etc." In: *Annals of Philosophy* 9 (1821), pp. 273–293 (see p. 17).

[7] S. G. Brush. *The kind of motion we call heat*. North-Holland Publishing Company, 1976 (see p. 18).

[8] E. Garber, S. G. Brush, and C. W. F. Everitt, eds. *Maxwell on molecules and gases*. Cambridge: The M.I.T Press, 1986 (see p. 18).

[9] P. E. A. von Lenard. "Nobel Lecture: on cathode rays". In: *Nobelprize.org* (1906) (see p. 21).

[10] J. J. Thomson. "The Nobel Prize in Physics 1906". In: *Nobelprize.org* (1906) (see p. 21).

[11] A. Einstein. *Autobiographical Notes*. Ed. by P. A. Schlipp. Tudor Publishing Company, 1949, p. 47 (see p. 21).

[12] J. Mehra and H. Rechenberg. *The Historic Development of Quantum Theory*. New York: Springer, 1982 (see pp. 21, 22, 24).

[13] A. Einstein. "Über einen die Erzeugung und Verwandlung des Lichtes betreffenden heuristischen Gesichtspunkt". In: *Annalen der Physik* 17.6 (1905), pp. 132–148 (see pp. 21, 22).

[14] B. Friedrich and D. Herschbach. "Stern and Gerlach: How a Bad Cigar Helped Reorient Atomic Physics". In: *Physics Today* 56.12 (2003), p. 53 (see pp. 23, 24).

[15] N. F. Ramsey. "Molecular beams: our legacy from Otto Stern". In: *Zeitschrift für Physik D Atoms, Molecules and Clusters* 10.2-3 (1988), pp. 121–125 (see p. 24).

[16] M. Arndt et al. "Waveparticle duality of C60 molecules". In: *Nature* 401.6754 (Oct. 1999), pp. 680–682 (see p. 25).

[17] A. D. Cronin and D. E. Pritchard. "Optics and interferometry with atoms and molecules". In: *Reviews of Modern Physics* 81.3 (July 2009), pp. 1051–1129 (see pp. 25, 29).

[18] I. I. Rabi and R. F. Code. "Stories from the early days of quantum mechanics". In: *Physics Today* 59.8 (2006), p. 36 (see p. 26).

[19] P. Kusch. "Nobel lecture: the magnetic moment of the electron". In: *Nobelprize.org* (1955) (see p. 27).

[20] W. E. Lamb. "Nobel lecture: fine structure of the hydrogen atom". In: *Nobelprize.org* (1955) (see p. 27).

[21] A. Kastler. "Nobel Lecture: Optical Methods for Studying Hertzian Resonance". In: *Nobelprize.org* (1966) (see p. 27).

[22] J. Gordon, H. Zeiger, and C. Townes. "The maser–new type of microwave amplifier, frequency standard, and spectrometer". In: *Physical Review* 99.4 (1955), pp. 1264–1274 (see p. 28).

[23] N. G. Basov. "Nobel lecture: semiconductor lasers". In: *Nobelprize.org* (1964) (see p. 28).

[24] A. M. Pokhorov. "Nobel lecture: quantum electronics". In: *Nobelprize.org* (1964) (see p. 28).

[25] S. Chu. "Cold atoms and quantum control." In: *Nature* 416.6877 (2002), pp. 206–10 (see p. 29).

[26] I. Bloch, J. Dalibard, and S. Nascimbène. "Quantum simulations with ultracold quantum gases". In: *Nature Physics* 8.4 (2012), pp. 267–276 (see p. 29).

[27] S. Korenblit et al. "Quantum simulation of spin models on an arbitrary lattice with trapped ions". In: *New Journal of Physics* 14.9 (Sept. 2012), p. 095024 (see p. 29).

[28] D. J. Wineland. "Nobel lecture: superposition, entanglement, and raising Schrödinger's cat". In: *Reviews of Modern Physics* 85.3 (July 2013), pp. 1103–1114 (see p. 29).

[29] S. Haroche. "Nobel lecture: controlling photons in a box and exploring the quantum to classical boundary". In: *Reviews of Modern Physics* 85.3 (July 2013), pp. 1083–1102 (see p. 29).

[30] H. J. Kimble. "The quantum internet." In: *Nature* 453 (June 2008), pp. 1023–30 (see p. 29).

[31] M. Aspelmeyer, T. J. Kippenberg, and F. Marquardt. "Cavity optomechanics". In: *arXiv e-prints* (2013). arXiv:`1306.0912v1` (see p. 30).

[32] D. Hanneke, S. Fogwell, and G. Gabrielse. "New measurement of the electron magnetic moment and the fine structure constant". In: *Physical Review Letters* 100.12 (Mar. 2008) (see p. 30).

[33] C. W. Chou et al. "Frequency comparison of two high-accuracy Al^+ optical clocks". In: *Physical Review Letters* 104.7 (Feb. 2010), pp. 1–4 (see p. 30).

[34] T. Lee and C. Yang. "Question of parity conservation in weak interactions". In: *Physical Review* 104.1 (Oct. 1956), pp. 254–258 (see p. 31).

[35] C. S. Wu. "Experimental test of parity conservation in beta decay". In: *Physical Review* 105.4 (Feb. 1957), pp. 1413–1415 (see p. 31).

[36] J. Schwinger. "The theory of quantized fields. I". In: *Physical Review* 82.6 (June 1951), pp. 914–927 (see p. 31).

[37] A. D. Sakharov. "Violation of CP invariance, C asymmetry, and baryon asymmetry of the universe". In: *Journal of Experimental and Theoretical Physics Letters* 5 (1967), p. 24 (see p. 31).

[38] E. Purcell and N. Ramsey. "On the possibility of electric dipole moments for elementary particles and nuclei". In: *Physical Review* 78.6 (June 1950), pp. 807–807 (see p. 31).

[39] C. A. Baker et al. "Improved Experimental Limit on the Electric Dipole Moment of the Neutron". In: *Physical Review Letters* 97.13 (Sept. 2006), pp. 1–4 (see p. 32).

[40] L. I. Schiff. "Measurability of nuclear electric dipole moments". In: *Physical Review* 132.5 (Dec. 1963), pp. 2194–2200 (see p. 32).

[41] M. Romalis et al. "New limit on the permanent electric dipole moment of $^{1}99Hg$". In: *Physical Review Letters* 86.12 (Mar. 2001), pp. 2505–2508 (see p. 32).

[42] E. A. Hinds. "Testing time reversal symmetry using molecules". In: *Physica Scripta* 34 (1997) (see p. 33).

[43] B. Regan et al. "New limit on the electron electric dipole moment". In: *Physical Review Letters* 88.7 (Feb. 2002), pp. 18–21 (see p. 33).

[44] J. J. Hudson et al. "Improved measurement of the shape of the electron." In: *Nature* 473 (May 2011), pp. 493–6 (see p. 33).

[45] B. Darquié et al. "Progress toward the first observation of parity violation in chiral molecules by high-resolution laser spectroscopy." In: *Chirality* 22.10 (Nov. 2010), pp. 870–84 (see p. 34).

[46] J-P. Uzan. "Varying constants, gravitation and cosmology". In: *Living Reviews in Relativity* 14 (2011) (see pp. 34, 112, 116).

[47] P. A. M. Dirac. "The cosmological constants". In: *Nature* 139 (1937), p. 323 (see p. 34).

[48] E. Teller. "On the change of physical constants". In: *Physical Review* 73.7 (1948), pp. 801–802 (see p. 35).

[49] B. Ratra and P. Peebles. "Cosmological consequences of a rolling homogeneous scalar field". In: *Physical Review D* 37.12 (June 1988), pp. 3406–3427 (see p. 35).

[50] S. Carroll. "Quintessence and the rest of the world: suppressing long-range interactions". In: *Physical Review Letters* 81.15 (Oct. 1998), pp. 3067–3070 (see p. 35).

[51] J. Khoury and A. Weltman. "Chameleon fields: awaiting surprises for tests of gravity in space". In: *Physical Review Letters* 93.17 (Oct. 2004), p. 171104 (see pp. 36, 113).

[52] R. I. Thompson. "Constraints on quintessence and new physics from fundamental constants". In: *Monthly Notices of the Royal Astronomical Society: Letters* 422.1 (May 2012), pp. L67–L71 (see p. 36).

[53] T. Rosenband et al. "Frequency ratio of Al^{+} and Hg^{+} single-ion optical clocks; metrology at the 17th decimal place." In: *Science* 319 (Mar. 2008), pp. 1808–12 (see pp. 36, 115).

[54] S. Blatt et al. "New Limits on coupling of fundamental constants to gravity using $^{8}7Sr$ optical lattice clocks". In: *Physical Review Letters* 100.14 (Apr. 2008), pp. 2–5 (see pp. 36, 115).

[55] H. L. Bethlem et al. "Prospects for precision measurements on ammonia molecules in a fountain". In: *The European Physical Journal Special Topics* 163.1 (Nov. 2008), pp. 55–69 (see pp. 37, 176).

[56] R. V. Krems. "Cold controlled chemistry." In: *Physical Chemistry Chemical Physics* 10.28 (July 2008), pp. 4079–92 (see p. 37).

[57] N. Balakrishnan. "Chemistry at ultracold temperatures". In: *Chemical Physics Letters* 341.5-6 (June 2001), pp. 652–656 (see p. 37).

[58] M. H. Anderson et al. "Observation of Bose-Einstein condensation in a dilute atomic vapor." In: *Science* 269 (July 1995), pp. 198–201 (see pp. 37, 176).

[59] B. DeMarco and D. S. Jin. "Onset of Fermi degeneracy in a trapped atomic gas". In: *Science* 285 (Sept. 1999), pp. 1703–1706 (see pp. 37, 176).

[60] A. Griesmaier et al. "Bose-Einstein condensation of chromium". In: *Physical Review Letters* 94.16 (Apr. 2005), p. 160401 (see p. 38).

[61] K. Aikawa et al. "Bose-Einstein condensation of erbium". In: *Physical Review Letters* 108.21 (May 2012), p. 210401 (see p. 38).

[62] M. Lu, N. Q. Burdick, and B. L. Lev. "Quantum degenerate dipolar Fermi gas". In: *Physical Review Letters* 108.21 (May 2012), p. 215301 (see p. 38).

[63] L. D. Carr et al. "Cold and ultracold molecules: science, technology and applications". In: *New Journal of Physics* 11.5 (May 2009), p. 055049 (see pp. 38, 40).

[64] R. P. Feynman. "There's plenty of room at the bottom". In: *Caltech Engineering and Science* 23.5 (1960), pp. 22–36 (see p. 38).

[65] R. P. Feynman. "Simulating physics with computers". In: *International Journal of Theoretical Physics* 21.6-7 (June 1982), pp. 467–488 (see p. 39).

[66] J. I. Cirac and P. Zoller. "Goals and opportunities in quantum simulation". In: *Nature Physics* 8.4 (Apr. 2012), pp. 264–266 (see p. 39).

[67] M. Greiner et al. "Collapse and revival of the matter wave field of a Bose-Einstein condensate." In: *Nature* 419 (Sept. 2002), pp. 51–4 (see pp. 39, 176).

[68] I. Bloch and W. Zwerger. "Many-body physics with ultracold gases". In: *Reviews of Modern Physics* 80.3 (July 2008), pp. 885–964 (see p. 39).

[69] J. Simon et al. "Quantum simulation of antiferromagnetic spin chains in an optical lattice." In: *Nature* 472 (Apr. 2011), pp. 307–12 (see p. 39).

[70] A. Micheli, G. K. Brennen, and P. Zoller. "A toolbox for lattice-spin models with polar molecules". In: *Nature Physics* 2.5 (Apr. 2006), pp. 341–347 (see p. 40).

[71] M. D. Di Rosa. "Laser-cooling molecules". In: *The European Physical Journal D* 31.2 (Nov. 2004), pp. 395–402 (see pp. 40, 176, 217, 219).

[72] E. S. Shuman, J. F. Barry, and D. Demille. "Laser cooling of a diatomic molecule." In: *Nature* 467 (Oct. 2010), pp. 820–3 (see pp. 40, 176, 214, 218).

[73] P. Domokos and H. Ritsch. "Collective cooling and self-organization of atoms in a cavity". In: *Physical Review Letters* 89.25 (Dec. 2002), pp. 1–4 (see p. 40).

[74] G. Morigi et al. "Cavity cooling of internal molecular motion". In: *Physical Review Letters* 99.7 (Aug. 2007), pp. 1–4 (see p. 40).

[75] B. Lev et al. "Prospects for the cavity-assisted laser cooling of molecules". In: *Physical Review A* 77.2 (Feb. 2008), pp. 1–13 (see p. 40).

[76] J. D. Weinstein et al. "Magnetic trapping of calcium monohydride molecules at millikelvin temperatures". In: *Nature* 395 (1998), pp. 148–150 (see pp. 41, 176).

[77] H. Bethlem, G. Berden, and G. Meijer. "Decelerating Neutral Dipolar Molecules". In: *Physical Review Letters* 83.8 (Aug. 1999), pp. 1558–1561 (see p. 41).

[78] S. Hogan et al. "Zeeman deceleration of H and D". In: *Physical Review A* 76.2 (Aug. 2007), pp. 1–11 (see p. 41).

[79] E. Narevicius et al. "Stopping supersonic oxygen with a series of pulsed electromagnetic coils: A molecular coilgun". In: *Physical Review A* 77.5 (May 2008), pp. 1–4 (see p. 41).

[80] R. Fulton et al. "Controlling the motion of cold molecules with deep periodic optical potentials". In: *Nature Physics* 2.7 (June 2006), pp. 465–468 (see p. 41).

[81] M. Lemeshko et al. "Manipulation of molecules with electromagnetic fields". In: *arXiv e-prints* (2013), pp. 1–39. arXiv:1306.0912v1 (see pp. 41, 176).

[82] S. Rangwala et al. "Continuous source of translationally cold dipolar molecules". In: *Physical Review A* 67.4 (Apr. 2003), p. 043406 (see pp. 41, 176, 214).

[83] M.S. Elioff, J. J. Valentini, and D. W. Chandler. "Subkelvin cooling NO molecules via "billiard-like" collisions with argon." In: *Science* 302 (Dec. 2003), pp. 1940–3 (see p. 41).

[84] M. Gupta and D. Herschbach. "Slowing and speeding molecular beams by means of a rapidly rotating source". In: *The Journal of Physical Chemistry A* 105.9 (Mar. 2001), pp. 1626–1637 (see p. 41).

[85] A. Trottier, D. Carty, and E. Wrede. "Photostop: production of zero-velocity molecules by photodissociation in a molecular beam". In: *Molecular Physics* 109.5 (Mar. 2011), pp. 725–733 (see pp. 41, 215).

[86] S. Y. T. van de Meerakker et al. "Deceleration and Electrostatic Trapping of OH Radicals". In: *Physical Review Letters* 94.2 (Jan. 2005), p. 023004 (see p. 41).

[87] J. van Veldhoven, H. Bethlem, and G. Meijer. "Ac electric trap for ground-state molecules". In: *Physical Review Letters* 94.8 (Mar. 2005), pp. 1–4 (see pp. 41, 178).

[88] M. Zeppenfeld et al. "Optoelectrical cooling of polar molecules". In: *Physical Review A* 80.4 (Oct. 2009), p. 041401 (see pp. 41, 214).

[89] M. Zeppenfeld et al. "Sisyphus cooling of electrically trapped polyatomic molecules." In: *Nature* 491 (Nov. 2012), pp. 570–3 (see pp. 41, 214).

[90] B. K. Stuhl et al. "Evaporative cooling of the dipolar hydroxyl radical". In: *Nature* 492 (Dec. 2012), pp. 396–400 (see pp. 41, 62, 176).

[91] S. K. Tokunaga et al. "Prospects for sympathetic cooling of molecules in electrostatic, ac and microwave traps". In: *The European Physical Journal D* 65.1-2 (Apr. 2011), pp. 141–149 (see pp. 41, 178).

[92] L. P. Parazzoli et al. "Large effects of electric fields on atom-molecule collisions at millikelvin temperatures." In: *Physical Review Letters* 106.19 (May 2011), p. 193201 (see p. 41).

[93] B. Friedrich, R. V. Krems, and W. C. Stwalley, eds. *Cold Molecules: Theory, Experiment, Applications*. 1st ed. Bosa Roca, 2009, p. 753 (see p. 41).

[94] J. Sage et al. "Optical production of ultracold polar molecules". In: *Physical Review Letters* 94.20 (May 2005), pp. 27–30 (see p. 41).

[95] J. G. Danzl et al. "Quantum gas of deeply bound ground state molecules." In: *Science* 321 (Aug. 2008), pp. 1062–6 (see p. 42).

[96] F. Lang et al. "Ultracold triplet molecules in the rovibrational ground state". In: *Physical Review Letters* 101.13 (Sept. 2008), pp. 1–4 (see p. 42).

[97] K-K. Ni et al. "A high phase-space-density gas of polar molecules." In: *Science* 322 (Oct. 2008), pp. 231–5 (see p. 42).

[98] S Ospelkaus et al. "Quantum-state controlled chemical reactions of ultracold potassium-rubidium molecules." In: *Science* 327 (Feb. 2010), pp. 853–7 (see p. 42).

[99] M. H. G. de Miranda et al. "Controlling the quantum stereodynamics of ultracold bi-molecular reactions". In: *Nature Physics* 7.6 (Mar. 2011), pp. 502–507 (see p. 42).

[100] K-K. Ni et al. "Dipolar collisions of polar molecules in the quantum regime." In: *Nature* 464 (Apr. 2010), pp. 1324–8 (see p. 42).

[101] B. Yan et al. "Realizing a lattice spin model with polar molecules". In: *arXiv e-prints* (), pp. 1–18. arXiv:1305.5598v1 (see p. 42).

[102] S. D. Kraft et al. "Formation of ultracold LiCs molecules". In: *Journal of Physics B: Atomic, Molecular and Optical Physics* 39.19 (Oct. 2006), pp. 993–1000 (see p. 42).

[103] R. Rydberg. "Graphische Darstellung einiger bandenspektroskopischer Ergebnisse". In: *Zeitschrift für Physik* 73.5-6 (Aug. 1931), pp. 376–385 (see pp. 48, 219).

[104] O. Klein. "Zur Berechnung von Potentialkurven für zweiatomige Moleküle mit Hilfe von Spektraltermen". In: *Zeitschrift für Physik* 76.3-4 (Mar. 1932), pp. 226–235 (see pp. 48, 219).

[105] A. L. G. Rees. "The calculation of potential-energy curves from band-spectroscopic data". In: *Proceedings of the Physical Society* 59.6 (Nov. 1947), pp. 998–1008 (see pp. 48, 219).

[106] E. F. van Dishoeck. "Photodissociation processes in the CH molecule". In: *The Journal of Chemical Physics* 86.1 (1987), p. 196 (see p. 49).

[107] J. M. Brown and A. Carrington. *Rotational spectroscopy of diatomic molecules*. Cambridge: The Press Syndicate of the University of Cambridge, 2003, p. 1013 (see pp. 50, 55–57, 59, 138, 221, 223).

[108] R. N. Zare. *Angular momentum*. 1st ed. Wiley-Interscience, 1988, p. 368 (see p. 55).

[109] M. Jackson et al. "The far-infrared and microwave spectra of the CH radical in the v=1 level of the $X^2\Pi$ state". In: *Journal of Molecular Spectroscopy* 247.2 (Feb. 2008), pp. 128–139 (see p. 59).

[110] N. F. Ramsey. *Molecular beams.* Oxford University Press, Amen House, London EC4, 1956 (see p. 62).

[111] S. Ezekiel and R. Weiss. "Laser-induced fluorescence in a molecular beam of iodine". In: *Physical Review Letters* 20.3 (Jan. 1968), pp. 91–93 (see p. 64).

[112] P. Franken et al. "Generation of optical harmonics". In: *Physical Review Letters* 7.4 (Aug. 1961), pp. 118–119 (see p. 66).

[113] T. W. Hänsch and B. Couillaud. "Laser frequency stabilization by polarization spectroscopy of a reflecting reference cavity". In: *Optics Communications* 35.3 (Dec. 1980), pp. 441–444 (see p. 67).

[114] R. Balhorn, H. Kunzmann, and F. Lebowsky. "Frequency stabilization of internal-mirror helium-neon lasers". In: *Applied Optics* 11.4 (Apr. 1972), p. 742 (see p. 68).

[115] T. M. Niebauer et al. "Frequency stability measurements on polarization-stabilized He-Ne lasers". In: *Applied Optics* 27.7 (Apr. 1988), p. 1285 (see p. 68).

[116] R. Altkorn and R. N. Zare. "Effects of saturation on laser-induced fluorescence measurements of population and polarization". In: *Annual Review of Physical Chemistry* 35.1 (Oct. 1984), pp. 265–289 (see p. 72).

[117] M. R. Tarbutt et al. "Preparation and manipulation of molecules for fundamental physics tests". In: *Cold Molecules: Theory, Experiment, Applications.* Ed. by R. V. Krems. CRC Press, 2009. Chap. 15, p. 753 (see pp. 72, 73).

[118] C. J. Foot. *Atomic Physics.* 1st ed. Oxford: Oxford University Press, 2005, p. 346 (see p. 72).

[119] A. Kantrowitz and J. Grey. "A high intensity source for the molecular beam. Part I. Theoretical". In: *Review of Scientific Instruments* 22.5 (1951), p. 328 (see pp. 76, 80).

[120] G. B. Kistiakowsky and W. P. Slichter. "A high intensity source for the molecular beam. Part II. Experimental". In: *Review of Scientific Instruments* 22.5 (1951), p. 333 (see p. 76).

[121] E. W. Becker and K. Bier. "Die Erzeugung eines intensiven, teilweise monochromatisierten Wasserstoff-Molekularstrahles mit einer Laval-Düse". In: *Zeitschrift für Naturforschung* 9 (1954), p. 975 (see p. 76).

[122] O. F. Hagena. "Pulsed valve for supersonic nozzle experiments at cryogenic temperatures". In: *Zeitschrift für Angewandte Physik* 16 (1963), p. 183 (see p. 76).

[123] K. Luria, N. Lavie, and U. Even. "Dielectric barrier discharge source for supersonic beams." In: *The Review of scientific instruments* 80.10 (Oct. 2009), p. 104102 (see pp. 76, 106, 224).

[124] N. Abuaf et al. "Molecular beams with energies above one electron volt." In: *Science* 155 (Feb. 1967), pp. 997–9 (see p. 76).

[125] D. R. Miller. "Design and analysis of a high intensity fast oxygen atom source". In: *Review of Scientific Instruments* 40.12 (1969), p. 1566 (see p. 77).

[126] J. Q. Searcy. "A supersonic molecular beam metastable atom source initiated by direct discharge". In: *Review of Scientific Instruments* 45.4 (1974), p. 589 (see p. 77).

[127] R. A. Larsen. "Seeded supersonic alkali atom beams". In: *Review of Scientific Instruments* 45.12 (1974), p. 1511 (see p. 77).

[128] J. J. Valentini, M. J. Coggiola, and Y. T. Lee. "Supersonic atomic and molecular halogen nozzle beam source". In: *Review of Scientific Instruments* 48.1 (1977), p. 58 (see p. 77).

[129] A. T. Droege and P. C. Engelking. "Supersonic expansion cooling of electronically excited OH radicals". In: *Chemical Physics Letters* 96.3 (Apr. 1983), pp. 316–318 (see p. 77).

[130] P. C. Engelking. "Corona excited supersonic expansion". In: *Review of Scientific Instruments* 57.9 (1986), p. 2274 (see pp. 77, 86).

[131] R. G. W. Norrish and G. Porter. "Chemical reactions produced by very high light intensities". In: *Nature* 164 (Oct. 1949), pp. 658–658 (see p. 77).

[132] D. L. Monts et al. "New vibronic bands of CH_2 observed in a pulsed supersonic jet". In: *Chemical Physics* 45.1 (Jan. 1980), pp. 133–139 (see p. 78).

[133] M. A. Posthumus et al. "Laser desorption-mass spectrometry of polar nonvolatile bio-organic molecules". In: *Analytical Chemistry* 50.7 (June 1978), pp. 985–991 (see p. 78).

[134] R. E. Smalley. "Laser studies of metal cluster beams". In: *Laser Chemistry* 2.3-4 (1983), pp. 167–184 (see p. 78).

[135] B. Simard et al. "High-resolution spectroscopy and photophysics of refractory molecules at low temperature: The $C^1\Sigma^+$-$X^1\Sigma^+$ system of ZrO". In: *Journal of Molecular Spectroscopy* 129.1 (May 1988), pp. 186–201 (see p. 79).

[136] M. F. Cai, T. A. Miller, and V. E. Bondybey. "Generation of cold free radicals by the reaction of organic halides with metal atoms produced by laser vaporization". In: *Chemical Physics Letters* 158.6 (June 1989), pp. 475–479 (see p. 79).

[137] M. Ebben, G. Meijer, and J. J. Meulen. "Laser evaporation as a source of small free radicals". In: *Applied Physics B Photophysics and Laser Chemistry* 50.1 (Jan. 1990), pp. 35–38 (see p. 79).

[138] G. Scoles. *Atomic and molecular beam methods.* Oxford University Press, Inc., 1988, p. 752 (see p. 82).

[139] H. C. W. Beijerinck and N. F. Verster. "Absolute intensities and perpendicular temperatures of supersonic beams of polyatomic gases". In: *Physica B+C* 111.2-3 (Nov. 1981), pp. 327–352 (see p. 82).

[140] M. R. Tarbutt et al. "A jet beam source of cold YbF radicals". In: *Journal of Physics B: Atomic, Molecular and Optical Physics* 35.24 (Dec. 2002), pp. 5013–5022 (see pp. 83, 84).

[141] T. Heurlinger. "Untersuchungen über die Struktur der Bandenspektra". PhD thesis. Llund, 1918 (see p. 85).

[142] E. Hulthén. "Über das Kombinationsprinzip und einige neue Bandentypen". In: *Zeitschrift für Physik* 11.1 (Dec. 1922), pp. 284–293 (see p. 85).

[143] A. Kratzer. "Die Terme der (C + H)-Banden". In: *Zeitschrift für Physik* 23.1 (Dec. 1924), pp. 298–323 (see p. 85).

[144] D. A. Ramsay. "Absorption Spectra of SH and SD Produced by Flash Photolysis of H_2S and D_2S". In: *The Journal of Chemical Physics* 20.12 (1952), p. 1920 (see p. 85).

[145] J. E. Butler et al. "Production, detection and reactions of the CH radical". In: *Chemical Physics Letters* 63.1 (May 1979), pp. 104–107 (see p. 85).

[146] H. Shinohara. "Laser photofragmentation dynamics of an acrolein supersonic molecular beam at 193 nm". In: *The Journal of Chemical Physics* 77.1 (1982), p. 234 (see p. 85).

[147] W. Ubachs et al. "Hyperfine structure and lifetime of the $C^2\Sigma^+$(v=0) state of CH". In: *The Journal of Chemical Physics* 84.6 (1986), p. 3032 (see p. 85).

[148] J. Lindner. "Multi-photon dissociation of $CHBr_3$ at 248 and 193 nm: observation of the electronically excited $CH(A^2\Delta)$ product". In: *Chemical Physics* 238.2 (Nov. 1998), pp. 329–341 (see pp. 86, 102).

[149] M. A. Weibel, T. D. Hain, and T. J. Curtiss. "Hexapole-selected supersonic beams of reactive radicals: CF, SiF, SH, CH, and C_2H". In: *The Journal of Chemical Physics* 108.8 (1998), p. 3134 (see p. 86).

[150] K. Ikejiri et al. "A highly intense state-selected CH radical beam and its application to the $CH+O_2$ reaction". In: *Chemical Physics Letters* 401.4-6 (Jan. 2005), pp. 465–469 (see p. 86).

[151] S. Davis et al. "Jet-cooled molecular radicals in slit supersonic discharges: Sub-Doppler infrared studies of methyl radical". In: *The Journal of Chemical Physics* 107.15 (1997), p. 5661 (see p. 87).

[152] H. J. Lewandowski et al. "A pulsed, low-temperature beam of supersonically cooled free radical OH molecules". In: *Chemical Physics Letters* 395.1-3 (Sept. 2004), pp. 53–57 (see p. 88).

[153] C. Romanzin et al. "CH radical production from 248 nm photolysis or discharge-jet dissociation of $CHBr_3$ probed by cavity ring-down absorption spectroscopy." In: *The Journal of Chemical Physics* 125.11 (Sept. 2006), p. 114312 (see pp. 89, 99, 100, 109).

[154] G. M. Jursich and J. R. Wiesenfeld. "Product energetics of the reaction $C(^1D)+H_2 \rightarrow CH + H$". In: *Chemical Physics Letters* 110.1 (Sept. 1984), pp. 14–19 (see p. 91).

[155] C. E. M. Strauss et al. "Dissociation dynamics of C_3O_2 excited at 157.6 nm". In: *The Journal of Chemical Physics* 94.3 (1991), p. 1837 (see p. 91).

[156] K. Mikulecky and K-H. Gericke. "Reaction dynamics of $C(^1D)+H_2 \rightarrow CH(X^2\Pi)+H$". In: *The Journal of Chemical Physics* 98.2 (1993), p. 1244 (see p. 91).

[157] W. B. Hurt. "Excitation Transfer and Penning Ionization Reactions between Helium Metastables and Carbon Monoxide". In: *The Journal of Chemical Physics* 57.2 (1972), p. 734 (see p. 92).

[158] Y. Nagamachi et al. "Development of a highly intense state-selected CH radical beam source for the study on the collision energy dependent reaction dynamics". In: *Chemical Physics Letters* 421.1-3 (Apr. 2006), pp. 124–128 (see p. 94).

[159] R. Weis, C. Winkler, and R. W. Schrittwieser. "A nozzle beam source for the production of metastable rare gas atoms". In: *Plasma Sources Science and Technology* 6.2 (May 1997), pp. 247–249 (see p. 97).

[160] T. Halfmann, J. Koensgen, and K. Bergmann. "A source for a high-intensity pulsed beam of metastable helium atoms". In: *Measurement Science and Technology* 11.10 (Oct. 2000), pp. 1510–1514 (see p. 97).

[161] O. Hideo. *Photochemistry of small molecules*. Wiley-Interscience, 1978 (see p. 98).

[162] J. B. Burkholder et al. "Temperature dependence of the HNO_3 UV absorption cross sections". In: *Journal of Geophysical Research* 98.D12 (1993), p. 22937 (see p. 99).

[163] A. A. Turnipseed et al. "Photodissociation of HNO_3 at 193, 222, and 248 nm: Products and quantum yields". In: *The Journal of Chemical Physics* 96.8 (1992), p. 5887 (see p. 99).

[164] P. Zou et al. "Photodissociation of Bromoform at 248 nm: Single and Multiphoton Processes". In: *The Journal of Physical Chemistry A* 108.9 (Mar. 2004), pp. 1482–1488 (see p. 99).

[165] K. Luria, W. Christen, and U. Even. "Generation and propagation of intense supersonic beams." In: *The Journal of Physical Chemistry A* 115.25 (June 2011), pp. 7362–7 (see pp. 105, 107, 108).

[166] G. I. Dimov. "Quick acting valves for admitting short gas pulses into vacuum devices". In: *Pribory I Teknhnika Eksperimenta* 5 (1968), pp. 168–171 (see p. 105).

[167] W. R. Gentry and C. F. Giese. "Ten-microsecond pulsed molecular beam source and a fast ionization detector." In: *The Review of scientific instruments* 49.5 (May 1978), p. 595 (see p. 105).

[168] D. Gerlich. *Schnelles Gasventil zur Erzeugung eines Gaspulses im μ-sekunden Bereich*. 1968 (see p. 105).

[169] D. Irimia et al. "A short pulse (7 micros FWHM) and high repetition rate (dc-5 kHz) cantilever piezovalve for pulsed atomic and molecular beams." In: *Review of Scientific Instruments* 80.11 (Nov. 2009), p. 113303 (see pp. 105, 106).

[170] J. B. Cross. "High repetition rate pulsed nozzle beam source". In: *Review of Scientific Instruments* 53.1 (1982), p. 38 (see p. 106).

[171] P. Andresen et al. "Characteristics of a piezoelectric pulsed nozzle beam". In: *Review of Scientific Instruments* 56.11 (1985), p. 2038 (see p. 106).

[172] D. Proch and T. Trickl. "A high-intensity multi-purpose piezoelectric pulsed molecular beam source". In: *Review of Scientific Instruments* 60.4 (1989), p. 713 (see p. 106).

[173] P. Maksyutenko et al. "A crossed molecular beam study on the reaction of methylidyne radicals $CH(X^2\Pi)$ with acetylene $C_2H_2(X^1\Sigma_g^+)$ - competing $C_3H_2 + H$ and $C_3H + H_2$ channels." In: *Physical Chemistry Chemical Physics* 13.1 (Jan. 2011), pp. 240–52 (see p. 108).

[174] F. Zhang, P. Maksyutenko, and R. I. Kaiser. "Chemical dynamics of the CH($X^2\Pi$) + $C_2H_4(X^1A_{1g})$, CH($X^2\Pi$) + $C_2D_4(X^1A_{1g})$, and CD($X^2\Pi$) + $C^2H_4(X^1A_{1g})$ reactions studied under single collision conditions." In: *Physical Chemistry Chemical Physics* 14.2 (Jan. 2012), pp. 529–37 (see pp. 108, 109).

[175] K. A. Olive and M. Pospelov. "Environmental dependence of masses and coupling constants". In: *Physical Review D* 77.4 (Feb. 2008), p. 043524 (see p. 113).

[176] M. G. Kozlov. "Λ-doublet spectra of diatomic radicals and their dependence on fundamental constants". In: *Physical Review A* 80.2 (Aug. 2009), pp. 1–10 (see pp. 114, 119, 156).

[177] X. Calmet and H. Fritzsch. "The cosmological evolution of the nucleon mass and the electroweak coupling constants". In: *The European Physical Journal C* 24.4 (Aug. 2002), pp. 639–642 (see p. 114).

[178] V. Dzuba, V. Flambaum, and J. K. Webb. "Space-time variation of physical constants and relativistic corrections in atoms". In: *Physical Review Letters* 82.5 (Feb. 1999), pp. 888–891 (see pp. 115, 116).

[179] N. Leefer et al. "New limits on variation of the fine-structure constant using atomic dysprosium". In: *arXiv e-prints* (Apr. 2013), pp. 1–5. arXiv:`1304.6940` (see p. 115).

[180] H. L. Bethlem and W. Ubachs. "Testing the time-invariance of fundamental constants using microwave spectroscopy on cold diatomic radicals". In: *Faraday Discussions* 142 (2009), p. 25 (see p. 115).

[181] A. Shelkovnikov et al. "Stability of the proton-to-electron mass ratio". In: *Physical Review Letters* 100.15 (Apr. 2008) (see p. 115).

[182] M. P. Savedoff. "Physical constants in extra-galactic nebulæ". In: *Nature* 178 (Sept. 1956), pp. 688–689 (see p. 116).

[183] G. Gamow. "Electricity, Gravity, and Cosmology". In: *Physical Review Letters* 19.13 (Sept. 1967), pp. 759–761 (see p. 116).

[184] J-P. Uzan. "The fundamental constants and their variation: observational and theoretical status". In: *Reviews of Modern Physics* 75.2 (Apr. 2003), pp. 403–455 (see p. 116).

[185] A. I. Shlyakhter. "Direct test of the constancy of fundamental nuclear constants". In: *Nature* 264 (Nov. 1976), pp. 340–340 (see p. 116).

[186] S. Lamoreaux and J. Torgerson. "Neutron moderation in the Oklo natural reactor and the time variation of α". In: *Physical Review D* 69.12 (June 2004), p. 121701 (see p. 116).

[187] J. K. Webb et al. "Search for Time Variation of the Fine Structure Constant". In: *Physical Review Letters* 82.5 (Feb. 1999), pp. 884–887 (see p. 116).

[188] M. T. Murphy, J. K. Webb, and V. V. Flambaum. "Further evidence for a variable fine-structure constant from Keck/HIRES QSO absorption spectra". In: *Monthly Notices of the Royal Astronomical Society* 345.2 (Oct. 2003), pp. 609–638 (see p. 117).

[189] J. K. Webb et al. "Indications of a spatial variation of the fine structure constant". In: *Physical Review Letters* 107.19 (Oct. 2011), pp. 1–5 (see p. 117).

[190] J. C. Berengut and V. V. Flambaum. "Manifestations of a spatial variation of fundamental constants on atomic clocks, Oklo, meteorites, and cosmological phenomena". In: *arXiv e-prints* August (2010). arXiv:`1008.3957v1` (see p. 117).

[191] I. I. Agafonova et al. "First measurement of Mg isotope abundances at high redshifts and accurate estimate of $\Delta\alpha/\alpha$". In: *Astronomy & Astrophysics* 529 (Mar. 2011), A28 (see p. 117).

[192] P. Molaro et al. "Bounds on the fine structure constant variability from Fe ii absorption lines in QSO spectra". In: *The European Physical Journal Special Topics* 163.1 (Nov. 2008), pp. 173–189 (see p. 117).

[193] K. Griest et al. "Wavelength accuracy of the keck hires spectrograph and measuring changes in the fine structure constant". In: *The Astrophysical Journal* 708.1 (Jan. 2010), pp. 158–170 (see p. 117).

[194] F. van Weerdenburg et al. "First constraint on cosmological variation of the proton-to-electron mass ratio from two independent telescopes". In: *Physical Review Letters* 106.18 (May 2011), p. 180802 (see p. 117).

[195] T. Steinmetz et al. "Laser frequency combs for astronomical observations." In: *Science* 321 (Sept. 2008), pp. 1335–7 (see p. 117).

[196] J. A. King et al. "New constraint on cosmological variation of the proton-to-electron mass ratio from Q0528250". In: *Monthly Notices of the Royal Astronomical Society* 417.4 (Nov. 2011), pp. 3010–3024 (see p. 118).

[197] J. Bagdonaite et al. "A stringent limit on a drifting proton-to-electron mass ratio from alcohol in the early universe." In: *Science* 339 (Jan. 2013), pp. 46–8 (see p. 118).

[198] N. Kanekar et al. "Constraining fundamental constant evolution with H I and OH lines". In: *The Astrophysical Journal* 746.2 (Feb. 2012), p. L16 (see pp. 118, 162).

[199] S. A. Levshakov et al. "An upper limit to the variation in the fundamental constants at redshift z = 5.2". In: *Astronomy & Astrophysics* 540 (Apr. 2012), p. L9 (see p. 118).

[200] S. A. Levshakov, M. G. Kozlov, and D. Reimers. "Methanol As a Tracer of Fundamental Constants". In: *The Astrophysical Journal* 738.1 (Sept. 2011), p. 26 (see p. 118).

[201] A. Lapinov. "Private communication". In: (2013) (see p. 118).

[202] L. M. Ziurys and B. E. Turner. "Detection of interstellar rotationally excited CH". In: *The Astrophysical Journal* 292 (May 1985), p. L25 (see pp. 119, 154–157, 160).

[203] R. Genzel et al. "Interstellar CH - Excitation temperatures and abundance relative to H_2CO". In: *Astronomy & Astrophysics* 79.3 (1979), pp. 253–259 (see pp. 119, 157, 160).

[204] N. F. Ramsey. "Experiments with separated oscillatory fields and hydrogen masers." In: *Science* 248 (June 1990), pp. 1612–9 (see p. 120).

[205] N. F. Ramsey. "A molecular beam resonance method with separated oscillating fields". In: *Physical Review* 78.6 (June 1950), pp. 695–699 (see pp. 120, 125).

[206] D. Kleppner. "Norman Ramsey and his method". In: *Physics Today* 66.1 (2013), p. 25 (see p. 120).

[207] M. O. Scully. *Quantum optics*. Cambridge University Press, 1997 (see p. 122).

[208] T. J. Sumner, J. M. Pendlebury, and K. F. Smith. "Convectional magnetic shielding". In: *Journal of Physics D: Applied Physics* 20.9 (Sept. 1987), pp. 1095–1101 (see p. 129).

[209] I. B. Khriplovich and S. K. Lamoreaux. *CP violation without strangeness*. Berlin, Heidelberg: Springer Berlin Heidelberg, 1997 (see p. 129).

[210] P. F. Goldsmith. *Quasioptical systems*. 1st ed. Wiley-IEEE Press, 1998, p. 430 (see pp. 131, 168, 181).

[211] B. Lev et al. "OH hyperfine ground state: from precision measurement to molecular qubits". In: *Physical Review A* 74.6 (Dec. 2006), pp. 1–4 (see p. 139).

[212] W. M. Itano, L. Lewis, and D. J. Wineland. "Shift of $^2S_{1/2}$ hyperfine splittings due to blackbody radiation". In: *Physical Review A* 25.2 (Feb. 1982), pp. 1233–1235 (see p. 142).

[213] N. Vanhaecke and O. Dulieu. "Precision measurements with polar molecules: the role of the black body radiation". In: *Molecular Physics* 105.11-12 (2008), pp. 11–12 (see p. 142).

[214] S. Y. T. van de Meerakker, H. L. Bethlem, and G. Meijer. "Taming molecular beams". In: *Nature Physics* 4.8 (Aug. 2008), pp. 595–602 (see pp. 145, 176).

[215] G. Westerhout. "A survey of the continuous radiation from the Galactic System at a frequency of 1390 Mc/s". In: *Bulletin of the Astronomical Institutes of the Netherlands* 14 (1958), p. 215 (see p. 154).

[216] NASA and JPL-Caltech. *W51* (see p. 154).

[217] D. Gerlich and S. Horning. "Experimental investigation of radiative association processes as related to interstellar chemistry". In: *Chemical Reviews* 92.7 (Nov. 1992), pp. 1509–1539 (see p. 154).

[218] B. E. Turner. "Rotationally excited interstellar CH - Detection of satellite lines and analysis of abundance and excitation". In: *The Astrophysical Journal* 329 (June 1988), p. 425 (see pp. 155–157).

[219] M. G. Kozlov and S. A. Levshakov. "Sensitivity of the H_3O^+ Inversion-Rotational Spectrum To Changes in the Electron-To-Proton Mass Ratio". In: *The Astrophysical Journal* 726.2 (Jan. 2011), p. 65 (see pp. 159, 163).

[220] O. E. H. Rydbeck et al. "Radio astronomical determination of ground state transition frequencies of CH". In: *Astronomy and Astrophysics* 34.3 (1974), pp. 479–482 (see p. 160).

[221] O. E. H. Rydbeck et al. "Radio observations of interstellar CH. I". In: *The Astrophysical Journal Supplement Series* 31 (July 1976), p. 333 (see pp. 160, 161).

[222] J. B. Whiteoak, F. F. Gardner, and M. W. Sinclair. "Observations of the 3.3 GHz ground-state transitions of interstellar CH". In: *Monthly Notices of the Royal Astronomical Society* 184 (1978), pp. 235–257 (see p. 160).

[223] B. E. Turner and B. Zuckerman. "Microwave detection of interstellar CH". In: *The Astrophysical Journal* 187 (Jan. 1974), p. L59 (see p. 160).

[224] L. M. Ziurys. "Private communication". In: (2013) (see p. 160).

[225] J. Harju, A. Winnberg, and J. G. A. Wouterloot. "The distribution of OH in Taurus Molecular Cloud-1". In: *Astronomy & Astrophysics* 1073 (2000), pp. 1065–1073 (see pp. 159, 160).

[226] N. Sakai et al. "CH radio emission from Heiles Cloud 2 as a tracer of molecular cloud evolution". In: *Astronomy & Astrophysics* 546 (Oct. 2012), A103 (see pp. 159–161, 163, 231).

[227] A. Suutarinen et al. "CH abundance gradient in TMC-1". In: *Astronomy & Astrophysics* 531 (June 2011), A121 (see p. 161).

[228] M. C. McCarthy et al. "Detection of low-frequency lambda-doublet transitions of the free ^{12}CH and ^{13}CH radicals." In: *Proceedings of the National Academy of Sciences of the United States of America* 103.33 (Aug. 2006), pp. 12263–8 (see p. 161).

[229] R. Subrahmanyan et al. "1830-211: gravitationally lensed images of a flat-spectrum radio core?" In: *Monthly Notices of the Royal Astronomical Society1* 246 (1990), pp. 263–272 (see p. 161).

[230] D. L. Jauncey et al. "An unusually strong Einstein ring in the radio source PKS1830–211". In: *Nature* 352 (July 1991), pp. 132–134 (see p. 161).

[231] T. Wiklind and F. Combes. "The redshift of the gravitational lens of PKS1830–211 determined from molecular absorption lines". In: *Nature* 379 (Jan. 1996), pp. 139–141 (see p. 161).

[232] S. Muller. "Private communication". In: (2013) (see pp. 162, 165, 173).

[233] F. Combes. "Molecular absorptions in high-z objects". In: *Astrophysics and Space Science* 313.1-3 (Sept. 2007), pp. 321–326 (see p. 162).

[234] E. R. Hudson et al. "Cold molecule spectroscopy for constraining the evolution of the fine structure constant". In: *Physical Review Letters* 96.14 (Apr. 2006), pp. 1–4 (see p. 162).

[235] N. Kanekar, J. Chengalur, and T. Ghosh. "Conjugate 18 cm OH satellite lines at a cosmological distance". In: *Physical Review Letters* 93.5 (July 2004), pp. 1–4 (see p. 162).

[236] M. G. Kozlov. "Linear polyatomic molecules with Π ground state: Sensitivity to variation of the fundamental constants". In: *Physical Review A* 87.3 (Mar. 2013), p. 032104 (see p. 163).

[237] R. J. Chastain, D. Cotten, and L. Magnani. "High-resolution CH observations of two translucent molecular clouds". In: *The Astronomical Journal* 139.1 (Jan. 2010), pp. 267–278 (see pp. 163, 164).

[238] M. H. D. van der Wiel et al. "Herschel /HIFI observations of spectrally resolved methylidyne signatures toward the high-mass star-forming core NGC 6334I". In: *Astronomy & Astrophysics* 521 (Oct. 2010), p. L43 (see p. 165).

[239] M. Gerin et al. "Interstellar CH absorption in the diffuse interstellar medium along the sight-lines to G10.6-0.4 (W31C), W49N, and W51". In: *Astronomy & Astrophysics* 521 (Oct. 2010), p. L16 (see p. 165).

[240] S.-L. Qin et al. "Herschel observations of EXtra-Ordinary Sources (HEXOS): detecting spiral arm clouds by CH absorption lines". In: *Astronomy & Astrophysics* 521 (Oct. 2010), p. L14 (see p. 165).

[241] V. Ossenkopf. "pirvate communication". In: (2013) (see pp. 165, 166).

[242] K. M. Evenson. "CH free radicals detected by infrared laser magnetic resonance". In: *Applied Physics Letters* 18.10 (1971), p. 426 (see p. 166).

[243] J. T. Hougen et al. "Far infrared laser magnetic resonance spectrum of CH". In: *Journal of Molecular Spectroscopy* 72.3 (Sept. 1978), pp. 463–483 (see p. 166).

[244] J. M. Brown and K. M. Evenson. "The far-infrared laser magnetic resonance spectrum of the CH radical and determination of ground-state parameters". In: *Journal of Molecular Spectroscopy* 98.2 (Apr. 1983), pp. 392–403 (see p. 166).

[245] K. M. Evenson, D. A. Jennings, and F. R. Petersen. "Tunable far-infrared spectroscopy". In: *Applied Physics Letters* 44.6 (1984), p. 576 (see p. 166).

[246] T. Amano. "The lowest submillimeter-wave transitions of CH: the laboratory measurement of the rest frequencies". In: *The Astrophysical Journal* 531.2 (Mar. 2000), pp. L161–L164 (see pp. 166, 173).

[247] S. A. Davidson, K. M. Evenson, and J. M. Brown. "A measurement of the rotational spectrum of the CH radical in the Far-Infrared". In: *The Astrophysical Journal* 546.1 (Jan. 2001), pp. 330–337 (see p. 166).

[248] A. J. de Nijs, W. Ubachs, and H. L. Bethlem. "Sensitivity of rotational transitions in CH and CD to a possible variation of fundamental constants". In: *Physical Review A* 86.3 (Sept. 2012), p. 032501 (see p. 173).

[249]   E. S. Shuman et al. "Radiative force from optical cycling on a diatomic molecule". In: *Physical Review Letters* 103.22 (Nov. 2009), pp. 1–4 (see pp. 176, 214).

[250]   J. F. Barry et al. "Laser radiation pressure slowing of a molecular beam". In: *Physical Review Letters* 108.10 (Mar. 2012), p. 103002 (see pp. 176, 218).

[251]   V. Zhelyazkova et al. "Laser cooling and slowing of CaF molecules". In: *arXiv e-prints* (Aug. 2013). arXiv:1308.0421 (see pp. 176, 214, 218).

[252]   M. R. Tarbutt et al. "Design for a fountain of YbF molecules to measure the electron's electric dipole moment". In: *New Journal of Physics* 15.5 (May 2013), p. 053034 (see p. 176).

[253]   K. Davis et al. "Bose-Einstein condensation in a gas of sodium atoms". In: *Physical Review Letters* 75.22 (Nov. 1995), pp. 3969–3973 (see p. 176).

[254]   R. E. Drullinger, D. J. Wineland, and J. C. Bergquist. "High-resolution optical spectra of laser cooled ions". In: *Applied Physics* 22.4 (Aug. 1980), pp. 365–368 (see p. 176).

[255]   C. Myatt et al. "Production of two overlapping Bose-Einstein condensates by sympathetic cooling". In: *Physical Review Letters* 78.4 (Jan. 1997), pp. 586–589 (see p. 176).

[256]   A. G. Truscott et al. "Observation of Fermi pressure in a gas of trapped atoms." In: *Science* 291.5513 (Mar. 2001), pp. 2570–2 (see p. 176).

[257]   G. Modugno et al. "Bose-Einstein condensation of potassium atoms by sympathetic cooling." In: *Science* 294 (Nov. 2001), pp. 1320–2 (see p. 176).

[258]   H. L. Bethlem et al. "Electrostatic trapping of ammonia molecules". In: *Nature* 406.6795 (Aug. 2000), pp. 491–4 (see p. 177).

[259]   C. E. Heiner et al. "A molecular synchrotron". In: *Nature Physics* 3.2 (Jan. 2007), pp. 115–118 (see p. 177).

[260]   P. C. Zieger et al. "Multiple packets of neutral molecules revolving for over a mile". In: *Physical Review Letters* 105.17 (Oct. 2010), p. 173001 (see p. 177).

[261]   W. Ketterle and D. E. Pritchard. "Trapping and focusing ground state atoms with static fields". In: *Applied Physics B Photophysics and Laser Chemistry* 54.5 (May 1992), pp. 403–406 (see p. 177).

[262]   T. Takekoshi, B. M. Patterson, and R. J. Knize. "Observation of optically trapped cold cesium molecules". In: *Physical Review Letters* 81.23 (1998), pp. 5105–5108 (see p. 178).

[263]   R. Grimm, M.s Weidemüller, and Y. B. Ovchinnikov. "Optical dipole traps for neutral atoms". In: *arXiv e-print* (Feb. 1999). arXiv:9902072 [physics] (see p. 178).

[264]   R. Spreeuw et al. "Demonstration of neutral atom trapping with microwaves". In: *Physical Review Letters* 72.20 (May 1994), pp. 3162–3165 (see p. 178).

[265]   D. DeMille, D. R. Glenn, and J. Petricka. "Microwave traps for cold polar molecules". In: *The European Physical Journal D* 31.2 (Nov. 2004), pp. 375–384 (see pp. 178–180, 187).

[266]   S. Alyabyshev, T. Tscherbul, and R. Krems. "Microwave-laser-field modification of molecular collisions at low temperatures". In: *Physical Review A* 79.6 (June 2009), p. 060703 (see p. 178).

[267]   M. Kajita and A. V. Avdeenkov. "Collisions between linear polar molecules trapped in a microwave field". In: *The European Physical Journal D* 41.3 (Nov. 2006), pp. 499–504 (see p. 178).

[268]   A. V. Avdeenkov. "Dipolar collisions of ultracold polar molecules in a microwave field". In: *Physical Review A* 86.2 (Aug. 2012), p. 022707 (see pp. 178, 179).

[269] H. Odashima et al. "Microwave lens for polar molecules". In: *Physical Review Letters* 104.25 (June 2010), p. 4 (see p. 179).

[270] S. Merz et al. "Decelerating molecules with microwave fields". In: *Physical Review A* 85.6 (June 2012), p. 063411 (see pp. 179, 214).

[271] R. Hill and T. Gallagher. "Deflection of CsF molecules by resonant inhomogeneous electric fields". In: *Physical Review A* 12.2 (Aug. 1975), pp. 451–459 (see p. 179).

[272] K. Enomoto and T. Momose. "Microwave Stark decelerator for polar molecules". In: *Physical Review A* 72.6 (Dec. 2005), p. 061403 (see p. 179).

[273] K. Enomoto et al. "Superconducting microwave cavity towards controlling the motion of polar molecules". In: *Applied Physics B* 109.1 (Sept. 2012), pp. 149–157 (see p. 179).

[274] D. R. Glenn. "Development of Techniques for Cooling and Trapping Polar Diatomic Molecules". PhD thesis. Yale University, 2009, p. 171 (see pp. 179, 180, 187).

[275] A. Schawlow and C. Townes. "Infrared and optical masers". In: *Physical Review* 112.6 (Dec. 1958), pp. 1940–1949 (see p. 181).

[276] A. G. Fox and T. Li. "Resonant modes in maser interferometer". In: *Bell System Technical Journal* 40 (1961), pp. 453–488 (see p. 181).

[277] A. G. Fox and T. Li. "Modes in a maser interferometer with curved and tilted mirrors". In: *Proceedings of the IEEE* 51.1 (1963), pp. 80–89 (see p. 181).

[278] B. E. A. Saleh and M. C. Teich. *Fundamentals of photonics*. Wiely-Balckwell, 2007, p. 1200 (see pp. 181, 184).

[279] J. D. Jackson. *Classical electrodynamics*. 3rd ed. Wiley, 1998, p. 808 (see pp. 181, 187).

[280] H. E. Bussey. "Standards and measurements of microwave surface impedance, skin depth, conductivity and Q". In: *IRE Transactions on Instrumentation* I-9.2 (Sept. 1960), pp. 171–175 (see p. 182).

[281] R. A. Matula. "Electrical resistivity of copper, gold, palladium, and silver". In: *Journal of Physical and Chemical Reference Data* 8.4 (1979), p. 1147 (see pp. 182, 195, 196).

[282] F. A. Benson and D. H. Steven. "Rectangular-waveguide attenuation at millimetre wavelengths". In: *Proceedings of the Institution of Electrical Engineers* 110.6 (1963), p. 1008 (see p. 182).

[283] A. Hernandez et al. "Resonant cavities for measuring the surface resistance of metals at X-band frequencies". In: *Journal of Physics E: Scientific Instruments* 19.3 (Mar. 1986), pp. 222–225 (see pp. 182, 186).

[284] S. P. Morgan. "Effect of surface roughness on eddy current losses at microwave frequencies". In: *Journal of Applied Physics* 20.4 (1949), p. 352 (see p. 186).

[285] J. A. Ogilvy. *Theory of wave scattering from random rough surfaces*. 1st ed. Institute of Physics Publishing, 1991, p. 304 (see p. 186).

[286] S. A. Zhevakin and A. P. Naumov. "The propagation of centimeter, millimeter, and submillimeter radio waves in the earth's atmosphere". In: *Radiophysics and Quantum Electronics* 10.9-10 (1971), pp. 678–694 (see p. 186).

[287] H. Bethe. "Theory of diffraction by small holes". In: *Physical Review* 66.7-8 (Oct. 1944), pp. 163–182 (see p. 187).

[288] R. E. Collin. *Foundations for microwave engineering*. 2nd. Wiley-Blackwell, 2000, p. 944 (see p. 187).

[289] R. K. Mongia and R. K. Arora. "Equivalent circuit parameters of an aperture coupled open resonator cavity". In: *IEEE Transactions on Microwave Theory and Techniques* 41.8 (1993), pp. 1245–1250 (see p. 187).

[290] R. E. Collin. *Field Theory of Guided Waves*. Wiley-IEEE Press, 1990, p. 864 (see p. 187).

[291] R. Levy. "Improved single and multiaperature waveguide coupling theory, including explanation of mutual interactions". In: *IEEE Transactions on Microwave Theory and Techniques* 28.4 (Apr. 1980), pp. 331–338 (see p. 188).

[292] R. H. Dicke. "A computational method applicable to microwave networks". In: *Journal of Applied Physics* 18.10 (1947), p. 873 (see p. 190).

[293] "Agilent Network Analyzer Basics". In: (2013) (see p. 190).

[294] B. E. Sauer et al. "Precise calibration of a microwave cavity with a nonideal waveguide system". In: *Review of Scientific Instruments* 62.1 (1991), p. 189 (see p. 193).

[295] F. J. Tischer and Y. H. Choung. "Anomalous temperature dependence of the surface resistance of copper at 10 GHz". In: *IEE Proceedings-H Microwaves Antennas and Propagation* 129.2 (1982), pp. 56–60 (see p. 197).

[296] J. S. Thorp. "R.F. conductivity in copper at 8mm wavlengths". In: *Proceedings of the IEE - Part III: Radio and Communication Engineering* 101.74 (1954), pp. 357–359 (see pp. 197, 198).

[297] F. J. Tischer. "Surface resistance of single-crystal copper in the millimeter-wave region at room temperature". In: *Proceedings of the IEEE* 62.5 (1974), pp. 635–636 (see p. 197).

[298] R. Courant, K. Friedrichs, and H. Lewy. "Über die partiellen Differenzengleichungen der mathematischen Physik". In: *Mathematische Annalen* 100.1 (Dec. 1928), pp. 32–74 (see p. 198).

[299] K. S. Yee. "Numerical solution of initial boundary value problems involving Maxwell's equations in isotropic media". In: *IEEE Transactions on Antennas and Propagation* 14.3 (May 1966), pp. 302–307 (see p. 199).

[300] J. Bardeen, L. Cooper, and J. Schrieffer. "Microscopic theory of superconductivity". In: *Physical Review* 106.1 (Apr. 1957), pp. 162–164 (see p. 209).

[301] J. Halbritter. "On surface resistance of superconductors". In: *Zeitschrift für Physik* 266.3 (June 1974), pp. 209–217 (see p. 209).

[302] H. Padamsee. *RF superconductivity: science, technology and applications*. Weinheim: Wiley-VCH, 2009 (see p. 210).

[303] C. Fabre, P. Goy, and S. Haroche. "Millimetre resonances in Na Rydberg levels detected by field ionization: quantum defects and Stark-effect studies". In: *Journal of Physics B: Atomic and Molecular Physics* 10.6 (Apr. 1977), pp. L183–L189 (see p. 211).

[304] J. Raimond et al. "Statistics of millimeter-wave photons emitted by a Rydberg-atom maser: an experimental study of fluctuations in single-mode superradiance". In: *Physical Review Letters* 49.26 (Dec. 1982), pp. 1924–1927 (see p. 211).

[305] P. Goy et al. "Observation of cavity-enhanced single-atom spontaneous emission". In: *Physical Review Letters* 50.24 (June 1983), pp. 1903–1906 (see p. 211).

[306] S. Kuhr et al. "Ultrahigh finesse Fabry-Pérot superconducting resonator". In: *Applied Physics Letters* 90.16 (2007), p. 164101 (see pp. 211, 212).

[307] A. Rauschenbeutel. "Atomes et cavité: préparation et manipulation d'états intriqués complexes". PhD thesis. L'Ecole Normal Superieure, 2001, p. 176 (see p. 212).

[308] G. Nogues. "Détection sans destruction d'un seul photon". PhD thesis. Ecole Normale Superieure, 1999, p. 191 (see p. 212).

[309] J-M. Raimond, M. Brune, and S. Haroche. "Manipulating quantum entanglement with atoms and photons in a cavity". In: *Reviews of Modern Physics* 73.3 (Aug. 2001), pp. 565–582 (see p. 212).

[310] P. Horak et al. "Cavity-induced atom cooling in the strong coupling regime". In: *Physical Review Letters* 79.25 (Dec. 1997), pp. 4974–4977 (see p. 213).

[311] V. Vuletic and S. Chu. "Laser cooling of atoms, ions, or molecules by coherent scattering". In: *Physical Review Letters* 84.17 (Apr. 2000), pp. 3787–90 (see p. 213).

[312] S. Nimmrichter et al. "Master equation for the motion of a polarizable particle in a multimode cavity". In: *New Journal of Physics* 12.8 (Aug. 2010), p. 083003 (see p. 213).

[313] M. T. Hummon et al. "2D magneto-optical trapping of diatomic molecules". In: *Physical Review Letters* 110.14 (Apr. 2013), p. 143001 (see p. 214).

[314] H.-I Lu et al. "A cold and slow molecular beam." In: *Physical Chemistry Chemical Physics* 13.42 (Nov. 2011), pp. 18986–90 (see p. 214).

[315] G. Price et al. "Single-photon atomic cooling". In: *Physical Review Letters* 100.9 (Mar. 2008), p. 093004 (see p. 214).

[316] Hendrick Bethlem et al. "Deceleration and trapping of ammonia using time-varying electric fields". In: *Physical Review A* 65.5 (May 2002), pp. 1–20 (see p. 214).

[317] S. J. Matthews, S. Willitsch, and T. P. Softley. "Fully state-selected VMI study of the near-threshold photodissociation of NO(2): variation of the angular anisotropy parameter." In: *Physical Chemistry Chemical Physics* 9.42 (Nov. 2007), pp. 5656–63 (see p. 215).

[318] B. S. Zhao et al. "Slow molecules produced by photodissociation". In: *Journal of the Physical Society of Japan* 78.9 (Sept. 2009), p. 094302 (see p. 215).

[319] B. K. Stuhl et al. "Magneto-optical trap for polar molecules". In: *Physical Review Letters* 101.24 (Dec. 2008), p. 243002 (see pp. 218, 219).

[320] J. Clark et al. "The $A^1\Pi$-$X^1\Sigma^+$(2,0) transition in ^{11}BH and ^{10}BH observed by (1+2)-photon resonance-enhanced multiphoton ionization spectroscopy". In: *Chemical Physics Letters* 340.1-2 (May 2001), pp. 45–54 (see p. 219).

[321] J. W. C. Johns, F. A. Grimm, and R. F. Porter. "On the spectrum of BH in the near ultraviolet". In: *Journal of Molecular Spectroscopy* 22.1-4 (Jan. 1967), pp. 435–451 (see pp. 219, 223).

[322] W. T. M. L. Fernando and P. F. Bernath. "Fourier transform spectroscopy of the $A^1\Pi$-$X^1\Sigma^+$ transition of BH and BD". In: *Journal of Molecular Spectroscopy* 145.2 (Feb. 1991), pp. 392–402 (see pp. 219, 224).

[323] R. C. Viteri et al. "Rovibrational characterization of $X^2\Sigma^+$ ^{11}BH$^+$ by the extrapolation of photoselected high Rydberg series in ^{11}BH." In: *The Journal of Chemical Physics* 124.14 (Apr. 2006), p. 144312 (see p. 219).

[324] R. Thomson and F. W. Dalby. "An experimental determination of the dipole moments of the $X^1\Sigma^+$ and $A^1\Pi$ states of the BH molecule". In: *Canadian Journal of Physics* 47.11 (June 1969), pp. 1155–1158 (see pp. 219, 225).

[325] C. H. Douglass, H. H. Nelson, and J. K. Rice. "Spectra, radiative lifetimes, and band oscillator strengths of the $A^1\Pi$-$X^1\Sigma^+$ transition of BH". In: *The Journal of Chemical Physics* 90.12 (1989), p. 6940 (see pp. 219, 224).

[326] W. H. Smith. "Absolute oscillator strengths for the CH^+, CD^+, and BH $A^1\Pi$-$X^1\Sigma^+$ transition". In: *The Journal of Chemical Physics* 54.3 (1971), p. 1384 (see p. 219).

[327] J. Dufayard and O. Nedelec. "Lifetime of the BH $A^1\Pi$ state excited by a pulsed dye laser". In: *The Journal of Chemical Physics* 69.10 (1978), p. 4708 (see pp. 219, 223).

[328] O. Gustafsson and M. Rittby. "A study of the predissociation in the $A^1\Pi$ state of BH". In: *Journal of Molecular Spectroscopy* 131.2 (Oct. 1988), pp. 325–339 (see pp. 219, 223).

[329] W.-T. Luh and W. C. Stwalley. "The $X^1\Sigma^+$, $A^1\Pi$, and $B^1\Sigma^+$ potential energy curves and spectroscopy of BH". In: *Journal of Molecular Spectroscopy* 102.1 (Nov. 1983), pp. 212–223 (see pp. 219, 220).

[330] S. P. A. Sauer and I. Paidarová. "Calculations of magnetic hyperfine structure constants for the low-lying rovibrational levels of LiH, HF, CH^+, and BH". In: *Chemical Physics* 201.2-3 (Dec. 1995), pp. 405–425 (see pp. 221, 222, 226).

[331] H. J. Metcalf and P. van der Straten. *Laser cooling and trapping*. Springer-Verlag New York, 1999 (see p. 221).

[332] W. Lochte-Holtgreven and E. S. Vleugel. "Über ein Bandenspektrum des Borhydrides". In: *Zeitschrift für Physik* 70.3-4 (Mar. 1931), pp. 188–203 (see p. 223).

[333] S. H. Bauer, G. Herzberg, and J. W. C. Johns. "The absorption spectrum of BH and BD in the vacuum ultraviolet". In: *Journal of Molecular Spectroscopy* 13.1-4 (Jan. 1964), pp. 256–280 (see p. 223).

[334] F. S. Pianalto et al. "Vibration-rotation spectrum of BH $X^1\Sigma^+$ by Fourier transform emission spectroscopy". In: *Journal of Molecular Spectroscopy* 129.2 (June 1988), pp. 348–353 (see p. 223).

[335] A. T. Gilkison, C. Viteri, and E. Grant. "Coupling of electron orbital motion with rotation in the high rydberg states of BH". In: *Physical Review Letters* 92.17 (Apr. 2004), p. 173005 (see p. 224).

[336] E. R. Grant. "Private Communication". In: (2011) (see p. 224).

[337] M. P. Irion. "UV-laser photochemistry of diborane at 193.3 nm: The exchange reaction with deuterium". In: *The Journal of Chemical Physics* 76.5 (1982), p. 2338 (see p. 224).

[338] J. A. Harrison, R. F. Meads, and L. F. Phillips. "Emission spectra of BH_n fragments (n=0-3) from the 193 nm photolysis of diborane". In: *Chemical Physics Letters* 148.2-3 (July 1988), pp. 125–129 (see p. 224).

[339] W. C. Price. "The Absorption Spectrum of Diborane". In: *The Journal of Chemical Physics* 16.9 (1948), p. 894 (see p. 224).

[340] M. P. Irion and K-L. Kompa. "UV laser photochemistry and diborane at 193 nm: quantum yield for BH_3 production". In: *Journal of Photochemistry* 32.2 (Feb. 1986), pp. 139–142 (see p. 224).

[341] X. Zhuang et al. "Franck-Condon factors and radiative lifetime of the $A^2\Pi_{1/2}-X^2\Sigma^+$ transition of ytterbium monofluoride, YbF." In: *Physical Chemistry Chemical Physics* 13.42 (Nov. 2011), pp. 19013–7 (see p. 227).